Electrical and magnetic properties of II-VI diluted magnetic semiconductors

Horsfall, Alton Barrett

Electrical and Magnetic Properties of II-VI Diluted Magnetic Semiconductors

by

Alton Barrett Horsfall

A Thesis submitted in partial fufilment of the requirements for the degree of Doctor of Philosophy

University of Durham

1997

Abstract

The electrical and magnetic properties of MOVPE grown epitaxial layers of $Hg_{1-x}Mn_xTe$ layers has been investigated using a number of techniques. The samples have been grown by the Inter Diffused Multilayer Process (IMP) on (100) semi insulating GaAs substrates with ZnTe and CdTe buffer layers. The samples have been shown to show a number of phenomena nopt observed in the bulk material, such as an anomaly in the resistivity, magnetoresistance related to the intrinsic magnetism of the material, and saturation of the room temperature magnetisation.

In general the samples are of a highly compensated nature with the value of $|R_He|^{-1}$ varying between 10^{14} and $5x10^{17}$ cm^{-3} at 20K, the Hall mobilities varying between 8 and $3.5x10^5$ $cm^2V^{-1}s^{-1}$ at 20K. Magnetically, the samples generally show a paramagnetic signal that is swamped by the diamagnetic background of the substrate and buffer layers. The paramagnetism can be well modelled using a Curie Weiss fit. A number of the samples show a saturation in the magnetisation, which has been explained via the use of vacancy ordering within MnTe regions in the sample. The susceptibility of the samples has been investigated using a Faraday balance system, and this data has been fitted using a cluster model for Mn ions within the sample.

The photomagnetisation of $Cd_{0.9}Mn_{0.1}Te$:In has been investigated using a Faraday balance system, and modelled using the work of Dietl and Spalek, to calculate the number of polarons that had formed on donors in the sample, $\Delta N_D{}^{MAG} = 1.28x10^{15} cm^{-3}$. The number of donors in the sample has been measured by means of the Hall effect, $\Delta N_D{}^{ELEC} = 1.92x10^{15} cm^{-3}$, and this value compared to that obtained from the model. We have propsed a model to explain this discrepancy based on the concept of band tails in the impurity band.

To all those
who believed,
and helped
turn a dream,
into reality.

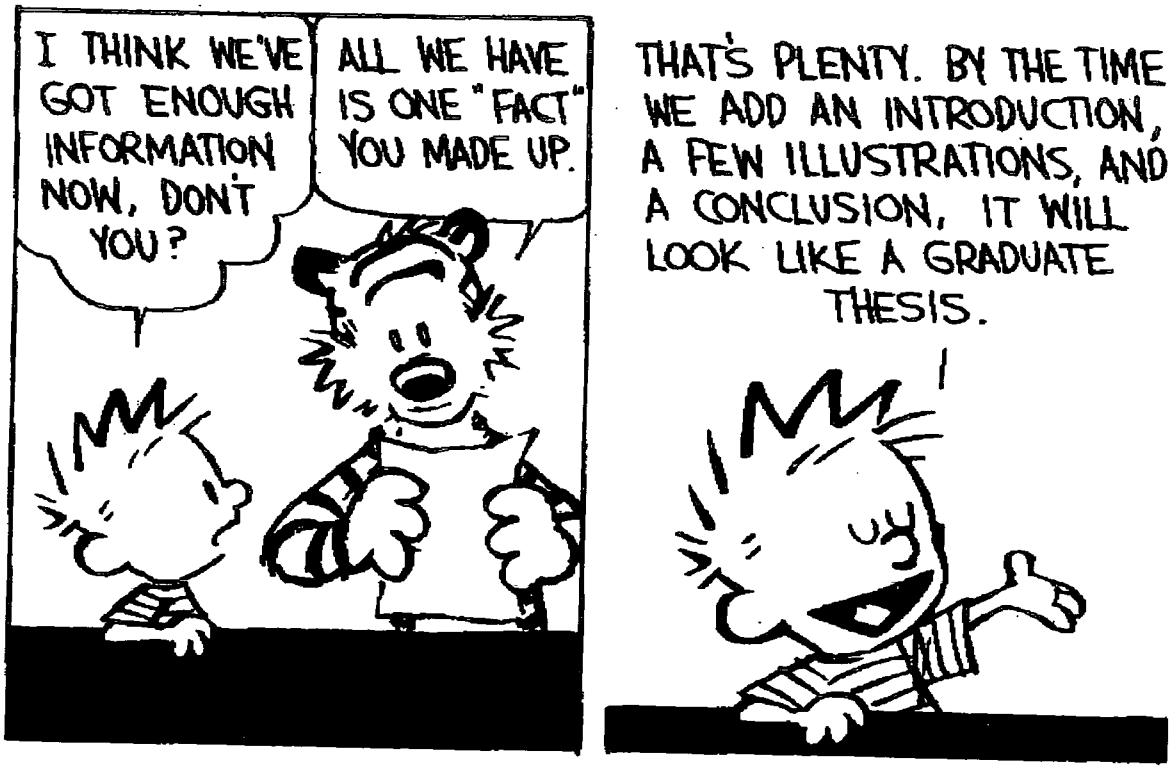

If only it was that easy.....

Acknowledgements

I would like to thank my supervisor Dr. Ian Terry for the help, wisdom, guidance and sense of humour over the past few years, it has been invaluable!

I am thankful to Professor Bloor and latterly Professor Tanner, the heads of department during my work, for the use of their facilities.

My heartfelt thanks to John Dobson for his technical support *par excellence*, as long as it didn't involve distracting him from his latest money making scheme.

Thanks to Dr Andy Brinkman and Dr Sener Oktik who grew the HgMnTe layers, and to Dr Piota Becla who provided me with the bulk samples.

Great thanks to Drs. Jon Makar and Toni Rogers who between them stopped me going completely crackers during the third year, and giving me hope that eventually I would escape the place, possibly in reasonable health.

To all the members of the solid state loony bin during my sentence, which in no particular order are Chris (Kermit) Gregory, Rob Luscombe, Chris (Mr Angry) Friend, Harry (Fashion Victim) Ramsbottom, Salamat (16 bit soundcard) Ali, Tom (HKT) Hase, Ian (Mr Nice Guy??) Daniel, Caroline (Rod) Moore, Ian (Gonzo) Pape, Brian Fulthorpe, John Clarke, Chris (Mackham) Leighton, and Hamidi Hamid, thanks a load. Also to the members of the polymer empire along the corridor, who have tret our office like a second home, namely James (Eggie) Egglestone and Stuart (Stu) Dailey.

Thanks to Paul Edwards and Matt Hogan, who have still not learnt to find a good excuse when I ask questions about the non operation of the electron microscope, and have stopped me trying to belt it with a large hammer on more than one occasion.

Thanks to Ed Holland, the greatest air-guitar player of all time (bar none) for his humour and assistance in room 57, when he really should have been writing up.

The staff in the workshops who regularly took my witterings and doodles and turned them into something resembling what I had anticipated (in varying timescales) and who didn't swear too much when I went back for the third alteration.....

Everybody in the teaching labs who allowed me to 'borrow' things on the promise they may see them again, eventually....

The entire secretarial staff and their wild Friday night outings.

Dan Read, one of my project students for his work on the Hall rig, which resulted in some fantastic data sets, and more unanswered (and unanswerable!) questions, Gwyn Ashcroft for his amazing MH loop for the MnTe sample, and Cathy Balch who obtained the MH loop for MMT16. Dr Caroline Moore who is responsible for the X-ray data in chapter one, John Lewis in the U.S. who is responsible for the optical transmission work, also in chapter one.

The exec of the orienteering club, who have managed to drag me off to some cold, wet, muddy, and dense forest despite my pleas that I really should be working, and then forcing me to drive. It'll be strange not having UDOC after seven years.....

To my parents, who supported me financially, and who often wondered whether I was ever going to finish this thing, well I have now!

And finally, to my fiance Dianne, who has kept a smile on my face over the past three years, maybe August 22nd will come a little faster now!

Contents

Chapter One Introduction

1.1 Introduction

A Diluted Magnetic Semiconductor (DMS) is a solid solution of a magnetic semiconductor and a non-magnetic semiconductor host lattice, in the case of HgMnTe, these are MnTe and HgTe. Most of the materials studied are of the form $A^{II}_{1-x}Mn_xB^{VI}$, although other materials have been investigated including $A^{IV}_{1-x}Mn_xB^{VI}$, $(A^{II}_{1-x}Mn_x)_3B^{V}_2$,[1] and more recently $A^{III}_{1-x}Mn_xB^{V}$. [2] Other magnetic ions can be used in the material, such as iron, chromium and europium, each of which give slightly different properties. Manganese is a popular choice for a number of reasons. It can be substituted into a lattice in large quantities, up to 80% in $Cd_{1-x}Mn_xTe$ and 75% in $Hg_{1-x}Mn_xTe$. Manganese has a large magnetic moment $5\mu_B$, (although europium has a magnetic moment of $7\mu_B$) and in a II-VI semiconductor such as HgTe it acts as a neutral impurity, and hence does not produce donors or acceptors.

1.2 Brief review of work performed on HgMnTe

The original work in the field was performed by Delves and Lewis [3] in 1963, when they investigated the growth of material with manganese concentrations between $0 < x < 0.8$. The majority of samples investigated were in the compositional range of $0 < x < 0.35$, because above this range precipitates of $MnTe_2$ are formed. [4] This is analogous to the behaviour observed in the growth of HgCdTe bulk samples. [5] The growth technique used for bulk samples is that of Vertical Bridgeman [6,7]. Further work [6] by Delves investigated the band structure, showing that the material is a direct gap semiconductor, with E_g varying as a function of manganese concentration.

The band structure of HgMnTe was later analysed by Davydov et al [8] using galvanometric measurements, who showed that the $E(k)$ energy spectrum could be explained using Kane's model [9]. This model states that the structure of the material can be explained by considering the effect of three bands. This is very similar to other zinc blende structure semiconductors, and the band structure in low field is very similar to that of HgCdTe. [10] This was confirmed by a number of groups work on the magneto-optical behaviour, such as Bastard et al [11]. The behaviour of E_g as a function of x is shown below in figure 1.1.

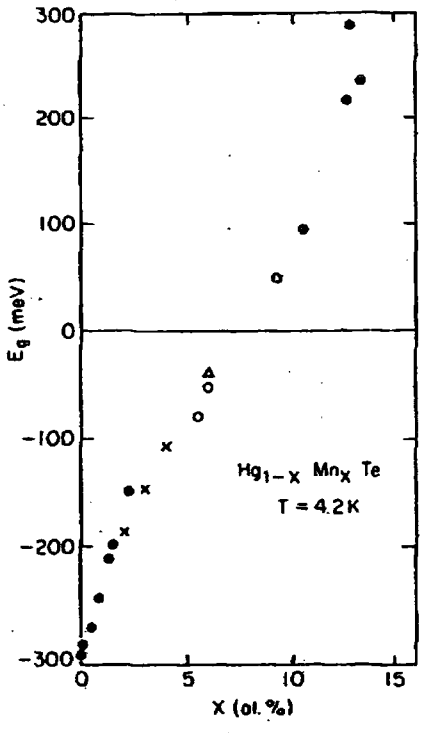

Figure 1.1 The band gap E_g as a function of manganese concentration in HgMnTe. The dots are from Bastard et al [11], the crosses from Jaczynski et al [12] and the triangle from McKnight et al [13].

The trend in E_g as a function of manganese substitution is very similar to that observed in HgCdTe with the change in cadmium concentration. The gradient $\frac{\delta E_g}{\delta x}$ in

HgMnTe is twice that in HgCdTe. [14]

The lattice parameter of the material has been measured using X-ray diffraction [15] and neutron diffraction [16]. A continuous transition from the lattice parameter of HgTe to that of zinc blende MnTe (grown by MBE), with a change in manganese concentration is observed. Hence the lattice parameter of $Hg_{1-x}Mn_xTe$ can be expressed using a form of Vegard's law, as discussed in section 1.5.3.

The crystal structure of HgMnTe has been determined from neutron diffraction experiments [17] to be that of zinc blende, and from these experiments it has been possible to determine that the lattice is arranged in an antiferromagnetic manner. The preferred order in DMS is that of type III antiferromagnetism, and this will be explained in more detail in chapter 3.

Electrically, it was shown by Delves [6] that as-grown undoped samples of HgMnTe show p-type behaviour with an acceptor concentration between 1 and $3x10^{16} cm^{-3}$, although the work of Furdyna has shown a value of $5x10^{18} cm^{-3}$ [4]. Delves' work postulated that the acceptors were due to copper impurities within the samples,[6] although more recent work [4] [18] has shown that the origin of these acceptors is mercury vacancies in the material. This observation is supported by the existence of acceptors caused by mercury vacancies in HgCdTe [19], and their affect on the electron transport. These vacancies are observable in the resistivity of the sample, and their activation energy is dependant on the composition of the sample [18]. Bulk samples are generally annealed under a mercury overpressure for 200 hours per mm of sample thickness at 200 °C after growth to remove this problem. [18]

The magnetoresistance of HgMnTe has been extensively studied, and the initial results are those of Delves [3]. He observed that in fields of upto 1T, the

magnetoresistance is positive, and shows evidence of saturation at high field. Davydov *et al* [20,21] saw a magnetoresistance that was positive at low field before turning over and becoming negative at fields above 0.7T. They explain this phenomena as being due to the exchange interaction in the sample, and the high field results are indicative of impurity band conduction.

The first investigations of the magnetism in HgMnTe were via the use of electron paramagnetic resonance (EPR). The variation of the line width and position as a function of manganese concentration has been analysed by a number of groups [22] who have shown that the gyromagnetic factor g is very nearly that of the free electron, $1.99 < g < 2.02$. [23] The EPR signal for low manganese concentrations, $x < 0.001$, is comprised of six hyperfine structure lines, which merge as the concentration is raised above $x = 0.02$. [24] The resultant line broadens as the concentration is raised above $x = 0.03$ [25] and also broadens with decreasing temperature [25]. This broadening with decreasing temperature is attributed to the internal field of the clusters, as they become more dominant at low temperatures.

Susceptibility measurements on HgMnTe showed that the material has a positive susceptibility, which at high temperatures follows a Curie Weiss law. [26,27] The value of θ shows a relationship to the manganese concentration, and is always -ve, showing the existence of antiferromagnetic interactions in the material.

At low temperatures, below 50K, the samples deviate from the Curie Weiss law, due to the interactions between the manganese ions [4,28]. The temperature at which the inverse susceptibility deviates has been shown to be dependant on the managanese concentration [4] The inverse susceptibility falls, and the value of θ approaches zero. The susceptibility can now be explained by the Curie law, [10] using

an effective number of ions in the sample. This effective number of ions can be translated as the number of ions that are uncoupled and can respond to the field. At low temperatures, the manganese ions form into clusters for concentrations above $x = 0.027$[10] and these clusters dominate the magnetisation.[29] The magnetisation in this region can be expressed using an empirically fitted Brillouin function [4] where the number of ions and the manganese concentration are replaced with effective values, which are used as fitting parameters. These values are tabulated and can be used to express the low temperature magnetic behaviour of HgMnTe samples.

The interaction that causes the formation of the clumps in the samples is that of the super exchange interaction [30], which is also responsible for the short range antiferromagnetic interaction observed in HgMnTe.

The specific heat of HgMnTe has been investigated by Nagata *et al* [29] who analysed the contribution of clusters as well as that of the single ions. From this they were able to calculate a distribution of cluster sizes, which were used to simulate his magnetic susceptibility, using a value for the exchange integral of $J / k_B = -7K$. The specific heat has also been modelled by Shapira [31] who used a random distribution, but used a higher value of the exchange integral, $J / k_B = -10K$.

In the quantum limit, the band structure of HgMnTe is no longer similar to that of HgCdTe, [32] because of the band splitting, and the lifting of the band degeneracy. One of the unique observations in DMS is the behaviour of the Shubnikov de Haas (SdH) oscillations. These oscillations arise from the crossing of the Fermi level and Landau levels in the sample. These oscillations were initially observed in HgMnTe by Delves [3] and by Morrissy [34], although a quantitative explanation was not possible due to a lack of knowledge of the band structure of the material. This was calculated

in 1978 by Bastard *et al* [11] and by Jaczynski *et al* [12]. From these measurements values of the exchange constants have been extracted. In the initial work, Jaczynski *et al* [12] obtained values of $\beta = 1.4\text{eV}$ and $\alpha = -0.7\text{eV}$, although later Sandauer and Byszewski [34] obtained $\beta = 0.8\text{eV}$ and $\alpha = -0.3\text{eV}$, which are closer to those obtained by other methods, including intra band magneto-absorption by Dobrowolska and Dobrowolski [35]. The amplitude of the SdH oscillations varies with temperature, and this is a phenomenon only observed in narrow band gap DMS, the basis of which is the temperature dependance of the Landau quantisation of the material, due to the contribution of the magnetic ions.

1.3 Growth of Bulk $Hg_{1-x}Mn_xTe$

The preferred method for bulk growth is the vertical Bridgeman technique [18] because of its simplicity. Pre-reacted HgTe and MnTe are ground and placed into a thick walled quartz tube. For samples with a Mn concentration greater than 5% the inside of the tube is coated in graphite. The tubes are sealed, evacuated and then heated to 450°C, where they are held for 24 hours, before being heated to 820°C where they are held for over 48 hours. [36] The growth is then performed at a rate of around 1mm hr^{-1}. This material in the as-grown state has a composition gradient along the growth direction as a result of the large segregation constant of the material. One way to overcome this is to use a travelling zone technique after the initial growth. The as grown bulk material crystallises with a Hg deficiency, hence creating Hg vacancies. These vacancies act as acceptors, with an acceptor energy of 9.4meV for a sample with a manganese concentration of x=0.15[37], and the as-grown material is p-type. N-type material is created by post growth annealing in a Hg rich vapour, usually for around 200 hours for every 1mm of sample thickness [36]

1.4 Growth of epitaxial $Hg_{1-x}Mn_xTe$

Epitaxial $Hg_{1-x}Mn_xTe$ can be grown by a number of methods, including LPE [38], MBE [39] and MOVPE [40]. The technique used in this study is metalorganic vapour phase epitaxy (MOVPE), in which the layer is deposited from the metalorganic species of the required element in the vapour phase. This requires a carrier gas, usually hydrogen, to transport the material to the substrate.

The quality of the samples grown by this technique is generally not as high as those grown by MBE, although due to the higher growth rate, they can be produced more rapidly. This is useful for commercial production of samples for industry.

Our samples were all grown on semi-insulating GaAs (100) substrates, which were cleaned by rinsing in trichloroethane and then etched in hydrogen peroxide /sulphuric acid mix. For the majority of the samples two buffer layers were grown before the $Hg_{1-x}Mn_xTe$ layer was started. The first of these is a 0.1μm thick layer of ZnTe, which forces the following layer to grow in the (100) direction. Without this the CdTe is likely to grow in the (111) direction on the GaAs [41] The second layer is a 1μm thick layer of CdTe, which acts as a lattice match to the $Hg_{1-x}Mn_xTe$ layer.

Two methods can be used to grow $Hg_{1-x}Mn_xTe$ by MOVPE. The first of these is Direct Alloy Growth (DAG) where the precursors are used simultaneously to grow $Hg_{1-x}Mn_xTe$ directly. The composition of the layer is determined by the relative partial pressures of the precursors. This was the first technique used to grow $Hg_{1-x}Mn_xTe$, [42] and it leads to compositional variations over the sample, sometimes in excess of 5% mm^{-1} [43]. Models of the gas flow within a MOVPE reactor during growth show that composition changes are inevitable.[44] This is not acceptable if the layer is to be used for devices. A refinement of this was to use to the technique of Interdiffuse

Multilayer Process (IMP) which had first been used by Tunnicliffe *et al* in the growth of $Hg_{1-x}Cd_xTe$.[45]

In IMP growth, a layer of MnTe is grown, and then a layer of HgTe, whilst the substrate is kept heated. This produces a layer in which the composition x is varied by the relative thicknesses of the two layers as shown in equation 1.1

$$x = \frac{t_2}{t_1 + t_2} \qquad (1.1)$$

where t_1 and t_2 are the thicknesses of the HgTe and MnTe layers respectively. This is shown schematically in figure 1.2.

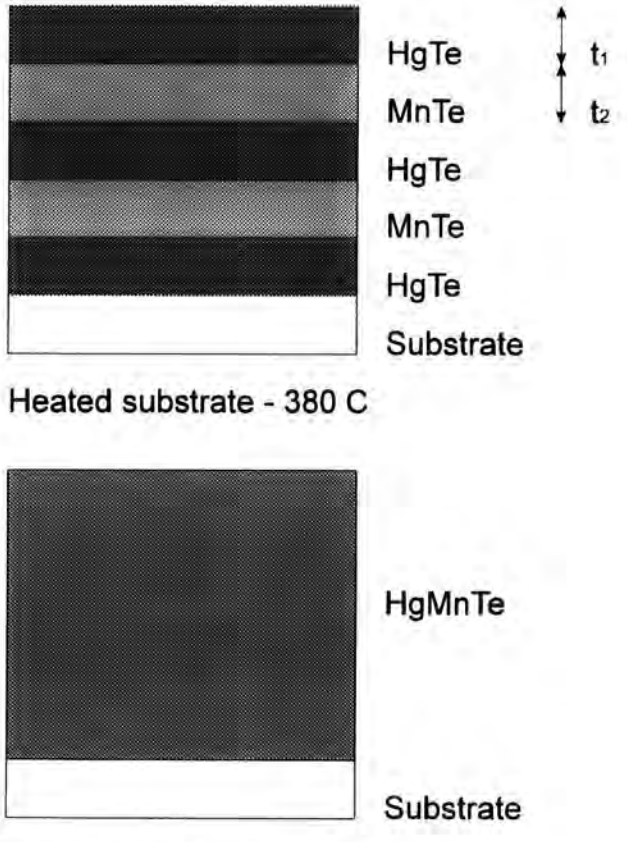

Figure 1.2 Schematic of the IMP growth process

Because of the technique there is a certain amount of time during which no growth occurs, as the source materials are being switched, from Mn to Hg. This time is generally referred to as the flush time, and for the samples grown in Durham is

usually about 39 seconds.

It has been found from work on HgCdTe [45] that providing the individual layers have a thickness below 0.1μm, then difussion will be complete within a 10 minute anneal at growth temperature in a flow of hydrogen and under a mercury overpressure. This anneal generally renders the sample to be n-type as the mercury overpressure compensates the mercury vacancies found in the as grown material.

Rapid interdifussion of the Hg and Mn in the layer is desirable to stop diffusion of material from the GaAs substrate. Hence, the thinner the grown layers, the less chance of this being a problem, because the growth process will be shorter in duration. The thickness of the buffer layer is also important in the control of substrate diffusion, and it has been shown that in HgCdTe the CdTe buffer layer has to be around 8μm before diffusion can be completely eradicated.[46]

This technique gives a compositional gradient that can be as low as 0.3% mm^{-1}, although some have gradients far higher than this, up to 2.8%mm^{-1} in some cases [47]. Examples of the compositional gradient are shown in figure 1.3 below.

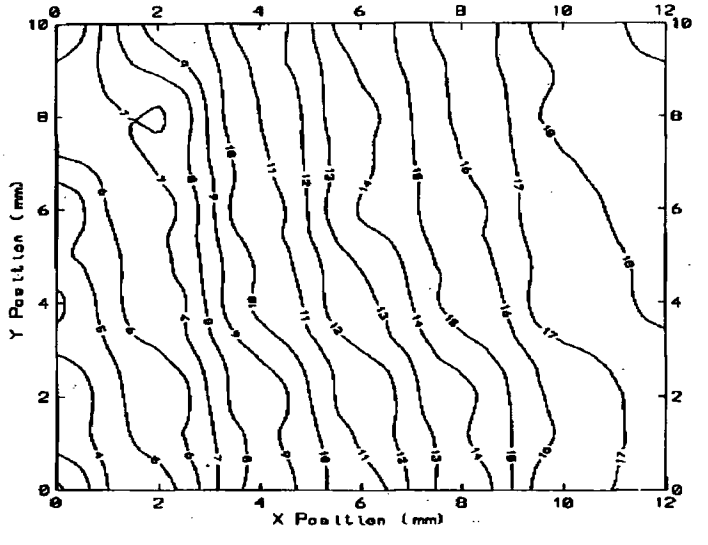

Figure 1.3 An example of the compositional gradient in HgMnTe epitaxial films, where the contour lines indicate percentage concentrations.

1.5 Characterisation of $Hg_{1-x}Mn_xTe$ films

Two techniques that have been used to characterise the films are electron microprobe analysis, also known as energy dispersive analysis of X-rays (EDAX) and high resolution X-ray diffraction. These allow calculation of the manganese concentration, layer thickness and an assessment of the sample quality, and are performed on samples prior to the magnetic and electron transport work, usually within six months of the layer being grown. The samples are sometimes examined under a scanning electron microscope to look for any surface features.

1.5.1 Scanning Electron Microscopy

The microcope ejects electrons from a cathode, which are then accelerated using a high potential (typically as high as 25KV), focused by electro-magnetic lenses and are then incident onto the sample. The current leaving the sample is then collected on the detector plate marked as P on figure 1.4

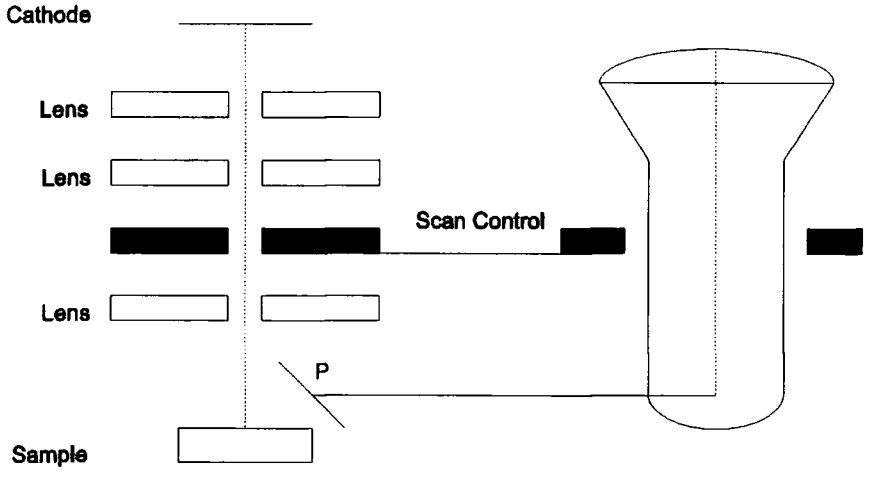

Figure 1.4 The scanning electron microscope

A number of different interactions occur when the electrons are incident on the sample. These occur at different locations within the generation volume, shown in figure 1.5.

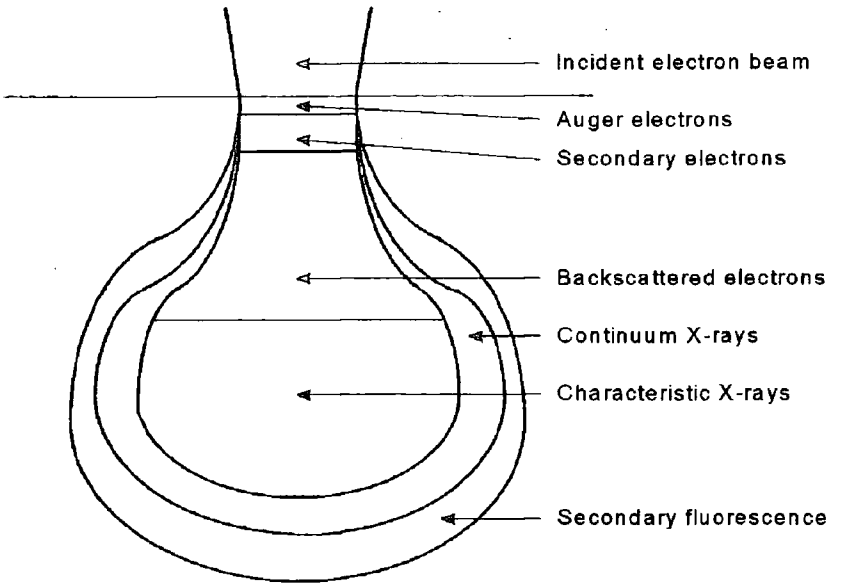

Figure 1.5 The electron - specimen generation volume

Imaging can be achieved using most of the interactions shown, although the most commonly used in Durham are secondary electron imaging and the use of the Xrays.

1.5.2 Electron Microprobe Analysis

Some of the incident electrons produce X-rays, which are a characteristic of the material in the sample. It is possible to analyse these X-rays by either wavelength or energy dispersion, the former having greater resolution, although the latter is a more rapid technique and more simple to operate. The measurements performed have all been via the energy dispersion method. The incident X-ray produces an electron - hole pair in the lithium drifted silicon detector, which is then accelerated by an applied voltage. The energy of the pair is then analysed by use of discriminators to give the energy spectrum.

To obtain the concentration of the samples under investigation, a number of bulk samples of known composition have been analysed by Hallam, [48] who has

found that the concentration is linked to the relative peak heights of the manganese and tellurium.

$$x = -0.0049 + 1.3738\left(\frac{I_{Mn}}{I_{Te}}\right) \qquad (1.2)$$

where I_{Mn} is the height of the Mn Kα peak, and I_{Te} the height of the Te L peak.

The use of the calibration removes the requirement to calculate the so called ZAF correction for the measurements. This correction is used to allow for the absorption of the X-ray emission by the sample.

For the samples under consideration, it was often seen that the layer was thin enough that the CdTe buffer layer was also visible in the spectra. This is because the X-rays are produced in the generation volume of the electron specimen interactions, which can have a depth of around 3μm, which is larger than some of the sample thicknesses.

To combat this, the ratio of $\frac{I_{Cd}}{I_{Te}}$ is used to calculate the contribution from the buffer layer. For bulk CdTe the ratio is 0.79, and hence the Te contribution from the buffer layer, can be calculated and subtracted. It is also possible to obtain an idea for the thickness of the sample using this analysis. This method of determining the thickness, provides in certain samples a large discrepancy with the thickness measured from cross-sectional SEM. A graph of manganese concentration and thickness taken from EDAX is shown in figure 1.6.

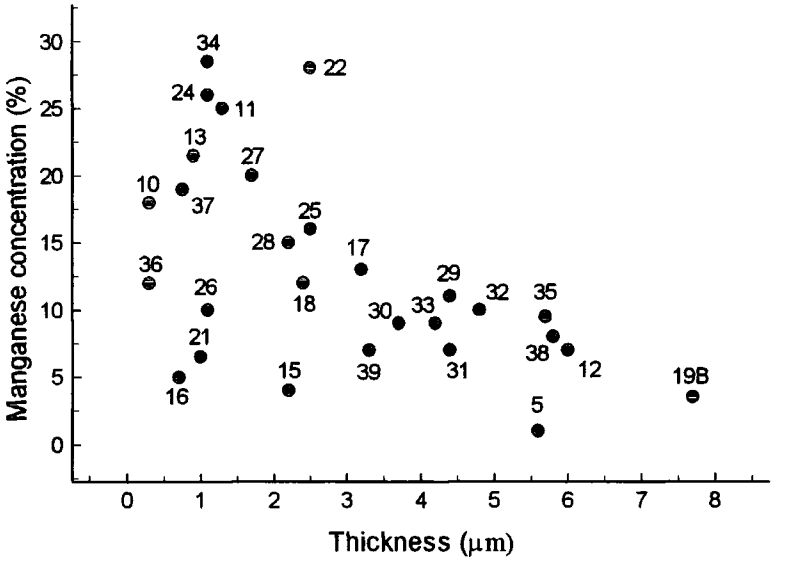

Figure 1.6 The thickness and manganese concentration of samples as determined from EDAX

The limit of accuracy for this technique is approximately 1%, and there are a number of problems in detecting light elements, as the efficency of X-ray production falls off rapidly for elements with a low atomic number, such as manganese.

1.5.3 High resolution X-ray diffraction

Compositional changes across the sample can be measured by the use of X-ray double axis diffraction. The lattice constant of the layer can be evaluated from the position of the Bragg peak and Bragg's law. The lattice constant is related to the manganese concentration by Vegard's Law for HgMnTe, equation 1.3.[1]

$$a = (1 - x)6.46 + 6.334x \qquad (1.3)$$

where a is the lattice parameter in the material measured in Å, and x the manganese concentration.

There is however a complication in performing this measurement on these samples. The $Hg_{1-x}Mn_xTe$ layer is grown on two buffer layers, as mentioned in section

1.4, and there will be a lattice mismatch between them. The purpose of the CdTe buffer layer is to lattice match the ZnTe buffer layer to the $Hg_{1-x}Mn_xTe$ layer grown above, through the formation of misfit dislocations. A certain amount of strain will be present in the $Hg_{1-x}Mn_xTe$ layer, from the small mismatch to the CdTe layer, changing the lattice parameter slightly from that observed in the bulk. This strain will also affect the position of the Bragg peak, and will give the impression of an incorrect Mn concentration. This means that the relaxation of the layer can be expressed as

$$R = \frac{a_l - a_o}{a_r - a_o} \qquad (1.4)$$

where a_l is the measured lattice parameter, a_r the relaxed lattice parameter, and a_o the lattice parameter of the substrate.

For the samples investigated the relaxation has been calculated as 95% [49], which means that the strain is almost completely removed by the presence of the buffer layer and the formation of dislocations at the interface.

The thickness of the samples can also be evaluated from X-ray data. The intensity of the peak from the GaAs substrate is compared to that obtained when the layer has been grown. The thickness can then be obtained

$$\frac{I_{(t)}}{I_{(0)}} = e^{\frac{-2\mu t}{\sin\theta_B}} \qquad (1.5)$$

where μt is the sum of the product of the absorption coefficent and the thickness for all the layers of the sample. [49] The absorption of the sample is dependant on the Mn concentration in the layer, and so this has to be corrected in any calculations. The technique gives the total thickness of the layer from the GaAs substrate, and so assumptions must be made as to the thickness of the buffer layers, to give a measure of the thickness of the $Hg_{1-x}Mn_xTe$. The calculated thickness of some

of the samples has been compared to that observed using a scanning electron microscope looking at the edge of the samples, and from estimates from the EDAX data.

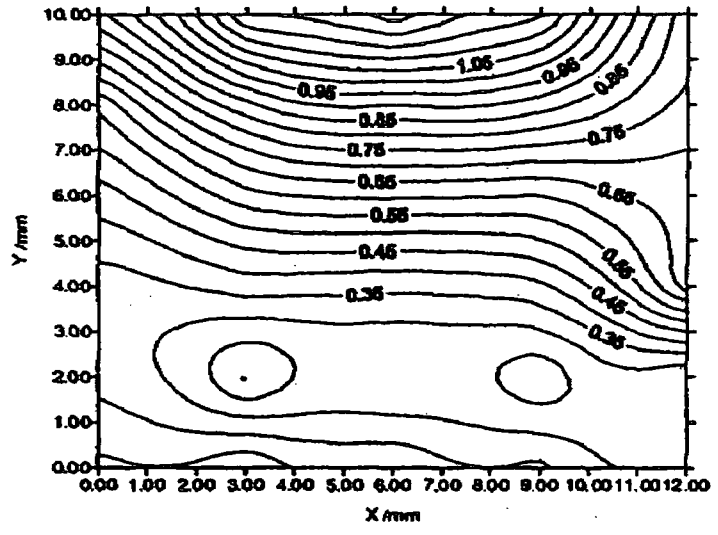

(a)

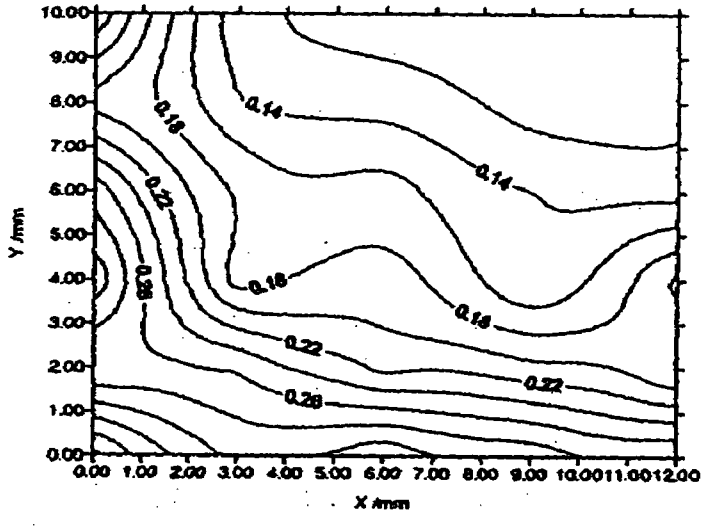

(b)

Figure 1.7 The thickness in microns (a) and manganese concentration (b) for sample MMT12 as determined by double axis X-ray diffraction [49]

The X-ray data has also shown that some of the samples, especially MMT16 and MMT28, have a high degree of polycrystallinity [49]. This is shown in the lack of a peak in the expected position for MMT, and the CdTe buffer layer is showing evidence of tilting and a high dislocation density. It has been suggested that in this circumstance MnTe will have deposited in a non epitaxial manner, and clusters will have been formed.

Other samples investigated in this manner have been shown to show the possible existence of MnTe clumps. In particular sample MMT18A has shown evidence of a peak occuring in a position that could be explained by existence of these clumps. [49] This is shown in figure 1.8.

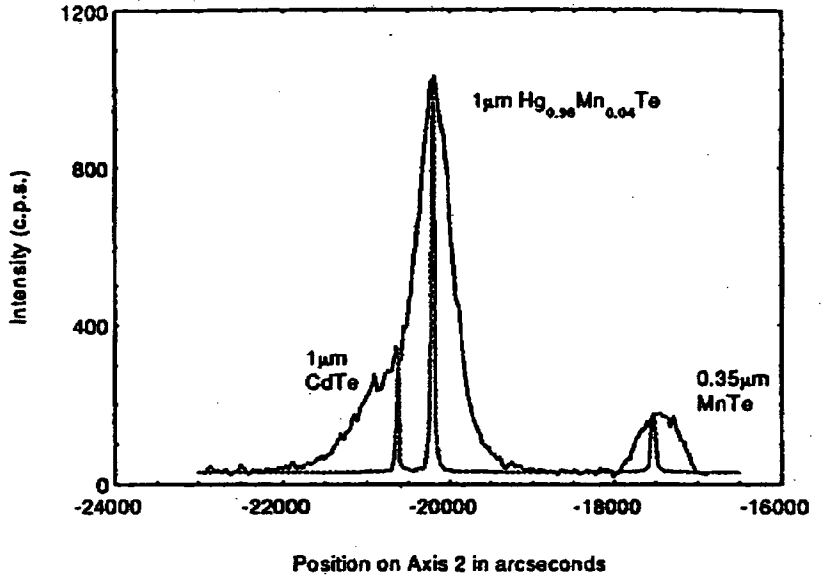

Figure 1.8 The presence of a MnTe peak in MMT18A

Other samples investigated have not shown the existence of such peaks, although it is still possible that they exist and are smaller than the limit of resolution of the system, which in this instance is 100nm [50].

1.5.4 Optical absorption

The transmission of a number of samples as a function of wavelength has been measured. The data is shown below in figure 1.9.

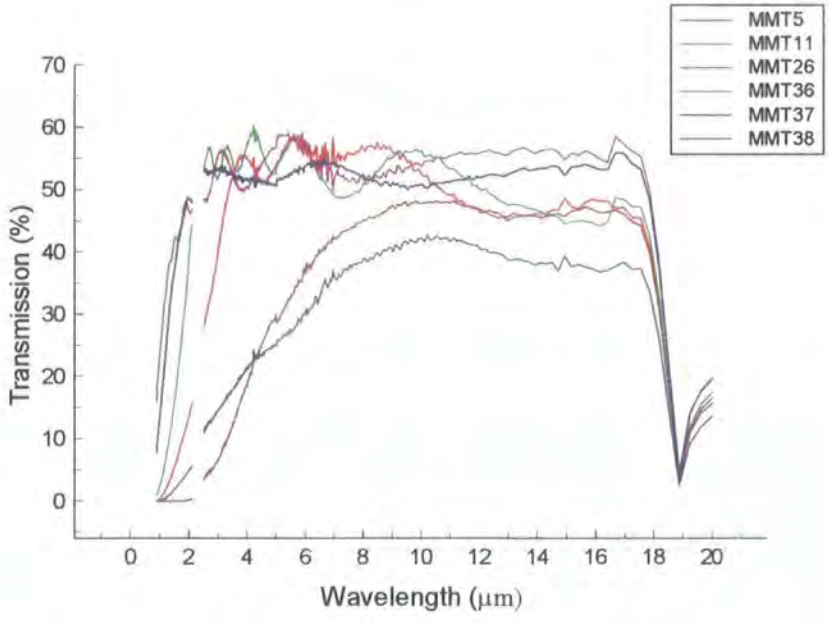

Figure 1.9 The optical absorption data

The gap in the data between 2.1μm and 2.5μm is due to contamination of the data from carbon dioxide and water vapour present. From the figure, it can be seen that the quality of samples MMT11, 26, 35, 36 and 37 is apparently higher than for MMT5 and 38. The data on sample MMT38 is misleading, as the thickness of this sample is 5.5μm, whilst the others are around 2μm.

The transmission of a sample can be expressed as

$$I_{out} = I_{in} e^{-\alpha d} \qquad (1.6)$$

where I_{in} and I_{out} are the incident and emergent intensities, d the thickness, and α the absorption coefficient.

The absorption coefficient of the investigated samples is shown in figure 1.10.

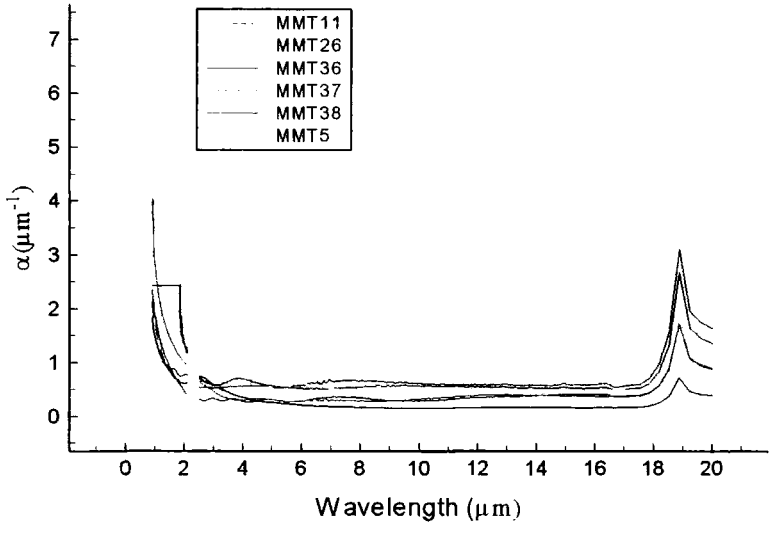

Figure 1.10 The absorption coefficient of the investigated samples

The drop in transmission at 18μm is due to the GaAs substrate on which the samples are grown. [51] The drop in the transmission that can be observed in all the samples at low wavelength, is absorption due to the band edge. This allows a calculation of the manganese concentration to be made, which is compared to that obtained by EDAX in table 1.1.

Sample	Manganese concentration (optical transmission)	Manganese concentration (EDAX)
MMT5	8%	Small
MMT11	21%	20 - 25%
MMT26	16%	10%
MMT36	21%	11%
MMT37	26%	14 - 29%
MMT38A	9.4%	5 - 8%

Table 1.1 The manganese concentration obtained from optical absorption.

The more gradual drop in the transmission data observed in samples MMT5 and 38 is due to there being a spread of managnese concentrations, and hence the band gap varies throughout the sample.

A comparison to the transmission data can be made to MBE grown material [40]

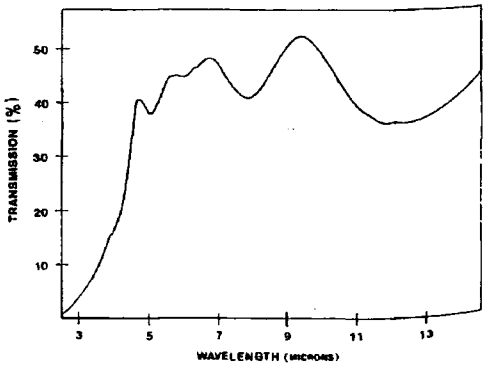

Figure 1.11 Optical transmission of MBE grown HgMnTe

Similar features can be observed in this sample as in the MOVPE grown samples investigated. The quality of this sample is similar to that of those investigated, as can be observed in the blurred band edge at around $4\mu m$.

Some of the samples show a set of fringes in the transmission data, an example of these are shown in figure 1.12.

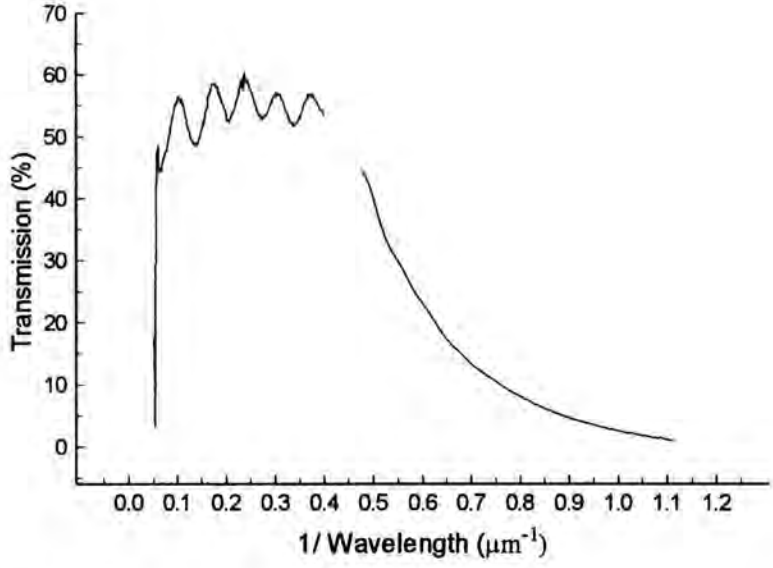

Figure 1.12 The transmission of sample MMT11

The fringes occur because of the interference of light from reflections within the sample and the direct transmission. This is shown in figure 1.13.

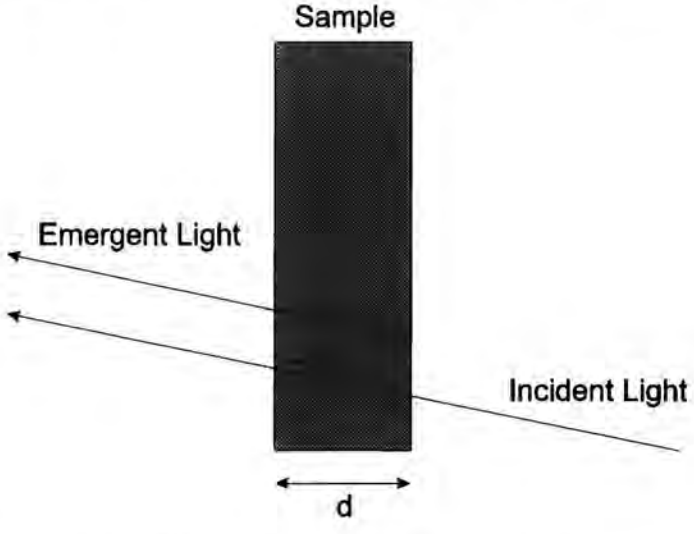

Figure 1.13 The origin of the fringes in the transmission data

The fringes can be expressed in the following equation [41]

$$m\lambda = 2dn \qquad (1.7)$$

where λ is the wavelength of the incident light, m the fringe number, d the thickness, and n the refractive index of the sample.

The refractive index is generally assumed to be independant of wavelength, and can be calculated from $n = \sqrt{\varepsilon}$, where ε is the relative permitivity of the sample, which is 15 in the case of HgMnTe.

The relationship is shown below for sample MMT11.

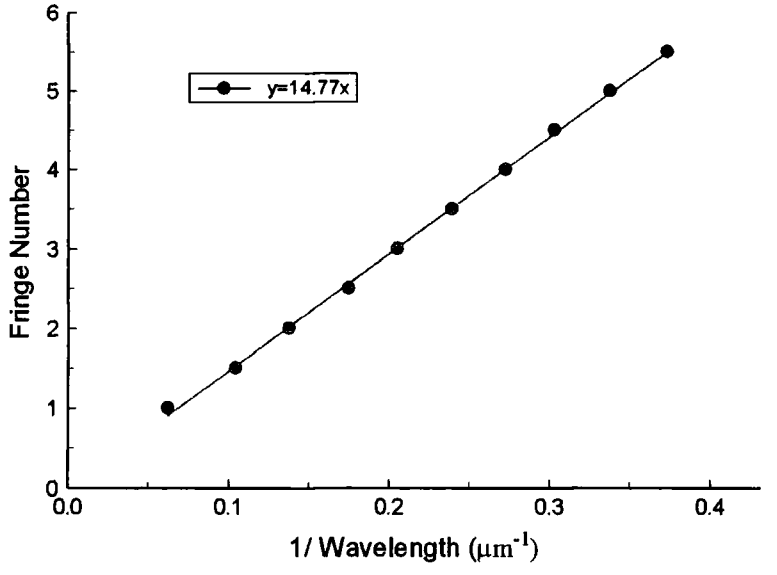

Figure 1.15 Fringe number as a function of inverse wavelength for MMT11

From this it is possible to give an estimate of the thickness of the layers, which for sample MMT11 is 1.91μm. The thicknesses of the other samples calculated by this technique are shown in table 1.2

Sample	Thickness (μm)
MMT5	No fringes
MMT11	1.91
MMT26	7.2
MMT36	0.989
MMT37	1.23
MMT38A	No fringes

Table 1.2 The thickness of samples determined from the fringe seperation

1.6 Motivation

The main importance of this work is to examine the suitability of MOVPE grown epitaxial HgMnTe as material for device construction. There are two main reasons why epitaxial material is preferred for device construction :

1. The growth of epitaxial layers takes place at relatively low temperatures (380°C rather than the 800°C required for bulk manufacture) and the layers are generally of higher quality than their bulk counterparts.

2. Epitaxial layers are necessary if physically smaller devices are to be manufactured.

A number of devices have been fabricated using HgMnTe.

1.6.1 Photodetectors

The main use for HgMnTe has been in the use of infra red photodetectors. For intrinsic material, the energy of the incoming photon will excite an electron to the conduction band if its energy is greater or equal to that of the energy gap of the

material. The wavelength that this occurs at is given by

$$\lambda_g = \frac{1.24}{\varepsilon_g} \qquad \text{Equation 1.7}$$

where λ_g is the wavelength of the incident light in μm and ε_g the energy gap in eV.

Because the energy gap of the material can be altered from 0eV up to 600meV, a wide range of photon energies can be detected using HgMnTe. Because of the large Zeeman splitting the energy gap in the material can be altered with the application of a magnetic field, and work by Wong et al [52] at 4.2K has shown this to be feasible. To be more useful to industry, this effect needs to be achievable at 77K or above, and this has been demostrated by Jain [53] in HgMnTe superlattices.

1.6.2 Light Emitting Diodes

The device is based around the injection of charge carriers across a p-n junction, as shown in figure 1.16.

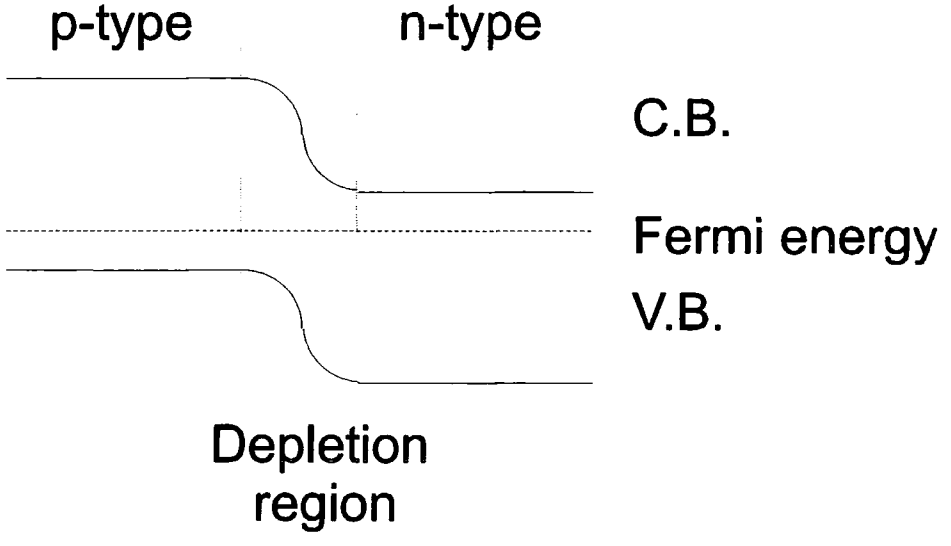

Figure 1.16 p-n junction structure

Under foward bias conditions, electrons are injected into the n-type region and holes into the p-type region. These carriers undergo recombination, which produces

photons, providing energy and momentum are conserved. This process is most efficient in direct gap material, such as GaAs and HgMnTe, as no momentum transfer is required.

The initial work on creating light emitting diodes from HgMnTe samples was performed by Becla [54] who created p-n junctions by partially annealing p type material under Hg.

More recently light emitting diodes have been fabricated in HgMnTe by the technique of two step liquid phase epitaxy on graded HgCdMnTe substrates by Becla [55]. These devices have been operated at 77K with an injection current of 12KAcm^{-2}, and have an output wavelength of 5.3 to 5.7μm. A higher saturation current density can be achieved by applying a transverse magnetic field to the device, because of the magnetoresistance of the material.[55]

1.6.3 Lasers

Very similar to the light emitting diode in the previous section, laser light can be produced from a semiconductor quantum well structure. The probability of electrons being in the conduction band is greater than that of them being found in the valence band, and a population inversion is produced. When a current is applied, spontaneous emission will occur from the recombination mechanisms that control the LEDs. The semiconductors has been cleaved so that the photons produced are internally reflected, and these photons cause other electrons to relax back into the valence band, creating further photons with the same phase as the original, i.e. stimulated emission. Hence the semiconductor begins to lase. Lasers in HgMnTe have been demonstrated by the work of Samarth and Furdyna [56].

Reference List Chapter One

[1] Furdyna, J.K., J Appl Phys, **64**, (1988), R29

[2] Ohno, H., Munekata, H., von Molnar, S., Chang, L.L., J Appl Phys, 69, (1991), 6103

[3] Delves, R.T., Lewis, B., J Phys Chem Solids, **24**, (1963), 549

[4] Furdyna, J.K., J Vac Sci Tech, **B9**, (1991), 1309

[5] Giriat, W., Furdyna, J.K., in 'Semiconductors and Semimetals', vol 25, eds Willardson, R.K., Beer, A.C., Academic Press, Boston, 1988, p1

[6] Delves, R.T., Br J App Phys, **16**, (1965), 343

[7] Holm, R.T., Furdyna, J.K., Phys Rev, **B15**, (1977), 844

[8] Davydov, A.B., Ponikarov, B.B., Tsidil'kovskii, I.M., Sov Phys Semicond, **15**, (1981), 504

[9] Kane, E., J Phys Chem Solids, **1**, 1956, 82

[10] Brandt, N.B., Moshchalcov, V.V., Advances in Physics, **33**, (1984), 193

[11] Bastard, G., Rigaux, C., Guldner, Y., Mycielski, J., Mycielski, A., J Phys Paris, **39**, (1978), 87

[12] Jaczynski, M, Kossut, J., Galazka, R.R., Phys Stat Sol, **b102**, (1980), 195

[13] McKnight, S.W., Amirtharaj, P.M., Perkowitz, S., Sol Stat Com, **25**, (1978), 357

[14] Furdyna, J.K., J Vac Sci Tech, **B9**, (1991), 1308

[15] Moore, C.D., 'X-Ray scattering studies of compound semiconductors', PhD thesis, University of Durham, 1997

[16] Furdyna, J.K., J Appl Phys, **53**, 7637

[17] Giebultowicz, T., Holden, T.M., in 'Diluted magnetic semiconductors', vol 25, eds Willardson, R.K., Beer, A.C., Academic Press, Boston, (1988), p125

[18] Giriat, W., Furdyna, J.K., in Semiconductors and Semimetals, vol 25, eds Willardson, R.K., Beer, A.C., Academic Bress, Boston, 1988, p.1

[19] Capper, P., J Vac Sci Tech, **B9**, (1991, 1667

[20] Davydov, A.B., Ponikarov, B.B., Tsidil'kovskii, I.M., Sov Phys Semicond, **15**, (1981), 504

[21] Davydov, A.B., Ponikarov, B.B., Tsidil'kovskii, I.M., Phys Stat Sol, **b101**,

(1980), 127

[22] Oseroff, S., Keesom, P.H., in Semiconductors and Semimetals, vol 25, eds Willardson, R.K., Beer, A.C., Academic Bress, Boston, 1988, p73 and references therein

[23] Materrese, L.M., Kikuchi, C., J Phys Chem Solids, **1**, (1956), 117

[24] Ishikawa, Y., J Phys Soc Japan, **21**, (1966), 1473

[25] Oseroff, S.B., Phys Rev, B25, (1982), 6584

[26] Andrianov, D.G., Gimmelfarb, F.A., Kushnir, P.I., Lopatinskii, I.V., Pashkovskii, M.I., Savelev, A.S., Fistul, V.I., Fiz Tech Polup, **10**, (1976), 111

[27] Savage, H., Rhyne, J.J., Holm, R, Cullen, J.R., Carroll, C.E., Wohlfarth, E.P., Phys Stat Sol, **58**, (1973), 685

[28] Brumage, W.H., Yarger, C.R., Lin C.C., Phys Rev, **133**, (1964), A765

[29] Nagata, S., Galazka, R.R., Mullin, D.P., Akbarzadeh, M., Khattak, G.D., Furdyna, J.K., Keesom, P.H., Phys Rev, **B22**, (1980), 331

[30] Spalek, J., Lewicki, A., Tarnawski, Z., Furdyna, J.K., Galazka, R.R., Obuszko, Z., Phys Rev, **B33**, (1986), 3407

[31] Shapira, Y., Foner, S., Ridgley, D.H., Dwight, K., Wold A., Phys Rev, **B30**, (1984), 4021

[32] Stankiewicz, J., Giriat, W., Bien, M.V., Phys Stat Sol, **b68**, (1975), 485

[33] Morrissy, C., PhD thesis, Oxford University, (1973)

[34] Sandauer, A.M., Byszewski, P., Phys Stat Sol, **b109**, (1982), 167

[35] Dobrowolska, M., Dobrowolski, W, J Phys C, **14**, (1981), 5689

[36] Kaniewski, J Cryst Grow. **60**, (1982), 179

[37] Wojtowicz, A., Mycielski, A., Act Phys Pol, **A67**, (1984), 363

[38] Becla, P., J Vac Sci Tech, **A3**, (1985), 116

[39] Reno, App Phys Lett, **47**, (1985), 1168

[40] Clifton, Semicon Sci Tech, **5**, (1990), 1067

[41] Maxey, C.D. *et al*, Semicon Sci Tech, **8**, (1993), S183

[42] Funaki, M., Brinkman, A.W., Hallam, T.D., Tanner, B.K., App Phys Lett, **62**, (1993), 2983

[43] Hallam, T.D. *et al*, J Cryst Grow, **146**, (1995), 604

[44] Funaki, M., Brinkman, A.W., J Cryst Grow, **139**, (1994), 211

[45] Tunnicliffe, J Cryst Grow, **68**, (1984), 245

[46] Port, R.I., 'Structural defects in MOVPE grwon CdTe/GaAs', PhD thesis, University of Durham, 1995

[47] Hallam, T.D., et al, J Cryst Grow, **146**, (1995), 604

[48] Hallam, T.D., 'The characterisation of epitaxial layers of the dilute magnetic semiconductor $Hg_{1-x}Mn_xTe$', PhD thesis, University of Durham, 1995

[49] Moore, C.D., 'X-Ray scattering studies of compound semiconductors', PhD thesis, University of Durham, 1997

[50] Tanner, B.K., Private communication

[51] Lewis, J., Private communication

[52] Wong, J Vac Sci Tech, **A4**, (1986), 2019

[53] Pain, G.N., in 'Diluted magnetic semiconductors', ed Jain, M., World Scientific, Singapore, 1991

[54] Becla, P., J Vac Sci Tech, **A4**, (1986), 2019

[55] Becla, P., J Vac Sci Tech, **A6**, (1988), 2725

[56] Samarth, Furdyna, J.K., Proc IEEE, **78**, (1990), 990

Chapter Two Electrical Theory

2.1 Outline of electrical transport

Electrical transport measurements can provide an insight in to band structure, lattice defects and impurity levels of the material under investigation. The motion of a charge carrier in a semiconductor lattice is determined by the scattering mechanisms that act upon it. Hence the mobility, which can be defined by $\sigma = ne\mu$, is a useful method for the evaluation of the dominant scattering mechanism in the material under investigation.

2.2 Mobility in semiconductors

2.2.1 Phonon Scattering

In polar crystals the most dominant form of phonon scattering is that associated with optical phonon scatter[1]. The initial work on this form of scattering was undertaken by Froehlich and Mott [2] and the application to polar semiconductors discussed by Petritz and Scanlon [3]. The strength of the interaction between the electron and the optical modes of vibration is characterised by a coupling constant α, given by

$$\alpha = \frac{l_e}{a_o}\left(\frac{m_e}{m}\right)\frac{\varepsilon_o(\varepsilon - \varepsilon')}{\varepsilon\varepsilon'} \qquad (2.1)$$

where a_o is the Bohr radius of the electron, m_e the effective mass of the electron, ε the static and ε' the high frequency permitivity, and l_e is a length scale defined as $\left(\frac{\hbar}{2m_e\nu_e}\right)^{\frac{1}{2}}$.

where ν_e is the frequency of the phonon.

For most semiconductors, being non-polar, the difference in the two permitivities is small, and so the value of α is also small. For polar materials such as II-VI compounds, ε' will include the polarization due to the motion of the ions, and so this will lead to the difference being larger. This is borne out by the fact that for CdTe the value of α is 0.35, whilst for GaAs it is only 0.06. Providing the value of α is below one then the mobility contribution from optical phonon scattering, μ_o, can be calculated following the work of Petritz and Scanlon,

$$\frac{1}{\mu_o} = \frac{3\pi^{\frac{3}{2}} \alpha m_e v_e}{2e} [f(z)]^{-1} \qquad (2.2)$$

$f(z)$ is an exponential factor given by

$$f(z) = \chi(z) \frac{[e^z - 1]}{z^{\frac{1}{2}}} \qquad (2.3)$$

where $z = \frac{h v_e}{kT}$ and $\chi(z)$ is a function that varies weakly with z.

From the above equations it can be seen that, due to the exponential behaviour of $f(z)$, $\frac{1}{\mu_o}$ becomes very small at low temperatures. This is because to create a phonon requires the lattice to have an energy of the order of $h v_e$, and this is just not possible at low temperatures. For polar materials such as cadmium telluride, it has been shown that optical phonon is the dominant scattering mechanism at high temperature[4]. This observation has been supported by Hallam, when considering the high temperature mobility of electrons in HgMnTe [5]

2.2.2 Ionized Impurity Scattering

The radius of the potential from a Coulombic impurity is infinite, hence a Coulombic impurity will have an infinite cross-section for scattering. This problem is overcome by the use of approximations, usually Cornell-Weiskopf or the Brooks-Herring. The calculation of the scattering of an electron by the Coulomb field of an ionized impurity can be calculated by the use of both classical mechanics and quantum mechanics, yielding the same result. In the Cornell-Wesikopf approximation the mobility is calculated from the standard scattering cross-section for scattering through θ into solid angle dw

$$\sigma(\theta)dw = \frac{1}{4}R^2\text{cosec}^4\left(\frac{\theta}{2}\right)dw \qquad (2.4)$$

where R is the maximum radius of cross-section, and is evaluated by equating the kinetic energy of the incoming electron and its potential in the Coulomb field of the impurity. Mathematically $R = \frac{Ze^2}{4\pi\varepsilon m_e v^2}$, Z is the atomic number of the impurity, ε is the permitivity of the material, m_e the mass of the electron, v the velocity of the incident electron.

This is integrated to get a value of σ_c, which is then placed into equation 2.5

$$(\tau_I)^{-1} = N_I\sigma_c v \qquad (2.5)$$

where N_I is the impurity concentration in the sample.

The average of this equation is taken to form $\langle\tau_I\rangle$ which is then substituted into equation 2.6

$$\mu_I = \frac{e}{m_e}\langle\tau_I\rangle \qquad (2.6)$$

This substitution gives the Cornell-Weiskopf formula for ionized impurity scattering

$$\mu_I = \frac{64\pi^{1/2}\varepsilon^2(2kT)^{3/2}}{N_I Z^2 e^3 m_e^{1/3}}\left[\ln\left(1+\left(\frac{12\pi\varepsilon kT}{Ze^2 N_I^{1/3}}\right)^2\right)\right]^{-1}$$

(2.7)

This equation shows the expected dependence of the mobility with temperature, namely that $\mu_I \propto T^{3/2}$.

The Brooks-Herring approach starts from Poisson's equation, with spherical symmetry assumed. The potential is calculated from

$$\frac{1}{r}\frac{d^2(r\phi)}{dr^2} = \frac{e(n'-n)}{\varepsilon} \qquad (2.8)$$

where n' is the potential of the scattering centre at distance r, n the potential at infinite r, and ε the permitivity of the material.

Taking the energy of the system to be of a Boltzman distribution we obtain

$$\phi = \frac{Ze}{4\pi\varepsilon r}e^{\frac{-r}{L_D}} \qquad (2.9)$$

where Z is the atomic number, and L_D the Debye length. The Debye length is a measure of the maximum distance at which the Coulomb field of the impurity can scatter carriers.

The scattering cross section can be calculated from this, which leads to the mobility relation of

$$\mu_I = \frac{64\pi^{\frac{1}{2}}\varepsilon^2(3kT)^{\frac{3}{2}}}{N_I Z^2 e^3 m_e^{\frac{1}{2}}}\left[\ln\left(\frac{24m_e k^2 T^2 \varepsilon}{e^2\hbar^2 n}\right)\right]^{-1}$$

(2.10)

As in the case of the Cornell-Weisskopf formula above, this shows the $T^{\frac{3}{2}}$ behaviour.

Obviously one of the problems of assuming a Coulomb-like potential is the problem of the potential becoming infinite at zero distance. Both of the above models counteract this by having a maximum potential set at a distance of a fraction of a Bohr radius [6], and then defining the potential at any smaller distance to being this value.

2.2.3 Neutral Impurity Scattering

This form of scattering is less likely to be dominant at high temperatures, where most of the donors in a system are expected to be ionized, but at low temperatures the number of neutral donors will far exceed the number of ionized ones. This system is thought to be analogous to the electron scattering by neutral hydrogen atoms [7]. Further work has shown that as long as the energy of the incident electron is sufficiently low, $E < \frac{E_i}{4}$, then this approximation will hold. (E_i is the ionization energy of the impurity) In this case the scattering cross-section can be given by [8]

$$\sigma_c = \frac{20a_1}{k} \qquad (2.11)$$

Where k is the magnitude of the wavevector of the electron, a_1 is the radius of the orbit of the outer electron in the neutral impurity.

The relaxation time of this system is given by

$$(\tau_N)^{-1} = \frac{20a_1 \upsilon N_n}{k} \qquad (2.12)$$

As τ_N is independent of energy, then the energy averaged value, $\langle \tau_N \rangle = \tau_N$. The mobility for neutral impurity scattering is given by the Erginsoy relation

$$\mu_N = \frac{2\pi\varepsilon W_n}{5N_n\hbar e m_e} \qquad (2.13)$$

where W_n is the binding energy of the impurity.

In this approximation the mobility is independent of both temperature and the energy of the incident charge carrier.

When the condition of $E < \frac{E_i}{4}$ is not held, the above relation is not valid, as is usually in the case of high temperatures. In this situation the impurity is treated like a square well potential that traps an electron in an excited state denoted by E_T, which is below the conduction band. If the value of E_T is smaller than the depth of the well, and the effective mass approximation is valid, we can obtain

$$\sigma_c = \frac{2\pi\hbar^2}{(E_k + E_T)m} \qquad (2.14)$$

which is referred to as Sclar's result [9]. This gives a mobility of

$$\mu = \frac{m^{3/2}}{2^{3/2}\pi\hbar^2 N_I}\left(\frac{E_k + E_T}{\sqrt{E_k}}\right) \qquad (2.15)$$

This Neutral Impurity scatter has a temperature coefficent with an exponent of 1/2 (from the energy term), compared to Erginsoy's equation which has $\mu\alpha T^0$. It should be remembered that this formula is only valid for neutral impurities at high temperatures.

2.2.4 Alloy Scattering

For a semiconductor that is constituted of two different materials, such as $Hg_{1-x}Mn_xTe$, then scattering can occur from the parts of the crystal which have different stoichiometry. The band structure of the alloy is written using the virtual crystal

potential, which gives an average of the pseudo-potential over the lattice sites. Any deviation from this is taken to be a perturbation, and is expressed as

$$V(r) = \sum_q V(q)\exp(iqr) \qquad (2.16)$$

Calculating the Fourier amplitude then allows the r.m.s. deviation from the mean field, and from this the rate of scatter can be determined by

$$\langle k|H|k'\rangle = (V_a - V_b)\left(\frac{x(1-x)}{N_c}\right)^{-1} \delta_{k \pm q - k',0} \qquad (2.17)$$

where $\delta_{k \pm q - k',0}$ is a Kroenecker delta function, which requires the momentum of the system before and after scattering to be conserved, x is the composition of the material (eg $Hg_{1-x}Mn_xTe$), N_c the density of states at the conduction band, and V_a and V_b are the potentials of the bands in the two constituent materials, k the incident wavevector, k' the emergent wavevector and H the interaction Hamiltonian.

and the scattering rate can be written as

$$W(k) = \frac{1}{2\pi\hbar^4}(V_a - V_b)^2 \Omega_o x(1-x)(2m)^{3/2} E(k)^{1/2} \qquad (2.18)$$

where Ω_o is the volume of the unit cell.

From the above equation it can be seen that the temperature dependence of $W(k)$ is $T^{1/2}$ (from $E(k)$), so that of the mobility will be $T^{1/2}$.

2.2.5 Dipole Scattering

In compensated systems oppositely charged impurities may associate themselves into pairs. These pairs can scatter electrons in the same way as a dipole, but they will have a distribution of the separation between the impurities. For a dipole moment of M the scattering potential of the dipole will be given by

$$V(r) = \frac{M.r}{4\pi\varepsilon r^3} \qquad (2.19)$$

From the Born approximation of wave scattering

$$\langle k'|eV(r)|k\rangle = \frac{ieM.(k'-k)}{\varepsilon V(k'-k)^2} \qquad (2.20)$$

The cross-section can be calculated in a manner similar to that used in the derivation of the Brooks-Herring model, leading to

$$\sigma(\theta) = \frac{e^2 M^2 N(E_k)}{24\varepsilon^2 \hbar v k^2 \sin^2\left(\frac{\theta}{2}\right)} \qquad (2.21)$$

From this the mobility of an electron, limited by dipole scatter is given by

$$\mu_D = \frac{3\pi 2^{3/2} \varepsilon^2 \hbar^2 E_k^{1/2}}{e^4 m^{1/2} r_o^{\,2} N_{DIP}} \qquad (2.22)$$

The temperature dependance of this form of mobility is $T^{1/2}$.

2.2.6 Dislocation scattering

This form of scattering has a negligible effect on the measurements of a material unless the dislocation density is larger than 10^8 cm^{-2}. They are thought to behave as cylindrical acceptor centres within the material, and as such will be highly anisotropic, with electrons incident normal to the cylinder being scattered far more than those being parallel. This form of scatter is of particular importance for material with low effective masses [10] The materials investigated by the author have a dislocation density of approx 10^9 cm^{-2} [11], but the dislocations are mostly located close to the interface with the buffer layer, and have a concentration which is inversely dependant on thickness[11]. As such, the upper part of the layer will have a far lower

dislocation density than the lower part, and as this part is more likley to be the region under investigation in any transport work on the samples, the scattering mechanism is not thought to be important in this case.

It has been found [12] that the mobility averaged over the electron energy distribution can be expressed as follows

$$\mu_{DIS} = \frac{30\sqrt{2}\varepsilon^2 d^2 (k_B T)^{\frac{3}{2}}}{q^3 N_{dis} f^2 L_D m^{*\frac{1}{2}}} \qquad (2.23)$$

where d is the distance between adjacent broken bonds (usually taken to be close to the lattice parameter), f the fraction of the acceptor centres occupied, N_{dis} the number of dislocations per unit area, L_D the Debye length, m^* the effective mass of the carrier, ε the permeability of the sample, and T the temperature.

2.2.7 Other forms of electron scattering

The main form of scattering not listed above is electron - electron scattering, which is only important for intrinsic narrow gap semiconductors at room temperature. For this scattering to be significant [13]

$$\tau_m \approx 10^{-5} n \qquad (2.24)$$

In order to obtain a relaxation time of the order of the other forms of scattering, which is 10^{-12} s, we require $n>10^{17}cm^{-3}$. As this is only applicable in intrinsic material, it can safely be ignored in this study.

The dependence of each of the scattering mechanisms on the effective mass of the carriers and the temperature is summarised below in table 2.1

Scattering mechanism	Temperature dependence	Effective mass
Optical phonon	$e^{\frac{1}{T}}T^{-\frac{1}{2}}$	m
Ionised impurity	$T^{\frac{3}{2}}(\ln T^2)^{-1}$	$m^{-\frac{1}{2}}[\ln(m)]^{-1}$
Neutral impurity	T^0	m^{-1}
Alloy	$T^{-\frac{1}{2}}$	$m^{-\frac{3}{2}}$
Dipole	$T^{\frac{1}{2}}$	$m^{-\frac{1}{2}}$
Dislocation	$T^{-\frac{3}{2}}$	$m^{-\frac{1}{2}}$

Table 2.1 Summary of scattering mechanisms

2.3 Mobility calculations

2.3.1 Matthiesen's Rule

In a sample with more than one form of distinguisable scattering mechanism, the relaxation time for the carriers can be calculated using Matthiesen's rule, which states

$$\frac{1}{\tau_{TOT}} = \sum_i \frac{1}{\tau_i} \qquad (2.25)$$

The equation is generally written in form of the mobility in the sample, as shown in equation 2.26

$$\frac{1}{\mu_{TOT}} = \sum_i \frac{1}{\mu_i} \qquad (2.26)$$

This equation does not hold if the relaxation time of the scattering is a function of k, the wave vector, as in this case the required averages $\frac{1}{\langle\tau\rangle}$ and $\left\langle\frac{1}{\tau}\right\rangle$ are not equal. A more realistic picture of collisions casts further doubts over the validity of equation 2.26. The assumtion that the scattering rate due to one mechanism is independent of the presence of the second, especially if the assumptions of the averaging of the relaxation times are dropped, becomes unlikely. It may be that the distribution function of the scattering machanisms are independent of each other, but in general they will not be. More accurately it can be shown that Matthiessen's rule can be expressed as an inequality [14]

$$\rho \geq \sum_i \rho_i \qquad (2.27)$$

2.3.2 The mean free path of carriers.

For electrons moving in a semiconductor between scattering sites it is possible to define a mean free path, similar to the one found in kinetic gas theory, to estimate the average distance travelled between scattering events. This can be expressed as

$$l = v_F \tau \qquad (2.28)$$

where v_F is the velocity of the carriers at the Fermi surface, and τ the relaxation time of the carriers.

The velocity of the carriers at the Fermi surface can be expressed as

$$v_F = \frac{\hbar k_F}{m_e} \qquad (2.29)$$

where m_e is the effective mass of the carrier at the Fermi surface, and k_F the wave vector at the Fermi surface, which, according to the free electron approximation can be expressed as $k_F = \left(3\pi^2 n\right)^{\frac{1}{3}}$.

The relaxation time of a carrier between scattering events is given by

$$\tau = \frac{\sigma m_e}{e^2 n} \qquad (2.30)$$

where σ is the conductivity of the sample.

Combining the above equations, we obtain

$$l = \frac{\hbar\sigma}{e^2}\left(\frac{3\pi^2}{n^2}\right)^{\frac{1}{3}} \qquad (2.31)$$

Linked to this is the Ioffe-Regel criterion, which states for real conduction [15]

$$\lambda^{-1} l \geq 1 \qquad (2.32)$$

If this criterion is not matched then the carrier is said to undergo hopping conduction, and the standard analysis of Hall effect and other such phenomena breaks down.

2.4 Van der Pauw analysis

The conventional method for transport measurements is to form a bar of the material under investigation and to place contacts along its length. An example of this is shown in figure 2.1

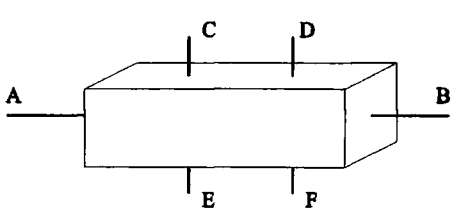

Figure 2.1 Conventional Hall bar

The current is passed between contacts A and B. The resistivity is calculated by measuring the resistance between a pair of adjacent contacts, eg C and D, and knowledge of the dimensions of the sample. The Hall effect can be measured across either of the two pairs of opposite contacts, i.e. C and E, D and F. This technique is often modified to the bridge shaped sample shown below, where the area under investigation is sufficently far from the contacts to allow the lines of current flow to be sufficently parallel.

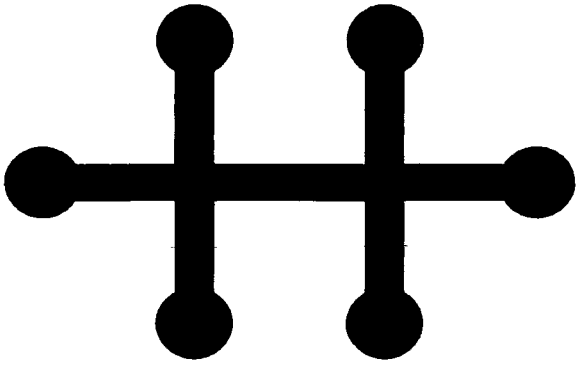

Figure 2.2 The bridge orientation for samples.

For samples of arbitary shape it is possible to use the Van der Pauw technique to calculate the resistivity without detailed knowledge of the sample area. Providing that the contacts used are small, located on the circumference of the sample, the sample thickness is homogeneous and is singularly connected then the resistivity of the sample can be easily calculated. The sample is considered in the complex plane and integrated around an open path t

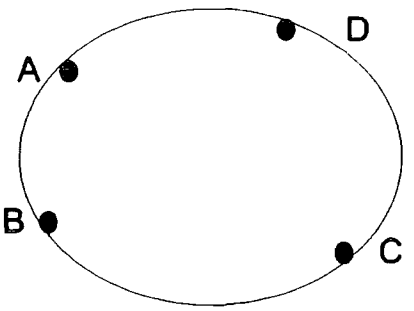

Figure 2.3 A Van Der Pauw contact arrangement

For the sample under investigation the current is passed between two adjacent conatcts A,B and the potential difference measured between the other two contacts C,D. This measurement is referred to as $R_{AB,CD}$. The resistivity can be calculated from

$$\rho = \frac{\pi d}{\ln 2} \frac{(R_{AB,CD} + R_{BC,DA})}{2} f\left(\frac{R_{AB,CD}}{R_{BC,DA}}\right)$$

(2.33)

where d is the sample thickness, and $f\left(\frac{R_{AB,CD}}{R_{BC,DA}}\right)$ is a function of the ratio that will satisfy the equation

$$\frac{R_{AB,CD} - R_{BC,DA}}{R_{AB,CD} + R_{BC,DA}} = f\operatorname{arcosh}\left(\frac{\exp\left(\frac{\ln 2}{f}\right)}{2}\right)$$

(2.34)

For isotropic samples $\frac{R_{AB,CD}}{R_{BC,DA}} \approx 1$ the equation can be expanded to give the following more useable form

$$f \approx 1 - \left(\frac{R_{AB,CD} - R_{BC,DA}}{R_{AB,CD} + R_{BC,DA}}\right)^2 \frac{\ln 2}{2} - \left(\frac{R_{AB,CD} - R_{BC,DA}}{R_{AB,CD} + R_{BC,DA}}\right)^4 \left(\frac{(\ln 2)^2}{4} - \frac{(\ln 2)^3}{12}\right)$$

(2.35)

Which leads to the following graph.

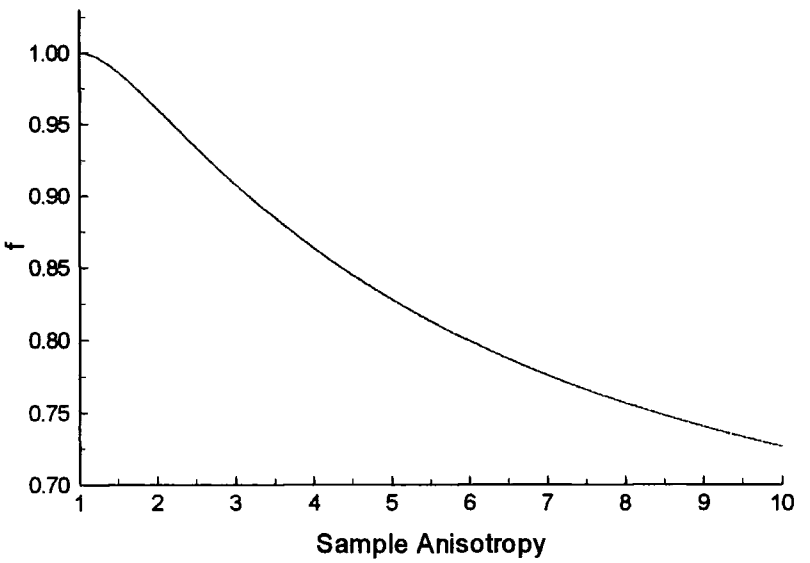

Figure 2.4 Variation of the anisotropy correction factor for low anisotropy of resistance.

The main problems with the analysis comes from the assumptions made in the derivation. If one of the contacts is misaligned towards the centre of the sample (i.e. away from the circumference) then errors will be introduced to the results. Considering one contact misplaced, the errors on the resistivity and Hall mobility can be given by equations 2.36

$$\frac{\Delta\rho}{\rho} = -\frac{d^2}{2D^2 \ln 2} \qquad (2.36.a)$$

$$\frac{\Delta\mu_H}{\mu_H} = -\frac{2d}{\pi D} \qquad (2.36.b)$$

where d is the displacement of the contact and D the size of the sample (usually taken to be circular in this analysis).

For a contact which has a finite size, s, (i.e. $\frac{s}{D}$ is not very small) then the errors on the measurement can be given by equations 2.37

$$\frac{\Delta\rho}{\rho} = -\frac{s^2}{16D^2 \ln 2} \qquad (2.37.a)$$

$$\frac{\Delta\mu_H}{\mu_H} = -\frac{2s}{\pi^2 D} \qquad (2.37.b)$$

The two errors are simply summed if both of these occur in the same sample.

An error on the resistivity measurement of 1%, is obtained if the value of $\frac{s}{D} < 0.33$ or the value of $\frac{d}{D} < 0.118$. For the mobility measurement the same error can be obtained with the value of $\frac{s}{D} < 4.93\text{x}10^{-2}$, or the value of $\frac{d}{D} < 1.57\text{x}10^{-2}$.

2.5 The Hall effect

2.5.1 Single carrier conduction

The Hall effect is a manifestation of the Lorentz force on a charged carrier moving under the influence of an applied electrical field. The force can be expressed as

$$\underline{F} = q(\underline{E} + \underline{v} \times \underline{B}) \qquad (2.38)$$

where q is the electronic charge, $\underline{E}$ the electric field vector, $\underline{v}$ the drift velocity of the carrier, $\underline{B}$ the applied magnetic field.

The most common form for the Hall voltage which is given [16] in 2.39.

$$V_H = \frac{BIR_H}{t} \qquad (2.39)$$

where I is the current through the sample, t is the sample thickness, and R_H is the Hall coefficient given by equation 2.40

$$R_H = \frac{-r}{nq} \qquad (2.40)$$

where n is the carrier density, and r is the Hall coefficent factor.

The Hall coefficent factor depends on the material under investigation, being a weak function of the band structure, the dominant scattering mechanism, and the energy distribution of the carriers [17]. However,as the dependance on these properties is weak, and the value of r is close to unity, and is often used as 1 in analysis. It can also be defined as the ratio of the Hall mobility of the material to the drift mobility of the material, as shown in equation 2.41.

$$r = \frac{\mu_H}{\mu} \qquad (2.41)$$

The Hall mobility μ_H can be expressed as a function of the carrier concentration and resistivity, and can be evaluated from the Hall voltage observed.

$$\mu_H = \frac{1}{ne\rho} \qquad (2.42)$$

and because of equation 2.39, this can be expressed as

$$\mu_H = \frac{t}{\rho}\left(\frac{V_H}{BI}\right) \qquad (2.43)$$

where $\left(\frac{V_H}{BI}\right)$ is the gradient of the experimental Hall effect data taken.

2.5.2 Multiple carrier conduction

If the material has a contribution from both the conduction and valence bands, then the Hall coefficent will also receive contributions from both bands. The weighting

of the contribution is proportional to the square of the mobilities of the respective carriers, as shown in equation 2.44 [17]

$$R_H = \frac{-\left(r_n \mu_n{}^2 n - r_p \mu_p{}^2 p\right)}{|e|\left(\mu_n n + \mu_p p\right)^2} \qquad (2.44)$$

where r_n is the Hall coefficent factor for electrons, μ_n the electron mobility, n the electron concentration, r_p the Hall coefficent factor for holes, μ_p the hole mobility, p the hole concentration.

This can also be expressed as a function of the mobility ratio, $b = \frac{\mu_n}{\mu_p}$, providing that $r_o = r_n = r_p$. [17]

$$R_H = \frac{r_o(p - b^2 n)}{|e|(p + bn)^2} \qquad (2.45)$$

The value of b can be calculated from the experimental data by examining the ratio of the maximum of the Hall coefficent to its value in the extrinsic region. Taking $R_H{}^{max}$ and $R_H{}^{ext}$ to be the Hall coefficent maximum and extrinsic value respectively, we obtain [17]

$$\frac{R_H{}^{max}}{R_H{}^{ext}} = \frac{-(b-1)^2}{4b} \qquad (2.46)$$

From equation 2.44 it can be seen that the Hall coefficient of a sample can be dominated by the minority carriers if their mobility is high enough. As an example if the concentration of holes in a p-type sample is $p = 1600n$ then the Hall coefficient will be negative as long as $\mu_n > 40\mu_p$. As the magnetic field is increased the Hall coefficient will become positive, as in the high field limit equation 2.44 can be expressed as

$$R_H = \frac{-1}{|e|(n-p)} \qquad (2.47)$$

and so the Hall coefficient is no longer affected by carrier mobilities.

2.5.3 The anomalous Hall effect

In a magnetic material, there is a contribution to the Hall voltage that is proportional to the magnetisation of the material. [18] This extra contribution is referred to as the anomalous Hall effect.

$$R_H^{meas} = R_H^{act} + R_H^{anom} \qquad (2.48)$$

Where R_H^{meas} is the measured value of the Hall coefficient, R_H^{act} the value from the 'real' Hall effect, and R_H^{anom} the anomalous contribution.

In a ferromagnetic material, the anomalous Hall coefficient, R_H^{anom}, can be expressed as [19]

$$R_H^{anom} = MR_S \qquad (2.49)$$

where M is the magnetisation of the sample, and R_S is proportional to the magnetic scattering in the material, and hence ρ. From this we can write [19]

$$R_H^{meas} = R_H^{act} + C\rho\chi \qquad (2.50)$$

where R_H^{meas} is the measured Hall coefficient, R_H^{act} the actual Hall coefficient in the sample, ρ the sample resistivity, χ the susceptibility, and C a constant.

This phenomena has been observed in ferromagnetic materials, amorphous magnetic alloys, and in InMnAs [20]

2.6 Magnetoresistance

When a magnetic field is applied to a material its resistance changes. The Lorentz force on the electron, which gives rise to the Hall effect, forces the move in a circular trajectory about the applied magnetic field. The resistivity of the material will increase as a consequence of this, as the mean free path of the electron is reduced. The mobility of the electron also shows a similar reduction with the application of a magnetic field. Hence the resistivity of the material should increase according to [21]

$$\frac{\Delta\rho}{\rho_o} \alpha B^2 \qquad (2.51)$$

Where B is the applied field.

This is the form of magnetoresistance observed in metals and some semiconductors. A more general form of the above equation shows that the magnitude of the magnetoresistance is proportional to the carrier mobility, and so for a material with one carrier type [22]

$$\frac{\Delta\rho}{\rho_o} = \mu^2 B^2 \qquad (2.52)$$

Where μ is the mobility of the carrier.

For a sample with a very small band gap and heavy compensation it has been shown that [23]

$$\frac{\Delta\rho}{\rho_o} = \mu_n \mu_h B^2 \qquad (2.53)$$

The majority of the samples studied can be considered as narrow band gap compensated material, and so equation 2.53 is likely to be applicable for most of the specimens in this work.

For a magnetic material, a negative magnetoresistance is often observed in the low field region, and is attributed to the scattering of the free carriers by magnetic impurities [24]. According to this theory,

$$\frac{\Delta\rho}{\rho_o} = -CM^2 \qquad (2.54)$$

Where M is the magnetisation of the sample, and C a constant.

Normally it would be expected in a system such as HgMnTe, that the magnetisation would be described via the use of either a Brillouin function or a Langevin function, as will be described in sections 3.3.3 and 3.3.4. It has been shown for very dilute systems containing manganese that the value of the magnetic moment used in the analysis is variant on temperature and field. The value of the total angular momentum J is found to be variant on the amount of manganese present, and this has been linked to the manganese forming clusters within the material [25].

Within the hopping regime, the magnetoresistance is dominated by the effect of electron wavelength shrinkage, which affects the tunneling ability of the carrier. Characteristics of the magnetoresistance in this regime are a positive magnetoresistance of the form [26]

$$\frac{\Delta\rho}{\rho_o} = Ce^{AB^2} \qquad (2.55)$$

Where C and A are constants.

2.7 Photoconductivity

The conductivity of a material can be defined from equation (2.42) as

$$\sigma = ne\mu \qquad (2.56)$$

Under illumination, a change in conductivity may occur, and so the new conductivity, $(\sigma + \Delta\sigma)$, can be expressed as

$$(\sigma + \Delta\sigma) = (n + \Delta n)e(\mu + \Delta\mu) \qquad (2.57)$$

From this it can be seen that there are two distinct methods of affecting the conductivity of the sample, changing the mobility of the carriers or changing the carrier density.

From simple semiconductor theory, illuminating a sample with light will produce a change in the carrier density if the energy of the incident photons are equal to the energy gap of the material. In this case an electron is promoted from the valence band to the conduction band, and a hole is formed in its place. This is shown in figure 2.5.

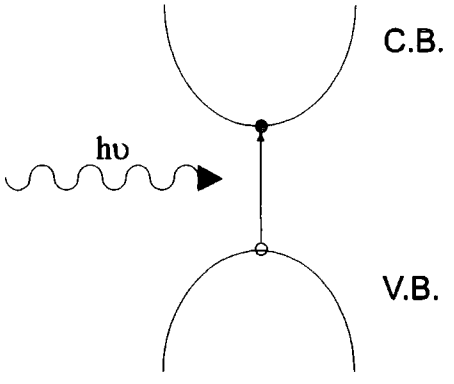

Figure 2.5 Intrinsic photoconductivity

Increases in mobility can be caused by a number of different mechanisms. If the scattering is dominated by charged impurities, the mobility can be affected by either changing the density of impurities in the material, or by changing their scattering cross-section.

If the material is polycrystalline in nature then illumination can reduce the height of the intergrain potential bariers, and reduce the depletion width at the interfaces.

If carriers are excited from one band to another, the mobilities of the two bands may be different, and so the overall mobility of the sample will change.

Reference List Chapter Two

[1] Smith, R.A., 'Semiconductors', Cambridge University Press, Cambridge, 1978, p 250

[2] Froehlich, H., Mott, N.F., Proc Roy Soc A **171**, (1939), 496

[3] Petritz, R.L., Scanlon, W.E., Phys Rev, **97**, (1955), 1620

[4] Smith, R.A., 'Semiconductors', Cambridge University Press, Cambridge, 1978, p 304

[5] Hallam, T.D., 'The characterisation of epitaxial layers of the dilute magnetic semiconductor $Hg_{1-x}Mn_xTe$', PhD thesis, University of Durham, 1995

[6] Ridley,B.K., Quantum processes in semiconductors, Clarendon Press, Oxford, 1988, p162

[7] Pearson, G.L.,Bardeen, J., Phys Rev **75**, (1949), 865

[8] Erginsoy, C., Phys Rev **79**, (1950), 1013

[9] Sclar, N., Phys Rev, **104**, (1956), 1548

[10] Egan, R.J., Chin, V.W.L., Journal of Applied Physics, **75**, (1994), 2475

[11] Moore,C.D., 'X-ray scattering studies of compound semiconductors', PhD thesis, University of Durham, 1997

[12] Podor, B., Phys Stat Sol, **16**, 1966, K167

[13] Ridley,B.K., Quantum processes in semiconductors, Clarendon Press, Oxford, 1988, p175

[14] Ziman, J., 'Electrons and phonons', Oxford, 1960, p286

[15] Ioffe, A.F., Regel, A., Prog Semicon, **4**, (1960), 237

[16] Hall, E.H., Am J Maths, **2**, (1879), 287

[17] Beer, A.C., in Hall effect and its applications, eds Chien, C.L., Westgate, C.R., Plenum Press, New York, (1980), p 42

[18] Pugh, E.M., Rostoker, N., Rev Mod Phys, **25**, (1953), 151

[19] Munekata, H., Penney, T., Chang, L.L., Surface Science, **267**, (1992), 342

[20] Ohno, H., Munekata, H., von Molnar, S., Chang, L.L., J App Phys, **68**, (1991), 6103

[21] Omel'yanovskii, E.M., Fistul, V.I., Transition metal impurities in semiconductors, Adam Hilger LTD, Bristol, 1986

[22] Beer, A.C., in Hall effect and its applications, eds Chien, C.L., Westgate, C.R., Plenum Press, New York, (1980)

[23] Li, D.X., Haga, Y., Shida, H., Suzuki, T., J Appl Phys, **80**, 1996, 264

[24] Toyozawa, Y., J Phys Soc Jpn, **17**, (1962), 986

[25] Krill, G., Lapierre, M.F., Phys Lett, **A35**, (1971), 301

Chapter Three Magnetic Theory

3.1 Introduction

Magnetism has fascinated man for centuries, and is one of the oldest areas of scientific study. The following chapter outlines the main forms of magnetism, and then concentrates on the magnetism relevant to HgMnTe.

3.2 Diamagnetism

For an ion or atom in a magnetic field, the total kinetic energy operator in the Schroedinger equation becomes [1]

$$T = -\frac{1}{2m}\sum_i \left(p_i - \frac{e}{2c} r_i \times H \right)^2 \qquad (3.1)$$

where p_i is the momentum of electron i, H the magnetic field, m the electron mass, e the electronic charge, c the velocity of light, and r_i the radius of the electron orbit.

At zero Kelvin, the magnetisation of a quantum mechanical system, $M_n(H)$, can be defined as [1], where $n = 0$.

$$M_n(H) = -\frac{1}{V}\frac{\partial E_n(H)}{\partial H} \qquad (3.2)$$

where V is the sample volume, and E_n the energy of the nth state of the system in a magnetic field H.

The value of the magnetisation at a finite temperature can be calculated from the thermal average of the magnetisation of each excited state of energy.

$$M(H,T) = \frac{\sum_n M_n(H) e^{\frac{-E_n}{k_B T}}}{\sum_n e^{\frac{-E_n}{k_B T}}} \qquad (3.3)$$

From this the susceptibility can be defined as

$$\chi = \frac{\partial M}{\partial H} \qquad (3.4)$$

The simplest material to consider is the case of an insulator with all the electronic shells filled. Such a material will have zero spin and zero orbital angular momentum in the ground state. This can be expressed using Pauli notation as

$$J|0\rangle = L|0\rangle = S|0\rangle = 0 \qquad (3.5)$$

from this it can be seen that only the ground state is important in the calculation, and this can be expressed as

$$E_o = \frac{e^2}{8mc^2} H^2 \langle 0|\sum_i (x_i^2 + y_i^2)|0\rangle \qquad (3.6)$$

Because of the spherical symmetry of the atom under consideration, it can be shown that the summation can be made over $\frac{1}{3} r_i^2$ rather than the Cartesian co-ordinate axes x_i^2 and y_i^2. Using this to calculate the susceptibility leads to

$$\chi = -\frac{N}{V}\frac{\partial^2 E_o}{\partial H^2} = -\frac{e^2}{6mc^2}\frac{N}{V}\langle 0|\sum_i r_i^2|0\rangle \qquad (3.7)$$

It is convenient to define a mean square radius by

$$\langle r^2 \rangle = \frac{1}{Z}\sum_i \langle 0|r_i^2|0\rangle \qquad (3.8)$$

where Z is the total number of electrons in the atom.

From this we can obtain the standard equation for diamagnetic susceptibility in a material.

$$\chi = -\frac{e^2}{6mc^2}\frac{NZ}{V}\langle r^2 \rangle \qquad (3.9)$$

This result is also referred to as the Langevin equation for diamagnetism, and can be obtained classically from a consideration of the orbits of electrons.

It should be noted from this equation that diamagnetism is a property of all material. The susceptibility of the material will always be negative, as the mean square radius of the electrons cannot be negative, and the temperature does not enter the equation implicitly. Any small fluctuation of the susceptibility with temperature is interpreted as the mean square radius fluctuating.

3.3 Paramagnetism

For a material that only has partially filled shells a different type of magnetism occurs. In this case the values of $|S\rangle$, $|L\rangle$ and hence $|J\rangle$ are unlikely to be zero, and methods of calculating these values have to be considered.

3.3.1 Hund's Rules

Originally derived from the atomic spectra of materials, these rules state the values of S, L and J. These can be expressed as

a. $S = \sum_i m_{si}$ The atom should have as many unpaired spins as possible, within the limits imposed by the Pauli exclusion principle.

b. $L = \sum_i m_{li}$ The angular momentum should be as high as possible, without contradicting rule a above. This is achieved by preferentially filling the L states to give the maximum value.

c. For a shell with less than half occupation $(n_e \leq (2l+1))$

$$J = |L - S|$$

For a shell with more than half occupation $(n_e \geq (2l+1))$

$$J = L + S$$

3.3.2 Van Vleck Paramagnetism

For a material with J=0, (one electron short of a half filled shell), the energy of the ground state can be expressed using second order perturbation theory as

$$E_o = \frac{e^2}{8mc^2} H^2 \langle 0 | \sum_i (x_i^2 + y_i^2) | 0 \rangle - \sum_n \frac{|\langle 0 | \mu_B H \cdot (L + g_o S) | n \rangle|^2}{E_n - E_o}$$

(3.10)

Calculating the susceptibility from this leads to an equation that gives two terms. The first of which is just the Langevin diamagnetism of the material, the other having a different sign. Hence this second term favours alignment parallel to the field, a behaviour referred to as paramagnetism.

$$\chi = -\frac{N}{V}\left[\frac{e^2}{4mc^2}\langle 0 | \sum_i (x_i^2 + y_i^2) | 0 \rangle - 2\mu_B^2 \sum_n \frac{|\langle 0 | (L_z + g_o S_z | n \rangle|^2}{E_n - E_o}\right]$$

(3.11)

This is the equation for Van Vleck Paramagnetism. Only the ground state of the system is occupied with any appreciable probability, and so this is most likely to be

observed at low temperatures. In many cases the next lowest energy state is also likely to be populated, and so the equation above has to be modified. This form of paramagnetism is temperature independent.

3.3.3 Paramagnetism in a set of identical ions

If in the ions only the lowest $2J+1$ states are thermally excited (to a reasonable probability), then the free energy of the system can expressed as

$$e^{-\beta G} = \sum_{J_z=-J}^{J} e^{-\beta\gamma H J_z} \qquad (3.12)$$

where $\gamma = g(JLS)\mu_B$ and $\beta = \frac{1}{k_B T}$.

The magnetisation in this system of N ions in volume V can, using (3.1) be given as

$$M = \frac{N}{V}\gamma J B_J(\beta\gamma JH) \qquad (3.13)$$

where $B_J(\beta\gamma JH)$ is the standard Brillouin function given by

$$B_J(x) = \frac{2J+1}{2J}\coth\left[\frac{(2J+1)x}{2J}\right] - \frac{1}{2J}\coth\left[\frac{x}{2J}\right] \qquad (3.14)$$

The value of the Brillouin function for several values of J is shown below.

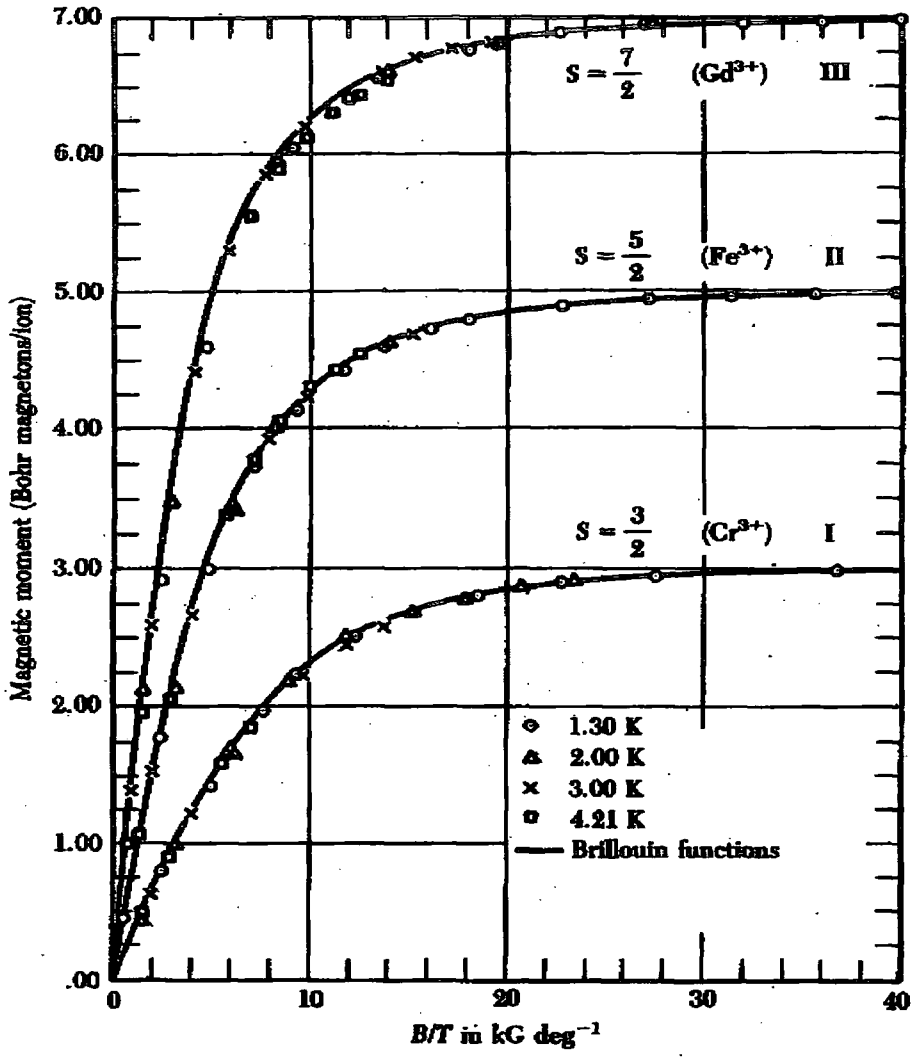

Figure 3.1 Brillouin function fits to paramagnetic materials [2]

In the small field limit, $\gamma H << k_B T$, the Brillouin function can be expressed as

$$B_J(x) \approx \frac{J+1}{3J} x \qquad (3.15)$$

This enables us to write the susceptibility of the material in low field as

$$\chi = \frac{N}{V} \frac{(g\mu_B)^2}{3} \frac{J(J+1)}{k_B T} \qquad (3.16)$$

Which compares to the classical Curie Law, expressed as

$$\chi = \frac{C}{T} \qquad (3.17)$$

This assumes that the interactions between the ions is far weaker than their interaction with the applied magnetic field.

In 1907 Weiss noted that the inverse susceptibility of some materials did not go to zero at 0K. Materials such as nickel and cobalt gave a positive intercept. Weiss postulated that these materials had internal interactions, which could be explained by the use of a molecular field. No justification of this postulation was made.

The susceptibility of a material in general can be explained by the use of the Curie Weiss Law.

$$\chi = \frac{C}{T - \theta} \qquad (3.18)$$

where θ is used as a fitting parameter. Positive values of θ are a characteristic of ferromagnetism, whilst negative values are antiferromagnetic. This is shown in figure 3.2.

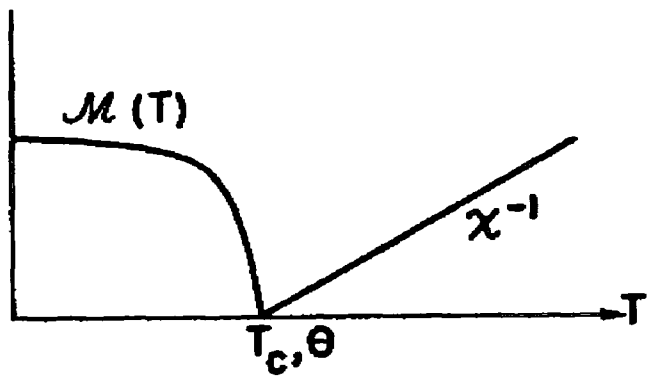

Figure 3.2.a The behaviour of magnetisation (M(T)) and inverse susceptibility (χ^{-1}) for ferromagnetic material [3]

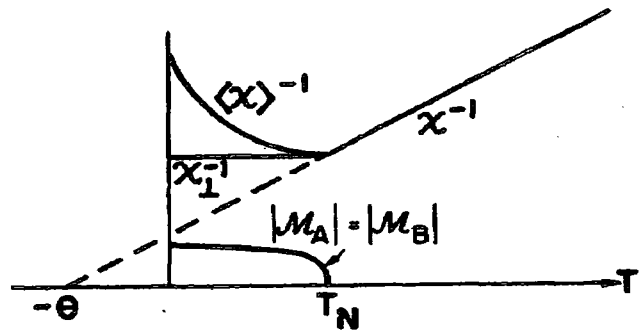

Figure 3.2.b The behaviour of magnetisation (M(T)) and inverse susceptibility (χ^{-1}) for antiferroferromagnetic material [3]

3.3.4 Superparamagnetism

The response of magnetic clusters within a non magnetic matrix has a behaviour which is similar to that of a paramagnet. Assuming that there is no interaction between the clusters, the magnetisation as a function of field and temperature is given by the Langevin function [4]

$$M = \coth\left(\frac{mB}{k_B T}\right) - \frac{k_B T}{mB} \qquad (3.19)$$

where $m = g\mu_B Jx$ and is often known as the number of effective Bohr magnetons per cluster. Another viewpoint on this is that $g\mu_B J$ is the magnetisation per ion and x is a measure of the number of ions within the cluster.

The above assumes that all the cluster have the same number of ions, whereas in reality there will be a distribution [4]. This distribution of sizes gives rise to a remanent field in the sample which increases as the temperature falls, and from the measurement of this it is possible to evaluate the distribution of particle sizes [5].

3.3.5 Zeeman splitting

In a magnetic field, an atom with magnetic moment μ will have a potential energy due to its orientation, which can be expressed as [6]

$$\Delta E = -\mu \cdot B \qquad (3.20)$$

In HgMnTe the electrons in the bands also gain a potential energy from this interaction. This energy removes the degeneracy for spin up and spin down carriers in the bands, forming two separate levels. The energy of each of these levels away from the original degenerate level can be expressed as,

$$\Delta E = \mu_B B g m_s \qquad (3.21)$$

where μ_B is the Bohr magneton, m_s the spin quantum number for electrons ($\pm 1/2$), and g the gyromagnetic ratio for electrons.

This is shown in figure 3.3

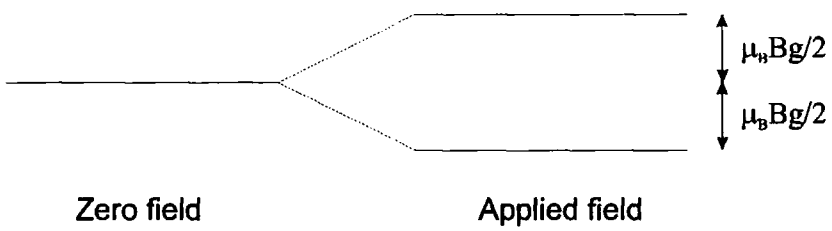

Figure 3.3 Effect of Zeeman splitting on a degenerate band

In a narrow gap semiconductor, such as HgMnTe, the Zeeman splitting can be of a sufficient magnitude to cause the bands to overlap, forcing the material to become semi-metallic. Because of the enhanced g factor in DMS, which can reach 300 or so at low temperature, the Zeeman splitting in HgMnTe is typically 20meV T^{-1}.

3.4 Direct exchange

The phenomenological internal field that was introduced by Weiss to explain the magnetism of ferromagnetic materials, had no explanation for twenty years. Then Dirac and Heissenberg independently discovered quantum mechanical exchange.

Consider two isolated atoms, each with one electron. Schroedingers equation for the system can be expressed as

$$\left[-\frac{\hbar^2}{2m}\left(\nabla_1^2+\nabla_2^2\right)+V(q_1)+V(q_2)\right]\psi = E\psi \qquad (3.22.a)$$

and the equivalent defining the Hamiltonian of the system,

$$H\psi = E\psi \qquad (3.22.b)$$

This assumes that the two electrons are distinguishable with co-ordinates q_1 and q_2. The solutions to this equation are given as

$$\psi_a(1)\psi_b(2) \qquad (3.23.a)$$

$$\psi_b(1)\psi_a(2) \qquad (3.23.b)$$

The total energy of this system can be expressed as $E = E_a + E_b$. In reality the electrons are indistinguishable and so these two waveforms cannot be solutions to this. Linear combinations of the two solutions can satisfy the requirements and so we obtain

$$\psi_{sym}(1,2) = \frac{1}{\sqrt{2}}\left[\psi_a(1)\psi_b(2) + \psi_b(1)\psi_a(2)\right] \qquad (3.24.a)$$

$$\psi_{anti}(1,2) = \frac{1}{\sqrt{2}}\left[\psi_a(1)\psi_b(2) - \psi_b(1)\psi_a(2)\right]$$

(3.24.b)

From the Pauli exclusion principle, all electron wavefunctions are anti-symmetric. The wavefunctions given above have spatial and spin components, which can be separated, $\psi_a = \phi_a(r)\chi_a$, $\psi_b = \phi_b(r)\chi_b$. The wavefunctions can now be constructed from a symmetrical spatial component and an antisymmetric spin component and vice versa.

This gives the electron wavefunctions to be

$$\psi_I = \frac{1}{\sqrt{2}}\left[\phi_a(1)\phi_b(2) + \phi_b(1)\phi_a(2)\right]\left[\chi_\alpha(1)\chi_\beta(2) - \chi_\beta(1)\chi_\alpha(2)\right]$$

$$\psi_{II} = \frac{1}{\sqrt{2}}\left[\phi_a(1)\phi_b(2) - \phi_b(1)\phi_a(2)\right]\left[\chi_\alpha(1)\chi_\alpha(2)\right]$$

$$\psi_{II} = \frac{1}{\sqrt{2}}\left[\phi_a(1)\phi_b(2) - \phi_b(1)\phi_a(2)\right]\left[\chi_\alpha(1)\chi_\beta(2) + \chi_\beta(1)\chi_\alpha(2)\right]$$

$$\psi_{II} = \frac{1}{\sqrt{2}}\left[\phi_a(1)\phi_b(2) - \phi_b(1)\phi_a(2)\right]\left[\chi_\beta(1)\chi_\beta(2)\right]$$

(3.25)

In the case of ψ_I a singlet state is produced with antiparallel spins, giving $S = 0$. In the case of ψ_{II} a triplet state is produced with parallel spins, giving $S = 1,0,-1$.

If the interaction between the atoms is considered, perturbation theory can be used to calculate the energy of the system.

$$E = \int \psi_I^* H_{12} \psi_{II} d\tau_1 d\tau_2 + \int \psi_{II}^* H_{12} \psi_{II} d\tau_1 d\tau_2$$

(3.26)

where H_{12} is the Hamiltonian of the interaction between the two electrons

The energies for the parallel and antiparallel states can be expressed as

$$E_I = K_{12} + J_{12} \qquad (3.27.a)$$

$$E_{II} = K_{12} - J_{12} \qquad (3.27.b)$$

where K_{12} is the average energy of the Coulomb interaction between the electrons, and J_{12} is the exchange integral that comes from the indistinguishability of the electrons. These are defined as

$$K_{12} = \int \phi_a^*(1)\phi_b^*(2)H_{12}\phi_a(1)\phi_b(2)d\tau_1 d\tau_2$$

$$J_{12} = \int \phi_a^*(1)\phi_b^*(2)H_{12}\phi_a(2)\phi_b(1)d\tau_1 d\tau_2$$

(3.28)

Considering the spins of the two possibilities, parallel and antiparallel, we can write the energy of the system to be

$$E = K_{12} - \frac{1}{2}J_{12} - 2J_{12}\underline{S}_1 \cdot \underline{S}_2 \qquad (3.29)$$

This equation is confusing, as the energy of the exchange appears to be related to the spin of the electrons, when in fact it is a function of the spatial part of the wavefunction. This can be represented by considering the spins of the system, as the two are related by Pauli's exclusion principle.

The exchange integral shows whether the material is ferromagnetically coupled or antiferromagnetically coupled. For antiparallel spins, the value of J_{12} is negative, i.e. antiferromagnetism. The parallel case leads to positive values of J_{12}, i.e. ferromagnetism.

3.5 Indirect exchange

In a material such as zinc blende MnTe, the distance between adjacent Mn ions is 4.5Å. According to the model of Heisenberg outlined in section 3.4 the material would be expected to show a weakly ferromagnetic behaviour. In fact cubic MnTe is antiferromagnetic below 60K [7], and so it follows that a different mechanism must be responsible, that of super exchange, introduced in 1934 by Kramers [8]. The anion that separates the Mn ions is responsible for the interaction between the Mn ions, although there will be a small contribution from the expected ferromagnetic mechanism. Although the distance between manganese ions is less for those which subtend a 90° angle at the cation, the interaction is stronger for those which are diametrically opposite, as shown in figure 3.4, for MnO. [9]

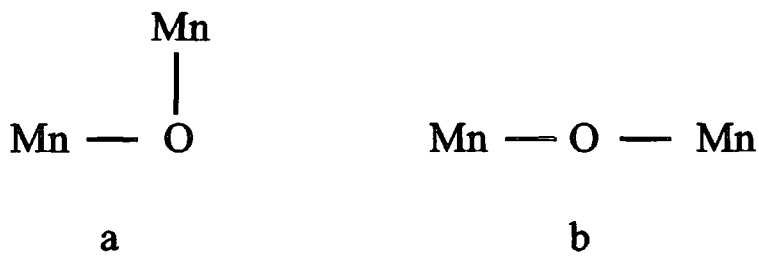

Figure 3.4 The contrast between the two orientations of the Mn - Mn interaction.

This is due to the shape of the p orbital in the anion which has a charge distribution concentrated in one dimension. A small interaction with the nearest neighbours is possible, [10] due to the hybridisation of the 2s and 2p orbitals of the ion. This is however, far smaller than that seen for just the p orbital.

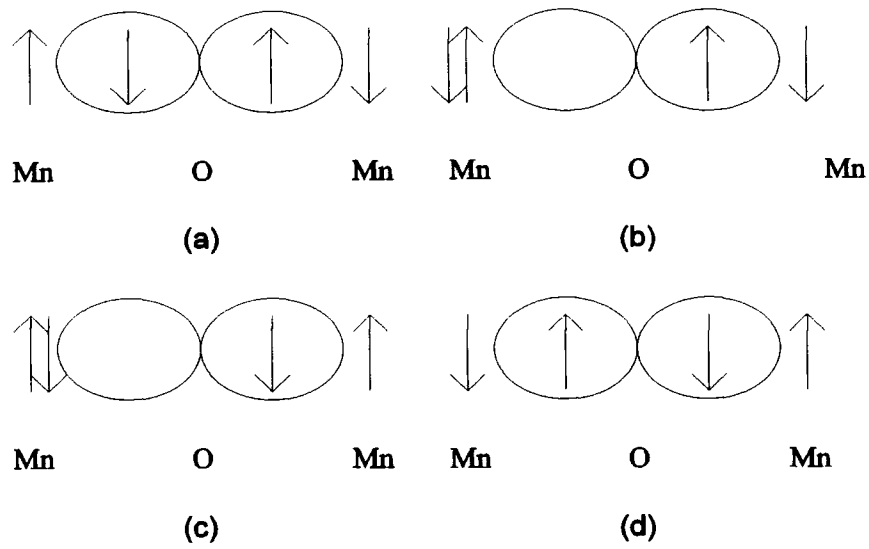

Figure 3.5 Schematic representation of super exchange

The mechanism can be explained in the following manner. The ground state of the system is shown in figure 3.5.a. One of the electrons from the anion (in this case oxygen) is transferred to the Mn ion adjacent, figure 3.5.b. Due to thermal excitation, the spin on the electron on the opposing Mn ion flips, forcing the electron spin on the anion to follow suit. The electron that made the initial transfer is now unable to return to the anion, because of Pauli's exclusion principle, and so the other electron is transferred instead. This gives rise to an antiferromagnetic coupling between the Mn ions.

This mechanism can be described by perturbation theory, and the coupling between the Mn ions is found to be,

$$S_{d1}S_{d2}\left[\frac{1}{E_{II}{}^2}-\frac{1}{E_{\perp}{}^2}\right]e^2J \qquad (3.30)$$

where S_{d1} and S_{d2} are the spins of the ions, E_{II} the energy required to form parallel spins, $E_{\perp}$ the energy required to form antiparallel spins.

The above description assumes that only one of the electrons on the oxygen is transferred to the manganese. Obviously both of the electrons are likely to move, hence the coupling coefficient is twice as large as would be derived from the above.

3.6 Long Range Interactions

In wide gap diluted magnetic semiconductors Larson [10] has shown that the interaction consists mainly of super exchange with around 5% Bloembergen Rowland interaction. For a narrow gap material one can expect gap dependant mechanisms such as Bloembergen Rowland and RKKY to become more significant. These mechanisms are discussed below.

3.6.1 Dipole interaction

The magnetic moments in the material are coupled by the dipole - dipole interaction, for which the Hamiltonian can be expressed as [15]

$$H_{ij} = \frac{g^2 \mu_B{}^2}{r_{ij}{}^3}\left[\underline{S}_i \cdot \underline{S}_j - 3\frac{(\underline{S}_i \cdot \underline{r}_{ij})(\underline{S}_j \cdot \underline{r}_{ij})}{r_{ij}{}^2}\right] \tag{3.31}$$

where $\underline{r}_{ij}$ is the spatial coordinates of the ions, and $\underline{S}_i$, $\underline{S}_j$ the spin of the two ions.

Typically this interaction is so weak that it will only be noticable at temperatures below 40mK.[15] So the long range interactions observed in material such as HgMnTe must be from a different mechanism.

3.6.2 Bloembergen Rowland Interaction

Unlike the superexchange mechanism outlined earlier, in this mechanism the localised spins interact via the virtual excitation of an electron from the valence to the conduction band. The strength of this interaction can be expressed as

$$e^{1/r}(E_g)^{-\frac{1}{2}} \qquad (3.31)$$

where r is the inter spin distance, and E_g the energy gap of the material.

In the case of HgMnTe it has been shown that this interaction will give rise to a long range antiferromagnetic interaction.[16]

Work by Bastard *et al* [17], has shown that in HgMnTe a mechanism very similar to the Bloembergen Rowland is responsible for the observed values of susceptibility at high temperatures. The interaction has a form of [15]

$$CR^{-5}\cos(k_F R) \qquad (3.32)$$

where k_F is the Fermi wave vector, R the separation of the ions, and C a constant.

3.6.3 RKKY Interaction

From linear response theory it can be shown that the magnetic field induces a spin - polarisation of the electron gas in a sample, which exists for a distance of $\frac{1}{2k_F}$, where k_F is the Fermi wave vector. In this way electrons can transfer information about spin orientation. In a diluted magnetic semiconductor such as HgMnTe, the concentration of free electrons is smaller than the concentration of localised spins (Mn ions), and the interaction is ferromagnetic [15]. Antiferromagnetic exchange is also possible using this

mechanism, when the seperation of the magnetic ions is sufficently high, i.e. the ratio of electron concentration to that of the localised spins drops.

Story et al, have observed a ferromagnetic phase transition in p-type PbSnMnTe [18] which is thought to originate from this mechanism.

3.7 The magnetism of HgMnTe

The magnetism of this material can only be calculated analytically in certain cases.

3.7.1 The dilute limit

For manganese concentrations below 0.01 the spins in the material can be considered independent of each other, and so the behaviour is that of Curie's law. The magnetisation can be described by the use of a Brillouin function as outlined in section 3.3.3 above.

3.7.2 High temperature regime

Although the magnetisation at all fields cannot be given by a Brillouin function because of the Mn-Mn interactions, the low field susceptibility is found to be linear as a function of field. This low field susceptibility has been shown to follow a Curie-Weiss form [19] and is normally expressed as

$$\chi = \frac{C}{T+\theta} \qquad (3.33)$$

Considering the system to be a randomly dilute Heisenberg antiferromagnet, we can express this as

$$\chi = \frac{C_o x}{T+\theta_o x} \qquad (3.34)$$

At low temperatures and high manganese concentrations, a deviation is observed in the inverse susceptibility from the expected linear behaviour [20]. This deviation is considered to be quantifiable by the inclusion of higher order expansion terms in the calculation of χ. Work on this have been performed by a number of authors, one of which is Nagata [21] and this is outlined below.

The susceptibility is calculated for the separate contributions of single ions, pair and triplets, and then multiplied by the probability of their occurrence in the sample. The contribution of larger clusters has been ignored in this work, and it has been shown by [22] that for a manganese concentration below 10%, the effect of these can be discounted. The probability of an ion forming one of the specified cluster types is given by

Cluster Type	Probability of occurrence
Single	$(1-x)^{12}$
Double	$12x(1-x)^{18}$
Closed Triangle	$18x^2(1-x)^{23}[5(1-x)+2]$
Open Triangle	$24x^2(1-x)^{22}$

Table 3.1 Cluster probabilities

The susceptibility for each group can be expressed as [21]

$$\chi_i(T) = \frac{g^2 \mu B^2}{3k_B T} \frac{\sum_s S(S+1)(2S+1)e^{\frac{-Es}{k_B T}}}{\sum_s (2S+1)e^{\frac{-Es}{k_B T}}} \qquad (3.35)$$

Where S is total spin of the group and is listed in reference [21], and Es the energy of the group in zero magnetic field. In high field this should be changed to $Es - g\mu_B mH$, where m is the magnetic quantum number, and H the applied field.

The predictions of this theory are in good agreement with the experimental data, although the values obtained are not in exact agreement. Figure 3.4 shows the data taken from Nagata's paper to illustrate the fits obtained with the above expression. Some of the fits are using a modified probability distribution, which is calculated from the specific heat data. The value of the exchange interaction J_{12} has been used as a fitting parameter for the data, and the value obtained, $J_{12} = -7K$, is comparable to those obtained by other groups.

The contribution to the susceptibility from clusters larger than three ions have been ignored in this work, will give rise to a larger susceptibility than those shown in the figure. This will force the inverse susceptibility to lower values, further away from the experimental values, showing that the model using the standard distribution is flawed.

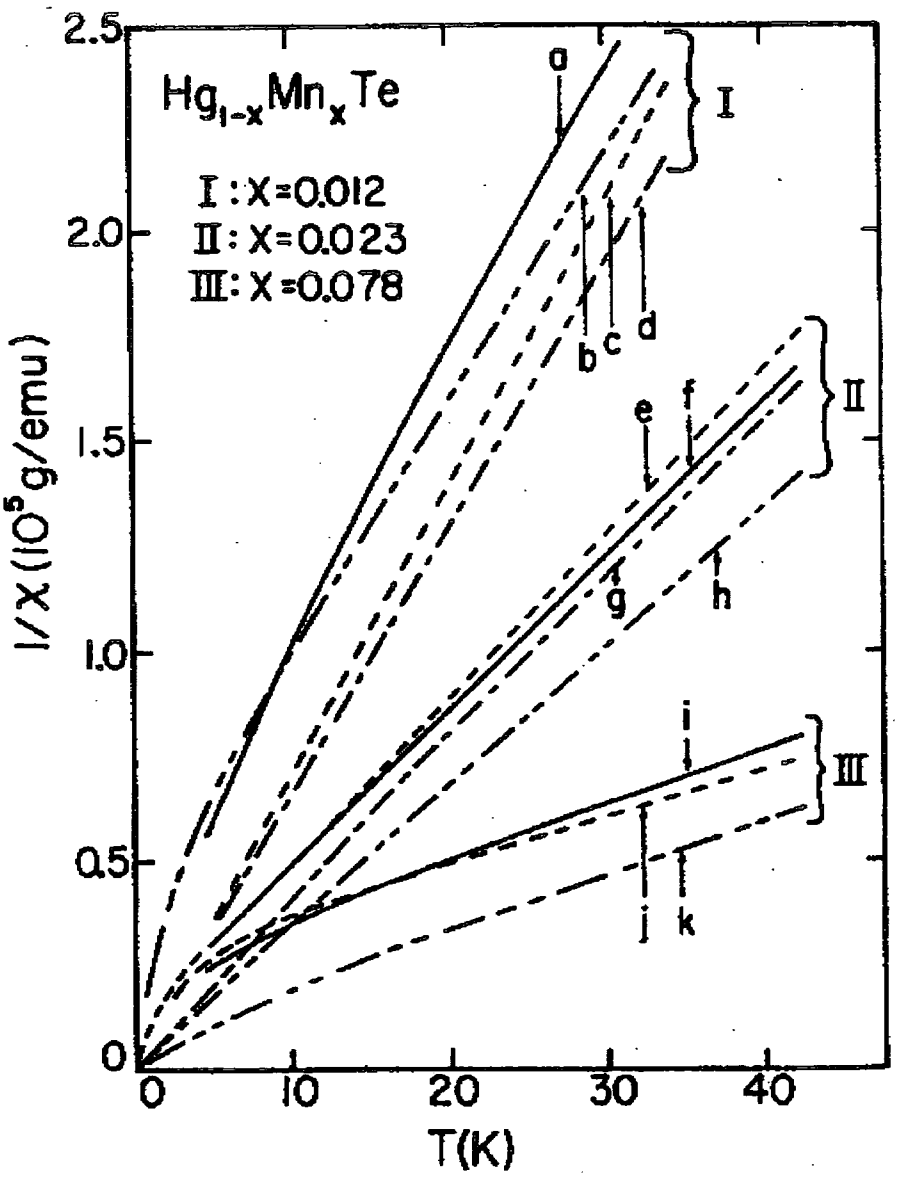

Figure 3.7 Inverse susceptibility of HgMnTe samples and the fits obtained using the method of Nagata *et al* [21]. The solid lines denote the experimental results. The dashed lines are fits based on the random probability distribution (c,d,g,h,k) or on the modified distribution (b,e,j).

3.7.3 Spin glass

At a sufficiently low temperature the susceptibility of HgMnTe shows a distinct cusp. This is interpreted as the transition to the spin glass phase, and is referred to as the spin glass transition temperature, T_g. An example of this is shown in figure 3.8.

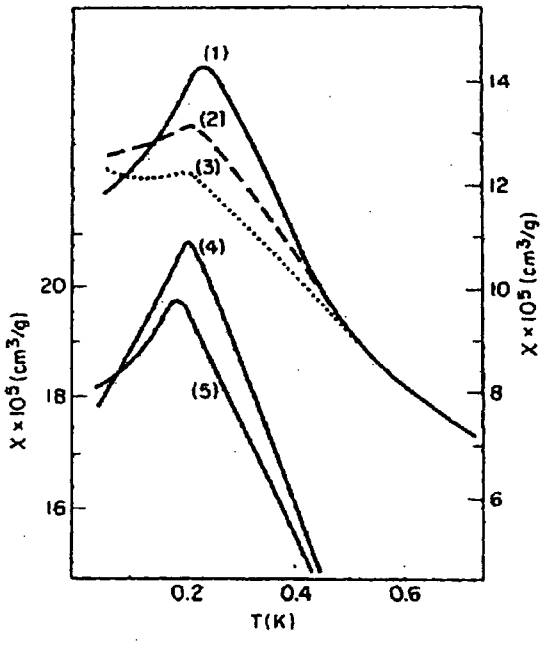

Figure 3.8 The susceptibility of HgMnTe at the spin glass transistion. Curves 1-3 are for a sample with x=0.034 (right hand axis) and curves 4-5 for a sample with x=0.02 (left hand axis) [23]

The original work in this field suggested that a spin glass could only form for a manganese concentration of $x > 0.19$. This value was based on the percolation threshold in HgMnTe and the work of Domb et al [24]

The mechanism responsible for the transition was thought to be linked to the growth of clusters within the sample [25]. Due to random fluctuation in the composition of the sample certain areas are found to be Mn rich.

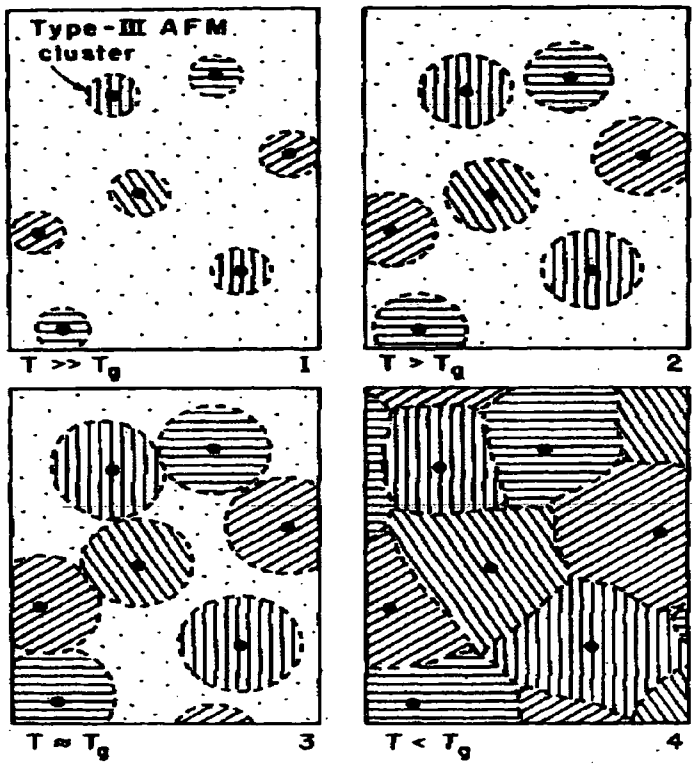

Figure 3.9 The cluster theory of Mydosh [26]

As the temperature is decreased the clusters increase in size, until they start to touch , picture 3 [26], at which point the spins can no longer react to an applied magnetic field.

The temperature at which the clusters touch can be interpreted as the spin glass transition temperature, and this has been supported by neutron diffraction experiments [27], that have observed that the magnetic correlation length becomes constant below T_g.

Later work has found a spin glass transition in samples with a negative bandgap, i.e. $x<0.07$. This concentration is well below the percolation limit and so another mechanism must be responsible. All tetrahedrally bonded zinc blende or nickel arsenide diluted magnetic semiconductors are predisposed to form AFM-III magnetic order, which can be observed directly via the use of neutron diffraction.

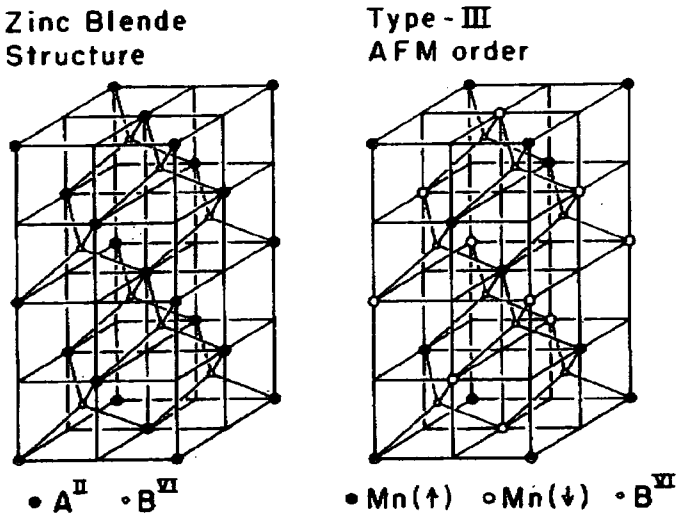

Figure 3.10 AFM-III order [23]

It has been noted that the interaction that produces a spin glass in samples with low manganese concentration is long range [28], and the usual theory is based on the concept of frustration of the exchange mechanisms within the lattice.

Consider an antiferromagnetically ordered triplet of ions. Two of the ions are arranged with their spins antiparallel as required from indirect exchange. The third ion cannot align antiparallel to both of the ions simultaneously, and this is the basis of the frustration mechanism.

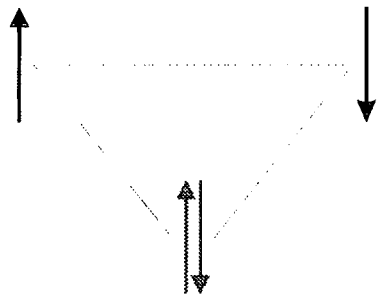

Figure 3.11 The frustration mechanism in an antiferromagnetic system.

The spin glass transition as a function of manganese concentration is shown below in figure 3.12.

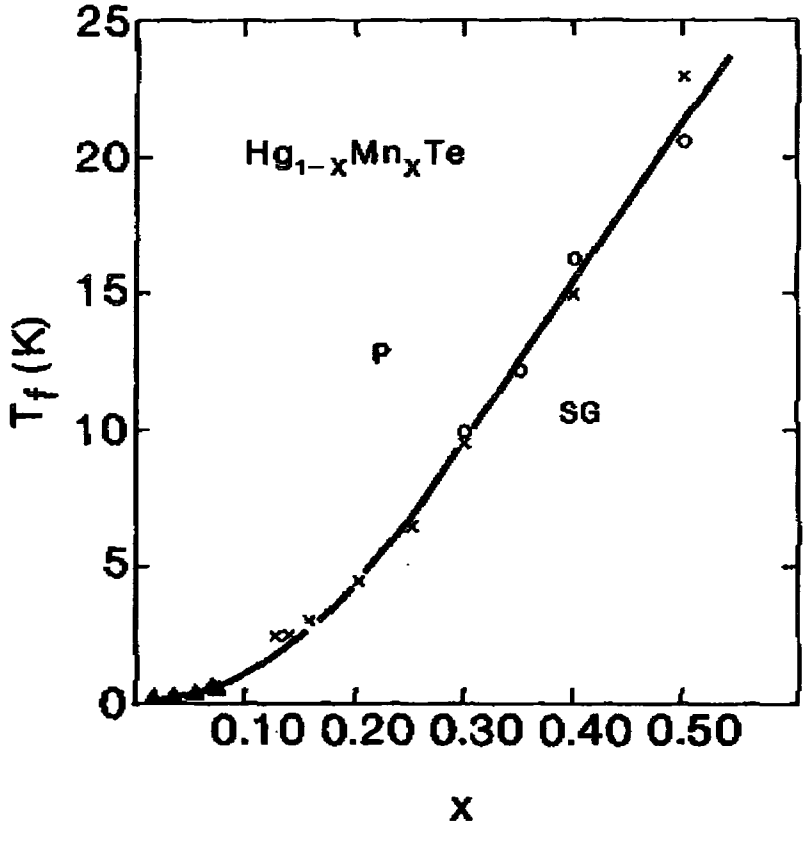

Figure 3.12 The spinglass transition temperature in HgMnTe [22]

The spin glass transition temperature in HgMnTe can be compared to that of other diluted magnetic semiconductors, as is shown in figure 3.13. The gradient of the line in

this plot gives an idea as to the range of the interaction that causes the spin glass transition. The line for HgMnTe has a more shallow gradient than for wide gap material, e.g. CdMnTe, denoting that long range interactions are more important.

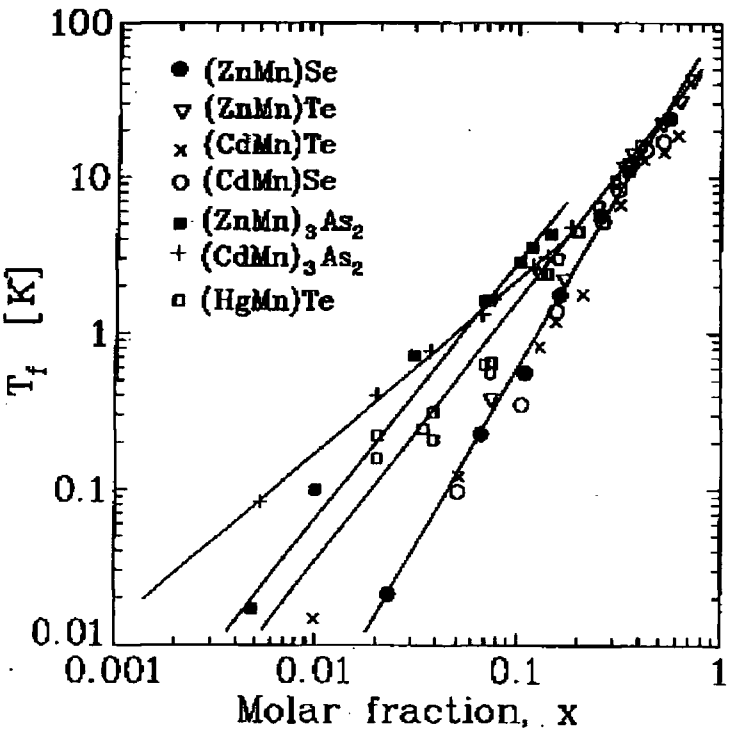

Figure 3.13 The spin glass transition temperature for a variety of DMS [14]

Reference List Chapter Three

[1] Ashcroft, N.W., Mermin, N.D., Solid State Physics, Saunders College, Philadelphia, 1976, p644

[2] Kittel, C., Introduction to Solid State Physics, John Wiley and Sons, Singapore, 1988, p402

[3] Mattis, D.C., The Theory of Magnetism, Harper and Row, New York, 1978

[4] Morrish, A.H., The Physical Principles of Magnetism, John Wiley and Sons, New York, 1965

[5] Henning, W., Vogt, E., Z. Naturforsh, 12A, (1957), 754

[6] Eisberg, R., Resnick, R., Quantum Physics of Atoms, Molecules, Solids, Nuclei and Particles, John Wiley, New York, 1976, p364

[7] Ando, K., Takahashi, K., Okuda, T., J Magn Magn Mater, **104-107**, (1992), 994

[8] Kramers, Physica, 1, (1934), 182

[9] Morrish, A.H., The Physical Principles of Magnetism, John Wiley and Sons, New York, 1965, p466

[10] Larson, B.E., Hass, K.C., Ehrenreich, H., Carlsson, A.E., Phys Rev, B37, (1988), 4137

[11] Woolley, J.C., Manoogian, A., Hodgson, R.J.W., Lamarche, G., JMMM,, 78, (1989), 164

[12] Kossutt, J., Dobrowolski, W., In Handbook of Magnetic Materials Vol. 7, ed. Buschow, K.H.J., North Holland, Amsterdam, 1993, p231

[13] Bastard, G.C., Phys Rev, B24, (1981) 1961

[14] de Jonge, W.J.M. *et al*,in Diluted Magnetic Semiconductors, Mater, Res. Soc. Symp., Vol 89, eds Aggarwal, R.L., Furdyna, J.K., von Molnar, S., Mater. Res. Soc., Pittsburgh, p153 With data added from [22] and [24]

[15] Dietl, T., in Handbook on Semiconductors, ed Moss, T.S., Elsevier, Amsterdam, 1994

[16] Kossut, J., Dobrowolski, W., in Handbook of magnetic materials, vol 7, ed Buschow, K.H.J, North Holland, Amsterdam

[17] Bastard, G.C., Phys Rev, B24, (**1981**), 1961

[18] Story, T., Galazka, R.R., Frankel, R.B., Wolff, P.A., Phys Rev Lett, **56**, (1986), 777

[19] Oseroff, S.B., Phys Rev, B25, (1982), 6484

[20] Original work ; Brumage, W.H., Yarger, C.R., Lin, C.C., Phys Rev, **133**, (1964), A765

[21] Nagata, Phys Rev, B22, (1980), 3331

[22] Oseroff, S., Keesom, P.H., in Semiconductors and Semimetals vol 25, series Eds, Willardson, R.K., Beer, A.C., Academic Press, Boston, 1988, p73

[23] Brandt, N.B., Moshchalkov, V.V., Advances in Physics, **33**, (1984), 193

[24] Domb, C., Dalton, N.W., Proc Phys Soc (London), 89, (1966), 859

[25] Furdyna, J.K., J App Phys, 64, (1988), R29

[26] Mydosh, J.A., In Magnetism in Solids, eds Cracknell, A.P., Vaughn, R.V., SUSSA Publications, Edinburgh, 1981, p6

[27] Dolling, G., Holden, T.M., Sears, V.F., Furdyna, J.K., Giriat, W., J App Phys, 53, (1982), 7644

[28] Twardowski, A., in Diluted Magnetic Semiconductors, Ed Jain, M., World Scientific, Singapore, 1991

Chapter Four Electrical Experimental Details

4.1 Techniques of Hall measurements

A number of problems can be encountered in the measurement of the Hall effect on samples. The most common one is a zero field offset which is due to the misalignment of the voltage probes, this gives a voltage which is proportional to the current and the resistivity of the material. The probes are separated by a small distance δx, which gives rise to a voltage from Ohms Law of $\Delta V = \frac{I\rho\delta x}{A}$. This voltage is almost completely field independent, unless the magnetoresistance of the sample is large compared to the Hall voltage, and can be easily removed during the analysis. The usual method for counteracting this problem is to use five electrical contacts method, as shown in figure 4.1, where two of the contacts are placed close together and are connected by a potential divider.

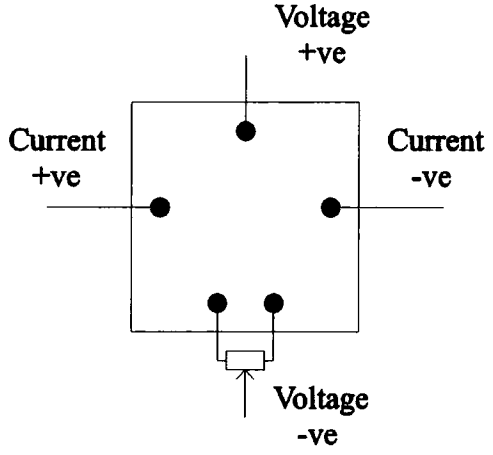

Figure 4.1 The five contact method

The potential divider is adjusted to give zero Hall voltage at zero field, at each temperature used. If the resistance of the potential divider is infinite, then the device will only have to be set once, and the off-set will be nulled at each temperature. In

reality the resistance of the potentiometer must be higher than the resistance of the sample between the two contacts, or it will act as a short. This allows the samples to be subjected to the usual van der Pauw analysis. Some of the work performed by the author, however, has been performed using four contacts and removing the offset at the data analysis stage.

Another problem that can be encountered in Hall measurements is the Ettinghausen effect. Although smaller in magnitude than the error induced by contact misalignment, it can be sufficiently large to give inaccurate results. A permanently maintained temperature gradient will appear in a sample if an electric current is subjected to a magnetic field perpendicular to the direction of flow, i.e. in the arrangement used for Hall effect measurements. The temperature gradient along a sample can be expressed as

$$\Delta T = \frac{PIH}{b} \qquad (4.1)$$

where ΔT is the temperature gradient across the sample, P the Ettinghausen co-efficient, I the current flowing in the sample, H the magnetic field applied, b the sample thickness. This will cause the two contacts to be at different temperatures and hence see different carrier concentrations.

Another source of error is the Nernst effect, which is a potential gradient in the sample perpendicular to a thermal current. This can be expressed as

$$E_N = Q\frac{wH}{K} \qquad (4.2)$$

where E_N is the potential gradient across the sample, w the thermal current density, K the sample's thermal conductivity, Q the Nernst coefficient.

The Righi-Leduc effect produces a temperature gradient in the y direction, when a thermal current flows in the x direction with a magnetic field applied in the z direction. This can be expressed as

$$\Delta T = \frac{SwHa}{K} \qquad (4.3)$$

where ΔT is the temperature difference across the sample, S is the Righi-Leduc coefficient, a is the sample width, w is the thermal current density, H is the applied magnetic field, K is the sample thermal conductivity.

The usual method for the removal of unwanted errors in the Hall effect is to reverse the current and the field to get a series of four measurements. This will also allow the removal of the contact misalignment offset voltage. Defining E_1 as

$$E_1 = V_H + V_E + V_N + V_{RL} + V_{IR} \qquad (4.4.a)$$

where V_H is the Hall voltage, V_E is the voltage from the Ettinghausen effect, V_N is the voltage from the Nernst effect, V_{RL} is the voltage from the Righi-Leduc effect and V_{IR} is the voltage from the contact misalignment.

Reversing the current gives

$$E_2 = -V_H - V_E + V_N + V_{RL} - V_{IR} \qquad (4.4.b)$$

Reversing the magnetic field gives

$$E_3 = V_H + V_E - V_N - V_{RL} - V_{IR} \qquad (4.4.c)$$

Reversing both the field and the current gives

$$E_4 = -V_H - V_E - V_N - V_{RL} + V_{IR} \qquad (4.4.d)$$

The four equations above can be combined to give

$$V_H + V_E = \frac{E_1 - E_2 + E_3 - E_4}{4} \qquad (4.5)$$

Hence the contributions for the Nernst effect, the Righi-Leduc effect and the effect of contact misalignment have been removed. The remaining contribution of the Ettinghausen effect is impossible to remove by the use of DC Hall effect measurements, and so AC techniques are required. Providing the frequency of the oscillations is higher than that associated with the thermal current, which is given as $\omega_o \approx 0.1$ [1] the effect can be cancelled out.

The use of AC techniques in measuring Hall voltages allows the use of lockin amplifiers, and hence a better signal to noise ratio can be achieved. Due to the higher ratio a smaller measuring current can be used, which avoids Joule heating in the sample, or in the case of the epitaxial layers, at the contacts which often have resistances of 1KΩ. This is because of the method of contact fabrication, which uses evaporated indium and silver epoxy. Further details of this can be found in section 4.5.2. The system used by the author uses a current of between 5 and 50μA, which will give a Joule heating of around 10^{-7}W at a contact as mentioned above.

4.2 Modifications to the ^{4}He cryostat

The author has performed a number of modifications to the group's existing magnet cryostat, the Durham University Central High fiEld Superconducting Solenoid (DUCHESS). The system was purchased in 1983 to allow VSM measurements in fields up to 13T and at temperatures down to 1.5K. A schematic of the present system is shown in figure 4.2.

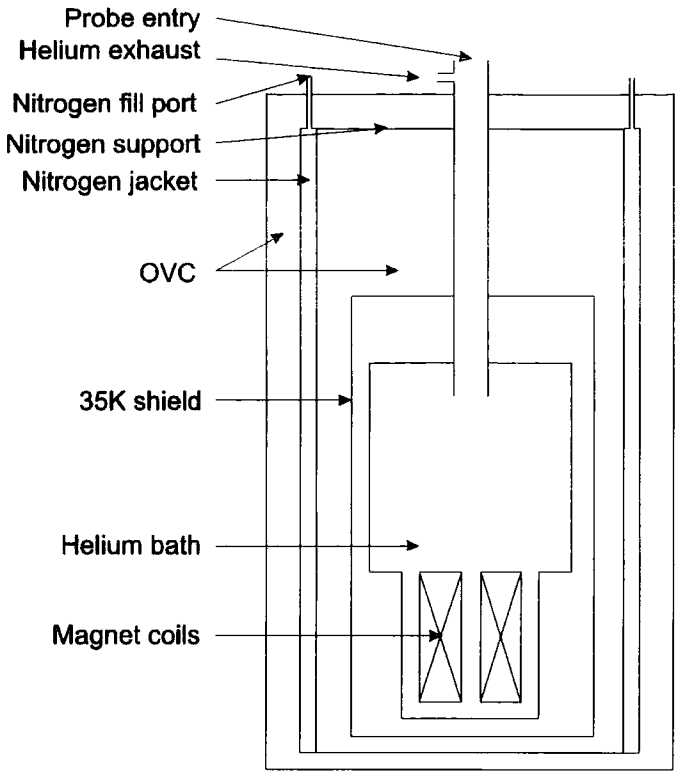

Figure 4.2 Schematic representation of the DUCHESS

The original Variable temperature insert (VTI) was taken out of the system and modifications were made to incorporate an Oxford Instruments Heliox refrigerator in the cryostat. (For further details see section 4.3) To this end the entry to the helium space was then altered to match the NW50 flange on the Heliox probe. The top plate was fabricated in the departmental workshop, and a tube welded onto the underside to aid guidance of the helium-3 refrigerator during insertion. This tube was fitted with copper baffles level with the top of the helium space, the 35K shield and the underside of the nitrogen jacket to help eliminate 300K radiation within the helium space. This modification required an alteration to the magnet power supply leads, as they were designed to fit into terminals in the VTI. The leads are of a vapour cooled multi filamentary type which were surrounded by a tufnol jacket to allow insertion and removal from the cryostat. The tufnol was removed and the wires covered in heat

shrink to allow more flexibility, and prevent shorting to the cryostat neck. They were then fastened into place on the magnet and the tops were taped to the side of the neck of the cryostat, before the free ends were soldered onto a standard Oxford Instruments connector. The choice of this connector was due to the space restrictions at the neck of the cryostat and in using a standard connector the author was able to use commercially available magnet leads.

The wiring within the cryostat, the helium level meter, the superconducting switch and two Allen Bradley resistors are terminated at a standard hermetically sealed ten pin connector on the side of the collar. The Allen Bradley Resistors are useful during the filling of the cryostat, one is located on the top of the magnet, the other on the base. They give a rough guide as to the temperature inside the helium space, and hence show when liquid is starting to collect before the level meter becomes useful.

Unfortunately the original design of the Thor cryostat had a serious flaw: too much strain was placed on the solder joint connecting the central neck to the nitrogen plate, as shown in figure 4.3.

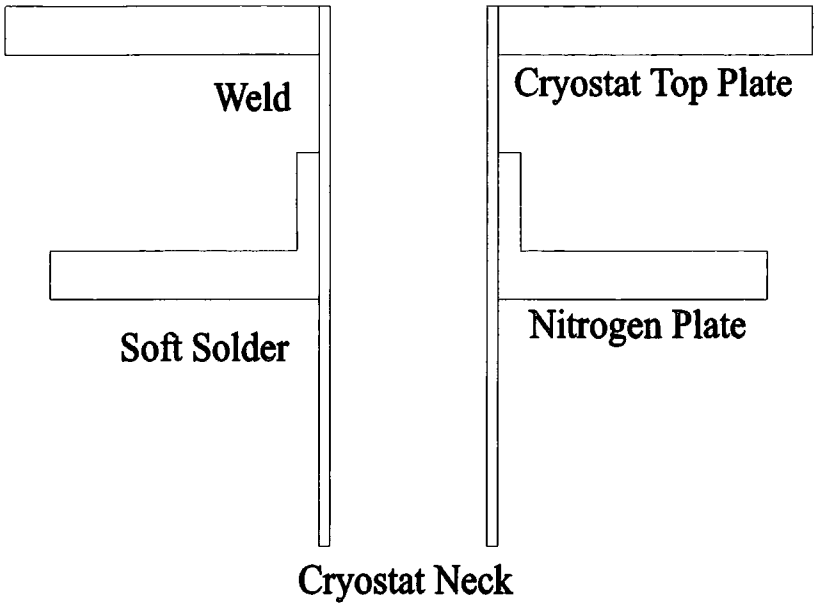

Figure 4.3 The location of the weak joint in the cryostat

When the cryostat had been in use for a long period of time, this joint became weak and eventually collapsed. Because of the large thermal mass of the object it was impossible to form a good join using soldering. Thus a new design was proposed and constructed, as illustrated in figure 4.4. Here the neck of the cryostat is held between a pair of plates which can be tightened by screws. These plates are held to the nitrogen plates by further screws. No further problems have been encountered with this plate since implementing this modification.

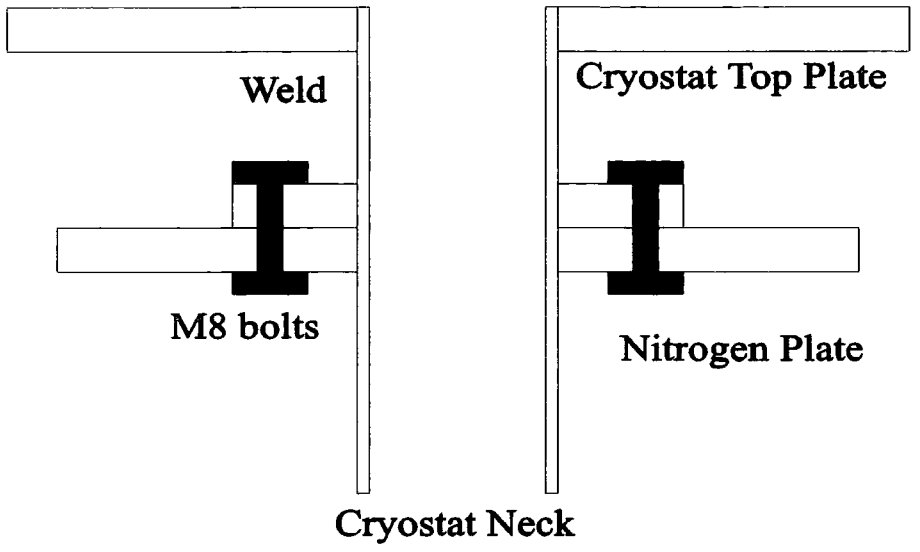

Figure 4.4 The new design for the nitrogen plate

Another problem with the original design of the cryostat is encountered during filling the nitrogen jacket. The fill ports which protrude from the top plate are kept leak tight from the outer vacuum jacket (OVC) by rubber orings. During filling the orings get cold and they start to leak. If the system is filled with liquid helium then the air is cryopumped and the change in vacuum in the OVC is negligible. However when the system warms above 65K, the pressure in the OVC will rise dramatically, being potentially dangerous. The author leaves a vacuum pump running on the OVC when it is warming to help alleviate this problem. The problem has not as yet been cured at source.

4.3 The Oxford Instruments Heliox Probe

The Heliox probe is an example of a "single shot" helium three system, manufactured by Oxford Instruments Limited, based on the low pressure boiling of He^3. It has a base temperature just below 300mK, and a hold time at this temperature

of over 24 hours providing the heat leak is kept below 10^{-8} W.[2] The experiment is attached to the base of the probe by screwing into the M6 thread located on the bottom of the He^3 pot. The probe is lowered into a helium bath, covering the end of the pickup tubes, as shown in figure 4.5

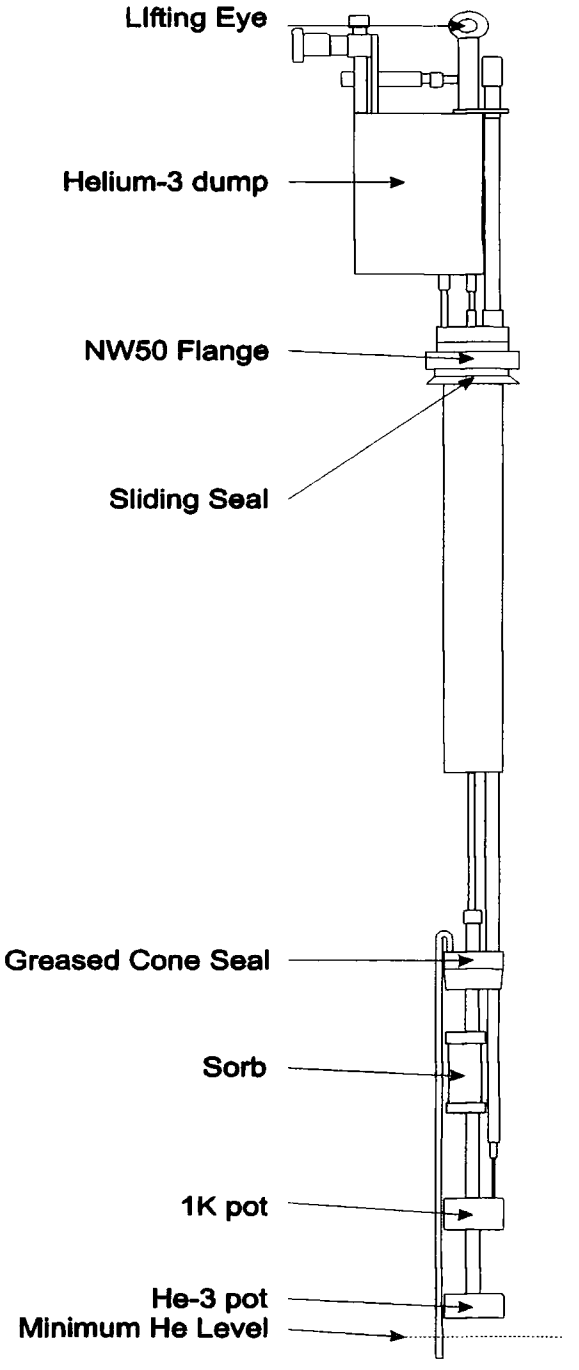

Figure 4.5 The Heliox Probe

4.3.1 Operation of the Heliox probe

The system operates as follows:

The sorb is activated charcoal, which will pump on helium gas if its temperature is below 10K, but it will completely expel any gas if kept above 40K. The 1K pot is cooled below 1.4K by filling with helium-4 from the surrounding bath, and then reducing liquid's vapour pressure mixture using an Edwards 40 rotary vacuum pump. During this stage of the operation the temperature of the sorb is kept above 40K, so that it has completely expelled the He^3 gas, which condenses on the 1K pot, and falls into the He^3 pot at the bottom of the probe. After a period, the sorb is cooled to below 10K, and the pressure over the He^3 liquid drops, reducing its boiling point.

4.3.2. Sample Holder

If a block of copper is placed in a rapidly changing magnetic field, electrical currents are induced in the copper to oppose the magnetic field that is applied. These eddy currents cause Ohmic heating, and are as such undesirable in a cryogenic system. For use in high magnetic field the probe comes with a low eddy current sample holder. This is a hollow tube made of steel and copper which affixes to the He^3 pot. The steel has a higher electrical resistance than the copper and so helps to suppress the eddy currents that are induced when magnetic fields are being ramped. The thermal conductivity of the steel ($2x10^{-5}$ W m^{-1} K^{-1}) [3] is very low compared to that of the copper ($7x10^{-1}$ W m^{-1} K^{-1}) [3]. It also means that the end of the probe is no longer close to the magnet, and so smaller eddy currents are induced in the end of the probe. A drawing of the sample holder is shown in figure 4.6

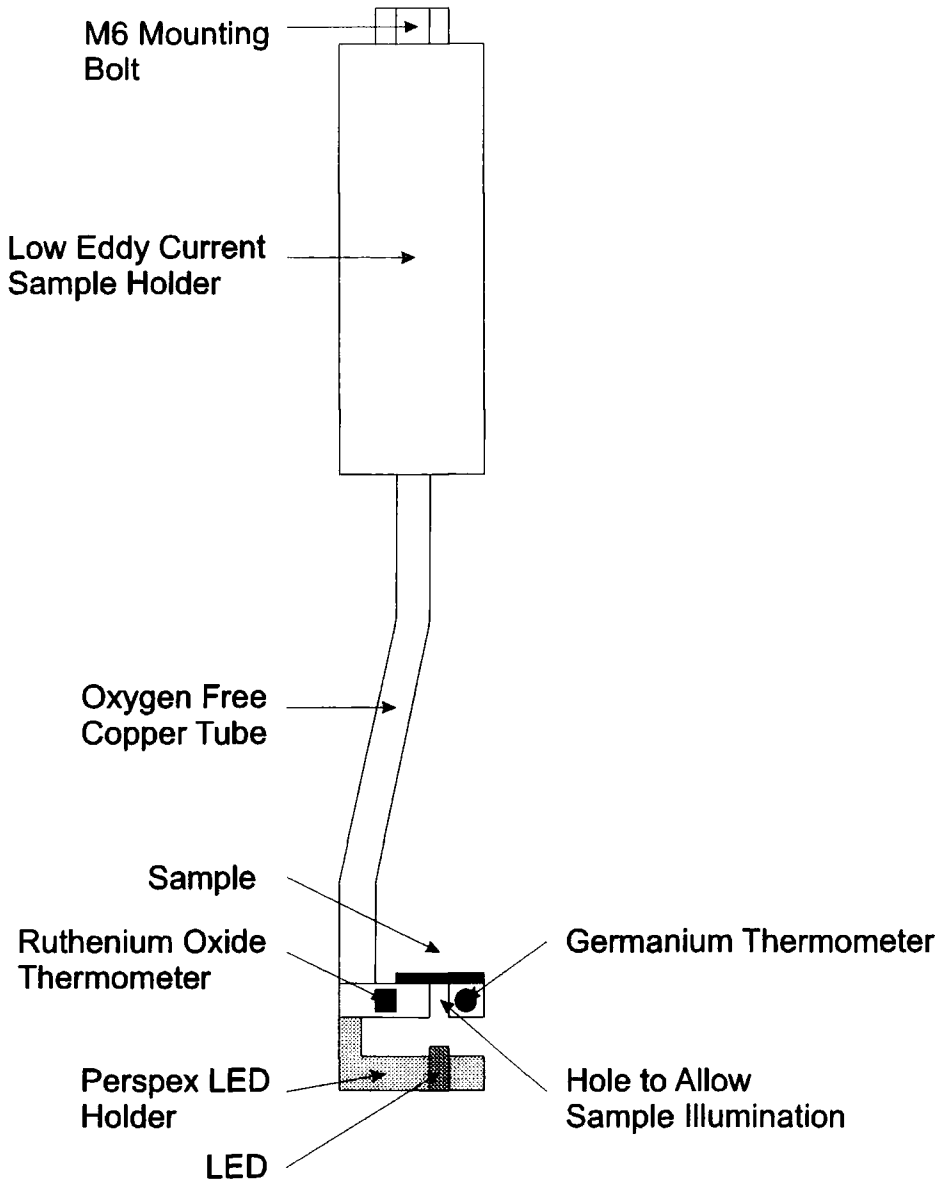

Figure 4.6 The low eddy current sample holder

4.3.3. Thermometry

The temperature of the probe is monitored by the use of a calibrated rhodium iron thermometer mounted on the He^3 pot, (for temperatures above 1.4K), and a speer resistor, uncalibrated, also on the He^3 pot. To obtain an accurate temperature a custom calibrated germanium sensor has been purchased, with a thirty point calibration. This has been mounted on the sample stage at the end of the low eddy current sample holder. Germanium thermometers have a large magnetoresistance

making them unsuitable for use in even modest magnetic fields at temperatures below 1K [4], and so another thermometer has had to be used for the high field work. Ruthenium oxide resistors have a small correctable magnetic field dependence if they are mounted parallel to the field direction, and are ideal for use at temperatures below 4K. The sensor used on the Heliox probe is a surface mount resistor, of the type used in electronics manufacture for their temperature stability, though they are uncalibrated.

The majority of the wiring on the Heliox probe is constantan to reduce the thermal leak from room temperature. The experimental wiring consists of 18 wires, six of which are 34 gauge copper, terminated at a Lemo connector just below the 1K pot. From this connector constantan twisted pairs are used down to the sample stage, and are thermally anchored along their length to cut down on thermal leakage. The wires for the sample are terminated on beryllium oxide heat sinks, onto which the sample wires are soldered.

The author has not performed any measurements on the Heliox probe with the samples under investigation because they would have a resistance greater than our measurement capability at 4.2K, and so investigations down to 0.3K would be pointless.

4.4 The Magnetotransport System

The system is based on an Air Products Displex closed cycle helium refrigeration system, which is capable of producing a base temperature of 10K, without the use of liquid cryogens. The cooling is performed by a form of modified Solvay cycle [5].

The thermometry for the system is a commercial Rhodium-Iron sensor with a factory supplied three point calibration. The sensor was chosen for its reliability and accuracy over the temperature range used, and the repeated thermal cycling. The accuracy quoted for this type of sensor is 200 p.p.m. [6] under repeated cycling. The sensor is connected to an Oxford Instruments ITC502 temperature controller, which is capable of maintaining a temperature to within 0.1K of the set point. The controller is calibrated for the 4.22K and 273K reference points supplied, and checked against the intervening 77.4K point, where the error was found to be less than 0.2K. This is due to the thermometer and the temperature controller being manufactured by two different companies, and shows the difference in the temperature behaviour of the device with that expected in the calibration. This error was found to be consistent within the accuracy of the controller.

The electrical measurements were carried out using a nominal 5μA current through the sample at a frequency of 13Hz. The use of low frequency is to enable the use of lockin amplifiers to assist in the noise reduction of the measurement and because the use of high frequencies will cause problems with rectifying contacts, and the inductance and capacitance of the connecting wires. The physics of the measurement will change if the frequency applied is sufficently high. For most of epilayers measured the Hall voltage is around 1mV at 0.3T. The current is kept as small as practicable to avoid Joule heating in the sample or at the contacts, which in the epitaxial layers measured often have resistances of 1KΩ or more. The lowest voltage which can be discerned from the noise is 1μV, which allows the system to see changes in resistance of better than 0.2Ω, even on resistances of over 10MΩ. The current is monitored by

measuring the voltage across a high stability 20KΩ resistor placed in series with the sample. This value was chosen because it allows a voltage of measurable size even for samples of high resistance.

The entire equipment is computer controlled via the General Purpose Interface Bus (GPIB) which allow bi-directional data transfer to devices at a baud rate of 1Mb sec^{-1}. The computer changes the applied magnetic field, then waits for the system to stabilise before taking a number of measurements of the field, and the Hall voltage and current, which are then averaged to get the final values. To achieve good stability the time constants on the lockin amplifier has been set to three seconds, so the computer waits for twelve seconds between readings to ensure that the present reading is not influenced by the one taken previously. [7]

The magnetic field is controlled by the use of a stepper motor connected to the current control of a stabilised power supply. For high field work this power supply is replaced with a Glassman 60-18 power supply, capable of 60V at 18A. This is controlled using the DAC card in the Stanford lockin. The current is reversed by the use of a reversing relay to allow pseudo bipolar operation. The stepper motor and the relay are controlled via the parallel port on the computer via a darlington driver, as shown in figure 4.6.

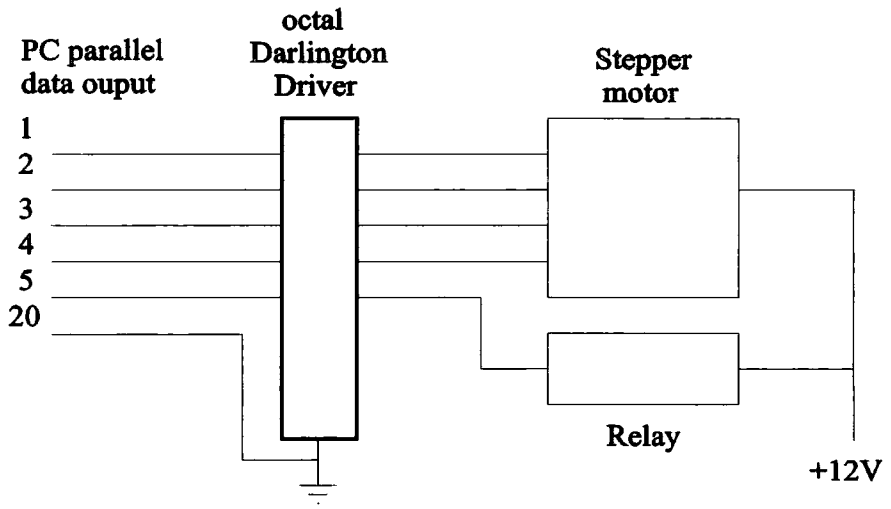

Figure 4.6 Wiring of the parallel port to the power supply

The computer sends logic pulses to the darlington chip which acts as a series of transistor switches, triggering the coils of the motor in the correct sequence.

The computer programming was performed in National Instruments Lab Windows BASIC, a language specifically written to allow easy interfacing to equipment via the GPIB and serial ports of a computer, as well as their range of Data Acquisition Boards (DAQ).

The applied magnetic field is measured using a standard Hall device which was calibrated against a calibrated gauss meter probe. The driving current for the device is 5mA, supplied by a small constant current device, the details of which are below.

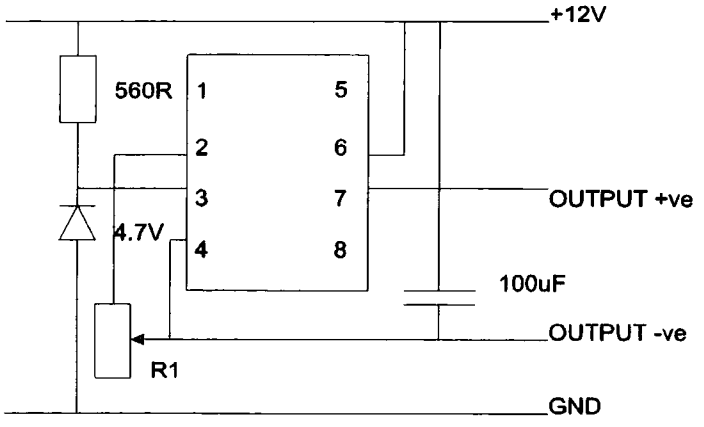

Figure 4.7 The constant current device circuit

The Hall voltage from the probe was read by a Solartron 7150 digital multimeter, and by the computer over the GPIB. The system schematic is shown below

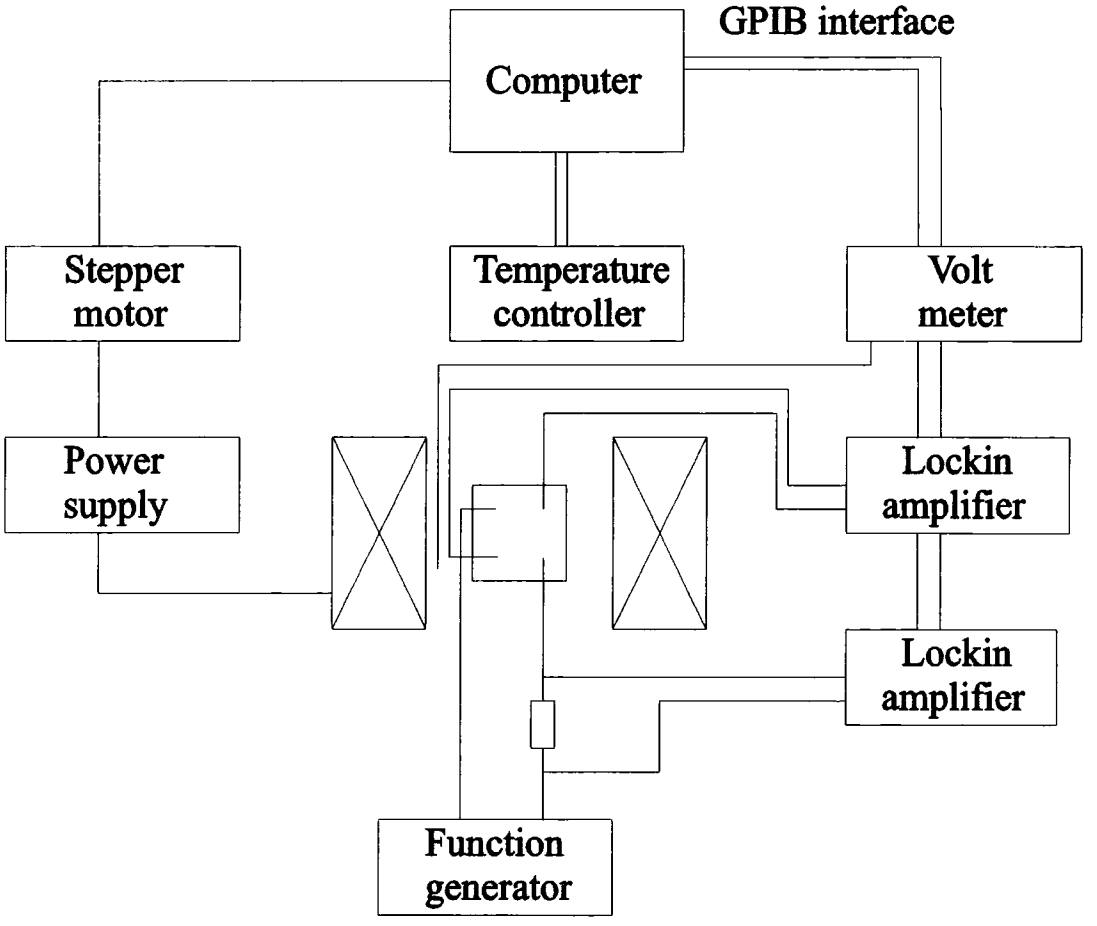

Figure 4.8 Wiring schematic of the system

The present software takes Hall data at a number of predetermined temperatures and saves them in an ASCII format, with comma delimiters, ready for input into most common graphics packages such as Axum. The program also removes the zero field offset from the data, by calculating the zero field value and subtracting that value from all readings taken from this temperature. The value of the zero field offset is found usually to follow the same trend as the sample resistance, and because of this has always been considered to be due to contact misalignment.

During cooldown of the system the resistivity of the sample is measured by using a four terminal resistance meter, such as a Keithley 199. This is not as sensitive as the AC technique used for measuring the Hall effect, but the resistance of the sample is, in general, approximately 100Ω at room temperature, which is easily measured with a good multimeter. This procedure is computer automated, with the computer reading the temperature and the resistance every thirty seconds during the cooldown, saving the data to an ASCII file as noted above.

For samples with a very high resistance a DC technique is preferred for the measurement. A Keithley Picoammeter was used in series with the sample and a high input impedance voltmeter (Keithley 199) used to measure the potential drop across the Hall contacts. A standard 12V supply drives the system, which can in theory measure samples with a resistance of $10^{13}\Omega$.

The noise on this system is higher than the AC system and the bare results have a maximum sensitivity of $10^{11}\Omega$, although this can be improved by averaging over a large number of readings. The main problem with samples that appear to have a very high resistance is to ensure that it is truly the sample that is being measured and not a poor contact, which is rectifying.

4.5 Sample preparation.

4.5.1 Bulk samples

The technique depended on the quality of the sample and its initial state. Some of the samples used were 'as cut' and required polishing before use, while others were already polished. The polishing of the samples was undertaken by machine, starting with a coarse grade abrasive (usually 6μm) and reducing this to 1μm diamond paste for the final surface. The machine rotated the sample whilst polishing to ensure that one side of the sample is not polished preferentially. After polishing, the samples were etched to remove the oxide layer on the surface. The normal method employed for this is to use a bromine / methanol solution which is roughly 2% bromine. Samples are subjected a twenty second etch, and are then washed in clean methanol. The contacts are then applied using a low temperature soldering iron and high purity indium.

4.5.2 Epitaxial layers.

These layers are not polished, they are so thin that any form of mechanical polishing would be extremely detrimental to them. They are etched in the same manner as the bulk samples, although the etching solution is generally a little weaker, and the duration of the etch reduced to around two seconds. The layers have indium pads evaporated on in the desired layout using a carefully machined mask. These pads have the wires affixed to them by using silver epoxy or sometimes silver paint. This technique does not give the same quality of contacts as the direct soldering technique employed on the bulk samples, but the epitaxial layers are not capable of withstanding

the heat of a soldering iron. The resistance of these contacts is often 1KΩ or more compared a few ohms that can be expected with the bulk samples.

4.5.3 Affixing the sample to the system

The sample is held onto the cold finger by the use of a very thin layer of Apezion N grease. This solidifies on cooling and holds the sample rigidly in place during the experiment, but allows easy removal on warming. The vacuum grease is used because of its "high" thermal conductivity 10^{-2} $Wm^{-1}K^{-1}$ at 4.2K [8](compared to copper $7x10^{-1}$ $Wm^{-1}K^{-1}$) [3], thus helping to ensure that the sample is at the same temperature as the system. The wires from the samples are connected to beryllium oxide heatsinks, which are also connected to the wires leading out of the cryostat. The heatsinks offer a convenient termination point for the wires and avoids any unnecessary heatleak down from 300K.

Reference list Chapter four

[1] Lindberg, O., Proceedings of the IRE, (1952)

[2] Operators manual, Oxford Instruments

[3] WADD technical report, 60-56, part IV

[4] Hu, Y., in Experimental Techniques, eds Richardson, R.C., Smith, E.N., Addison Wesley, Reading 1988, p316

[5] Operators Manual, Air Products Displex, Air Products LTD

[6] Manufacturers data sheet, Twickenham Scientific LTD.

[7] Operators manual, Brookdeal 5206 Lockin amplifier, Brookdeal Electronic Instruments LTD

[8] Extrapolated from data given in Lounasmaa, O.V., Experimental principles and methods below 1K, Academic Press, London, 1974

Chapter Five Magnetic Experimental Details

5.1 The Alternating Gradient Field Magnetometer

5.1.1 Theory of Operation

The operation of the Alternating Gradient Field Magnetometer (AGFM) is analogous to that of the Vibrating Sample Magnetometer (VSM) which is a common piece of apparatus in magnetism research labs. The sample is placed in a DC magnetic field of varying magnitude in the x direction, with a small AC field superimposed upon it. This ripple field is usually of the order of a few mT, and exerts a force on the sample of [1]

$$\underline{F} = -V\nabla(\underline{M}\cdot\underline{B_o}) \qquad (5.1)$$

where $\underline{B_o}$ is the field applied to the sample, M the magnetisation and V the volume of the sample.

Because of the arrangement of the system, the x component is the one of interest, and so we can write

$$\underline{F_x} = V\left(M_x\frac{\partial \underline{B^x}_o}{\partial x} + M_y\frac{\partial \underline{B^y}_o}{\partial x} + M_z\frac{\partial \underline{B^z}_o}{\partial x}\right) \qquad (5.2)$$

As the field has a component $\underline{B_o}$ which is of a sinusoidal form applied in the x direction, equation 5.2 can be expressed as [4]

$$\underline{F_x} = VM_x\frac{\partial(\underline{B_o}\sin w_B t)}{\partial x} \qquad (5.3)$$

where $\underline{B_o}$ is the magnitude and w_B the frequency of the ripple field, and M_x is the magnetisation of the sample in the x direction. For the operation of the system, it is

very important that the sample is set in the middle of the field gradient so that the terms in the y and z directions can be safely neglected. It is thought that these terms will cause a torque to be exerted on the sample suspension, causing unwanted errors in the signal.

The frequency of the resonance can be obtained by treating the sample suspension as a cantilever [4]. The resonant frequency of an unloaded bimorph can be expressed as

$$f_o = \frac{1}{2\pi}(M_b C_m)^{\frac{1}{2}} \qquad (5.4)$$

Where M_b is the mass of the bimorph, and C_m its mechanical compliance. The frequency of the loaded bimorph can then be expressed as [4]

$$\frac{f_o'}{f_o} = \left(\frac{M_b}{M_b + 4.2M_s}\right)^{\frac{1}{2}} \qquad (5.5)$$

Where M_s the mass of the suspension.

For the system used, this gives a fundamental resonance of 3KHz.

The force produces a small motion of the sample, which in the original systems of [2] was detected using a microscope and a stroboscopic light source. The sensitivity of the system for this method of detecting is given by

$$y_d = \frac{y_s}{Q} \qquad (5.6)$$

where y_d is the sensitivity of the dynamic system, y_s is the sensitivity of the static system and Q is the quality factor of the system.

Modern systems use piezoelectric bimorphs, which allow the use of lockin amplifiers (LIA). These allow higher sensitivities to be achieved (up to 10^{-12} J T^{-1}) and

give over 80dB of noise reduction.

The frequency of the ripple field is chosen to match the resonant frequency of the cantilever construction. On resonance the system is much more sensitive to any vibration of the sample, hence the sensitivity of the system is maximised. The gain from this method is proportional to the Q factor of the system which can be as high as 400 at resonance. This exceeds the values in the literature, which are typically around 70 [3]. The system is typically operated at a resonant frequency of around 800Hz. However, if the signal to noise ratio is too low at the fundamental frequency, working at the first overtone, approximately 1280 HZ, usually lowers the noise level to allow a higher signal to noise ratio. [4] Working at higher overtones is less advantageous because the drop in signal becomes excessive.

5.1.2 Construction and Development

The system is at present arranged in a pendulum style, [5] and is similar to the commercial instrument supplied by Princeton Electronics. The bimorph was held rigidly by a Perspex mount, which then clipped in to the brass block via the use of an 8-way IDC connector. This allowed more reproducible positioning of the bimorph substructure with respect to the magnetic field. The glass fibres were exchanged for quartz-glass fibres to reduce the background magnetisation of the system, and were affixed to the bimorph by the use of super glue, rather than the wax used by other groups [4]. The sample suspension is shown in figure 5.1.

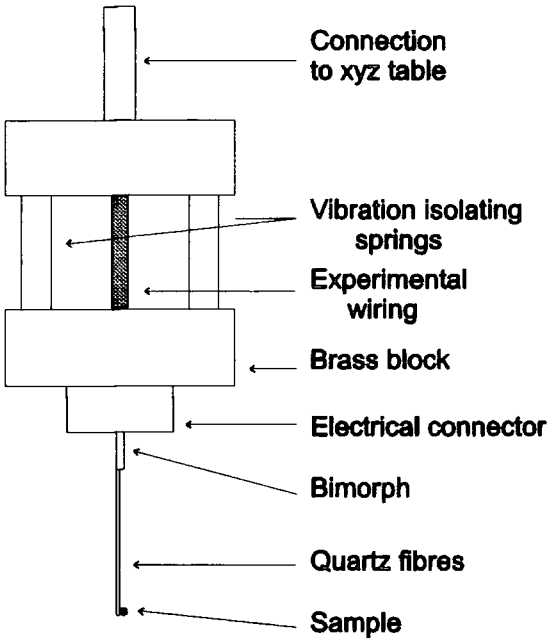

Figure 5.1 Detail of the AGFM sample holder

The AGFM is fully automated by use of a PC based data acquisition system. The equipment is interfaced to the computer via the GPIB bus, which allows high speed, bi-directional data transfer with compatible meters. A schematic of the system is shown in figure 5.2

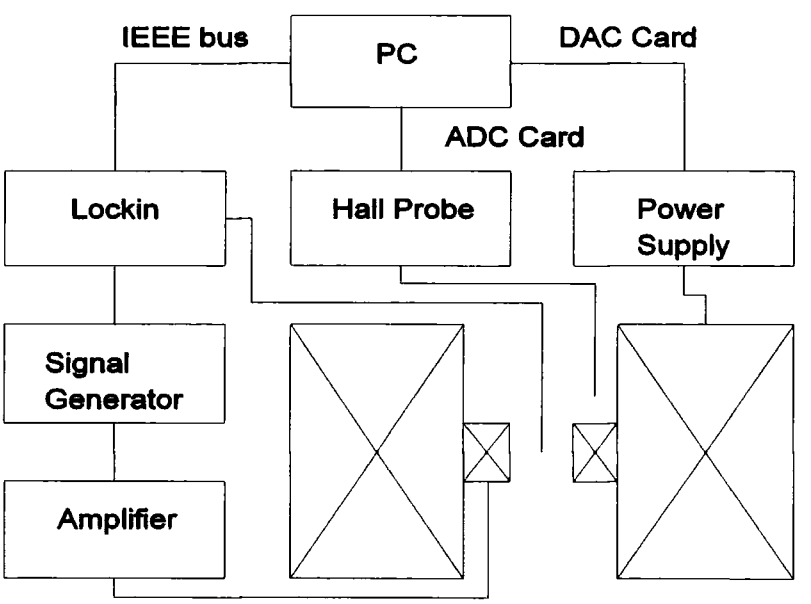

Figure 5.2 The wiring schematic for the AGFM

An attempt has been made to construct an AGFM to work at low temperatures. Groups have reported that the sensitivity of the system drops by two orders of magnitude as the temperature is lowered to 5K [6]. The work undertaken by the author showed a useable senisitivity below 10^{-7} J T^{-1} [7], which was considered to be of no use for the investigations, and less than that obtainable using the vibrating sample magnetometer in the laboratory [8]. The majority of the noise was believed to have been caused by the vibration of the boiling cryogen and the difficulty in mounting a thermometer onto the sample holder itself. The work was abandoned after the initial stages, as it was found that the behaviour of the piezoelectric bimorph is strongly temperature dependant. The other groups [6] have mounted their bimorphs in the horizontal plane, and away from the low temperatures of the sample, hence removing the problem. Mounting bimorphs horizontally has also been used successfully to build magnetometers for use at room temperature [5], although the initial construction is more difficult than for the pendulum style used here, and the sensitivities of the two styles is very close.

5.1.3 Calibration

The system is calibrated by the use of a known mass of nickel and looking at the saturation magnetisation. The samples used for this particular system is 4μm thick foil, usually in an approximately 1mm square. The voltage at which this saturates is then compared to the value of the saturation magnetisation of nickel. A typical calibration curve is shown in figure 5.3.

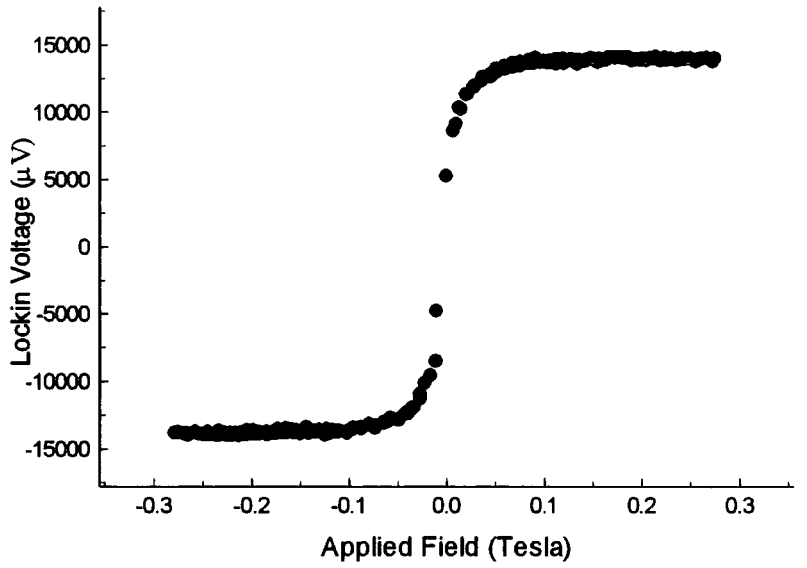

Figure 5.3 The saturation of nickel

An example of the calculation is shown below.

Mass of Ni $2.67\text{x}10^{-7}$ Kg

Saturation voltage 14.1mV

The saturation magnetisation of Ni at room temperature can be calculated using the following [11]

$$M = M_o(1 - a_{32}T^{\frac{3}{2}} - a_{52}T^{\frac{5}{2}}) \qquad (5.7)$$

where a_{32} =6.64x10^{-6}, a_{52}=1.85x10^{-8}, M_o=58.624 J T^{-1} Kg^{-1}, and T is the temperature.

For room temperature (288K), the magnetisation is 55.20 J T^{-1} Kg^{-1}.

The scaling factor for the magnetisation is therefore

$$\frac{55*2.67*10^{-7}}{14.1*10^{-3}} = 1.045*10^{-3} \text{ J T}^{-1} \text{ V}^{-1}$$

So 1V on the output of the lockin amplifier is equivalent to 1.045×10^{-3} J T^{-1}. The smallest voltage that can be detected on the lockin amplifier is 0.1μV with a time constant of 30 seconds, so the maximum sensitivity of the system is 1.045×10^{-10} J T^{-1}, compared to 10^{-12} J T^{-1} quoted in [4]. The sensitivity of the system can be increased by using a higher gradient field, although care has to be taken to avoid clipping the voltage applied to the coils, which increases the system noise.

Other methods of calibration include utilising the susceptibility of palladium or hydrated cupric sulphate ($CuSO_4:5H_2O$) which is useful for a low field system which cannot saturate nickel.

5.1.4 Operating Technique.

The sample under investigation is affixed to the sample holder with a small amount of vacuum grease. In the case of a very magnetic material such as nickel, GE 7031 varnish is used to attach the samples more rigidly to the holder to prevent movement. The power supply for the magnet is set to a high field (usually 2000 gauss). The system is then scanned through the frequency range where the resonant frequency is likely to be found. The computer varies the frequency of the system by applying a known voltage to the voltage controlled oscillator facility on the frequency generator. Both the in phase and the quadrature voltage are read and compared to that which is expected, which is shown in figure 5.4.

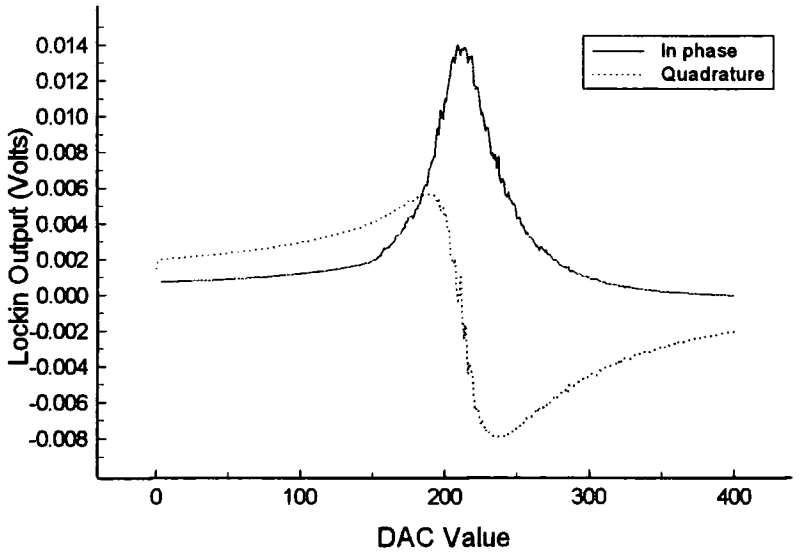

Figure 5.4 The resonant condition

If the two differ, then the frequency is set to the value which gives the largest signal and the phase of the system is maximised at this point. The frequency sweep is repeated, until the desired shape is obtained. Some of the data sets show what appears to be two resonance peaks, the second of which is taken to be oscillation in a different plane to the magnetic field, caused by the sample being offset in the field and producing torque on the cantilever.

The power supply is now set to zero, and the computer program started. This changes the field, reads the lockin amplifier and the teslameter, stores the values to disc, and so on. A full MH loop can be performed in a matter of minutes and stored in an ASCII format, ready for use with a graphics package.

5.2 2DEG Hall devices

5.2.1 Theory of operation

A Hall device is the most common method used for measuring the magnetic field at a point. It is based on measuring the Hall effect in the device, and after initial calibration provides a cheap and simple method of field measurement. The most sensitive Hall devices have a small number of free carriers and so produce the highest Hall voltage for a given field. It is also advantageous to be able to use high current through the chips as this will also increase the sensitivity, since according to equation 5.8, the Hall voltage is given by

$$V_H = \frac{BI}{net} \qquad (5.8)$$

where B is the applied field, I the current in the sample, n the carrier concentration, e the electronic charge, and t the thickness of the device

The problem in this is that, for a low carrier concentration, the resistance of the material is too high to allow a useable current to pass without Joule heating or damage to the chip. One way round this is to construct a two Dimensional Electron Gas (2DEG) where the mobility of electrons in the layer can be as high as $4.5\text{x}10^6\text{cm}^2\text{V}^{-1}\text{s}^{-1}$ at 4.2K, hence lowering the resistance to a more reasonable value. The typical number of carriers in such a device is $2.7\text{x}10^{11}$ cm^{-2} [9]. It can be shown that the sensitivity of the device is proportional to the mobility of the carriers, as is shown in equation 5.9

$$V_H = \frac{BA\mu E_{xx}}{t} \qquad (5.9)$$

where A is the cross sectional area of the chip, and E_{xx} the electric field associated with the current.

2DEG Hall devices have become a popular and highly sensitive method of obtaining magnetic profiles of materials. The original work was performed by Chang *et al* [10] who investigated the properties of superconductors using a linear array of Hall pairs. The latest work has been to use the Hall chip in the place of the tunnelling tip of a scanning tunnelling microscope, and to scan this across the surface of the material. The work of Simon Bending and his group at Bath University have managed to make simultaneous measurements of the tunnelling current from the tip, and the Hall voltage, to show both the surface morphology and the magnetisation of the sample[9]. The majority of the measurements performed using these systems has been in the investigations of the magnetism of superconductors, and this is the first attempt to use the chips to make observations on diluted magnetic semiconductors.

The Hall bars used in this work were fabricated at Bath University by Dr Simon Stoddart from a AlGaAs heterostructure grown at Nottingham University. The chips have nine Hall pairs along their length, as shown in figure 5.5, each of which are 50μm in cross section, and 7nm thick.

Figure 5.5 Optical Micrograph of a Hall device, showing the individual Hall pairs

The chips were tested at Bath University to ensure that all the voltage pairs

were functioning, and to find two pairs that were matched in their sensitivities. The chips are wired up so that two of the Hall bars are used, to allow differential measurements to be performed. One of these pairs has the sample mounted over it, the other is left uncovered. This allows for far more accurate and reproducible results to be taken as a background run is obtained for every measurement, and so small differences in the position of the chip in the magnet can be eliminated.

The signal from the chip with the sample sees an enhanced magnetic field from the magnetic properties of the sample according to equation 5.10.

$$B = \mu_o(H + M) \qquad (5.10)$$

Where H is the applied magnetic field, M is the magnetisation of the sample, μ_o is the permeability of free space, B is the enhanced magnetic flux density seen by the chip.

The sensitivity of the chip was calibrated using a known mass of nickel, and looking at the saturation produced. The sample was a 100(±50)μg foil sample, which gave a saturation of 26.6 Ohms. This gives a sensitivity of 10^{-9} J T^{-1}, which is comparable to other magnetometers used by the group. The sensitivity can also be expressed as 0.2 Ohms $Gauss^{-1}$, which corresponds very well with the values given in the literature of 0.3 Ohms $Gauss^{-1}$. [9]

5.2.2 Experimental Details

The chip is mounted in the Displex closed cycle system that has been outlined in section 4.4. Initially it was found that the Joule heating produced in the chip at low currents was in excess of the cooling power through the wires connecting it to the holder. The solution to this was to affix the chip down with a small layer of GE varnish, which had the added advantage that it would also hold the chip in place more

firmly and stop it moving in high field. The current in the chip is 13Hz AC, so that lockin techniques could be used to improve the signal to noise ratio. The noise on the chip can be lowered by using a higher frequency as the signal to noise ratio in these devices is given by [8]

$$S.N.R. = \frac{IR_H B}{\sqrt{4k_B T R_s f}} \qquad (5.11)$$

Where I is the Hall current, R_H the Hall coefficient, B the magnetic field, k_B Boltzmann's constant, T the temperature, R_s the device resistance, and f the frequency of the Hall current.

The chip is used in differential mode. One of the voltage pairs has the sample affixed over it, whilst the other is uncovered. This allows the background to be taken with every run, as it shows a strong temperature dependence, especially above 45K. This requires the sample positioning to be critical, because the two matched Hall pairs used are located close together in the middle of the chip. Hence, the background signal often has part of the sample trace superimposed onto it. The background of the chip behaves in the normal manner with V_H a linear function of B. By analysing the saturation resistance of a known nickel sample the sensitivity of the system can be calculated, in a manner similar to that used on the AGFM above.

5.3 The Faraday Balance

The Faraday balance is a commercial magnetometer supplied by Oxford Instruments LTD, and is based around a highly sensitive microbalance head.

This particular system is capable of 5 T in a temperature range of 1.4 to 320K, which gives it the ability to achieve a B/T ratio of 3.57T K^{-1}, greater than the value required to saturate paramagnets within 1%, which is 3T K^{-1}. [11,12].

The measurement procedure of the system is to compare the mass of a sample under magnetic field gradients of opposing direction. From Faraday's Law, and equation 5.2 we obtain the force on the sample [1]

$$F_x = V\chi B_o \frac{\partial B^x{}_o}{\partial x} \qquad (5.12)$$

Where $\frac{\partial B^x{}_o}{\partial x}$ is the field gradient in the x direction, B_o the applied field, V the volume and χ the volume susceptibility of the sample.

Hence by measuring the change in force on the sample, under the application of magnetic gradients in the +x and -x direction, a measure of its magnetic susceptibility can be obtained. Although in theory it is possible to calibrate the system directly from the above equation measurements are usually performed relative to a standard sample such as nickel. The saturation of nickel is often chosen because it is field independent above its saturation value, although other material such as Mercury-tetra-thio-cyanato-cobalate, $HgCo(SCN)_4$ is often used as a paramagetic standard, $\chi_g = 16.44 \times 10^{-6}$ emu g^{-1}.

5.3.2 Operating Procedure

A diagram of the balance system is given in figure 5.7

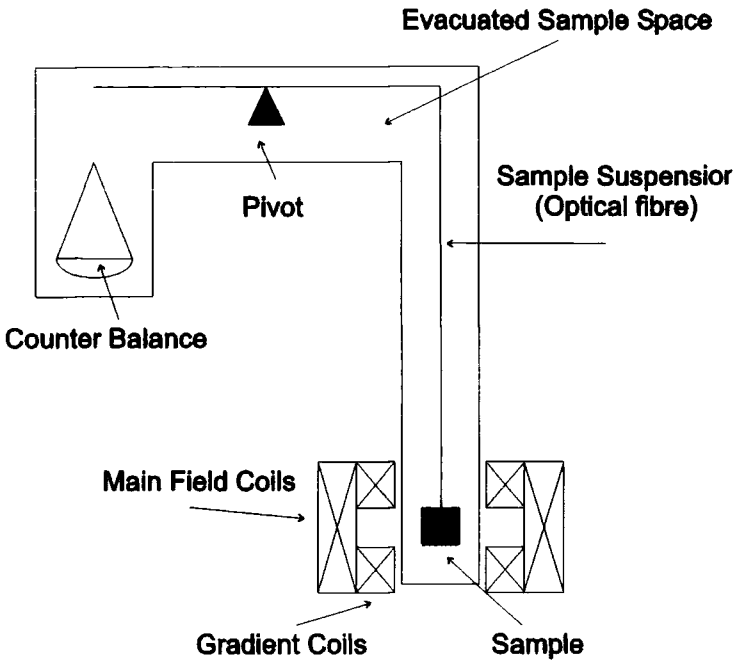

Figure 5.7 The Faraday balance

The sample under investigation is affixed to the lower end of an optical fibre, which is then hooked onto the end of the balance arm. The height of the balance head with respect to the cryostat had previously been set so that the sample was in the centre of the gradient field. Full details of the process can be found in ref. [12]. The sample space is then flushed with helium gas and evacuated down to 5mbar before cooldown. The pressure of exchange gas in the sample space relates directly to the thermal link to the variable temperature insert (VTI). The higher the pressure, the more rapid the temperature will achieve equilibrium, although it will also raise the noise on the system, and so for the epitaxial layers, the pressure was kept as low as possible, and the system left for long periods, typically fifteen minutes, to equilibrate. The magnetic field required is then set and the magnet set to run in persistent mode, usually at 1 Tesla so that a large signal can be obtained with weakly magnetic samples. The gradient field is then set and reversed so that the magnetisation can be obtained.

The output from the balance head is read by the computer via Object Bench software and saved as a datafile for later analysis. This procedure is then repeated for all the temperatures and fields required. The calibration curve for nickel at 4.3 K is shown below.

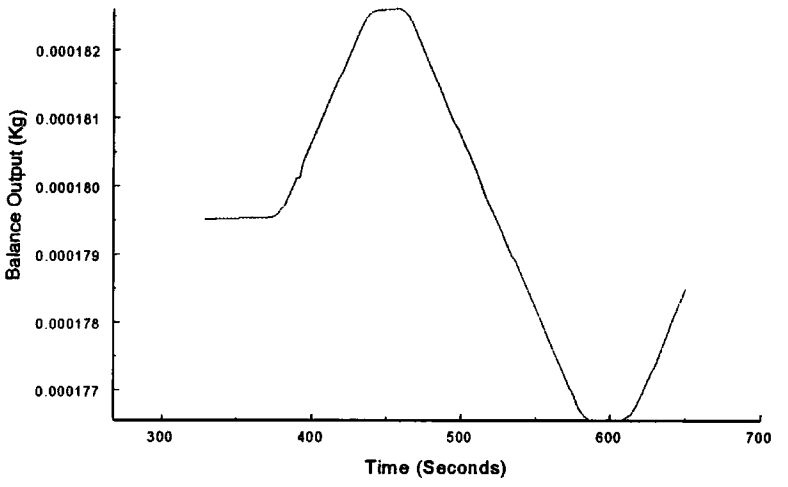

Figure 5.8 Nickel Calibration Curve (Raw Data) taken at 1 Tesla

It is noted that the positive field gradient is applied before the negative field gradient. From the shape of the graph it can be seen that the nickel has a positive susceptibility, as the graph has a positive deflection before the negative.

The calibration of the balance is very similar to that of the Hall devices outlined in section 5.2.2, using equation 5.9. From the standard deviation on the noise for this data set, it has been calculated that the noisebase on the system is 7.5683×10^{-11} JT^{-1}, which is comparable to that of the AGFM.

Reference List Chapter five

[1] Crangle, J., The magnetic properties of solids, Edward Arnold, London,1977, p158

[2] Zijlstra, H., Review Scientific Instruments, **41**, (1970), 1241

[3] Roos, W, Hempel, K.A., Voigt, C., Dedeirchs, H., Schippen, R., Review Scientific Instruments, **51**, (1980), 612

[4] Flanders, P.J., J App Phys, **63**, (1988), 3940

[5] Flanders, P.J., J App Phys, **67**, (1990), 5475

[6] O Grady, K., Lewis, V.G., Dickson, D.P.E., J App Phys, **73**, (1993), 5608

[7] Horsfall, A.B., Internal report University of Durham, unpublished

[8] Gregory, C.I., 'Magnetic properties of the itinerant helimagnets MnSi and FeGe', PhD Thesis, University of Durham, 1992

[9] Oral, A., Bending, S.J., App Phys Lett, **69**, (1996), 1324

[10] Chang, A.M., *et al*, App Phys Lett, **61**, (1992), 1974

[11] Graham, C.D., J App Phys, **53**, (1982), 2032

[12] Kobler, U., Deloie, F., Internal report Kernforschungsanlage Juelich GmbH

[13] Ashcroft, N.W., Mermin, N.D., 'Solid State Physics', Saunders College, Philadelphia, 1976

Chapter Six Electrical Results

6.1 Summary of samples investigated

The samples have been investigated using the experimental apparatus described in section 4.3, in the Van der Pauw configuration.

The samples investigated electrically are outlined in table 6.1 below.

Sample Number	Manganese Concentration (%) from EDAX	Thickness (μm) from SEM	Thickness (μm) from EDAX
MMT38A	5 - 8	5.5±0.2	5.8
MMT38B	5 - 8	5.5±0.2	5.8
MMT29A	8 - 11	1.6±0.2	4.4
MMT29B	8 - 11	1.7±0.2	4.4
MMT21A	5 - 6	1.5±0.2	1.1
MMT21B	5 - 6	1.5±0.2	1.1
MMT26	10	1.9±0.2	1.2
MMT19B	Very small	2.2±0.2	7.7
MMT34	25	1.5±0.1	1.2
MnTe	100	1.1±0.2	____

Table 6.1 Summary of samples investigated

The manganese concentrations of some of the samples show a spread of values, and this is due to the inhomogeneities present in the growth as outlined in chapter 1.

6.2 Sample MMT38

6.2.1 MMT38B

Results

Figure 6.1 shows the variance resistivity of as a function of temperature. The graph shows no evidence for an activation energy, as the line does not become linear for an appreciable part of the temperature range.

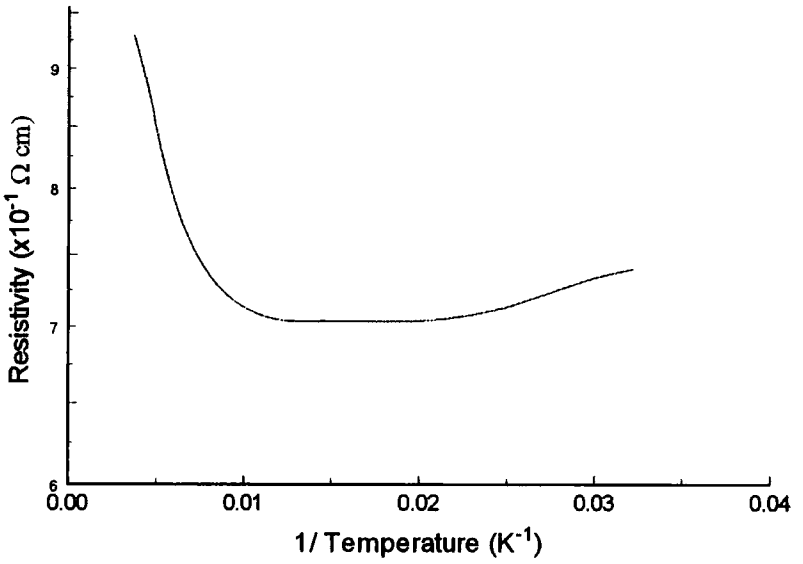

Figure 6.1 The resistivity of MMT38B

Figure 6.2 shows the number of effective carriers, $|R_H e|^{-1}$, in the material as a function of temperature. From the gradient of the graph at low temperatures it is possible to calculate an activation energy, see discussion.

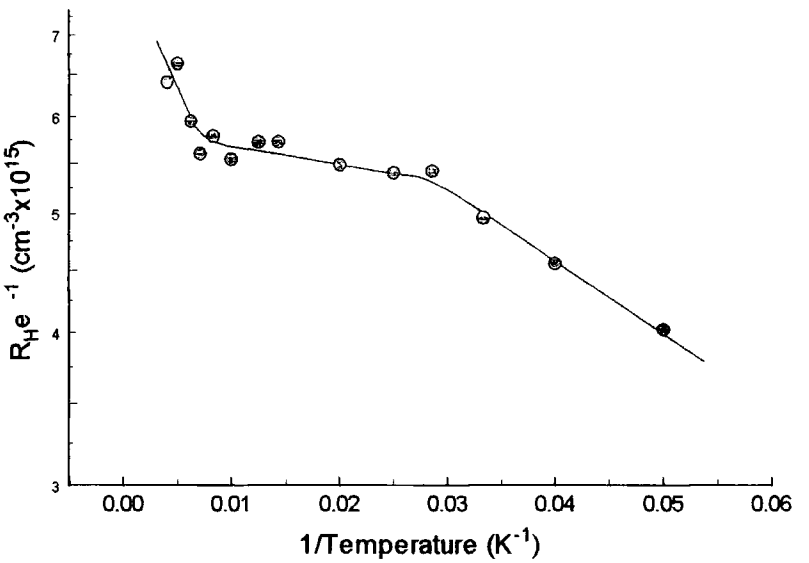

Figure 6.2 Effective Carrier Concentration in sample 38B

Figure 6.3 shows the variation of the Hall mobility of the carriers as a function of temperature. The fit shows the dominant form of scattering at high temperatures.

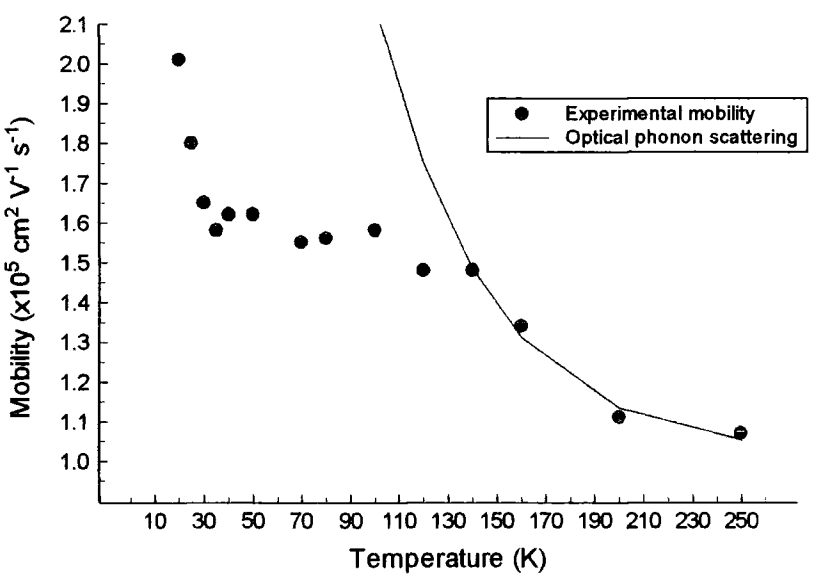

Figure 6.3 Mobility of sample 38B

Figure 6.4 shows the transverse magnetoresistance of the sample, measured in the Van der Pauw configuration, as a function of applied magnetic field. The small anisotropy on the figure is due to a contribution from the Hall effect originating in the misalignment of the electrical contacts.

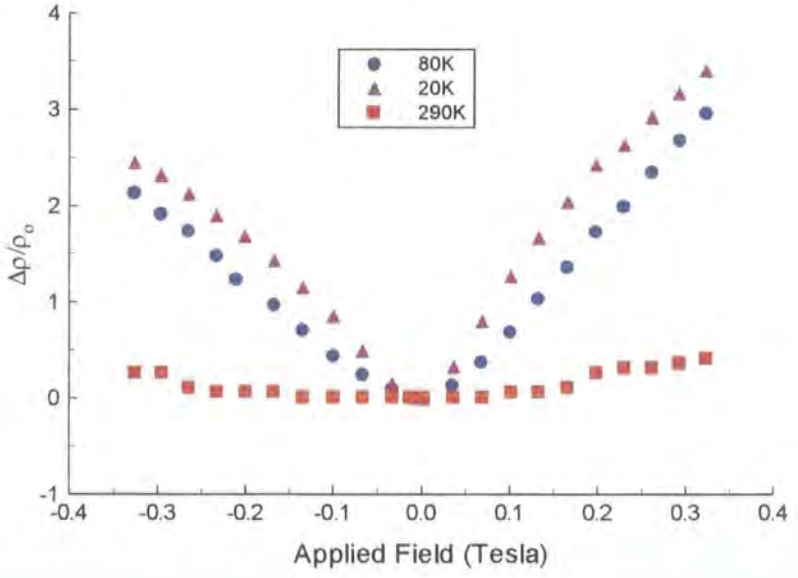

Figure 6.4 The magnetoresistance of sample MMT38

Discussion

The resistivity of fig 6.1 shows an initial drop which can be attributed to the rise in the mobility observed in fig 6.3. Below this the data shows evidence of carrier freezeout.

The value of $|R_H e|^{-1}$ shows intrinsic behaviour at the high temperatures, a plateau between 125 and 40K, and then carrier freezeout into a donor state of 1.2meV. The value for the activation energy is taken from the gradient of $\ln(|R_H e|^{-1})$ v $\frac{1}{T}$. The data can be

fitted using an equation for the number of donors and the number of intrinsic carriers. The intrinsic carrier concentration can be calculated from equation 6.1 [1]

$$n_i = (4.615 - 1.59x + 0.00264T - 0.017xT + 34.15x^2)\text{x}10^{14} Eg^{\frac{3}{4}} T^{\frac{3}{2}} e^{\left(\frac{-5802Eg}{T}\right)} \qquad (6.1)$$

and the donor concentration can be calculated from [2]

$$n_D = \frac{N_D}{1 + e^{\left(\frac{E_d}{2k_B T}\right)}} \qquad (6.2)$$

where N_D is the donor concentration, and E_d the energy of the donor.

Using this to obtain a fit to the data of $|R_H e|^{-1}$ shown in figure 6.2, gives a donor concentration of 5.5x10^{15} cm^{-3}, using E_d of 1.2meV, which corresponds very well to the plateau observed in the data.

The mobility of the carriers in this sample is very high, suggesting that the crystalline quality is also very high. The high temperature region of the data can be fitted with optical phonon scattering, using parameters of

Parameter	Value
θ	140K
m_e	$0.05m_o$
ν	1.32x10^{10}Hz

Table 6.2 Fitting Parameters to optical phonon scattering

The leveling off of the mobility looks to be similar to that observed by Sawicki et al [3], who observed a drop in mobility between 20K and 80K, before rising again below this. This is shown in figure 6.5 below.

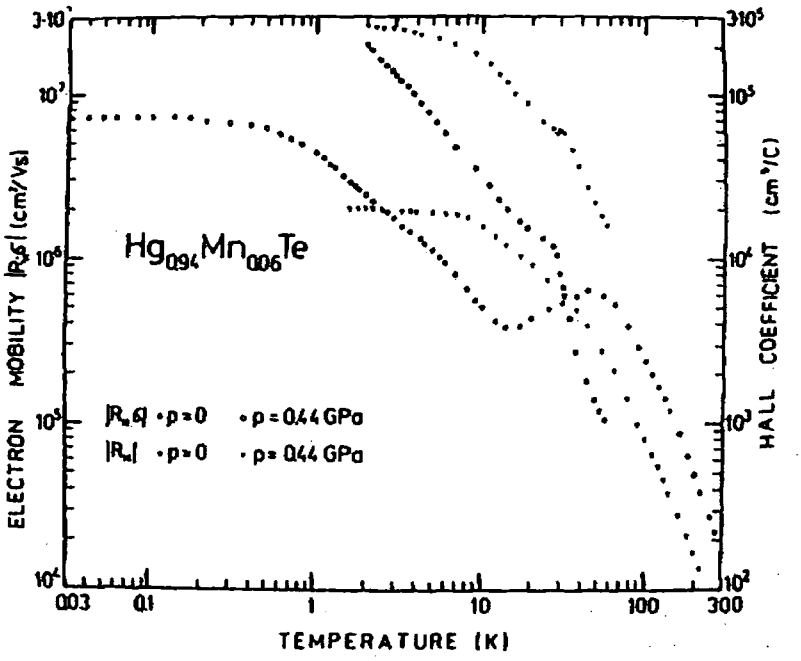

Figure 6.5 The mobility in $Hg_{0.94}Mn_{0.06}Te$ [3]

The explanation for this behaviour is that the ionised impurities form pairs, one acceptor and a donor, and hence lower their scattering efficiency.[4]

The transverse magnetoresistance of this sample is a positive quadratic, especially in the low field limit. A quadratic magnetoresistance can normally be fitted by equation 6.3

$$\frac{\Delta\rho}{\rho_o} = \mu_n^{\,2} B^2 \qquad (6.3)$$

At high temperatures the mobility in the sample is described by optical phonon scattering, and this leads to the temperature dependence of

$$\mu \alpha T^{-\frac{1}{2}} e^{\frac{\theta}{T}} \qquad (6.4)$$

The exponential term is only important at temperatures well below the Debye temperature (θ),which is 140K in HgMnTe, [5] and so the mobility can be described by a $T^{-\frac{1}{2}}$ dependence. Hence we can rewrite equation 6.3 as

$$\frac{\Delta\rho}{\rho_o} \alpha B^2 T^{-1} \qquad (6.5)$$

From this it can be seen that for optical phonon scattering, a plot of the magnetoresistance against B/T should result in the superposition of the data curves. This is shown in figure 6.6.

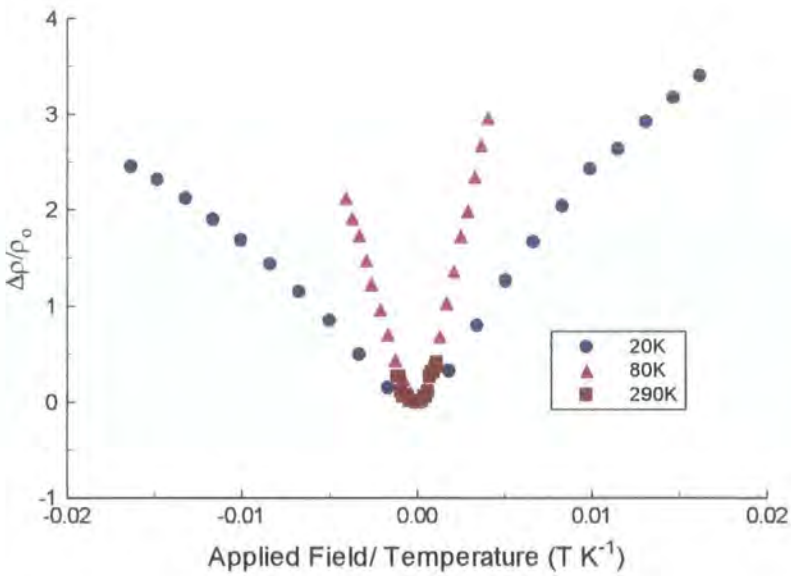

Figure 6.6 Magnetoresistance as a function of B/T

From this it can be seen that the scattering mechanism that is dominant at low temperatures is unlikely to be optical phonon. It is interesting to note that although the values for 290K and 80K overlap, the mobility of the sample as shown in figure 6.3 would suggest that optical phonon scattering is no longer responsible for the mobility at 80K.

In a compensated semiconductor, the above equations are not strictly true, as the contribution from the holes has to be taken into account. The revised formula can be expressed as [6]

$$\frac{\Delta\rho}{\rho_0} = \mu_n \mu_h B^2 \qquad (6.6)$$

The above calculations will hold in such a system providing that both the holes and electrons are dominated by optical phonon scattering.

The 20K data is showing evidence for saturation at high field. This is similar to the behaviour observed in bulk MMT by Davydov [4] and by Delves [7] where at 4.2K and fields above 1T the magnetoresistance changes from being positive to negative. This result is generally considered to be due to the bipolar conduction that occurs in these materials.

6.2.2 MMT38A

Results

Figure 6.7 shows the variance of the Hall voltage of sample MMT38A as a function of temperature. The curvature that is observed in the low temperature case, is an example of the anomalous Hall effect, that was discussed in section 2.5.3.

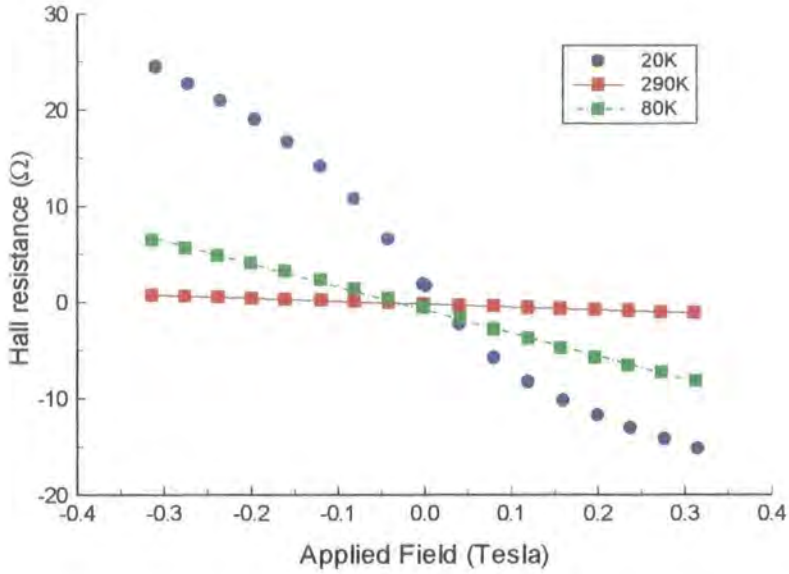

Figure 6.7 The anomalous Hall behaviour in sample MMT38A

Discussion

The Hall voltage in a magnetic material receives an extra contribution from the magnetisation as shown in equation 6.7. [8]

$$R_{Hmeas} = R_{Hact} + C\rho\chi \qquad (6.7)$$

Assuming that the susceptibility can be calculated using the Brillouin function for a paramagnetic material, we can attempt a fit to the 20K data. The value of θ used, is that obtained from the susceptibility data in chapter 7, $\theta = -25K$. The linear contribution at high field is assumed to be equal to R_{Hact}, and figure 6.8 below shows the fit to the anomalous component. The data has also been fitted to a Langevin function for a superparamagnetic material, as X-ray scattering and EDAX have shown the existence of MnTe clumps within the material (see chapter 1). The value of C obtained from this analysis is $8.235 \times 10^{9} m^2$.

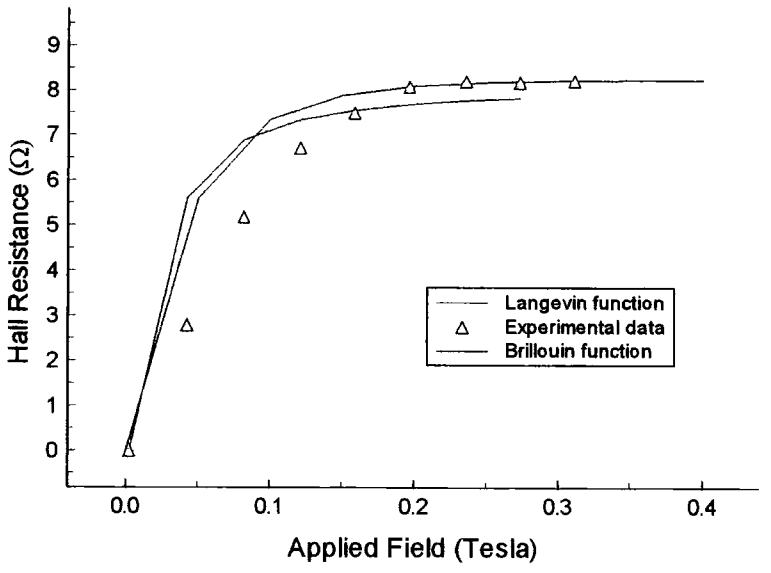

Figure 6.8 Fits to the anomalous Hall effect at 20K

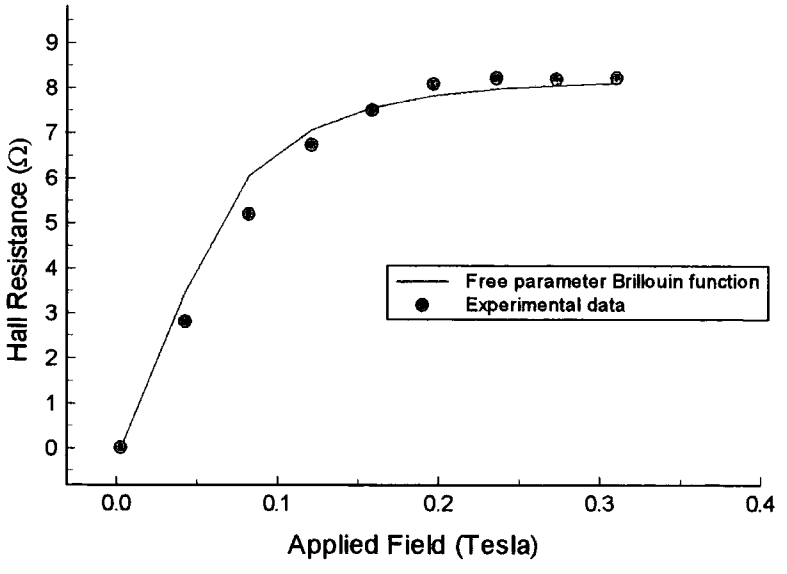

Figure 6.9 Free parameter fit to the saturation of the Hall effect

Figure 6.8 shows the results of a fit to the data where the value of θ is used as a fitting parameter. The value obtained from this is -19.88K, which corresponds to a Mn concentration of 5.7%. [9] This is very close to the value given by EDAX, of 5.5%.

From the data in the figure it can be seen that the magnetic anomalous Hall effect is unlikely to be responsible for the observed data. The other possible mechanism for the nonlinearity is the effect of two band conduction. It is difficult to check this hypothesis because the magnetic field has not been taken to a sufficiently high value to enter the 'high field regime', where this effect would become noticeable. The high field regime can be expressed as the field that satisfies the inequality

$$B\mu > 1 \qquad (6.8)$$

In this case, with a mobility of around $2\mathrm{m}^2\mathrm{V}^{-1}\mathrm{s}^{-1}$, it will require a field in excess of 0.5T to achieve this condition. The maximum applied field in these measurements was only 0.3T, and so the measurements are all in the low field limit.

6.3 Sample MMT29

6.3.1 Sample MMT29A

Results

Figure 6.10 shows the variation of the resistivity of sample MMT29A as a function of temperature, taken dynamically. The graph shows the existence of an activation energy of 9.0meV, taken from the linear region below 30K.

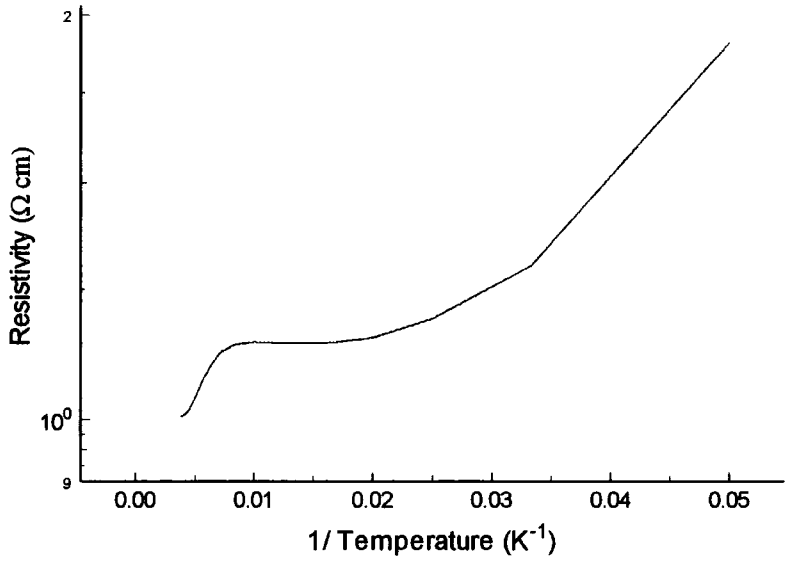

Figure 6.10 The resistivity of sample MMT29A

Figure 6.11 shows the variation of the magnitude of the number of effective carriers, $|R_H e|^{-1}$, in sample MMT29A.

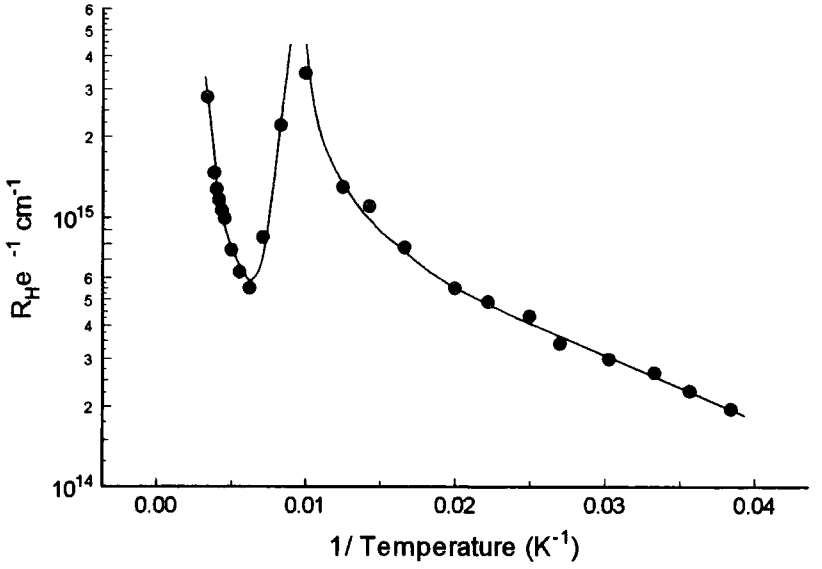

Figure 6.11 Effective carrier concentration in sample MMT29A

Figure 6.12 shows the variation of the Hall mobility in the sample with temperature.

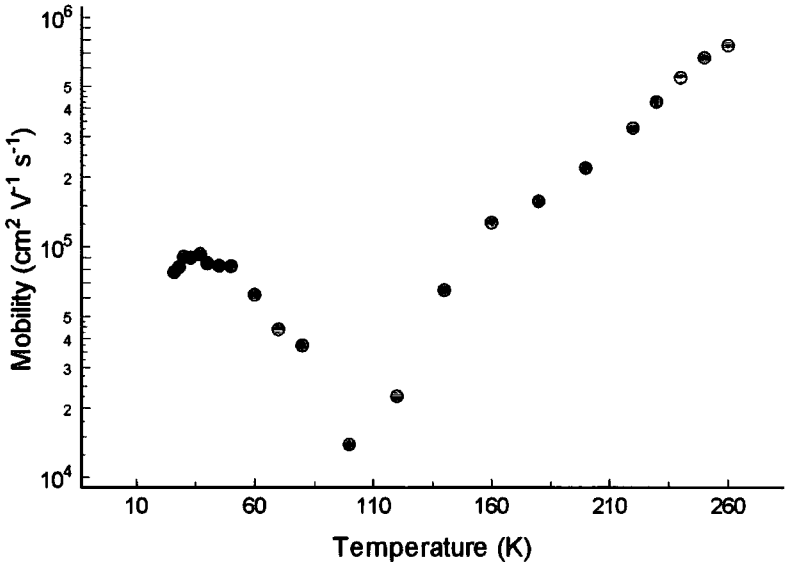

Figure 6.12 The mobility of sample MMT29A

Figure 6.13 shows the transverse magnetoresistance of sample MMT29A as a function of applied field at varying temperatures.

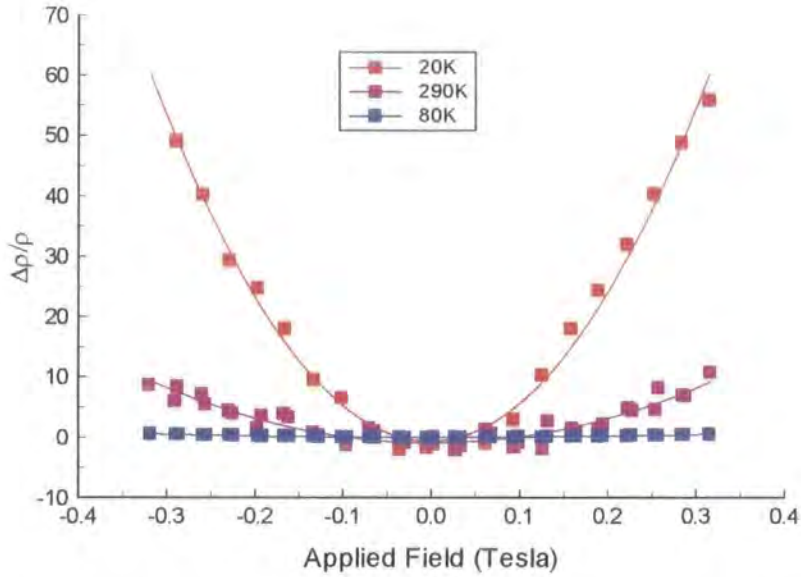

Figure 6.13 The transverse magnetoresistance of sample MMT29A

Discussion

The effective carrier concentration shows a discontinuity at approximately 100K, and this can be interpreted as the transition from electron to hole dominant carrier in the sample. The Hall coefficient for a mixed conduction sample can be expressed as

$$R_H = \frac{r_o}{e}\frac{(p-b^2n)}{(p+bn)^2} \qquad (6.9)$$

where r_o is the Hall coefficient factor outlined in section 2.5, p and n are the carrier concentrations of holes and electrons respectively, and b is the mobility ratio defined as

$$b = \frac{\mu_n}{\mu_p} \qquad (6.10)$$

The value of b can be calculated from the ratio of [10]

$$\frac{R_o^{max}}{R_o^{ext}} = -\frac{(b-1)^2}{4b} \qquad (6.11)$$

where R_o^{max} is the maximum value of the Hall coefficient, and R_o^{ext} is the value of the Hall coefficient in the extrinsic region, which can be assumed to be given by the value of $N_A - N_D = 4.0\text{x}10^{14}\,\text{cm}^{-3}$.

Using this, we can find that the value of b is 26.38, which compares to the values expressed in the literature of 70 [11] and 100 [12]. Using this, the mobility of the electrons at 20K would be expected to be $2.11\text{x}10^{6}\,\text{cm}^2\text{V}^{-1}\text{s}^{-1}$.

Below about 50K, the carrier concentration starts to drop once again, suggesting the freezing out of holes in to an acceptor with an energy of approximately 9.0 meV. This would support the suggestion that the p-type behaviour is due to Hg vacancies in the material, as the activation energy of these vacancies has been measured as 9.4meV for a sample with x=0.15. [13]

The magnetoresistance of this sample is a positive quadratic, which is very similar to the behaviour shown in MMT38. The curve at 80K is more shallow than the other curves shown. This is linked to the transition between electron and hole dominant conduction.

6.3.2 Sample MMT29B

Results

Figure 6.14 shows the resistivity of sample MMT29B. The pink curve shows the resistivity of the sample without illumination. The green curve shows the resistivity of the sample whilst being illuminated with infrared light from an LED. After the sample had cooled to the base temperature, the LED was turned off, and during the warming process, the blue curve was obtained. From the graph it can be seen that the sample has an activation energy that is varied by illumination.

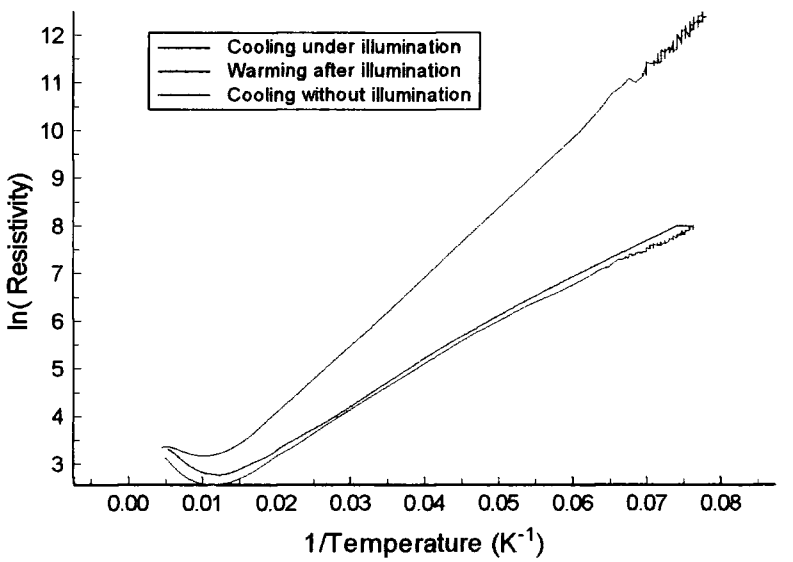

Figure 6.14 Resistivity of sample MMT29B

Figure 6.15 shows the effective carrier concentration, $|R_H e|^{-1}$, as a function of temperature for the dark (pink triangles) and illuminated (blue circles) cases.

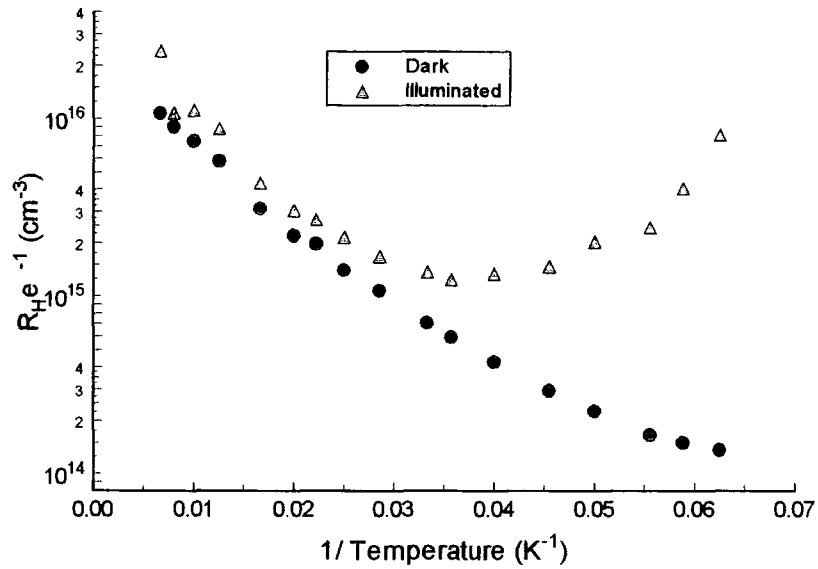

Figure 6.15 The comparison of the effective carrier concentrations for sample MMT29B

Figure 6.16 shows the mobility of the carriers for the unilluminated sample MMT29B as a function of temperature, and fits to this to demonstrate the possible dominant scattering mechanisms in the material.

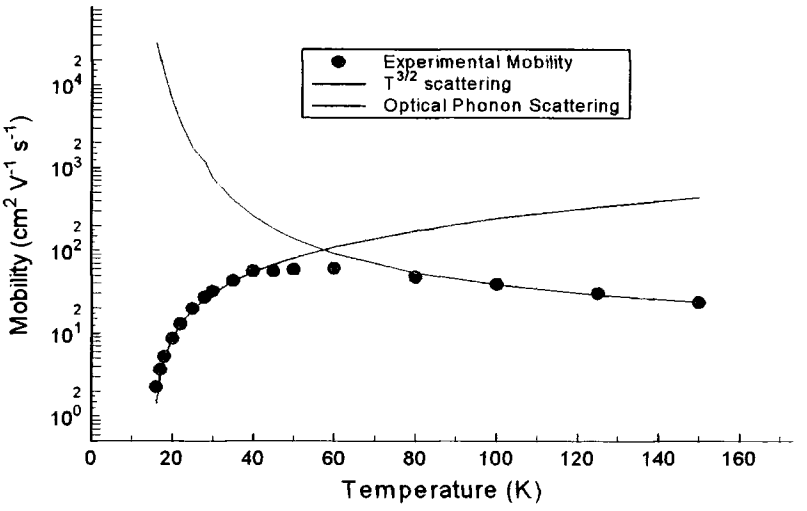

Figure 6.16 The mobility of MMT29B in the dark

Figure 6.17 shows the mobility of the carriers for the illuminated sample MMT29B as a function of temperature, and fits to this to demonstrate the dominant scattering mechanisms in the material.

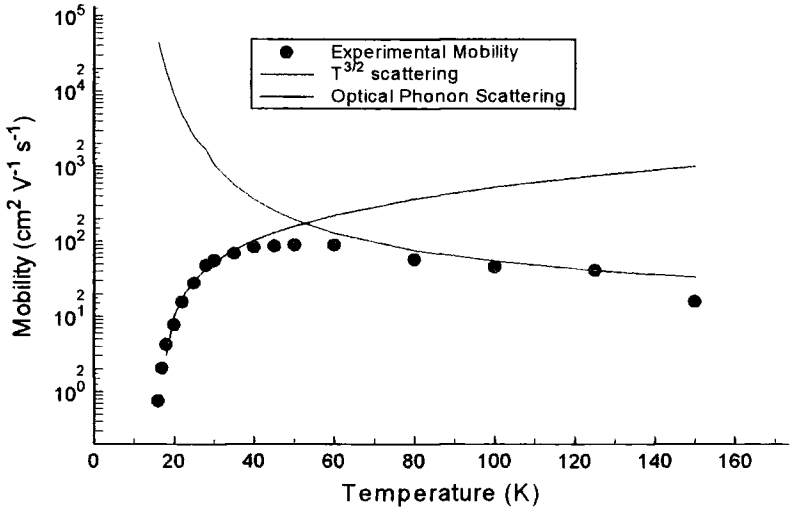

Figure 6.17 The mobility of sample MMT29B under illumination

Figure 6.18 shows the transverse magnetoresistance of sample MMT29B at 300K, under illumination and in the dark. The two curves have been normalised because of the change in the zero-field resistivity under illumination.

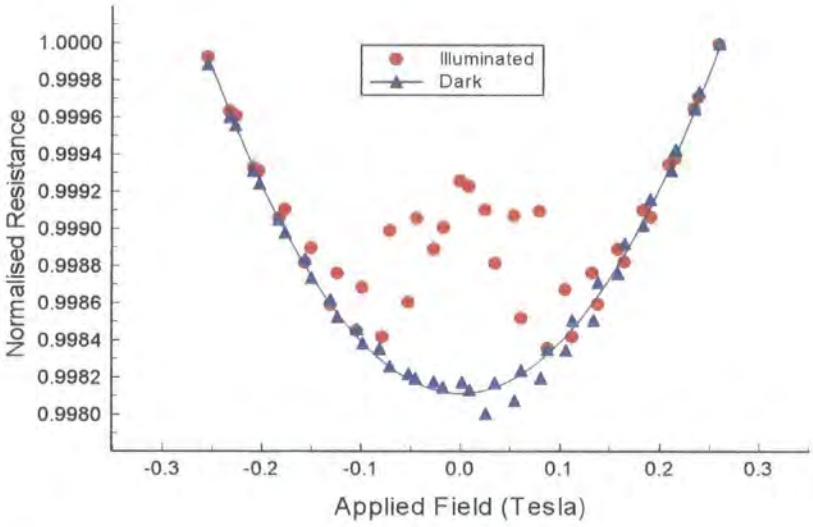

Figure 6.18 Magnetoresistance of sample MMT29B

Discussion

The resistivity of the sample in the dark shows the existence of activated conduction with an energy gap of 12.6meV. Under illumination, the resistivity shows a non linear behaviour, and an estimate of the energy gap from the lowest points, gives an estimate for the energy of 7.6meV. The resistivity of the illuminated sample can be shown to fit

$$\rho = \rho_o e^{\left(\frac{T_o}{T}\right)^{\frac{1}{2}}} \qquad (6.12)$$

as indicated in figure 6.19.This is the expected behaviour for Efros - Skhlovskii variable range hopping. [14] The value of T_o in this sample is 1352K, and from this the radius of the carrier orbit can be calculated using equation 6.13. [14]

$$T_o = \frac{2.8e^2}{4\pi k_B \varepsilon a_B} \qquad (6.13)$$

From this it has been calculated that the radius of the carrier orbit is 23Å. This compares to the values calculated from hydrogenic theory of 264Å for electrons and 30Å for holes in HgMnTe.

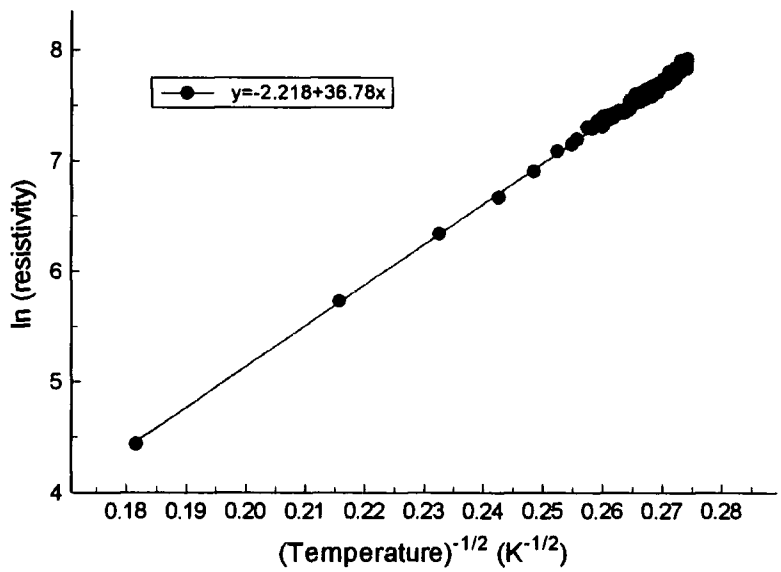

Figure 6.19 The Hopping regime in MMT29B

After illuminating the sample during cool down, the light was removed and then the resistivity monitored during the warming of the system. In fig 6.14, the resistivity can be seen to follow the illuminated case closely until 200K is reached. The small offset between the two cases is due to the relaxation that occurs as soon as the illumination

removed. This relaxation occurs too quickly for a quantitative measurement to be taken. After the initial relaxation of the sample, a different mechanism occurs, with a far longer time period.

This resistivity data looks very similar to that observed in persistent photoconductors, where upon illumination the resistivity of the sample drops and relaxes very slowly upon the removal of the illumination. The resistivity will only rejoin the dark value when the temperature exceeds a certain value, referred to as the quenching temperature. Comparing the resistivity data to that of a more conventional persistant photoconductor, e.g. CdMnTe:In in section 8.1, we can see that in this case of sample MMT29B, the quenching temperature can be defined as 200K. This is higher than is observed in many materials where the PPC is based on a microscopic mechanism such as the DX centre, in CdMnTe and AlGaAs. [15]

The variation of the measured $|R_{He}|^{-1}$ in the dark, shows the existence of an energy gap at high temperature, with a value of 13.82meV. This compares well to that obtained from the resistivity of 12.6meV. At low temperatures, the data shows a trend away from this activated conduction. This behaviour may be due to the sample starting to undergo the transition from electron to hole dominant carrier. A comparison to the data obtained in sample MMT29A, would seem to support this hypothesis. No activation energy can be obtained from the illuminated data. Below 40K the two carrier concentrations diverge, and the illuminated curve is showing a large increase. From this it would appear that the sample is undergoing the transition to hole majority carrier at a higher temperature than in the dark case.

If the resistivity behaviour at low temperatures in the illuminated case is dominated by the transition to variable range hopping conduction as has been speculated previously, then the value of $|R_{He}|^{-1}$, maybe expected to rise. This has been observed in p-type Ge samples by Fritzsche *et al* [17].

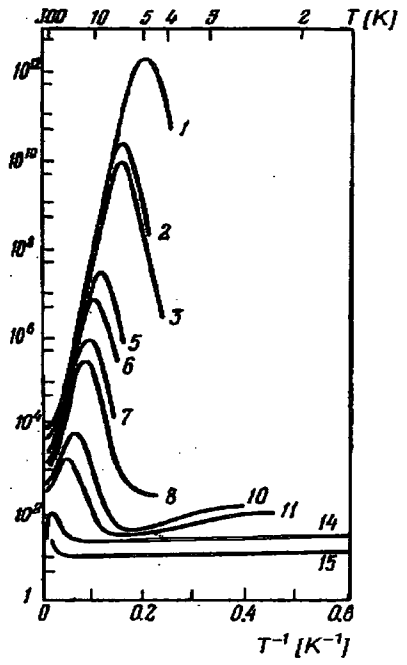

Figure 6.20 Behaviour of $|R_{He}|^{-1}$ in the hopping regime in p-type germanium

If this is indeed the case, then the mobility in this region cannot be expected to follow that of ionised impurity scattering, and the rapid fall off will be caused by the transition to variable range hopping conductivity. This would seem to be a reasonable hypothesis considering that the mobility of the carriers in this region is very low, of the order of $1 cm^2 V^{-1} s^{-1}$, which suggests hopping conduction.

The mobility of the sample in the dark shows a $T^{\frac{3}{2}}$ behaviour at low temperatures suggesting that ionised impurity scattering maybe the dominant mechanism. Attempting

to fit the experimental data to the Brooks Herring model outlined in section 2.2.2, showed that it is impossible to model the data without using a modified temperature, i.e. defining $\overline{T} = T - X$, where X is treated as a fitting parameter. No attempt is made to give a physical model to this concept. The fit to the experimental data can be made using the following parameters.

Parameter	Value
$\overline{T}$	T-13.85K
N_I	$5.6\text{x}10^{17}\text{cm}^{-3}$
m_e	$5\text{x}10^{-4}m_o$

Table 6.3 Fitting parameters to low temperature mobility

At high temperatures the mobility is dominated by optical phonon scattering, and this can be fitted using the following parameters.

Parameter	Value
θ	140K
m_e	$0.05m_o$
ν	$9.3\text{x}10^{13}\text{Hz}$

Table 6.4 Fitting parameters to optical phonon scattering

Under illumination the scattering mechanisms appear to be very similar to those observed in the dark. At high temperature the optical phonon scattering is dominant, and gives the following fitting parameters.

Parameter	Value
θ	140K
m_e	$0.05m_o$
ν	$6.7\text{x}10^{13}$Hz

Table 6.5 Fitting parameters for optical phonon scattering

At low temperatures the $T^{\frac{3}{2}}$ behaviour is observed, and using analysis similar to that in the dark case mentioned previously, we can obtain the following fitting parameters. ionised impurity scattering is seen to dominate the mobility, except at the lowest temperatures. The parameters obtained are summarised below.

Parameter	Value
$\overline{T}$	T-15.6K
N_I	$5.5\text{x}10^{16}\text{cm}^{-3}$
m_e	$5\text{x}10^{-4}m_o$

Table 6.6 Fitting parameters for low temperature mobility

From the consideration of $|R_H e|^{-1}$, it seemed that the illuminated sample was undergoing the transition to hole dominant carrier, and so if this is indeed the case, the mobility in this region would not be expected to be explained by ionised impurity scattering. During this transition the mobility falls rapidly, as can be seen in the data of MMT29A. The apparent agreement of the fit to ionised impurity scattering is because the sample has not yet been cooled far enough for the mobility to be dominated by the

transition. The trend in the resistivity that allows the Shlovskii Efros hopping to be fitted, may just be coincidental, and the only way to determine accurately the mechanism behind the mobility in MMT29B is to make measurements at lower tempertures.

At high temperatures the magnetoresistance of this sample can be shown to have a quadratic behaviour, which is similar to the majority of the other samples. Under illumination, the quadratic behaviour remains at high field, whilst the low field region becomes dominated by a hysteretic feature. This hysterisis is visible on the illuminated magnetoresistance of a number of the investigated samples, and one possibility for this behaviour is that the illumination is affecting the interaction of the free carriers with the magnetic ions within the samples. Certainly the low field magnetoresistance is very similar to that observed in MnTe samples by Wasscher [17], and he has atrributed this to spin disorder scattering. According to the work of Yosida *et al* [18] the trend for this form of scattering in semiconductors should be of the form

$$\frac{\Delta\rho}{\rho_o} = -\left[\frac{M}{M_{SAT}}\right]^2 \qquad (6.13)$$

where the ratio $\left[\frac{M}{M_{SAT}}\right]$ is generally explained by the use of a Brillouin function.

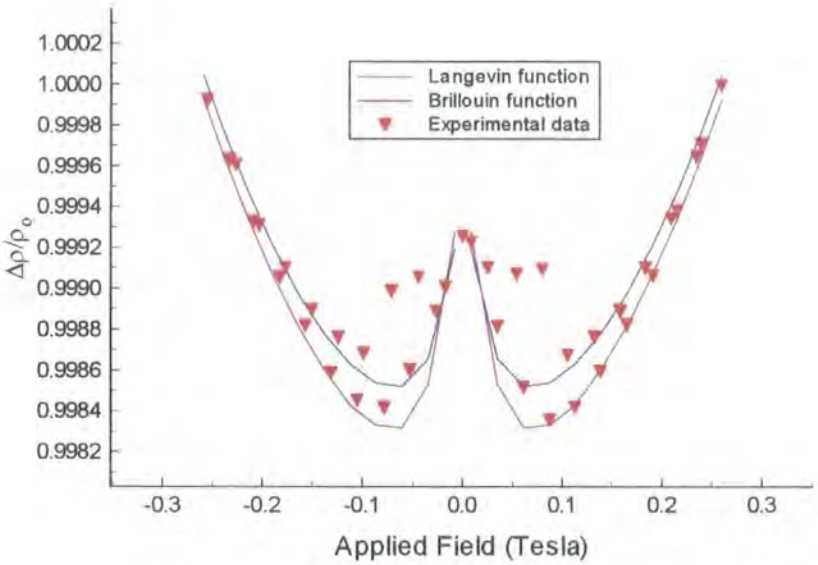

Figure 6.21 The fit to the magnetoresistance data using a Brillouin function and a Langevin function for $\left[\frac{M}{M_{SAT}}\right]$

The value of θ obtained from this fit is 289.94K, which suggests that ferromagnetic interactions would be required to explain this data. The origin of these interactions is not apparent as the interaction in MnTe is antiferromagnetic. The Langevin function fit, which assumes the existence of MnTe clumps, which respond in a superparamagnetic manner, gives a value for the number of Mn ions per clump of approximately 10000. This would represent a clump of MnTe of approximately 100Å in extent, which would be below the resolution of X-Ray diffraction, as outlined in section 1.5.3.

6.4 Sample MMT26

Results

Figure 6.22 shows the variance of the resistivity of sample MMT26 as a function of temperature. At low temperatures, this shows the existence of a shallow activation energy.

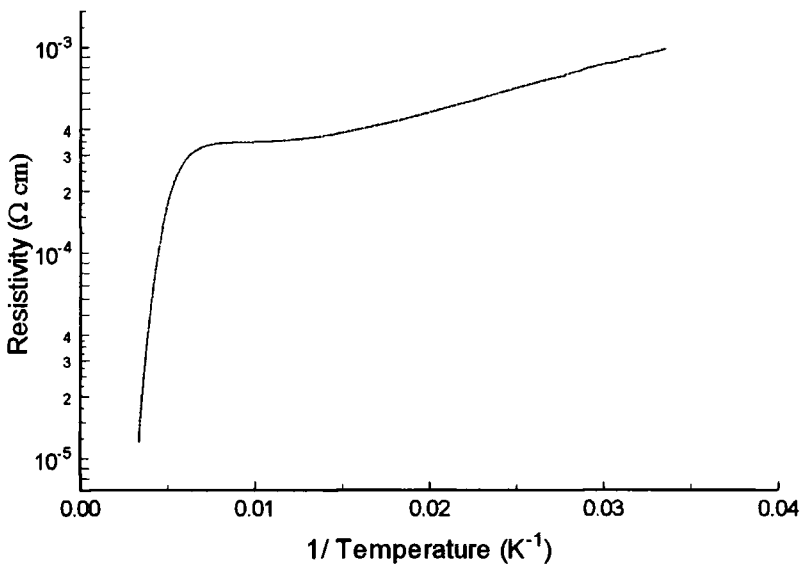

Figure 6.22 The resistivity of sample MMT26

Discussion

The activation energy calculated from the resistivity is 8.92meV. The resistivity does not show the anomaly at 50K, that can be observed in a number of the other samples.

Preliminary measurements, showed that this sample is p-type under going the transition to hole dominant carrier between 80 and 120K. The sample is not as good quality as MMT29A, as the mobility at 20K is only 50 $cm^2V^{-1}s^{-1}$ compared to $7x10^4cm^2V^{-1}s^{-1}$. The level of compensation is higher in this material than in MMT29A, as the value

for $N_A - N_D = 6.0\text{x}10^{16}\text{cm}^{-3}$ is about 150 times greater. This would explain the lower mobility in this sample, as highly compensated systems generally have a low mobility.

6.5 Sample MMT21

6.5.1 MMT21A

Results

The resistivity of this sample is shown in figure 6.23. No activation energy can be observed at low temperature, whereupon the high temperature activation energy is 6.9meV.

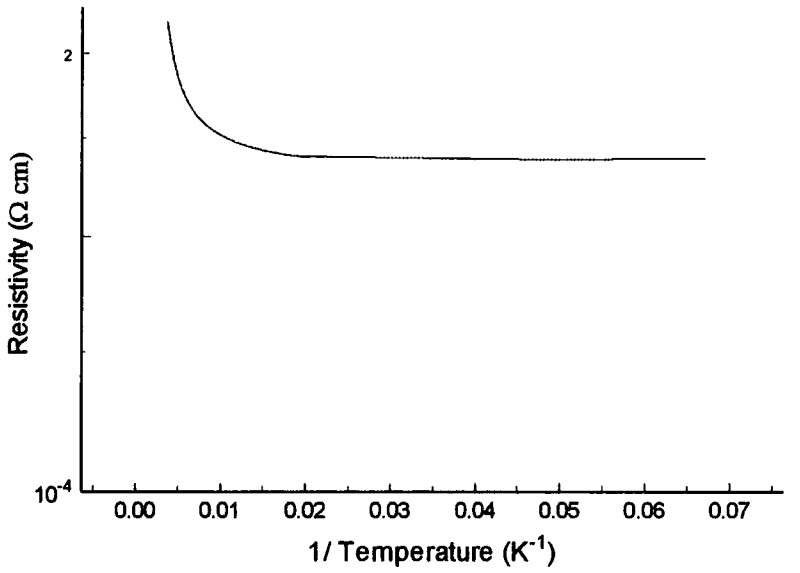

Figure 6.23 The resistivity of MMT21A

The effective carrier concentration, $|R_H e|^{-1}$, of sample MMT21A is shown in figure 6.24.

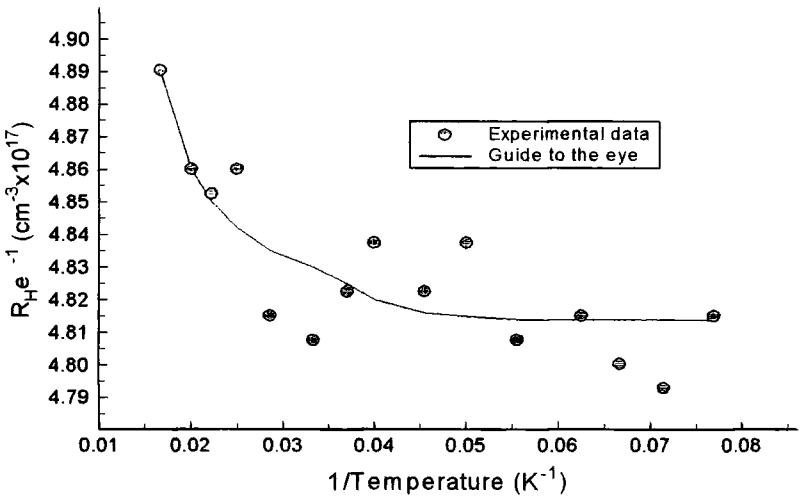

Figure 6.24 Effective carrier concentration of sample MMT21A

The mobility of the carriers in sample MMT21A, and a fit line indicating the dominant form of scattering, is shown in figure 6.25. The variation of the points from the fit line shown, can be taken as an estimate for the uncertainty on the measurement.

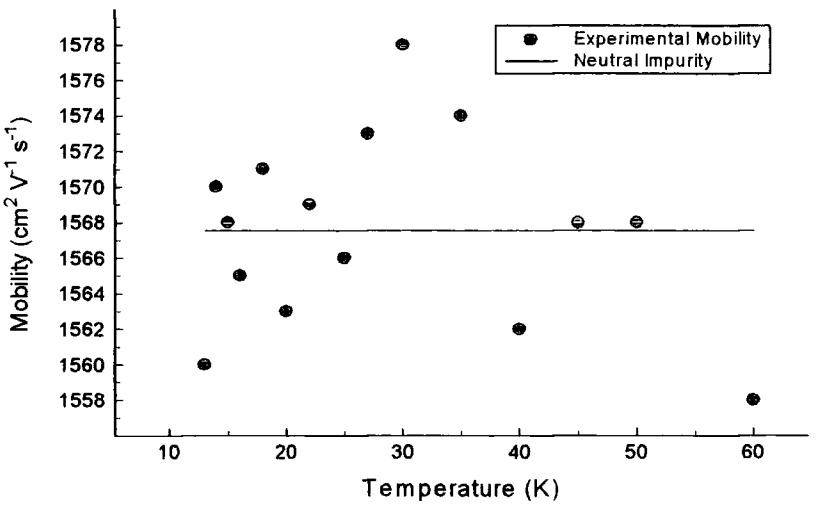

Figure 6.25 Carrier mobility in sample MMT21A

Discussion

The resistivity of the sample shows a monotonic decrease at high temperature and then levels off to give a constant value of ρ as temperature decreases. Extrapolating the value of the conductivity of the sample to 0K, gives a conductivity of 5900 $(\Omega\text{cm})^{-1}$. This would suggest that the sample is showing metallic behaviour.

The carrier concentration is showing a drop as the temperature is reduced, although a value of $|R_H e|^{-1} = 4.8\text{x}10^{17}(\text{cm}^{-3})$ is close to the value of n_c the critical concentration for HgMnTe, and so semimetallic behaviour could reasonably be expected, which reinforces the observation made from the resistivity. The value of n_c can be calculated from Mott's criterion, and is found to be $1\text{x}10^{18}\text{cm}^{-3}$. [19] The intrinsic carrier concentration for a semimetal at 20K is approximately $5\text{x}10^{17}\text{cm}^{-3}$ [20].

The mobility of the sample can be shown to be dominated by neutral impurity scattering. The points displacement from the fit can be taken as a measure of the uncertainty on the measurement, the standard deviation on this data being $4.72 cm^2 V^{-1} s^{-1}$.

6.5.2 MMT21B

Results

Figure 6.26 shows the variation of the resistivity of sample MMT21B with temperature. A feature can be observed at around $\frac{1}{T} = 0.024$, which is observed in other samples. The graph shows the existence of two activation energies.

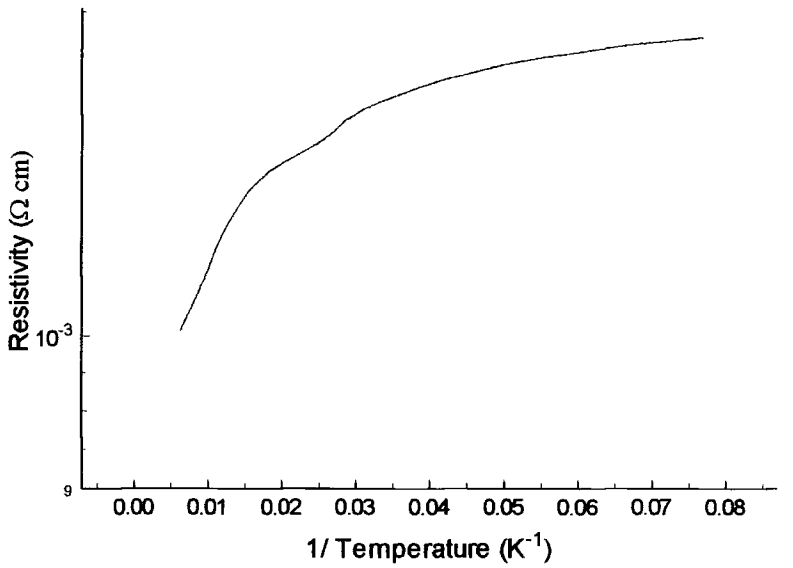

Figure 6.26 The resistivity of sample MMT21B

Figure 6.27 shows the effective carrier concentration, $|R_H e|^{-1}$, for sample MMT21B.

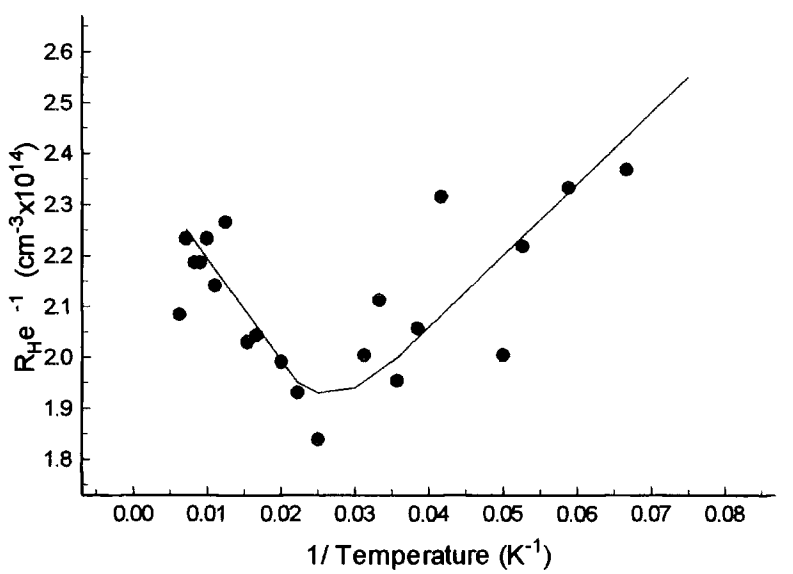

Figure 6.27 The carrier concentration in sample MMT21B.

Figure 6.28 shows the mobility of the carriers in sample MMT21B as a function of temperature. The fit to the high temperature part, would suggest that dipole scattering is the dominant scattering mechanism in this sample.

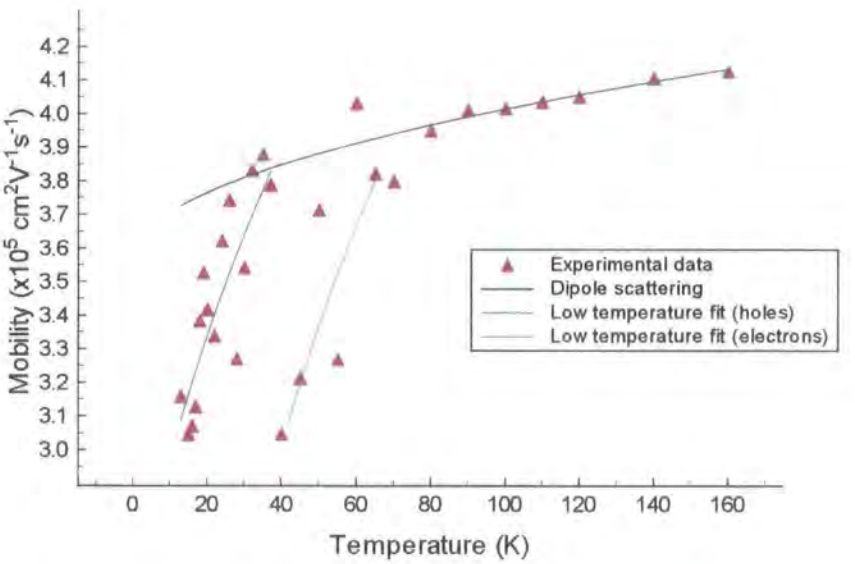

Figure 6.28 The mobility of sample MMT21B

Discussion

The resistivity of the sample shows the existence of a very shallow activation energy that cannot be calculated from the resistivity data. At 50K there is a feature on the resistivity which is observed on a number of the other samples.

The effective carrier concentration, $|R_H e|^{-1}$, shows a minima, and the line on the graph is a guide for the eye. The high temperature data would appear to show a linear region, from which an activation energy can be extracted, $Eg = 0.859\text{meV}$. At low temperature, the trend becomes very confused, as the spread on the data points becomes significant. It is unlikely that variable range hopping is responsible for the behaviour of

$|R_H e|^{-1}$ in this sample as the measured mobilities are far too large for this mechanism to occur.

The mobility of the sample shows the fit to dipole scattering at high temperatures. Oppositely charged impurities in a compensated system may form pairs, i.e. dipoles and these can scatter electrons. In this sample it is likely that Hg vacancies are responsible for the formation of the dipoles. An expression for this type of scattering can be given by

$$\mu_D = \frac{3\pi 2^{3/2} \varepsilon^2 \hbar^2 E_k^{1/2}}{e^4 m^{1/2} r_o^2 N_{DIP}} \qquad (6.14)$$

Below 40K the fall off in the mobility is too rapid to describe using ionised impurity scattering as is normal in these samples. Two lines are shown as the data seems to indicate the possibility of two different behaviours, most likely arising from the two carrier types. The cyan line shows the behaviour of the less mobile holes. One possible explanation for this temperature dependence of the mobility comes from the work of Moore [21], where he considers the case of the electron mean free path being greater than the distance between scattering centres. Hence the electron scatters more than once in its motion. The predicted mobility of this scattering has a temperature dependence that is greater than that expected from the Brooks Herring formula for ionised impurity scattering.

Another alternative for the sudden drop in the mobility is that the sample is heavily compensated and is about to undergo the transition to hole dominant carrier. If this is indeed the case then the value of $|R_H e|^{-1}$ should be seen to rise at low temperatures. This would seem possible with the available data and the guide to the eye in figure 6.20 was

made with this hypothesis in mind. The spread on the data point in the graph are from an unknown source as the Hall voltage traces obtained have a far smaller uncertainty than the spread on the values of $|R_H e|^{-1}$ would suggest.

6.6 Sample MMT19B

Results

Figure 6.29 shows the variation of the resistivity of sample MMT19B with temperature.

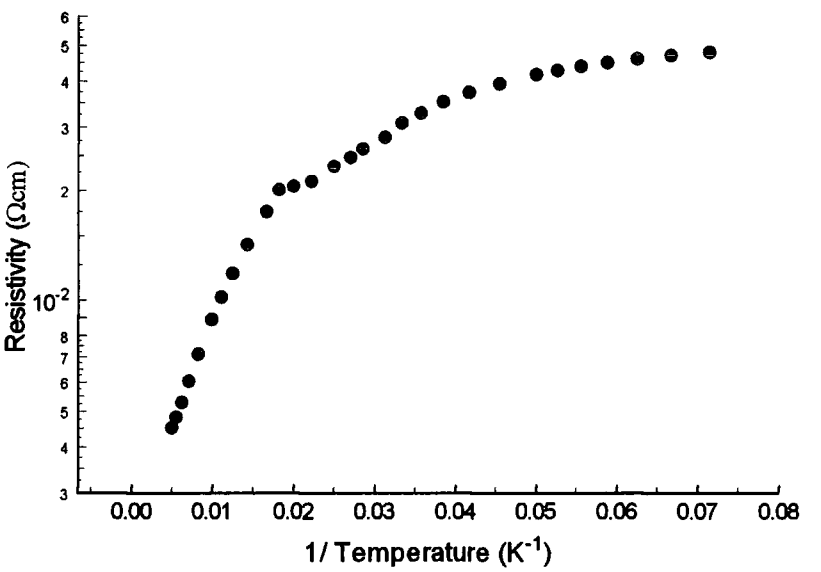

Figure 6.29 The resistivity of MMT19B

Figure 6.30 shows the effective carrier concentration, $|R_H e|^{-1}$, for sample MMT19B.

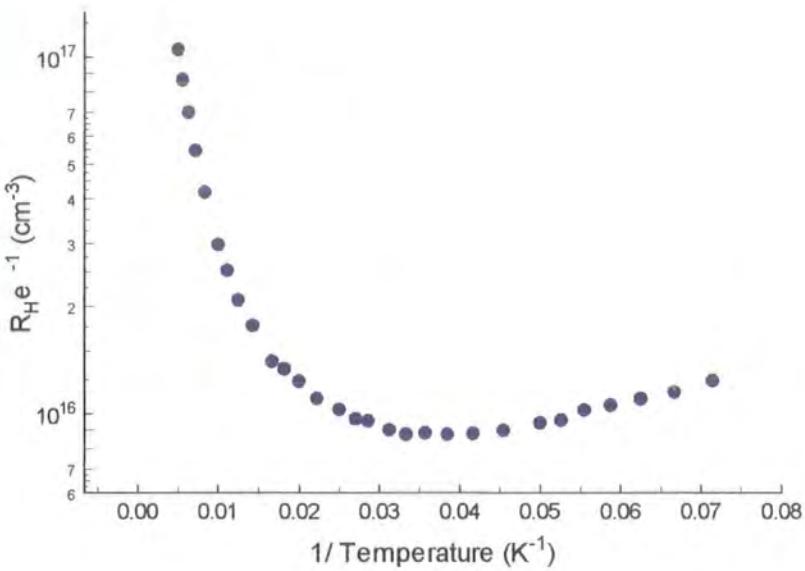

Figure 6.30 The effective carrier concentration in MMT19B

Figure 6.31 shows the non linearity of the Hall voltage in sample MMT19B at various temperatures.

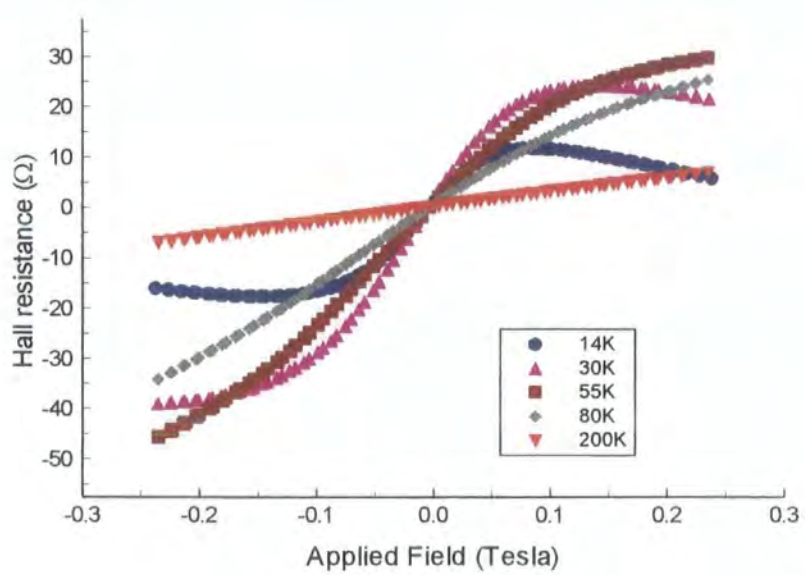

Figure 6.31 The nonlinearity of the Hall voltage in MMT19B

Figure 6.32 shows the mobility of the carriers in sample MMT19B. The upper temperature range is not dominated by optical phonon scattering as in the majority of the other samples. The low temperature region does not fit the expected ionised impurity scattering.

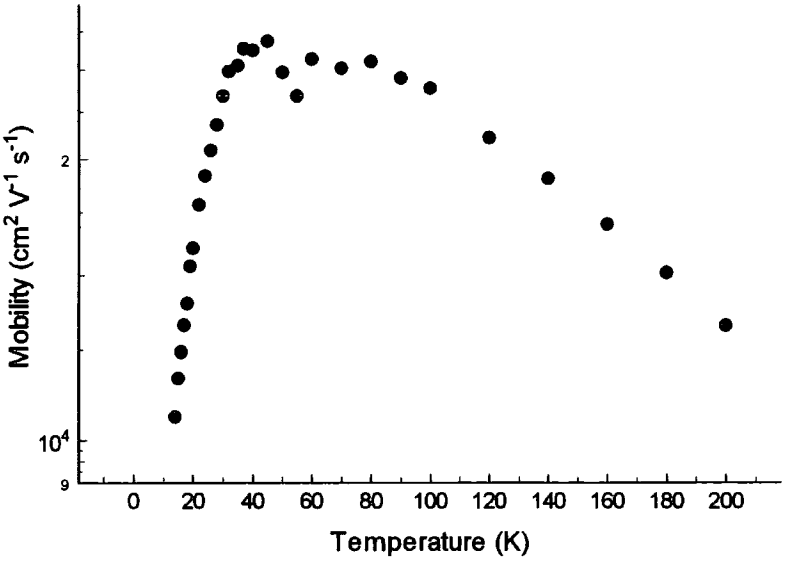

Figure 6.32 The mobility of the carriers in sample MMT19B

Figure 6.33 shows the transverse magnetoresistance of sample MMT19B at low temperatures. The saturation observed in the high field region is similar to that observed in MMT29A.

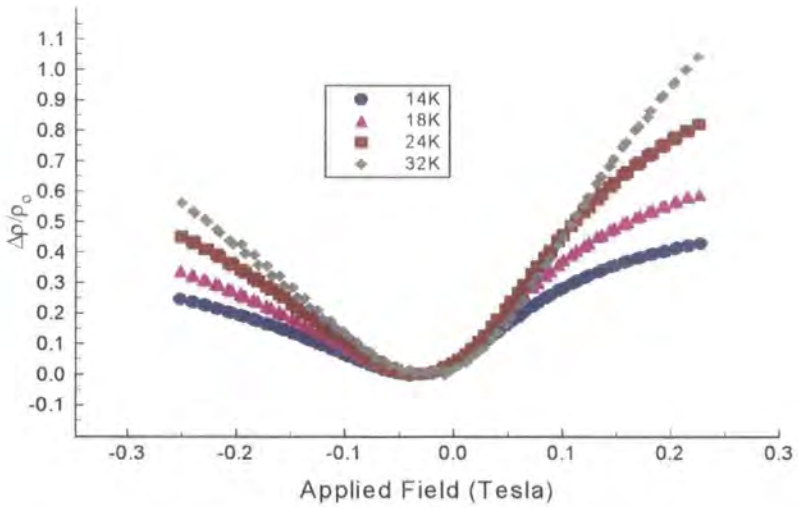

Figure 6.33 The transverse magnetoresistance of MMT19B at low temperatures

Figure 6.34 shows the high temperature magnetoresistance of sample MMT19B. The quadratic form is similar to that observed in a number of the other investigated samples.

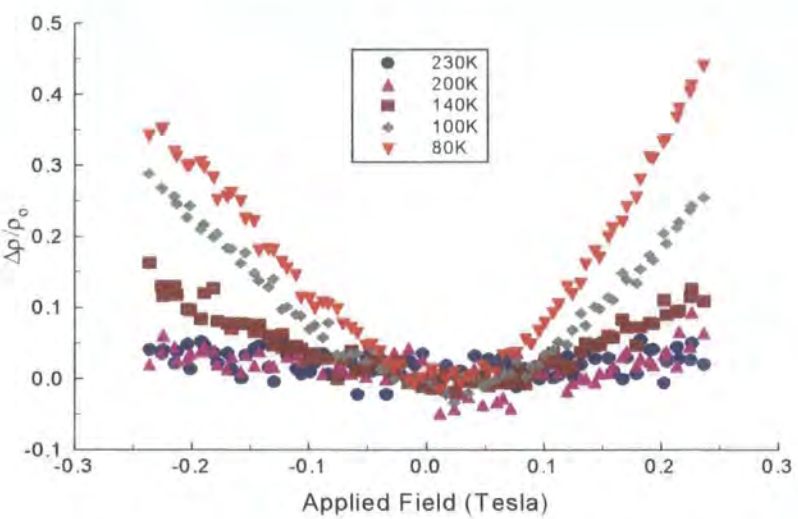

Figure 6.34 Magnetoresistance in sample MMT19B at high temperatures

Discussion

The resistivity of fig 6.29 shows the existence of two activation energies. The high temperature region gives a value of 11.64meV, whilst the low temperature energy state is too small to be determined from the resistivity. A feature is observable in the data at around 50K, which is very similar to that seen in a number of other samples.

The behaviour of the effective carrier concentration shows the existence of an activation energy, of 13.01meV. This value compares favourably with that observed in the resistivity. At low temperatures, the Hall voltage shows a striking non linear behaviour. This anomalous contribution to the Hall voltage can arise from two possible sources, the magnetisation of the sample or from two band conduction, as outlined previously.

The high field Hall measurements shown below in figure 6.35, are an attempt to ascertain the mechanism behind this anomalous behaviour. It can be seen from the data of fig 6.34 that the high field region is becoming linear, and that the gradient is in fact opposing that of the low field limit, in other words, the sample is appearing to be showing hole dominated transport. Comparing the low field data to equation (2.44)

$$R_H = \frac{r_o(p - b^2 n)}{|e|(p + bn)^2} \qquad (6.15)$$

and the high field region to equation (2.47)

$$R_H = \frac{-1}{|e|(n - p)} \qquad (6.16)$$

we can obtain an idea for the compensation within the sample. In general the value obtained from the high field region gives $(p - n) = 1.152\text{x}10^{17}(\text{cm}^{-3})$. The variation of

this value with temperature suggests that the sample is showing the existence of a very shallow acceptor, and the value obtained above for $(p-n)$ can in fact be evaluated as just p. From this it is possible to calculate the mobility ratio of the carriers, b, and hence calculate the value of n for this sample. From the use of equation 6.11, we find that $b = 28.63$, which is very close to the value obtained in sample MMT29A, of 26.38.

From this we can use equation 6.15, the value of n can be calculated, assuming that the ratio of the mobilities is temperature independant. The values of n are shown in figure 6.35 for comparison with the measured value of $|R_H e|^{-1}$.

The graph of $|R_H e|^{-1}$ is obtained by analysing the low field linear region of the curve. The low temperature data would suggest that the sample is compensated and on the verge of the transition from electron to hole dominant carrier. This is in good agreement with the explanation of the anomalous behaviour of the Hall voltage. The graph of $|R_H e|^{-1}$ using the high field region to calculate p, is shown below, with the experimental data for comparison.

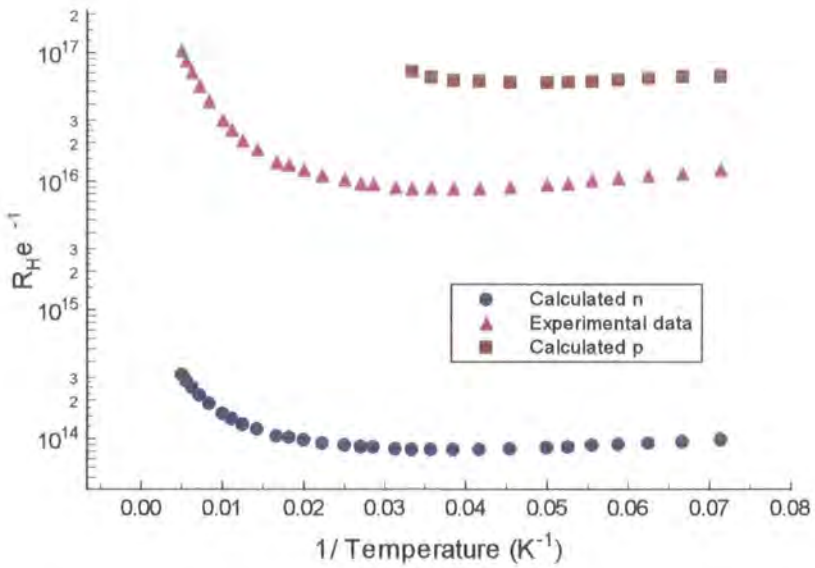

Figure 6.35 The comparison between the effective carrier concentration measured at low and high field

The measurement of a linear value of $|R_H e|^{-1}$ at high field is only possible at temperatures below 30K.

As was attempted for sample MMT38A, the anomalous Hall effect can also be explained via the consideration of the magnetism of the sample under investigation. The form for this was outlined in sections 2.2 and 6.2.2, [8]

$$R_{Hmeas} = R_{Hact} + C\rho\chi \qquad (6.17)$$

In attempting to fit the data to this equation, it has been assumed that the magnetisation of the sample can be described by either the paramagnetic Brillouin function or the superparamagnetic Langevin function. For the case of the 15K data, the linear high field data has been taken to be R_{Hact} and the magnetic behaviour has been used to describe the non linearity. The graph of these fits is shown below.

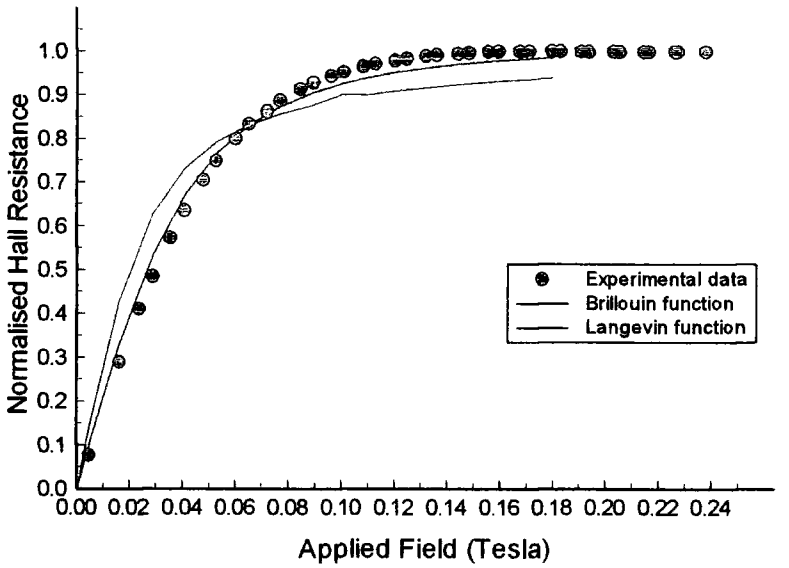

Figure 6.36 Fits to the anomalous Hall effect at 14K.

The parameters used in the fits are summarised in table 6.2 below.

Fitting Function	Fitting Parameter	Value
Brillouin Function	θ	-13.927K
Langevin Function	m	$875\mu_B$

Table 6.7 The fitting parameters used to model the anomalous Hall effect

The value obtained for θ suggests that the manganese concentration in the sample is around 7.53% [9]. The value for θ obtained from the fit at 14K cannot be used to model the data at any other temperature, because θ was found to vary with temperature. Similarly, the value of the magnetic moment of the superparamagnetic regions that is the fitting parameter in the Langevin function also seems to vary with temperature. These

descrepancies suggest very strongly that the non linearity in $|R_H e|^{-1}$ is not due to the anomalous Hall effect, but is due to two band conduction in this sample.

The magnetoresistance of the sample at temperatures above 80K can be expressed as a quadratic function in low field. This behaviour is similar to that seen in a number of other samples, and suggests that the sample is heavily compensated. This is in direct contrast with the mobility data, which due to its high value, would suggest little compensation in the material. In the low temperature regime the magnetoresistance shows a non quadratic low field region with a saturation being visible at high field. The low field data is complicated by the superposition of the Hall effect due to a small contact misalignment. Normally this contribution can be removed in the analysis by removing the component that is linear in field, but as the measurements on this sample show, the Hall effect is non linear, and so its removal is a non trivial matter. The data in high field shows evidence of saturation, although with the Hall effects superimposed, this is difficult to see. This is similar to that observed in MMT38, another sample that shows extraordinary Hall effect and evidence of two band conduction.

The mobility of this sample does not seem to fit the expected ionised impurity scattering mechanism at low temperatures. Attempts to fit this section of the data to a scattering mechanism have failed. This may be due to the mobility being calculated from the low field region of the Hall voltage, and so two band conduction will be complicating the picture.

6.7 MMT34

Results

Figure 6.37 shows the variation of the resistivity of sample MMT34 with temperature. The graph shows the existence of two activation energies. a feature can be observed in the resistivity at approximately 60K. Under illumination the resistivity of the sample changes dramatically. The feature at approximately 60K can still be observed in the illuminated data.

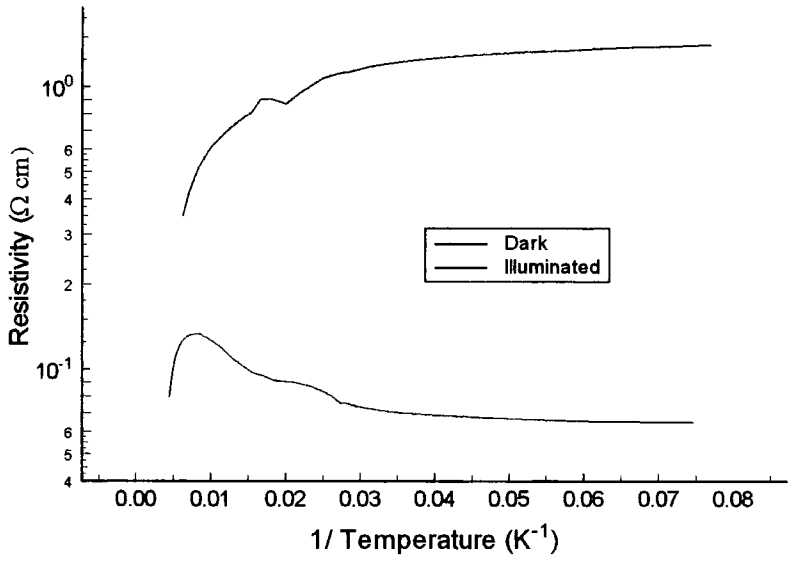

Figure 6.37 The resistivity of sample MMT34

Figure 6.38 shows the transverse magnetoresistance of sample MMT34 in the dark at 13K. Unlike the previous samples, the magnetoresistance is no longer positive and quadratic.

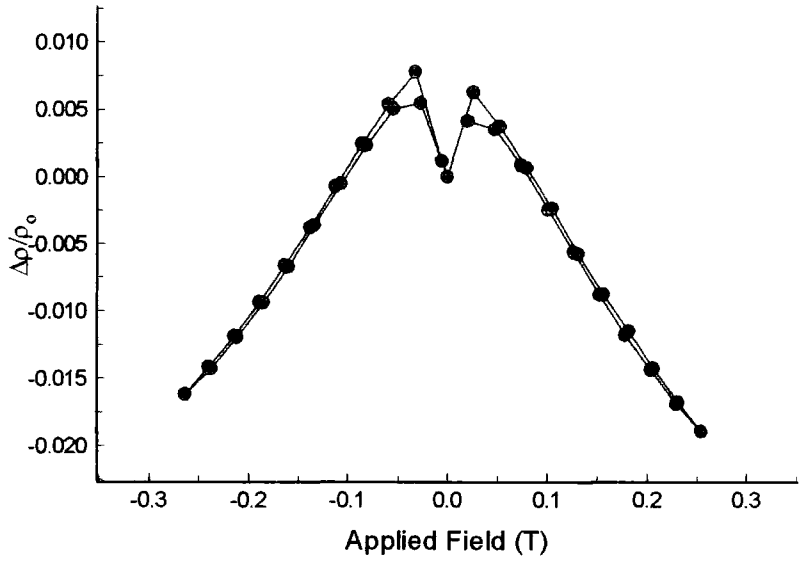

Figure 6.38 The magnetoresistance of MMT34 at 13K

The low field section of the magnetoresistance is shown in figure 6.39. From the graph it is apparent that this low field section is hysteretic.

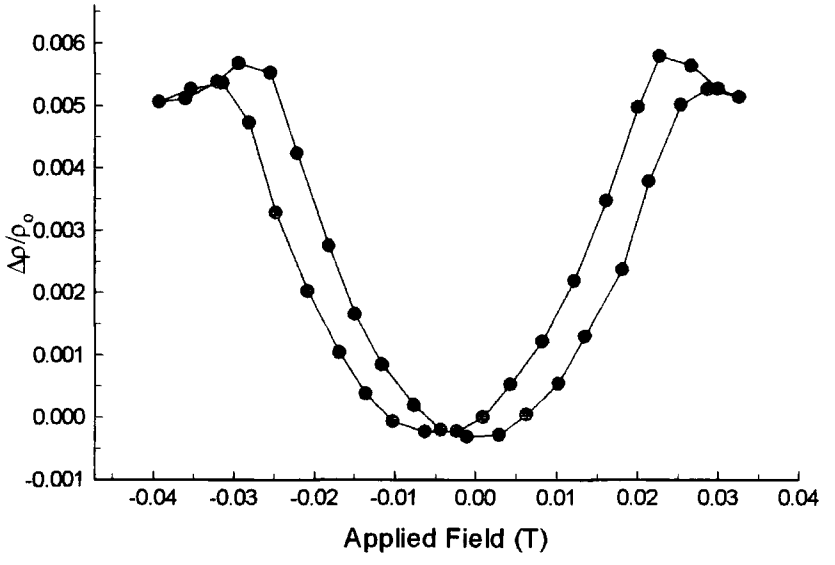

Figure 6.39 The low field magnetoresistance of MMT34 at 13K

Figure 6.40 shows the magnetoresistance of the sample under illumination. The positive low field section has disappeared.

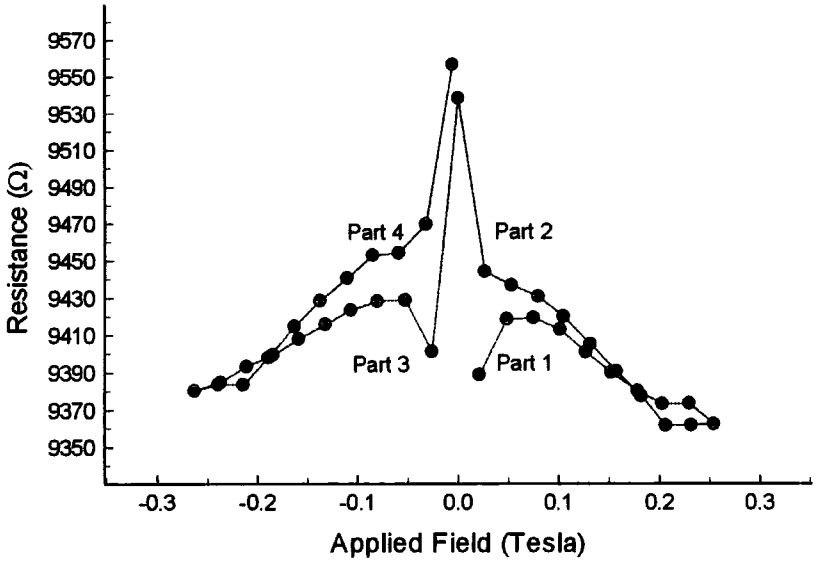

Figure 6.40 Illuminated magnetoresistance of sample MMT34 at 13K

Figure 6.41 shows the variation of the magnetoresistance as a function of temperature. From this it can be seen that the negative magnetoresistance seen at low temperatures becomes positive at approximately 30K. The difference of the point at 60K is linked to the feature observed in the zero-field resistivity, as shown in figure 6.37.

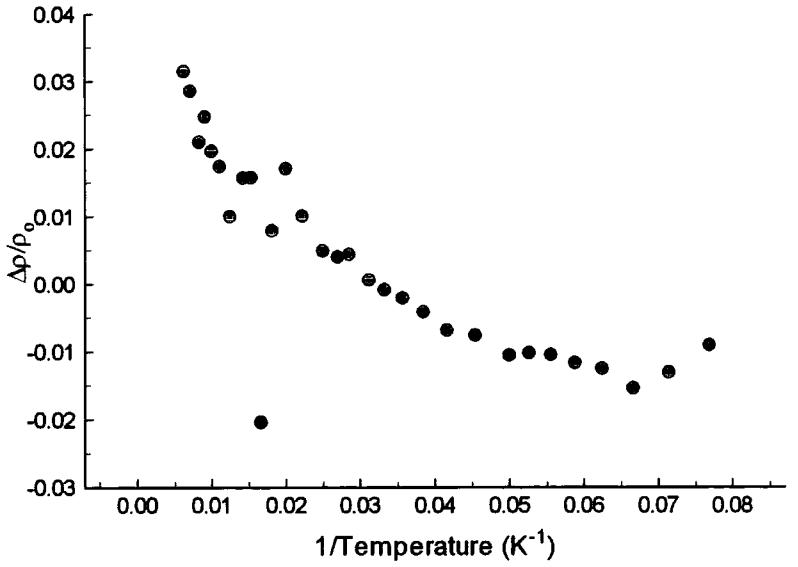

Figure 6.41 The variation of the magnetoresistance with temperature at 0.25T

Discussion

The resistivity of this sample shows the existence of a high temperature activation energy of 127meV. The data shows the same feature at 50K as a number of the others. Investigatations of the conductivity show that if the conductivity is extrapolated down to 0K then a non zero conductivity will obtained. This has a value of $\sigma_o = 0.62(\Omega\text{cm})^{-1}$. From the illuminated data an extrapolation shows another non zero conductivity, this time with a value of $\sigma_o = 15.4(\Omega\text{cm})^{-1}$. The dark data is shown in figure 6.42.

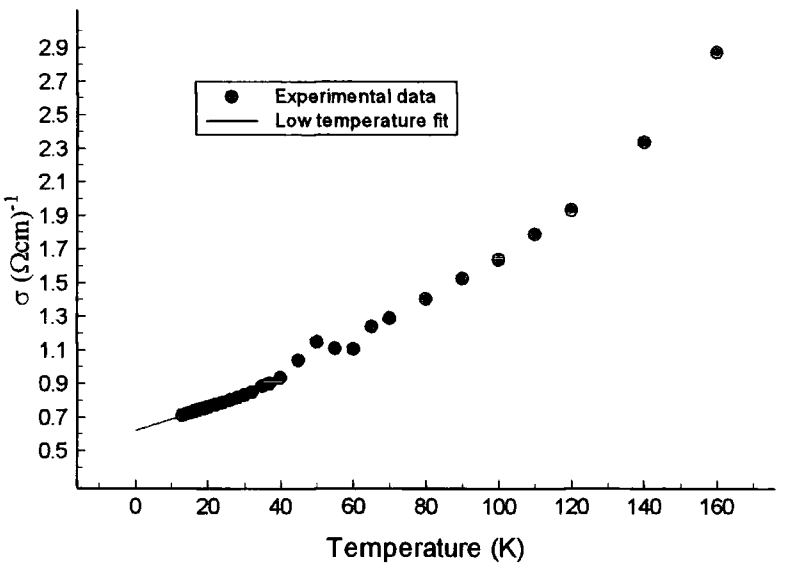

Figure 6.42 The conductivity of MMT34 in the dark

From these it would appear that the sample is metallic, albeit very slightly. The Mott minimum conductivity is defined as [22]

$$\sigma_o = \frac{Ce^2}{\hbar a_o} \qquad (6.18)$$

where e is the electronic charge, a_o the radius of the electron orbit, $\hbar$ Planck's constant divided by 2π and C is a constant, usually taken to be 0.2.

The value of this for HgMnTe is calculated to be $0.99(\Omega\text{cm})^{-1}$. This compares favourably with the value obtained in the dark, although the value under illumination is sufficiently different. The theory behind the Mott transition has never been proven experimentally, and a number of groups have reported metallic behaviour at conductivities well below the Mott minimum,[23] and in fact the $\sigma(0)$ has been found to go smoothly to

zero as carrier density is reduced, as predicted by scaling theory [24].Thus this sample, when under illumination could be considered a 'dirty metal'. [24]

The magnetoresistance of this sample is unique amongst those studied. The low field is a positive quadratic, whilst the high field is negative. The high field can be modelled assuming that

$$\frac{\Delta\rho}{\rho_o}\alpha\left(\frac{-M}{M_{SAT}}\right) \qquad (6.19)$$

and using the Langevin function to give the values of $\left(\frac{M}{M_{SAT}}\right)$. The model proposed to explain this phenomenon is as follows. The sample contains a number of superparamagnetic clumps, which in zero field have no net magnetic moment, due to internal domain type structures. As the field is increased, the clumps become polarised in a manner similar to that observed in ferromagnetic materials, until at a field of approximately 0.03T they are saturated. The resistance of the sample increases in this low field region as the magnetic moment of the clumps is increasing, although their direction is still partly random, and are hence more efficient scattering centres. At fields above this the clumps undergo rotation to allow their magnetic moment to lie parallel with the applied field. As the angle between the field and magnetic moment is decreased the scattering of the charge carriers is decreased, and hence the resistance falls, proportionally to the magnetisation of the sample. The fit is shown in figure 6.43 for the 13K data, along with the parameters used. It should be noted that our fit has a dependence of $\frac{\Delta\rho}{\rho o}\alpha\left(\frac{M}{M_{SAT}}\right)$, where the majority of the literature shows $\frac{\Delta\rho}{\rho o}\alpha\left(\frac{M}{M_{SAT}}\right)^2$.

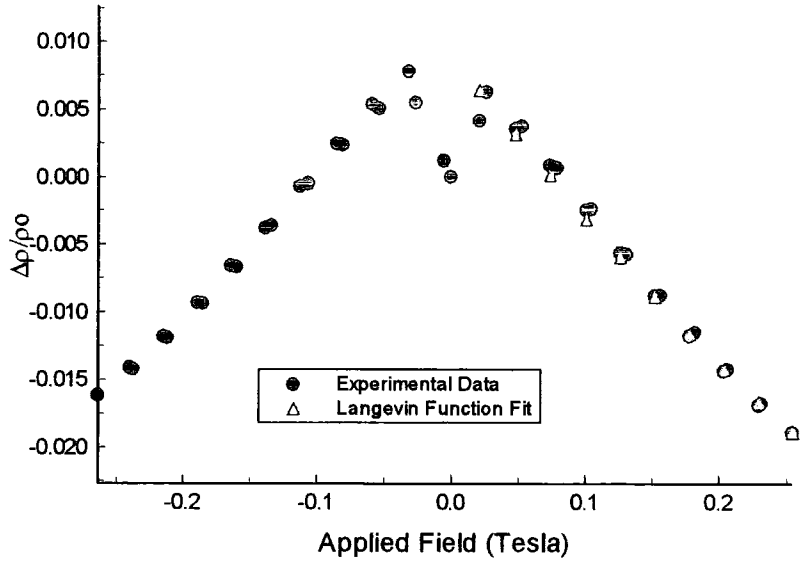

Figure 6.43 The fit to the magnetoresistance of MMT34

Fitting Equation	Fitting Parameter	Value
$\left(\frac{M}{M_{SAT}}\right) = \coth\left(\frac{xB}{k_BT}\right) - \left(\frac{k_BT}{xB}\right)$	x	$100\mu_B$

Table 6.8 The fitting parameters for figure 6.43

The same fit and parameters can be used to explain the magnetoresistance at temperatures up to 30K. Above this temperature the negative magnetoresistance is becoming positive, as the contribution from the low field region is stronger than the high field regime. Because the magnetoresistance can be described by a Langevin function, it can be postulated that the material comprises of a number of magnetic clumps, each of which have a magnetic moment of $100\mu_B$. Assuming that these clumps are made up of Mn ions, each with $\frac{5}{2}\mu_B$ then the clumps will contain 20 ions, as x is defined as

$x = Jg\mu_B N$, where N is the number of ions. If the clumps are MnTe, then the size of them is expected to be approximately 12Å.

It has not been possible to measure the Hall effect in this sample. The magnetoresistance swamps any attempt to measure the Hall voltage. This would suggest that the sample has a high carrier concentration, which would tie in with the suggestion that this sample is metallic.

6.8 MnTe

Results

Figure 6.44 shows the variation of the resistivity as a function of temperature for the MnTe sample grown by Dr Funaki. A feature is visible at 80K, which is similar in appearance to the ones observed in previous samples, though these were observed at approximately 50K. This anomaly is also observed under illumination.

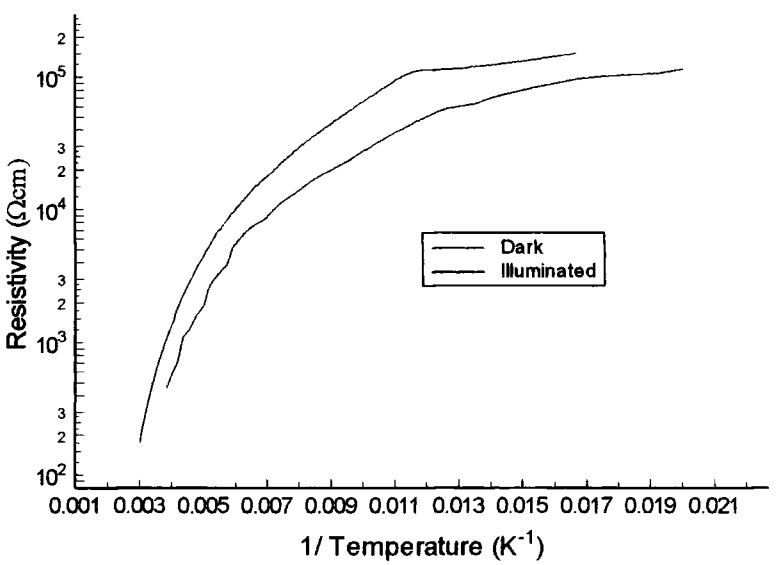

Figure 6.44 The resistivity of MnTe

The relaxation time of the photoconductivity of this sample is very short, and is faster than the meter can resolve.

The magnetoresistance of the sample at 60K is shown below in figure 6.45.

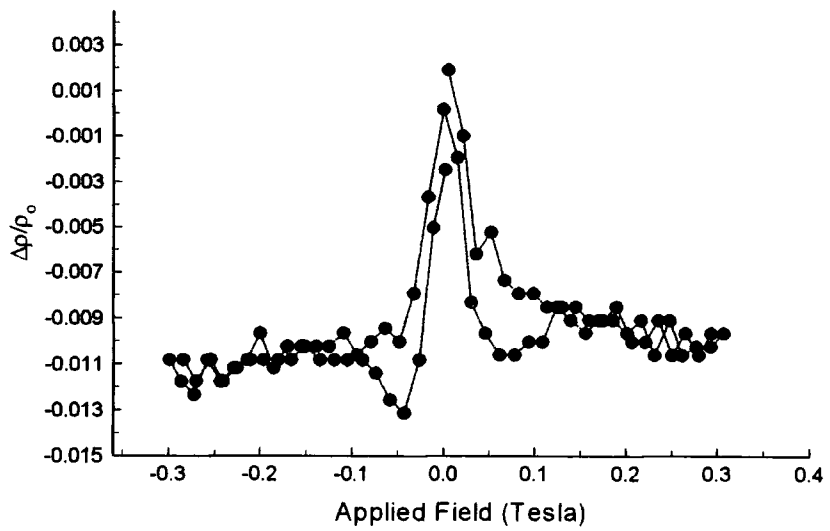

Figure 6.45 The magnetoresistance of MnTe at 60K

The variation of $\frac{\Delta\rho}{\rho_o}$ as a function of temperature is shown below in figure 6.46, along with a guide to the eye. The value of magnetic field used in these measurements is 0.246T.

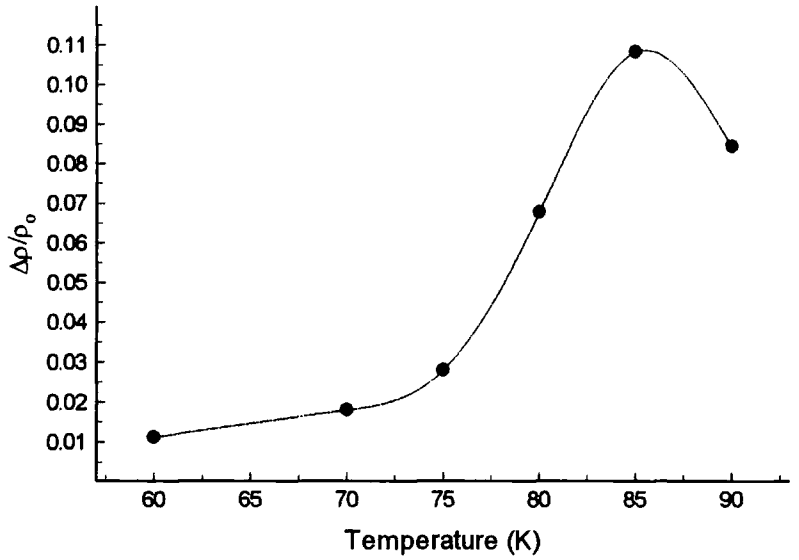

Figure 6.46 The variation of $\frac{\Delta\rho}{\rho_o}$ with temperature in MnTe

The magnetoresistance of the MnTe layer shown in figure 6.45 is very similar to that observed in MMT34 under illumination. It also similar to that observed by Wasscher [25] in his work on bulk MnTe samples. The negative low field region is attributed to spin disorder scattering, which in a semiconductor, has the general form of [9]

$$\frac{\Delta\rho}{\rho_o}\alpha\left[\frac{M}{M_{SAT}}\right]^2 \qquad (6.20)$$

The variation of $\frac{\Delta\rho}{\rho_o}$ with temperature is also very similar to that observed in certain bulk samples by Wasscher [25], which is shown in figure 6.47.

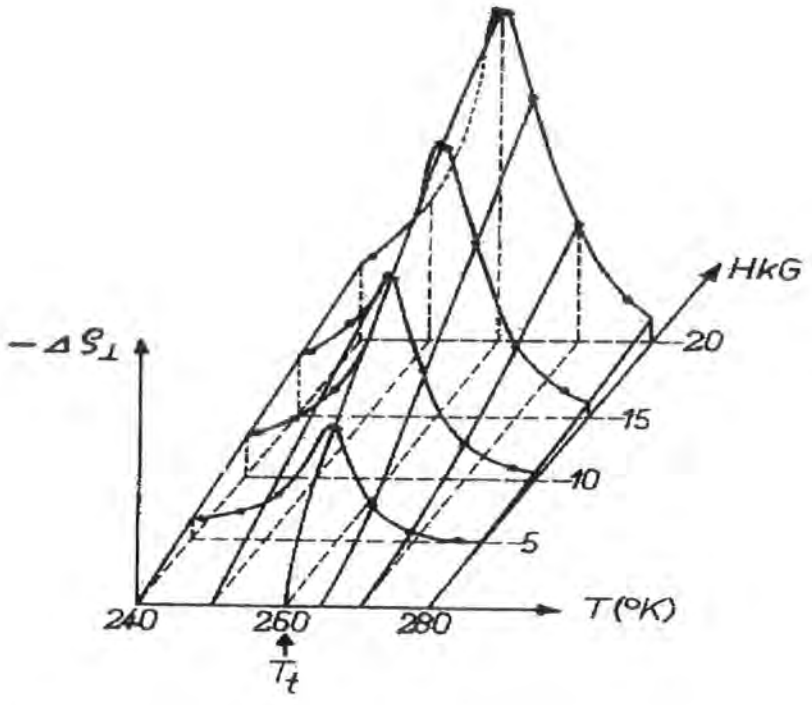

Figure 6.47 The behaviour of $\frac{\Delta\rho}{\rho_o}$ in selected MnTe samples

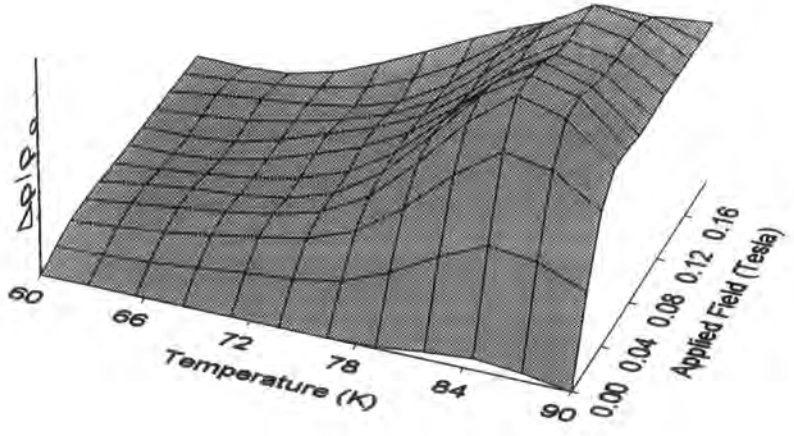

Figure 6.48 The behaviour of $\frac{\Delta\rho}{\rho_o}$ in our MnTe sample

This peak in $\frac{\Delta\rho}{\rho_o}$ was thought to originate from the onset of weak ferromagnetism in the samples, but only occurred in one sample of MnTe and others that had been intentionally doped with copper. It has been shown that in NiAs MnTe it is possible to obtain a weak ferromagnetic state when the antiferromagnetic state is collinear such that the two sublattices are perpendicular to the c-axis. [25]

6.9 Conclusions

The activation energies observed in the samples are summarised in table 6.9 below.

Sample No	E_A (from ρ) (meV)	E_A (from R_H) (meV)	Carrier type	$\rho(20K)$ (Ωcm)	$n(20K)$ cm^{-3}	$\mu(20K)$ $cm^2V^{-1}s^{-1}$
29B (dark)	12.6	13.82	n	8.2	2.5×10^{14}	10
29B (light)	7.76	____	p ?	5.5	2×10^{15}	8
21B	____	0.05	n	1.1×10^{-3}	2.2×10^{14}	3.4×10^{5}
34 (dark)	127	____	?	1.2	____	____
(light)	38.2	____	?	7×10^{-2}	____	____
29A	9.0	9.7	p	2	1×10^{14}	8×10^{4}
38B	____	1.2	n	7.8×10^{-3}	4×10^{15}	2×10^{5}
26	8.92	____	p	5	2.5×10^{16}	50
21A	____	____	n	1.5×10^{-4}	4.8×10^{17}	1568
19B	11.64	13.01	n	4×10^{-2}	1×10^{16}	1.5×10^{4}
MnTe (dark)	1068 High temp	____	?	$\sim3\times10^{5}$	____	____
MnTe (light)	884.1 High temp	____	?	1.71×10^{5}	____	____

Table 6.9 Summary of the activation energies of the samples studied

6.9.2 Resistivity

In general the resistivity of the investigated samples show a feature at around 50K. This feature is very similar to one observed in EuTe systems, where it is attributed to a magnetic phase transition from paramagnetic to Antiferromagnetic systems. [26] The value of the Neel temperature obtained from this technique is in good agreement with that obtained from magnetic susceptibility measurements. [27]

The temperature that these anomalies occurs is very close to the observed Neel temperature in zinc blende MnTe, which is 60K [28]. The spread on these values can be explained by noting that the Neel temperature of MnTe can be affected by the pressure applied to the sample, and hence the internal strain. [29] Because of lattice mismatch all the layers grown have a residual strain associated with them, and this will cause the Neel temperature to be moved from 60K. This is especially evident in the MnTe sample, where the anomaly is seen to occur at around 80K in the resistivity data and 85K in the magnetoresistance data. The lattice mismatch in a boundary between CdTe and MnTe is 0.1460Å rather than the 0.04Å mismatch between CdTe and a $Hg_{0.9}Mn_{0.1}Te$ sample. This larger mismatch will give rise to a higher strain in the sample, which will increase the chance of NiAs structure MnTe forming, and will move the Neel temperature away from 60K. Compressive strain will cause an increase in the Neel temperature, whilst tension will cause a reduction. The mechanism for this is thought to be due to the decrease in the exchange integral as the bond lengths are increased. [29]

6.9.3 Effective carrier concentration

In general the measurements of $|R_H e|^{-1}$ show that the samples appear to be heavily compensated in nature, and if taken to sufficiently low temperatures will exhibit hole dominated transport. This is in a stark contrast to the work of Hallam [30], where the majority of the investigated films were n-type in the whole of the measured temperature range. The reason for films being either n-type or p-type in the as grown state was initially thought to be related to the flush time in the growth cycle. This is the time between the growth of HgTe and MnTe, where the sources are changed and no growth occurs. During this time, the sample is kept heated and the mercury close to the surface is likely to boil off, leaving a higher concentration of mercury vacancies in the layer. Hence samples with higher flush times were expected to be p-type. This theory works for a number of the samples, but not others. The flush times and the carrier type of the samples is shown in table 6.10 below.

Sample	Flush Time	Carrier Type
19B	33	n
21	47	n
26	38	p
29	44	p
34	37	?
38	39	n
MnTe	____	?

Table 6.10 The flush times of the electrically investigated samples.

Hence the flush times are not the sole cause of the difference in the carrier type, although it is likely that they are a contributory factor.

In the work on MOVPE grown HgCdTe, Capper [31] has shown that it is possible to affect the carrier type in the sample by varying the mercury overpressure during the growth as a function of the temperature of the growth susceptor. This is shown in figure 6.48 below.

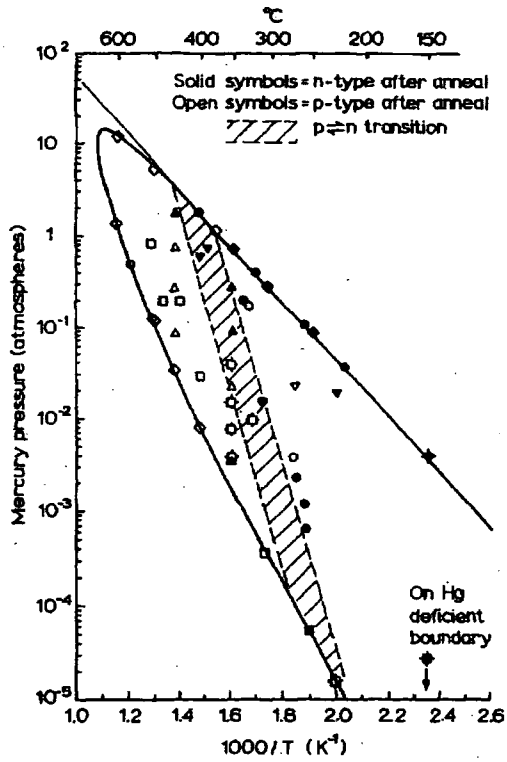

6.48 Hg pressure v growth temperature for HgCdTe samples

The growth of HgMnTe samples occurs at a temperature of approximately 385°C, in a mercury overpressure of about 76mm Hg. This puts our growth in the shaded area of the graph, and so any small deviation in either of the values will cause the samples to go from n-type to p-type conduction.

Samples of HgMnTe are normally annealed in hydrogen gas following their growth, as was outlined in section 1.4. This anneal is used to ensure that the diffusion of the growth layers is complete and also generally renders the sample n-type. It is the suspicion of the author that the samples grown in this study were not annealed, as they show high levels of compensation and the existence of incomplete difussion (MnTe clumps).

6.9.4 Mobility

The majority of the samples investigated showed a dependence on optical phonon scattering at high temperatures and ionised impurity scattering at low temperatures. This is in good agreement with previous work on this and similar materials. [30,32]

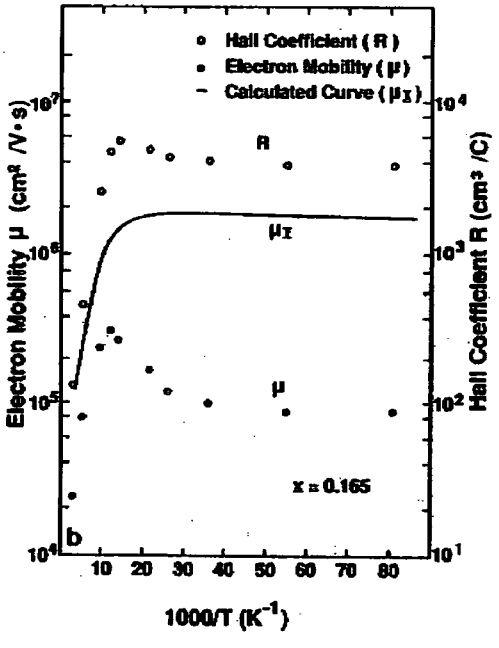

Figure 6.49 The mobility in HgCdTe samples

The values obtained for the fitting parameters for the optical phonon scattering, were in general sensible, although the values for the ionised impurity scattering were

unreasonable. This suggests that although the scattering is following a $T^{\frac{3}{2}}$ dependence over the temperature regime studied, the mobility is in fact being dominated by the transition to hole dominant conduction, and the mobility is starting to drop rapidly as the transition is reached. The mobility of certain samples (MMT38B and MMT19B) do not show the existence of ionised impurity scattering at low temperatures, and this may be due to the two band conduction in these samples that is giving rise to the non linear Hall effect. The mobilities have been calculated using the low field values for $|R_H e|^{-1}$, which is of course affected by both carrier types and their mobilities, from equation 6.21.

$$R_H = \frac{-\left(r_n \mu_n^2 n - r_p \mu_p^2 p\right)}{|e|\left(\mu_n n + \mu_p p\right)^2} \qquad (6.21)$$

where the symbols are defined in section 2.5.2.

The high field values of $|R_H e|^{-1}$, where available give more accurate values for the carrier concentrations in the sample. Unfortunately, there are insufficient values obtained by this method as the applied field was not high enough to reach the high field regime at the majority of temperatures studied.

6.9.5 Magnetoresistance (M.R.)

The majority of the samples show a positive M.R. with a quadratic field dependence, at least at high temperatures. This is the expected form of magnetoresistance for a semiconductor, and is due to the Lorentz force on the charge carriers.

A number of the samples show behaviour that is dominated by the effects of the magnetisation of the sample. Two of them, MMT29B and MMT34, under illumination, show something very similar to spin disorder scattering at low field, whilst sample

MMT34 appears to be related to the magnetisation of superparamagnetic clumps in the material. The magnetoresistance of the MnTe sample shows a maximum in $\frac{\Delta\rho}{\rho_o}$ at the same temperature as the anomaly in the resistivity, suggesting that these two phenomena are linked. The magnetoresistance is similar to that observed in other MnTe samples, which were undergoing a magnetic phase transition [25].

One major unanswered question about the magnetoresistance data is why the influence of spin disorder scattering should increase on illumination, as observed in MMT29B and MMT34. There are a number of possible explanations as to the origin of this effect. It is clear from the previous section that ionised impurity scattering tends to dominate the carrier mobility at low temperatures. Now from equation 2.10, such a scattering mechanism is dependant upon the free carrier density. Thus a photoinduced increase in the carrier concentration may produce a rise in mobility to the point that another mechanism, such as spin disorder scattering dominates. We may then expect the magnetoresistance to be related to the intrinsic magnetisation of the material only when the sample is illuminated. The change in carrier concentration for sample MMT29B is low, as can be observed in figure 6.15, whilst in MMT34 the carrier density cannot be measured, but the change in conductivity is approximately an order of magnitude.

Another possible explanation of the magnetoresistance of samples MMT34 and 29B is that in the dark, the conduction is via percolating pathways between regions of low manganese concentration. In this case the transport is not affected by the dominant magnetism of the sample (associated with the high manganese regions), and the magnetoresistance will be the quadratic form expected from the Lorentz force on the

carriers. Under illumination the high manganese regions may become more conducting, and therefore contribute to the overall conductivity of the sample. Thus conduction will occur in manganese rich regions of the material which will have a similar response to a magnetic field as that observed in MnTe. It is unlikely that the change in conductivity required for this mechanism arises solely from the photoexcitation in the MnTe regions. This is because the photoconductivity of MnTe is small (see figure 6.44). It has been noted that, in general, layers of MOVPE grown HgMnTe are of a non uniform thickness, and that the thinner regions have a higher manganese concentration [30,33,figure 1.6]. The direct band gap of zinc blende MnTe is 3.3eV [34], and so in these thinner regions, the incident photons will penetrate through to the CdTe buffer layer, which has a band gap of 1.3eV [35], very close to the energy of the illumination, 1.31eV. Hence electron hole pairs are formed in the CdTe. Given the difference in the bandgaps of CdTe and MnTe, and the fact that the band offset will be mostly in the conduction band, according to the anion rule [36], we might expect the holes to be free to diffuse from the CdTe to the MnTe. This would create a surplus of holes in the MnTe layer, as the electrons are trapped behind a large potential step, of roughly 2.0eV. This would result in a drop in the resistivity, and a move towards a p-type transition as observed in samples MMT34 and 29B. The spatial separation of the carriers over the CdTe/MnTe boundary can also give rise to the observed high temperature photoconductivity (see figure 6.14), as has been observed with other materials [37,38]. The holes will interact with the Mn ions via the ferromagnetic p-d interaction, which is stronger, $\left(N_o\beta = 1.4\text{eV}\right)$, than the s-d interaction of the electrons and the Mn ions, $\left(N_o\alpha = -0.7\text{eV}\right)$ [39], and such an interaction may even

produce a ferromagnetic order in the MnTe. In fact photoinduced magnetic phase transitions have recently been reported for quantum wells of CdMnTe/CdMgZnTe:N [40] and in III-V material [41].

6.10.6 Photoconductivity

The majority of the samples investigated showed some photoconductivity, although in some cases it was so small that it was virtually no different to the dark data. In general the resistivity of the sample changed very rapidly on illumination, and on the removal relaxed more rapidly than the meter could resolve. After this initial relaxation, the resistivity would then relax with a very long time constant, so slowly that it looked like a drift on the measurement, until it would become the initial unilluminated value. Sample MMT29B shows a photoconductivity that looks very similar to that observed in a persistent photoconductor, such as CdMnTe:In, where the DX centre is responsible. This mechanism cannot be responsible for the photoconductivity in HgMnTe as DX centres are not formed, and so a different mechanism must be responsible.

DX centres are a form of negative U centre, and it has been shown [42] that these are possible in HgMnTe, located on Hg vacancies. although they will be too shallow to give rise to persistent photoconductivity in these samples.

One method of creating a 'persistent' photoconductivity is to separate the charge carriers that are created under illumination. If the carriers are swept apart by the potential fluctuations, then their recombination will be less rapid then if they were allowed to remain spatially close. This is possible using a p-n juction, a heterojunction as discussed in the

previous section, or by the consideration of a random potential field [43]. The random potential theory is shown below in figure 6.49.

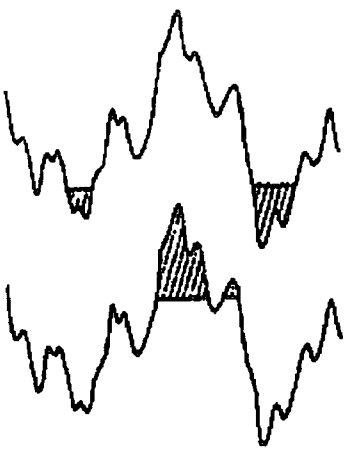

Figure 6.49 The random potential for persistent photoconductivity

The conduction and valence bands are shown in the figure. The shaded ares contain a quasiequilibrium of holes and electrons that have become spatially separated due to the shape of the band in that region. Hence the carriers cannot recombine without overcoming the potential barriers, and the recombination times are far longer than would be expected for the material, giving rise to a photoinduced conductivity with a very long time constant. This idea has been shown to be applicable in material in which the band structure is affected by the random location of inhomogeneities. [43]

Reference List Chapter 6

[1] Rogalski, A., Infrared Physics, **31**, (1991), 117

[2] Ashcroft, N.W., Mermin, N.D., Solid State Physics, Saunders College, Philadelphia, 1976

[3] Sawicki, M., Dietl, T., in Physics of Semiconducting Compounds, ed Zawadski, W., Institute of Physics, Warsaw, 1983, p1217

[4] Arapov, R.G., Davydov, A.B., Tsidilkovskii, I.M., Phys Tekh Pol., **17**, 1983, 24

[5] Oseroff, S., Keesom, P.H., in Semiconductors and Semimetals vol 25, eds Willardson, R.K., Beer, A.C., Academic Press, Boston, 1988, p73

[6] Li, D.X., Haga, Y., Shida, H., Suzuki, T., J App Phys, **80**, (1996), 264

[7] Delves, R.T., Proc Phys Soc, **87**, (1966), 809

[8] Ohno, H, Munekata, H., Penney, T., von Molnar, S., Chang, L.L., Phys Rev Lett, **68**, (1992), 2664

[9] Nagata, S., Galazka, R.R., Mullin, D.P., Akbarzadeh,, H., Khattak, G.D., Furdyna, J.K., Keesom, P.H., Phys Rev, B22, (1980), 3331

[10] Beer, A.C., in 'Hall effect and its Applications', eds Chien, C.L., Westgate, C.R., Plenum Press, New York, 1979

[11] Lawson, W.D., Nielsen, S., Putley, E.H., Young, A.S., J Phys Chem Solids, **9**, (1959), 325

[12] Harman, T.C., Logan, M.J., Goering, H.L., J Phys Chem Solids, 7, (1958), 228

[13] Giriat, W., Furdyna, J.K., in 'Semiconductors and Semimetals' vol 25, eds Willardson, R.K., Beer, A.C., Academic Press, Boston, 1988, p1

[14] Shlovskii, B.I., Efros, A.L., 'Electronic Properties of Doped Semiconductors', Springer, Berlin, 1984

[15] Chadi, D.J., Chang, K.J., Phys Rev Lett, **61**, (1988), 873

[16] Terry, I., Penney, T., von Molnar, S., Rigotty, J.M., Becla, P., Sol Stat Comm, **84**, (1992), 235

[17] Fritsche, H., Cuevas, M., Phys Rev, **119**, (1960), 1238

[18] Wasscher, J.D., Philips Research Reports, 1965

[19] Yosida, Phys Rev, **107**, (1957), 396

[20] Calculated from data in Rogalski, A., Infrared Phys, **31**, (1991), 117

[21] Moore, E.J., Phys Rev, **160**, (1967), 607

[22] Mott, N.F., 'Conduction in non crystalline material', OUP, Oxford, 1993

[23] Rosenbaum, T.F., Andres, K., Thomas, G.A., Bhatt, R.N., Phys Rev Lett, **43**, (1980), 1723

[24] Abrahams, E., Anderson, P.W., Liccindello, D.C., Ramakrishnan, T.W., Phys Rev Lett, **43**, (1980), 1723

[25] Wasscher, J.D., Philips Research Reports, 1965

[26] Alexander, S., Helman, J.J., Balberg, I., Phys Rev, **B13**, (1976), 304

[27] Shapira, Y., Foner,S., Oliveira, N.F., Reed, T.B., Phys Rev, **B5**, (1972), 2647

[28] Ando, K., Takahashi, K., Okuda, T., J Mag Magn Mat, **104-107**, (1992), 993

[29] Ozawa, K., Anzai, S., Hamaguchi, Y., Rhysics Letters, **20**, (1966), 132

[30] Hallam, T.D., 'The charcterisation of epitaxial layers of the dilute magnetic semiconductor $Hg_{1-x}Mn_xTe$', PhD thesis, University of Durham, 1995

[31] Capper, P., J Vac Sci Tech, **B9**, (1991), 1667

[32] Sone, S., Oda, N., Sasaki, T., Kawano, M., J Cryst Growth, **117**, (1992), 218

[33] Moore, C.D., 'X-Ray scattering studies of compound semiconductors', PhD thesis, University of Durham, 1997

[34] Ando, K., Phys Rev, **B47**, (1993), 19350

[35] Lautenschlager, P., Logothetidis, S., Vina, L., Cardona, M., Phys Rev, **B32**, (1985), 3811

[36] Zheng, X.L., Huber, C.A., Shih, M., Becla, P., Rao, A.M., Heiman, D., 20th Int Conf on Semicon, Thessaloniki (Greece), eds Anastassakis, E.M., Joannopulos, World Scientific, Singapore, p260

[37]

[38] Thio, T., Bennett, J.W., Chadi, D.J., Linke, R.A., Tamargo, M.C., J Electron Mat, **25**, (1996), 229

[39] Jaczynski, M., Kossut, J., Galazka, R.R., Phys Stat Sol, **b88**, (1978), 73

[40] Haury, A., Waisela, A., Arnoult, A., Cibert, J., Tatarenko, S., Dietl, T., Miele de Aubigne, Phys Rev Lett, **79**, (1997), 511

[41] Koshihara, S., Oiwa, A., Hirasawa, M., Katsumoto, S., Iye, Y., Urano, C., Takagi, H., Munekata, H., Phys Rev Lett, **78**, (1997), 4617

[42] Cooper, D.E., Harrison, W.A., J Vac Sci Tech, **A8**, (1990), 1112

[43] Sheinman, M.K., Shik, A.Y., Sov Phy Semicond, **10**, (1976), 128

Chapter Seven Magnetic Results

7.1 AGFM Data

All the susceptibilities given in the body of the text in this section, are expressed as volume susceptibilities (χ_V), and are in units of $(\text{mks} \cdot \text{m}^{-3})$, and is thought of as dimensionless. Comparisons between the experimental data and the theoretical data are scaled to a sample of dimension 1mm^2, as the samples are all slightly diffrent masses.

7.1.1 Buffer Layer

From calculations, it was found that the magnetisation of the samples was likely to be dominated by the GaAs substrate. The susceptibility of the constituents has been found in the literature, and the masses in the sample calculated. Hence, the first measurement was on a section of the buffer layer onto which the samples were grown. The magnetisation is shown in figure 7.1

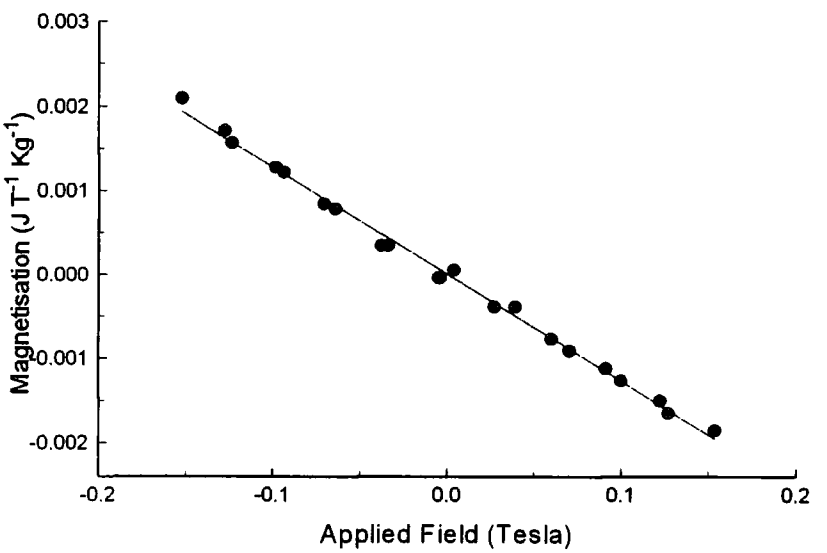

Figure 7.1 Magnetisation of the CdTe / ZnTe buffer layer

The susceptibilities of the constituents of a sample are

Name	Thickness (μm)	χ (emu g^{-1})	χ_V (mks)
GaAs	500	$-1.12\text{x}10^{-7}$ [1]	$-7.49\text{x}10^{-6}$
CdTe	1	$-3.5\text{x}10^{-7}$ [2]	$-2.43\text{x}10^{-5}$
CdTe	1	$-3.1\text{x}10^{-7}$ [3]	$-2.28\text{x}10^{-5}$
ZnTe	0.1	$-3.6\text{x}10^{-7}$ [4]	$-2.87\text{x}10^{-5}$
HgTe	variable	$-3.6\text{x}10^{-7}$ [5]	$-3.70\text{x}10^{-5}$
HgTe	variable	$-2.3\text{x}10^{-7}$ [4]	$-2.36\text{x}10^{-5}$

Table 7.1 The constituent susceptibilities of the samples investigated

The calculation for the susceptibility of a $1mm^2$ section of buffer layer is

Volume of GaAs substrate $1\text{x}10^{-3}\text{x}1\text{x}10^{-3}\text{x}500\text{x}10^{-6} = 5\text{x}10^{-10}m^3$

The susceptibility of this GaAs is therefore

$$\chi_V^{sub} = 5\text{x}10^{-10}\text{x}(-7.487\text{x}10^{-6}) = -3.74\text{x}10^{-15}$$

Similar calculations for the CdTe and ZnTe give a susceptibility of this $1mm^2$ section of buffer layer and substrate to be $\chi_V^{buf} = -3.77\text{x}10^{-15}$. This value is very similar to that of the GaAs substrate as was mentioned at the beginning of this section.

The value of the susceptibility obtained from the experiment is $\chi_V = -5.03(\pm 0.63)\text{x}10^{-15}$, and scaling this down to a sample of similar dimensions to that above, we find that $\chi_V = -3.51(\pm 0.44)\text{x}10^{-15}$.

7.1.2 MMT29

The room temperature susceptibility of MMT29A is shown in figure 7.2, and has a value of $-2.56(\pm 0.29)\text{x}10^{-15}$.

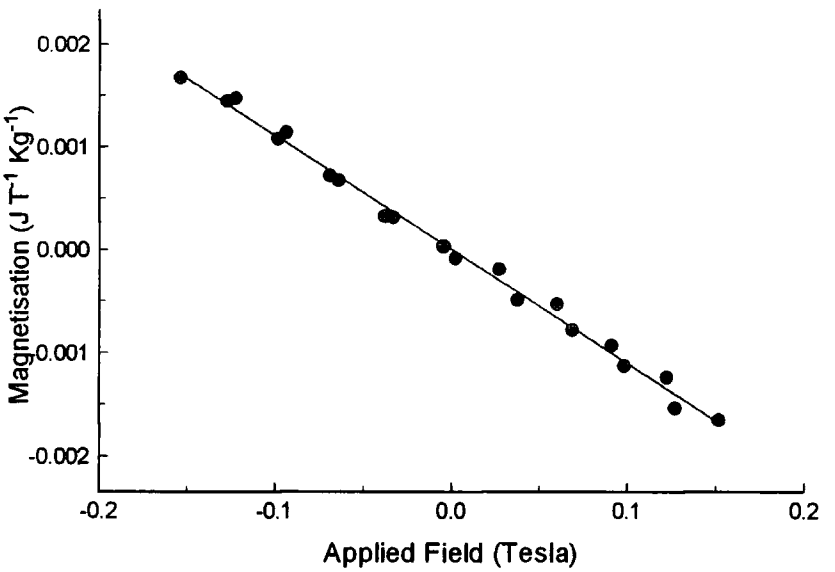

Figure 7.2 The susceptibility of MMT29A

Comparing this to that obtained for the buffer layer, we can find that the magnetic layer has a susceptibility of $\chi_V = 9.56(\pm 1.08)\text{x}10^{-16}$.

Calculation of the susceptibility of the HgMnTe layer is given by the Curie-Weiss law, and can be expressed as

$$\chi = \frac{N\mu_o {\mu_B}^2 g^2 J(J+1)}{3k_B(T+\theta)} - \chi_{HgMnTe} \qquad (7.1)$$

where N is the number of Mn ions (m^{-3}), and can be expressed as $\frac{1.5\text{x}10^{28}\,\text{x(Mn\%)}}{100}$, χ_{HgMnTe} is the diamagnetic susceptibility of the HgMnTe, which is

considered to be equal to the diamgnetic susceptibility of HgTe for low manganese concentrations, and all other symbols have their normal meaning.

The value of θ is obtained from figure 7.3 [6] assuming that they are equal to the bulk values.

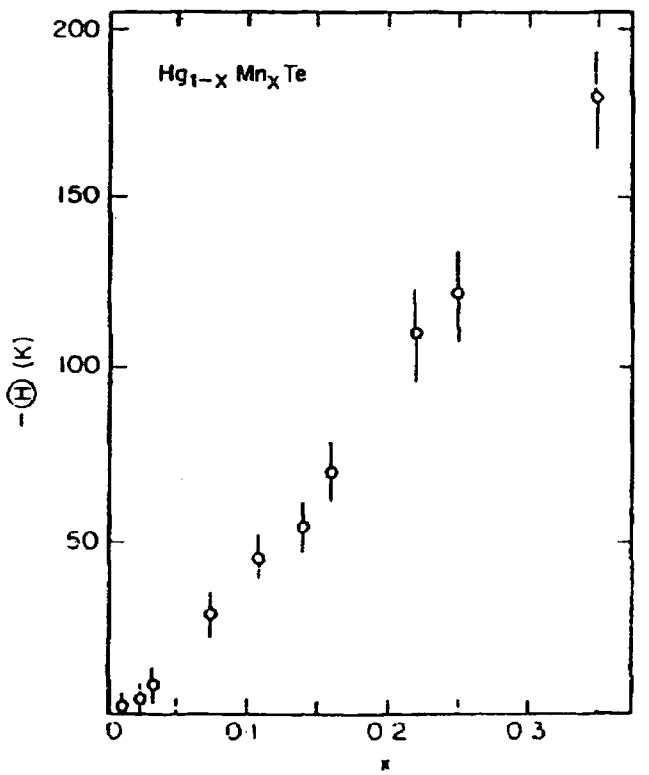

Figure 7.3 Value of θ in HgMnTe

The calculated susceptibility for a $1mm^2$ section of sample MMT29 is then $\chi_V = 1.64x10^{-15}$. This is based on a thickness of $2\mu m$ and a manganese concentration of $x = 0.1$. The descrepancy between this and the experimental value of $\chi_V = 9.57(\pm 1.08)x10^{-16}$ may be due to the inaccuracy of these numbers. The thickness can be measured to $\pm 0.1\mu m$ and the manganese concentration to 0.005, and so an error of $\Delta\chi_V = \pm 0.16x10^{-15}$ should be applied to the theoretical value.

7.1.3 MMT38B

The susceptibility of this sample is shown in figure 7.4.

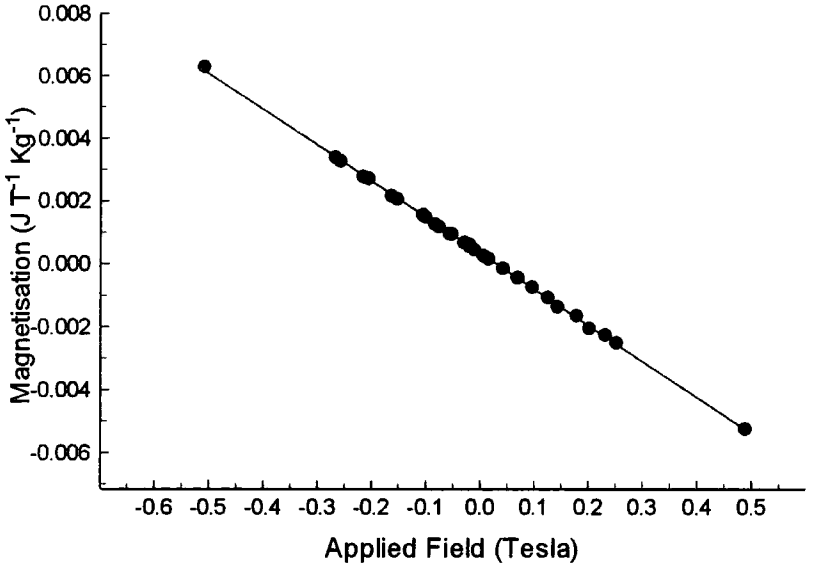

Figure 7.4 The susceptibility of MMT38B

Calculations reveal a susceptibility of the magnetic layer of $\chi_V = 2.49\text{x}10^{-15}$, which compares to the experimental value of $\chi_V = 2.33(\pm 0.23)\text{x}10^{-15}$. The same uncertainty has to be applied to the thickness and manganese concentration of this sample as the one analysed previously, here taken to be $5.5\mu m$ and $x = 0.055$ respectively. This gives an error on the theoretical value of $\Delta\chi_V = \pm 0.27\text{x}10^{-15}$.

7.1.4 MMT38A

The susceptibility of this sample is shown in figure 7.5

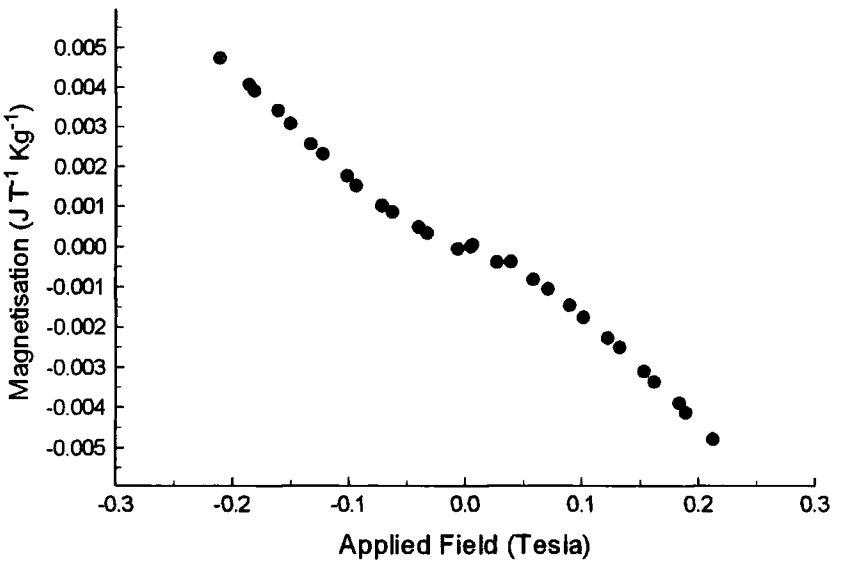

Figure 7.5 The susceptibility of MMT38A

The susceptibility of this sample is not of a linear nature as in the previous examples. A definite saturation can be observed at low field. Removing the linear background susceptibility, which is 4.11×10^{-15} in negative field and 4.25×10^{-15} in positive field, reveals this saturation, which is shown in figure 7.6.

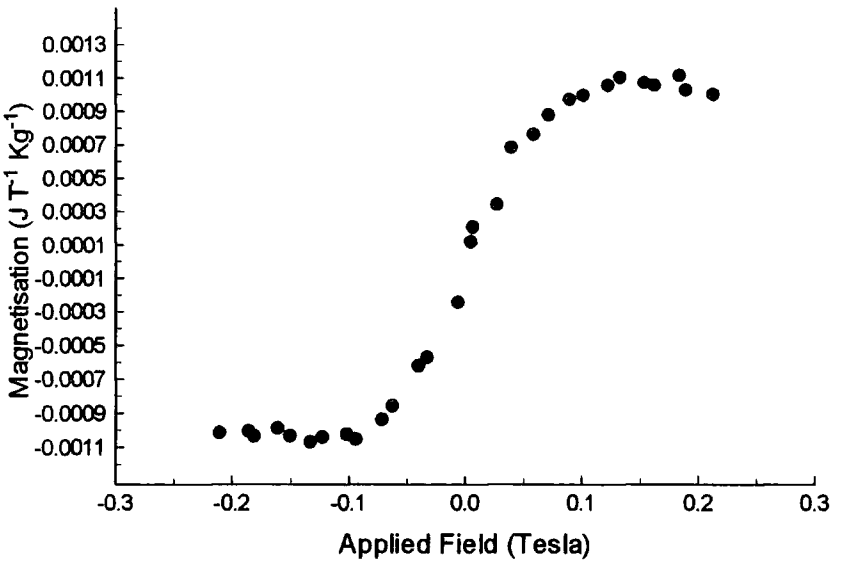

Figure 7.6 The satauration of MMT38A

From this saturation it is possible to evaluate the effective number of Bohr magnetons per manganese ion. From the volume of the sample the number of Mn ions is estimated to be $5x10^{15}$, and this gives an effective magnetic moment per ion of $0.271\mu_B$. A different approach would be to calculate the fraction of the Mn ions that are contributing to the saturation by defining the magnetic moment of each ion to be $5\mu_B$. This calculation states that only 5.4% of the managnese ions are contributing to the saturation in the material. Another method to calculate the fraction of Mn ions that are contributing to the saturation is to calculate the contribution to the paramagnetic behaviour of the sample. Considering the linear background of the magnetisation loop we can say that the susceptibility of the magnetic layer is $0.64(\pm 0.25)x10^{-15}$. This is far short of the predicted value from Curie Weiss theory, $1.72x10^{-15}$, and this descrepancy can be interpereted as the fraction of manganese ions that are contributing to the linear behaviour.

From this the fraction of manganese ions contributing to the paramagnetic behaviour is $37.1(\pm 15.2)\%$. This can be expressed as an effective manganese concentration of $\bar{x} = 2.3\%$.

7.1.5 MMT16

Another sample that shows evidence of a non linear susceptibility at room temperature is MMT16. The saturating component of this suceptibility is shown in figure 7.7.

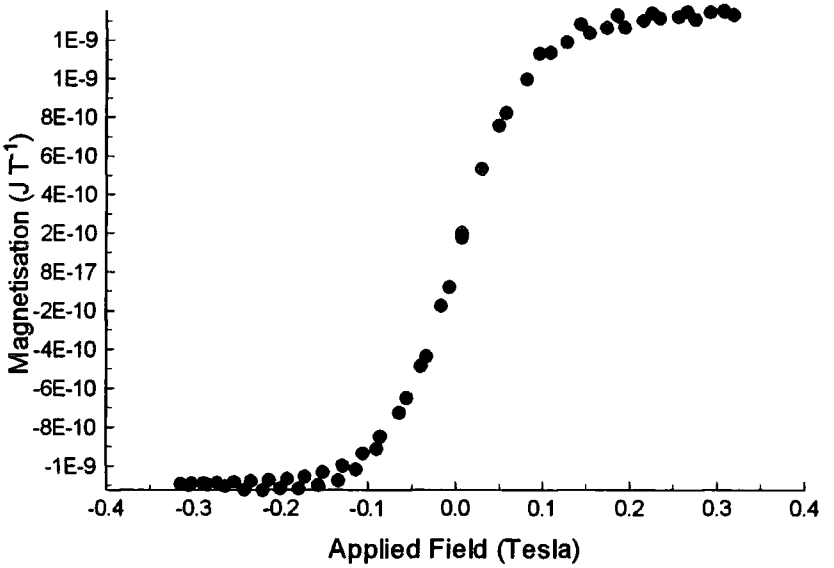

Figure 7.7 The saturation of MMT16

At saturation the effective number of Bohr magnetons in the sample can be calculated as being 6.47×10^{13} manganese ions, each of magnetic moment $5\mu_B$. Unfortunately there is no record as to the mass of this sample, although it has been estimated that it is similar to others measured in this study. Hence, as an estimate, the fraction of manganese ions contributing to the saturation in this sample is 2.2%.

It has been found that the epitaxial layer of HgMnTe in sample MMT16 is likely to be polycrystalline [8], and the MnTe is likely to congregate in clumps. Hence it can be postulated that the magnetic behaviour in this sample is dominated by the existence of MnTe clumps.

7.1.6 $Mn_{1-x}Te$

This sample is a layer of MnTe grown by MOVPE directly onto GaAs, where the manganese concentration is far lower than would be expected. EDAX data shows this in fact to be as low as 3% in parts of the crystal. It is therefore likely that the sample has a large defect concentration caused by the non-stoichiometry. This defect concentration is denoted by the x in the sample description. The sample can also be considered as MnTe clumps within a Te rich material. The susceptibility of the sample is shown in figure 7.8.

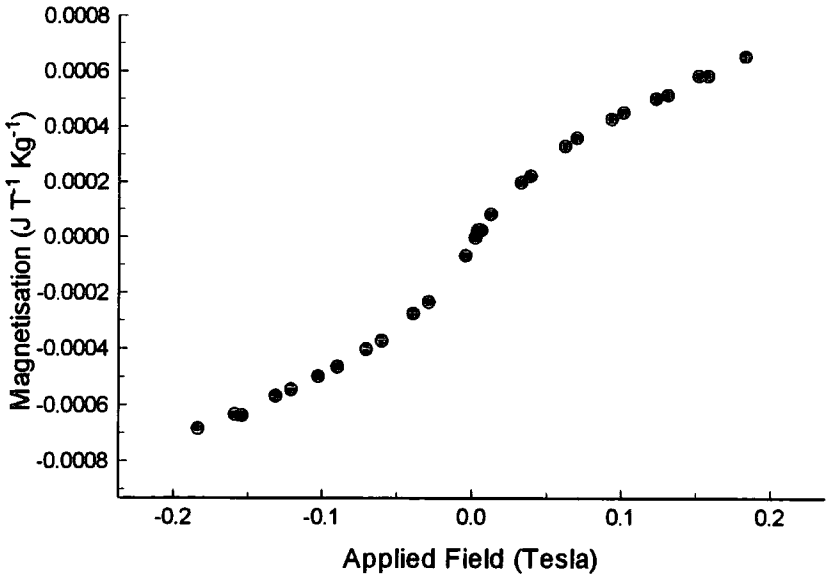

Figure 7.8 The raw data for $Mn_{1-x}Te$ sample

The major distinction of this sample from the others studied is the observation of a positive background susceptibility. The expected susceptibility of MnTe at low field will be positive because of the antiferromagnetic behaviour of the material.

As for the data of MMT38A and MMT16, the saturation of the sample can be removed from the background, giving rise to figure 7.9. The background in this case is $7.66\text{x}10^{-17}$.

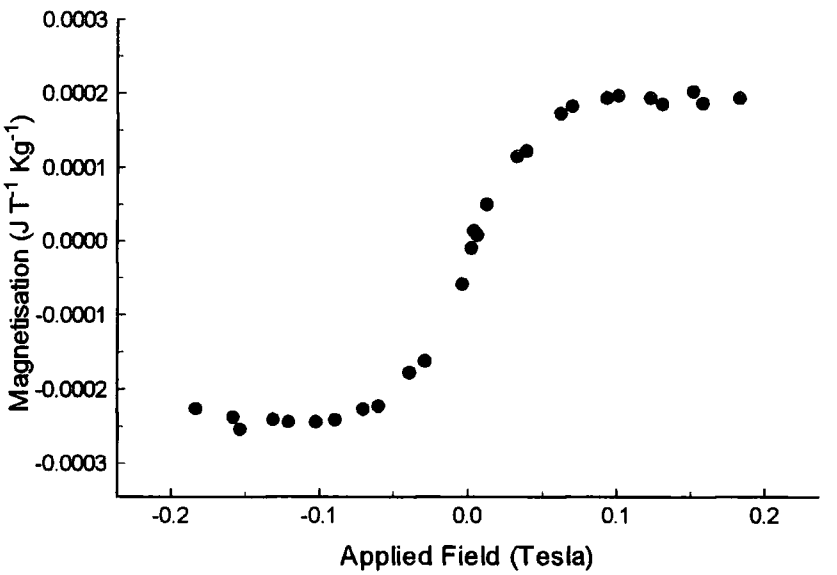

Figure 7.9 The saturation of $Mn_{1-x}Te$ from figure 7.8

The paramagnetic behaviour has a susceptibility (after removal of the diamagnetic contribution from the GaAs) of $3.74(\pm0.45)\text{x}10^{-15}$. In order to obtain a value for the Curie Weiss law, a value of θ is required. The value of θ for this sample is not known, as for a sample of MnTe the value of θ is expected to be -604K [9], although this is a dilute system, with about 3% Mn. Considering that HgMnTe is a system of dilute MnTe in a diamagnetic host, which is similar to this sample, it may be possible to estimate θ from the

HgMnTe value, which is -5K [6]. With this in mind, the Curie Weiss law has been fitted to evaluate the possible value of θ, which is +238.5K.

The saturation of the sample is the equivalent of $1.08 \times 10^{15} \mu_B$, and as the number of Mn ions in the sample is $2.13 \times 10^{15} cm^{-3}$, the effective fraction of the Mn ions contributing to the saturation can be calculated as 20%.

7.1.7 Proposed mechanism for the magnetisation

Superimposing the saturation of MMT38A, MMT16 and $Mn_{1-x}Te$ on the same figure suggests that the mechanism that is driving the magnetism in MMT16 and MMT38A, is also responsible for that in $Mn_{1-x}Te$. This can be seen in figure 7.10.

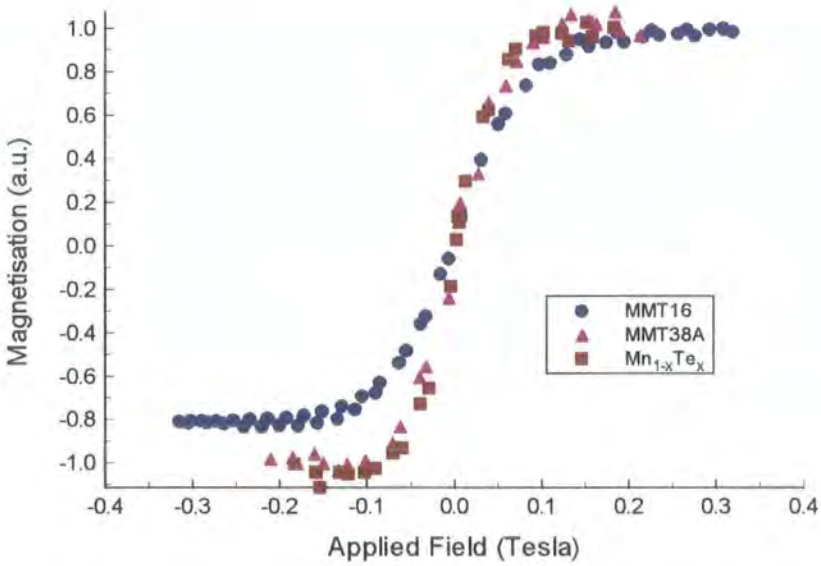

Figure 7.10 The comparison of the saturating components in MMT38A, MMT16, $Mn_{1-x}Te$

If the magnetisation in MMT16 is dominated by the behaviour of MnTe clumps, as has been postulated previously, then the magnetisation should be describable by one of the following methods.

Considering the clumps to be magnetic particles in a weakly magnetic sample, then the system should be analogous to that of a superparamagnet, and should be described by the Langevin function from section 3.3.4.

$$\frac{M}{M_{SAT}} = \coth\left(\frac{mB}{k_B T}\right) - \frac{k_B T}{mB} \qquad (7.2)$$

where m, the effective magnetic moment of the clumps is used as a fitting parameter. The fit to the average of the three data sets is shown in figure 7.11.

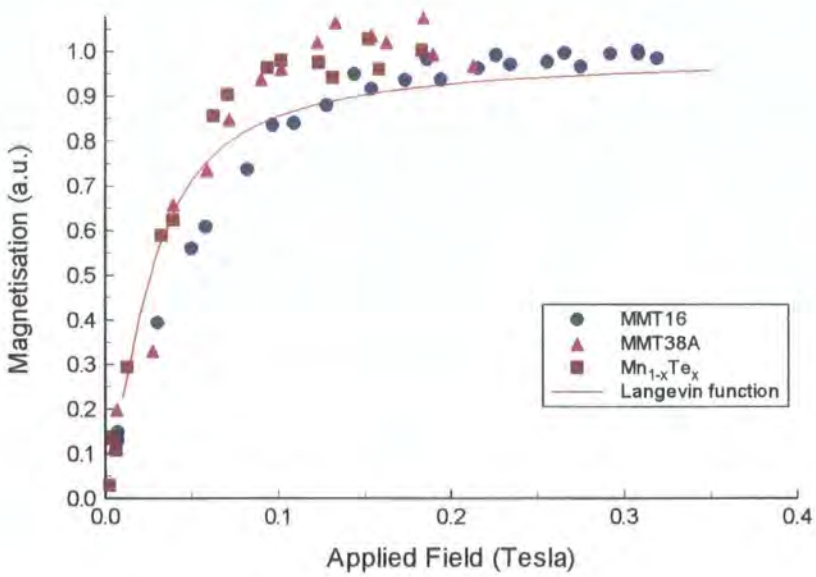

Figure 7.11. Comparison of the experimental data and the Langevin function

Using this equation with the data for sample MMT38A, gives a value of $m = 3\text{x}10^4 \mu_B$, which can be interpereted as a clump of 6000 manganese ions, each of

moment $5\mu_B$. Taking this hypothetical clump to be spherical, it would have an estimated radius of 25 Mn ions. If the clump is purely zinc blende MnTe, and the separation of Mn ions is 4.5 Å, [10] the diameter of the clump is approximately 225Å, which is well below the minimum resolution of the X-ray diffraction.

Another possibility is that the clumps are behaving like regions of high manganese concentration and they are behaving in a paramagnetic fashion, with antiferromagnetic interactions, and that their magnetisation should be explained by the use of a Brillouin function.

$$M = \frac{N}{V}\gamma J\left[\frac{2J+1}{2J}\coth\left[\frac{(2J+1)x}{2J}\right] - \frac{1}{2J}\coth\left[\frac{x}{2J}\right]\right]$$

(7.3)

For zinc blende MnTe clumps, the Neel temperature is 60K [11] and so no saturation should be visible in these measurements, at the fields used. However if the MnTe inclusions in the material are of a NiAs structure, then the antiferromagnetic ordering would occur at the Neel temperature of 310K [12], and be visible at room temperture, but at far higher fields than those used. Of course, this is not what would be expected from the MOVPE growth technique, but still should be considered as a possibility.

Using the value of θ as a fitting parameter yields figure 7.12.

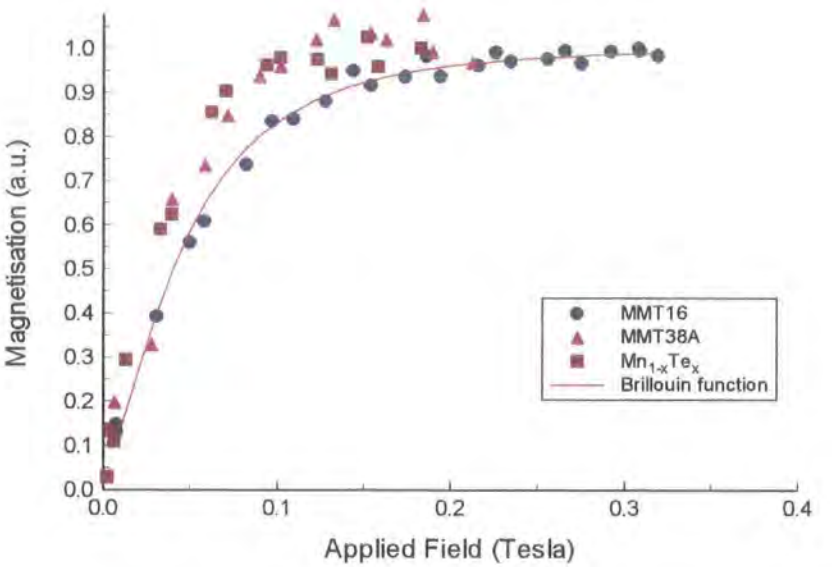

Figure 7.12. Comparison of experimental results and Brillouin function fit to MMT16

The Brillouin function gives a very good fit to the data of MMT16, and fits can be obtained to fit the other two samples. The value of θ obtained from this fit is $\theta = +289.89K$, and is $\theta = +289.92K$ for MMT38A and $Mn_{1-x}Te$. These values are for a ferromagnetic exchange interaction, and so the antiferromagnetic interaction cannot be responsible. One of the possibilities for the origin of the ferromagnetic behaviour is the concept of vacancy ordering. In a material such as Fe_7S_8 which has a NiAs structure, the observed room temperature magnetism is ferromagnetic [13], and this has been attributed to a magnetic ordering of the vacancies within the material. This mechanism is a contender to explain the magnetisation of the $Mn_{1-x}Te$ sample, where as a consequence of the growth, a large vacancy concentration exists within the sample. This maybe due to the formation of NiAs structure MnTe during the growth process as this sample has been

grown directly onto the GaAs substrate without the use of a buffer layer. Due to the lattice mismatch between the GaAs and the zinc blende MnTe, it is possible that the layer is very disordered and the preferential NiAs structure MnTe is present. The lattice mismatch between GaAs and zinc blende MnTe is 0.699Å, rather than the mismatch between the CdTe buffer layer and a $Hg_{0.9}Mn_{0.1}Te$ layer, which is 0.04Å. Hence the $Mn_{1-x}Te$ layer should be very highly strained, and liable to form defects to relieve the strain. It is also very likely that in such a strained system, the MnTe will form in its preffered form, namely NiAs structure, although it can be grown in the zinc blende structure via the use of molecular beam epitaxy, for small thicknesses.[11]

7.1.8 MnTe

A different sample of MnTe has been analysed, which was grown by M. Funaki using MOVPE. The susceptibility shows a very similar field dependance to the previous sample. The high field region is showing the contribution of the antiferromagnetically aligned spins. The magnetisation is shown below in figure 7.13.

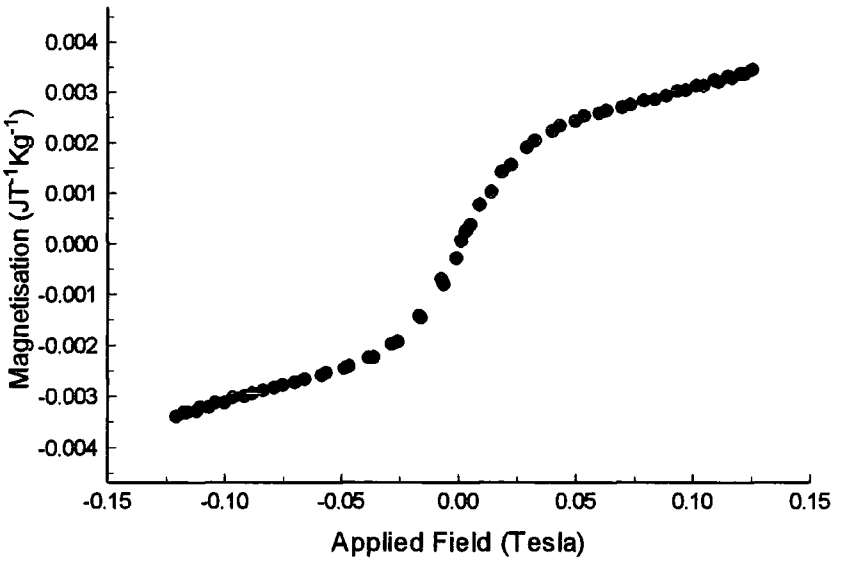

Figure 7.13. The magnetisation of epitaxial MnTe

From this it is possible to remove the paramagnetic component, of susceptibility 2.53×10^{-17}, to reveal the saturation, which is shown in figure 7.14.

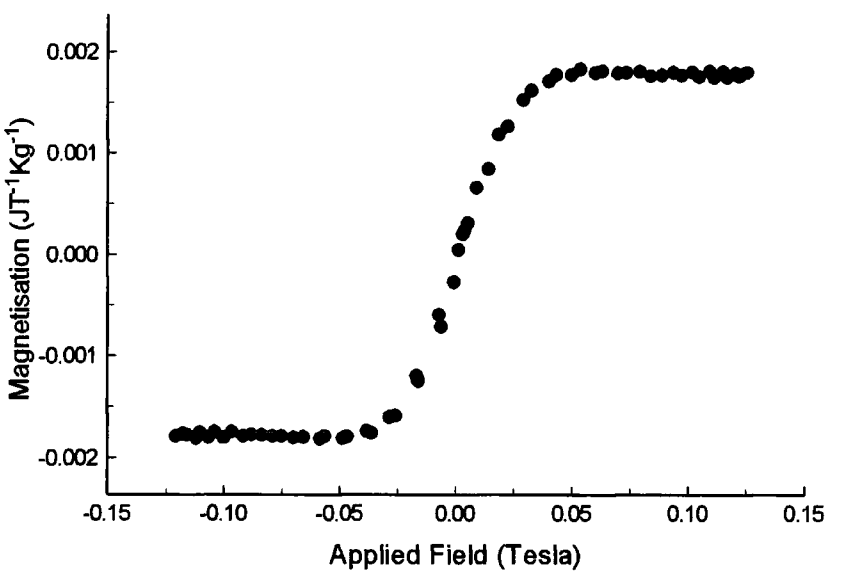

Figure 7.14. The saturation of epitaxial MnTe

The satauration of the MnTe sample is equivalent to $2.46 \times 10^{15} \mu_B$, and from this it is possible to calculate the fraction of the Mn ions that are contributing to this saturation, which is 0.5%.

Comparing this saturation with that obtained in the $Mn_{1-x}Te$ sample shows a difference in the saturation field.

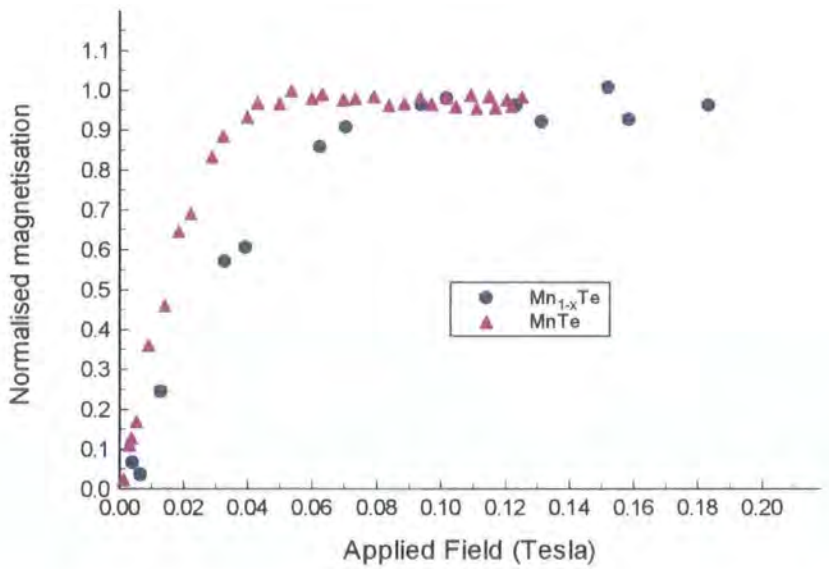

Figure 7.15. Comparison of the saturation in MMT38A and MnTe

Despite the difference in the saturation field visible in the above figure, it seems likely that the saturation in this MnTe sample is of a similar origin. This would seem to support the theory that the magnetism in these samples is linked to vacancy ordering.

It has been shown by Banfield *et al* [14], that the magnetisation of a sample can be dominated by the presence of a regular vacancy pseudo lattice in the sample. This observation has been made by the correlation of magnetic measurements and the direct observation of the vacancies in cross sectional transmission electron microscopy.

7.2 Hall Chip Data

The behaviour of the chip, an AlGaAs heterostructure, was investigated to ascertain the sensitivity of the device in the temperature range desired. It was noticed that the chip gave different sensitivities every time it was cooled down, due to the carriers freezing in to deep DX centre states [15], although it gave reproducible results under saturation illumination. The useable sensitivity can be defined as the number of Ohms per Tesla that the chip can show, under saturation illumination, above the noise base. The sensitivity of the chip as a function of temperature below 45K is shown in figure 7.16.

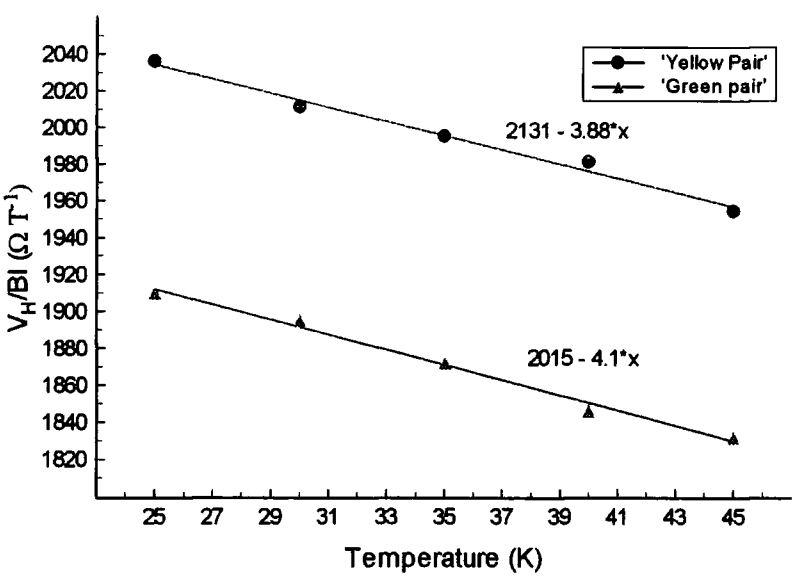

Figure 7.16 The sensitivity of the Hall device

The background of the chip was taken to be the gradient of the line on the $\frac{V_H}{I}$ v B and this was found to have a quadratic part to it. This is likely to occur from contact

offset and is caused by the strong quadratic magnetoresistance of the device, which is shown in figure 7.17.

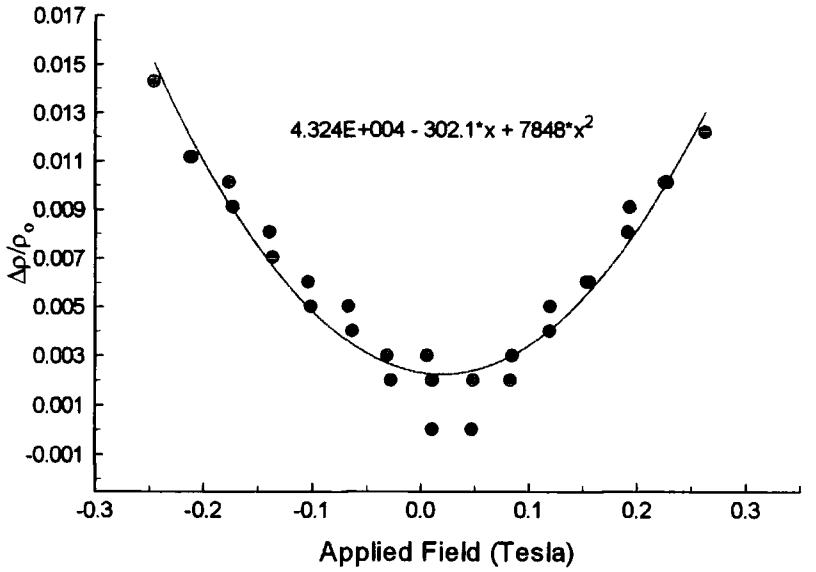

Figure 7.17 The magnetoresistance of the AlGaAs Hall device

Before attempting to measure an epitaxial layer of HgMnTe the chip was tried out using a piece of bulk $Cd_{0.8}Mn_{0.2}Te$:P, with a mass of 5.6mg. The signal due to the magnetisation of the sample, after the removal of the background is shown in figure 7.18.

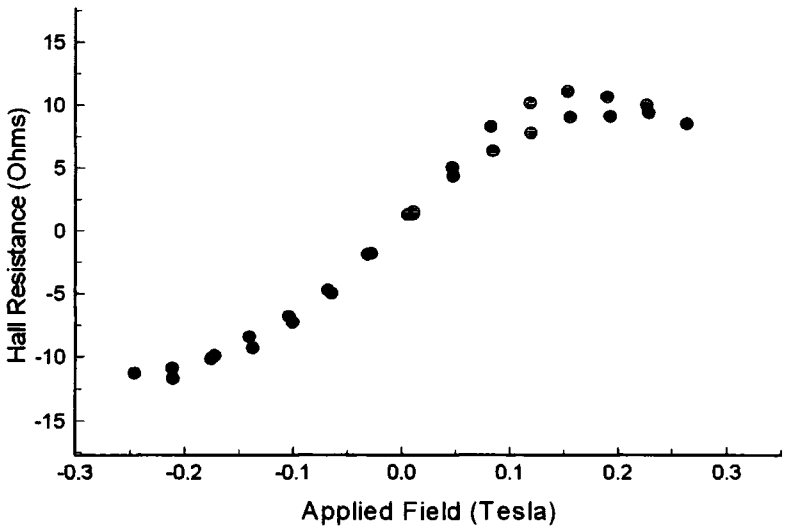

Figure 7.18 Sample 2 at 30K on the AlGaAs chip

The hysteretic region in low field was of great interest, and further investigations were undertaken to check if this was real or an artefact of the measurement. Running another piece of $Cd_{0.8}Mn_{0.2}Te$ gave very similar results as shown in figure 7.19.

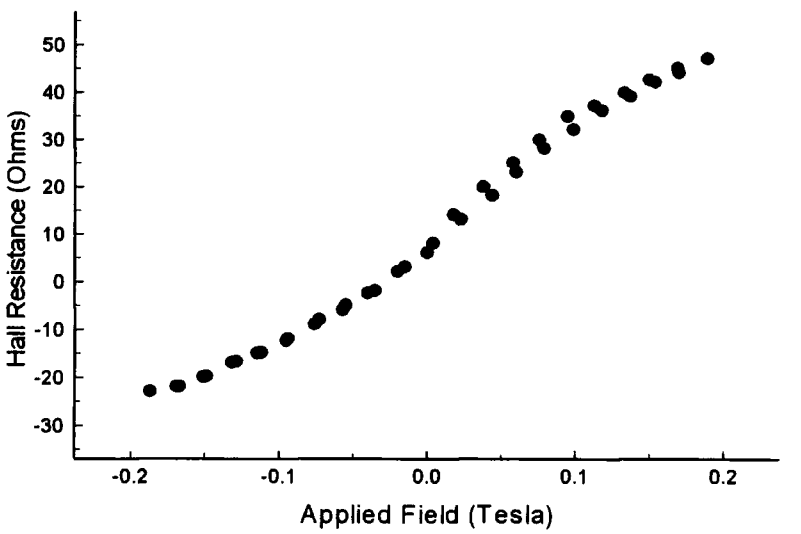

Figure 7.19 The second run of sample 2 at 30K

It was decided to check the linearity of the system by measuring a known paramagnet. A sample of $CuSO_4.5H_2O$ was prepared and measured, and the signal due to the sample magnetisation is shown in figure 7.20.

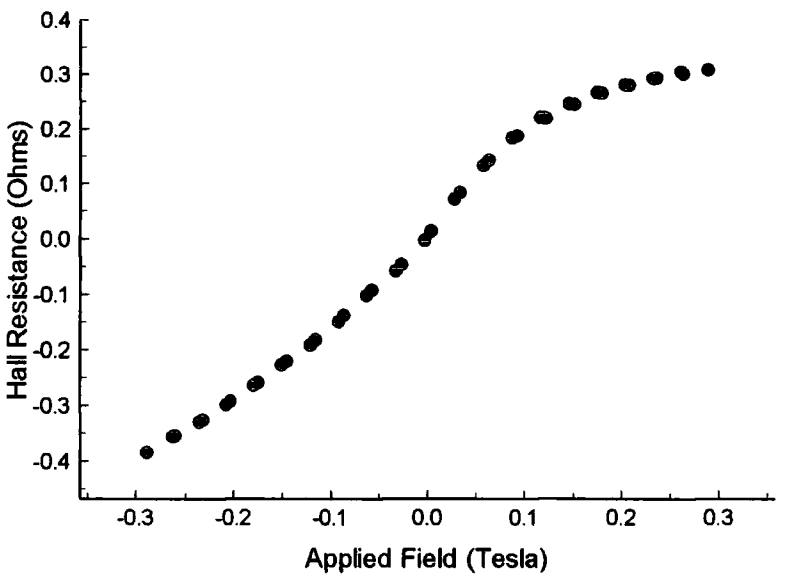

Figure 7.20 The magnetisation of the $CuSO_4$ sample

This shows that the system is non linear in the low field region and that the results obtained previously are more than likely to be a linear susceptibility without any hysterisis at low field. As this problem has not been resolved, the investigations on the Hall devices was stopped.

7.3 Faraday Balance Data

All the data in this section has been taken in the Faraday balance system, outlined in section 5.3, at a field of 1 Tesla to ensure a good signal to noise ratio. The susceptibility of the sample under investigation is extrapolated to infinite temperature, and

this value is taken to be the diamagnetic background from the sample holder, the GaAs substrate, the buffer layers, and the HgTe. This is shown in figure 7.21, for MMT38.

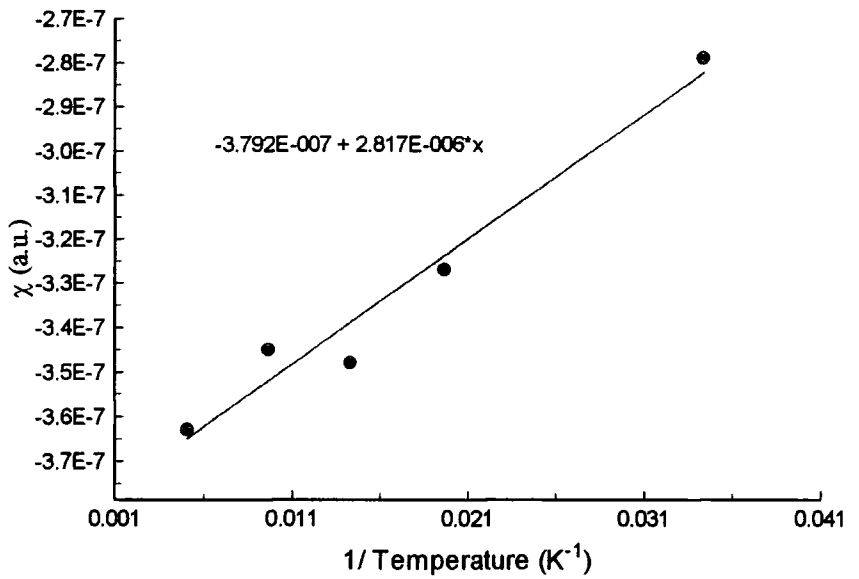

Figure 7.21 Calculating the diamagnetic contribution at infinite temperature

The value obtained from this is subtracted from the data before further analysis in undertaken.

Fitting a straight line to the high temperature region of the data gives an intercept on the temperature axis, which is the value of θ for that sample under investigation. This is shown in figure 7.22 below for MMT38.

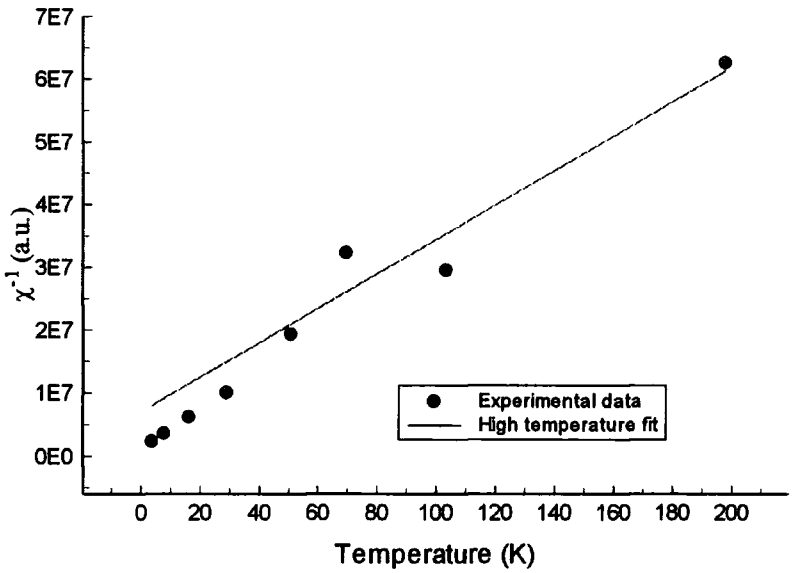

Figure 7.22 The extrapolation of the high temperature inverse susceptibility to obtain θ

The calculated value for θ is obtained by fitting a line to the data in [6] which gives the following equation

$$-\theta = 0.0317x^2 + 4.25x - 5.39 \qquad (7.4)$$

where x is the manganese concentration in percent and the value of θ is given in K. This equation gives a good fit in the region of $0 < x < 30$.

The values of θ obtained for the samples investigated are summarised in table 7.2 below.

Sample	Mn concentration (%)	$-\theta$ Experimental (K)	$-\theta$ Literature (K)	Background (a.u)
MMT12	5 - 12	129	16.65 - 54.42	-3.47×10^{-7}
MMT16	5 - 6	19.6	16.65 - 21.25	-4.27×10^{-7}
MMT25	13	80	55.20	-3.88×10^{-7}
MMT26	10	31.7	40.28	-4.21×10^{-7}
MMT29	8 - 11	0	30.64 - 45.20	-4.64×10^{-7}
MMT38	5 - 8	25.25	16.65 - 30.64	-3.79×10^{-7}

Table 7.2 Summary of the samples investigated

Using the work of Nagata *et al* [6] it is possible to simulate the susceptibility of the samples. The equations for this are given in section 3.7.2. In most of the work in this area the exchange integral J is treated as a fitting parameter. Using this method to determine J is notoriously inaccurate, as the value is influenced by long range interactions, as described in section 3.6. In the fits below, the value of J has been allocated the value taken from Nagata's work, to evaluate the accuracy of the model.

A comparison of the calculated susceptibility with that of the experimental data is shown below in figure 7.23 for MMT38.

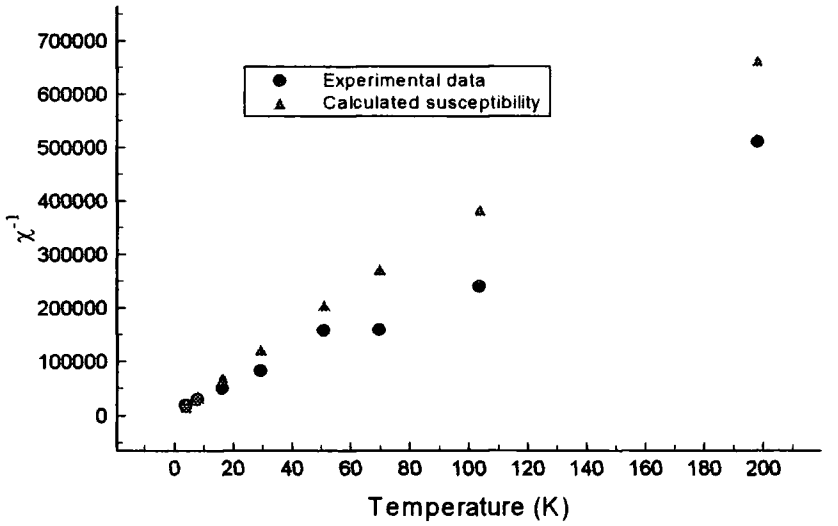

Figure 7.23 The comparison of experimental and calculated susceptibility for MMT38A

The other samples investigated are shown in the following figures.

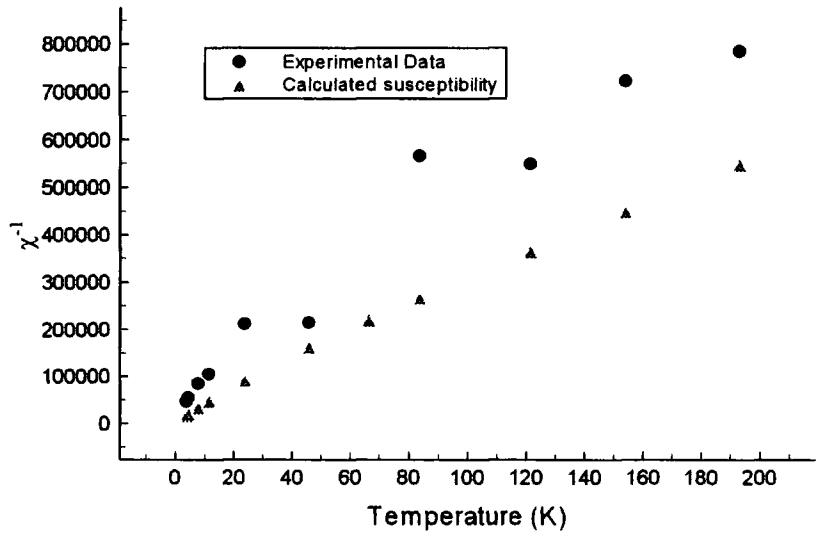

Figure 7.24 The comparison of experimental and calculated susceptibility for MMT16

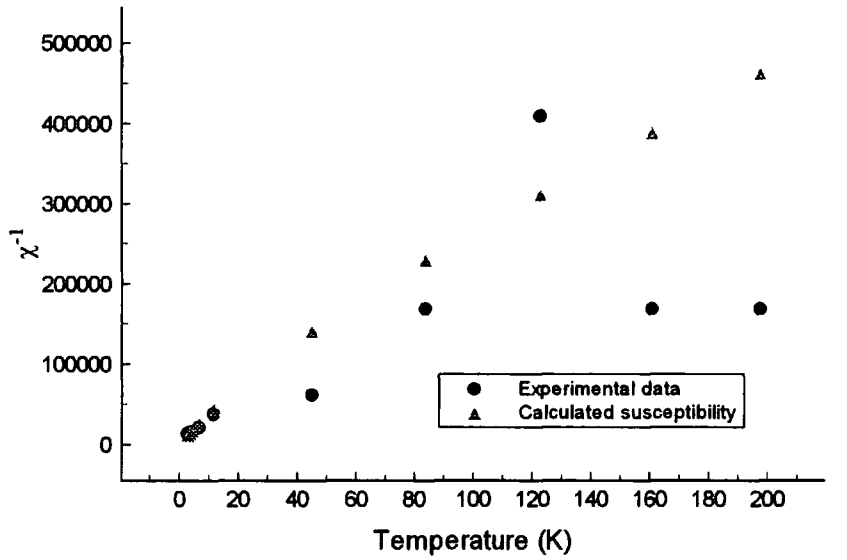

Figure 7.25 The comparison of experimental and calculated susceptibility for MMT12

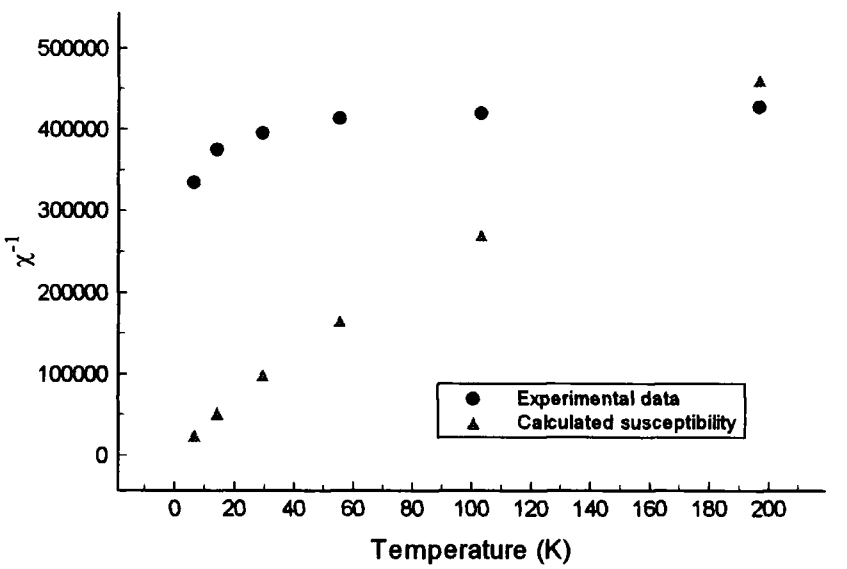

Figure 7.26 The comparison of experimental and calculated susceptibility for MMT29A

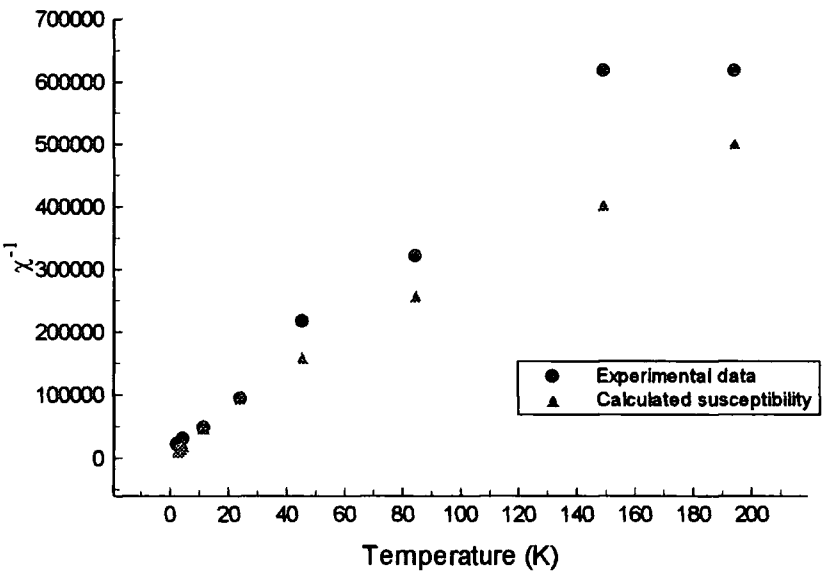

Figure 7.27 The comparison of experimental and calculated susceptibility for MMT25

The fits in general show a qualitative fit to the data. The quality of the fit is similar to that of Nagata using the random distribution. As no specific heat data is available for these samples, it is impossible to create a modified distribution for these samples. The work of Shapira *et al* [16] has shown that the specific heat can be modelled by using the standard distribution of ions and increasing the value of J to -10K. Assuming that this would allow the magnetisation to be explained using the same technique has not proved successful, and the fits obtained are no better than those shown above. Hence, it would appear that in order to successfully simulate the susceptibility of HgMnTe specific heat measurements are required in order to calculate the distribution of the manganese ions.

Reference List Chapter 7

[1] Chemical Rubber Company Handbook, vol 73, CRC Press, London, 1992

[2] Ivanovomslii, V.I., Kolomiets, B.T., Ogorodnikov, V.K., Rud, Y.V., Tsmots, V.M., Phys Stat Sol (a), **13**, (1972), 61

[3] Candea, R.M., Hugdens, S.J., Kastner, M., Phys Rev, **B18**, (1978), 2733

[4] Singh, S., Singh, P., J Phys Chem Sol., **41**, (1980), 135

[5] Ivanov-Omskii, V.I., Kolomiets, B.T., Ogorodinkov, V.K., Smekalova, K.P., Tsmots, V.M., Phys Stat Sol, **a14**, (1972), 51

[6] Nagata, S., Galazka, R.R., Mullin, D.P., Akbarzadeh,, H., Khattak, G.D., Furdyna, J.K., Keesom, P.H., Phys Rev, B22, (1980), 3331

[7] Balch, C., Internal report, University of Durham, unpublished

[8] Moore, C.D., X-ray scattering studies of compound semiconductors, 1997, University of Durham

[9] Extrapolated from data in [6]

[10] Furdyna, J.K, J Appl Phys, **64**, (1988) ,R29

[11] Ando, K., Takahashi, K., Okuda, T., J Mag and Mag Mat, **104 - 107**, (1992), 993

[12] Komatsubara, T., Murakami, M., Hirahara, E., J Phys Soc Japan, **18**, (1963), 356

[13] Bertaut, F., Acta Cryst, **6**, (1953), 557

[14] Banfield, J.F., Wasilewski, P.J., Veblen, D.R., American Mineralogist, **79**, (1994), 654

[15] Theis, T.N., Mooney, P.M., Parker, B.D., J Electron Matter, **20**, (1991), 35

[16] Shapira, Y., Foner, S., Ridgley, D.H., Dwight, K., Wold, A., Phys Rev, **B30**, (1984), 4021

Chapter Eight Photoinduced phenomena in CdMnTe:In

8.1 Persistent photoconductivity (PPC)

Conventional short lived photoconductivity was reviewed in section 1.7. However, there are certain materials that show photoconductivity, that remains for long periods after the illumination is removed. This persistent photoconductivity has been observed in CdZnTe [1], AlGaAs [2] and CdMnTe:In [3] samples to name but a few. Persistent photoconductivity typically exhibits the following features: Upon illumination the value of the resistivity drops to a lower value. After the removal of the illumination, the resistivity relaxes quickly to an intermediate level, where it remains for a period of many months, as long as the sample is kept below a certain temperature T_Q (e.g. $T_Q \approx 100K$ for CdMnTe:In) [3]. Upon warming, the resistivity of the illuminated case is consistently lower than that of the unilluminated sample, until T_Q is reached, (the quenching temperature) and the two curves join. An example of this is shown in figure 8.1.

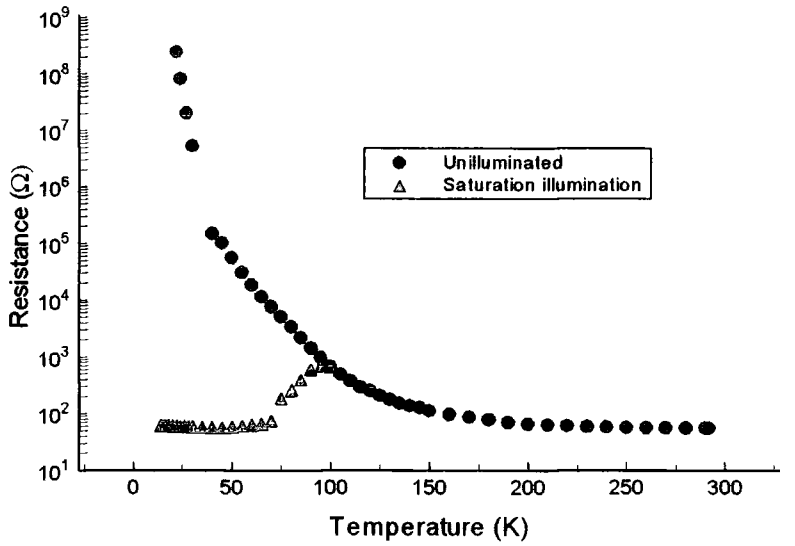

Figure 8.1 The behaviour of a typical persistent photoconductor, in this case $Cd_{0.9}Mn_{0.1}Te$:In.

The drop in resistivity is accompanied by a change in the carrier concentration, and this can be seen in figure 8.2 for the $Cd_{0.9}Mn_{0.1}Te$:In sample at 25.3K.

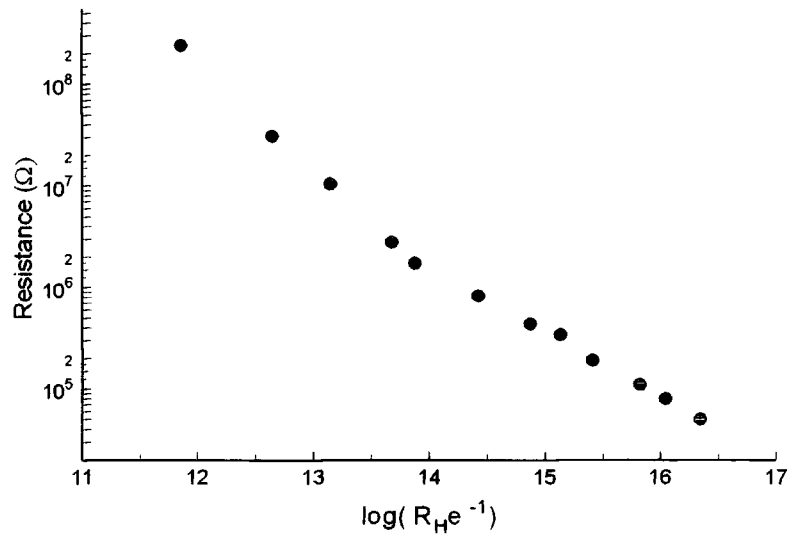

Figure 8.2 The relationship for resistivity as a function of carrier concentration

There are a number of mechanisms for PPC [5], some of which are outlined below. The mechanism for the observed effect in CdMnTe:In is that of the DX centre [4].

8.2 DX Centres

The DX centre is a consequence of the bistability of the In dopant in the material, as shown in figure 8.3. The indium dopant can substitute onto a cation site to form a shallow donor, but the ground state of the impurity is in fact as shown in figure 8.3.b, where the In atom occupies an interstitial site. This latter site has a binding energy which is roughly an order of magnitude greater than that of the shallow state, and it is believed that this deep state is stabilised if the indium donor is occupied by two electrons.

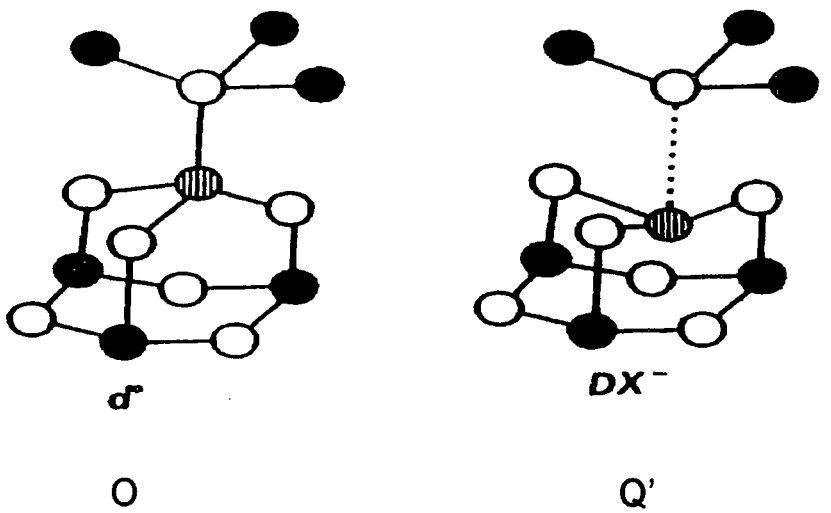

Figure 8.3 The distortion of the lattice around the deep state

The origin of PPC may be understood by considering the configuration co-ordinate diagram as shown in figure 8.4. [4]

On cooling the sample, the electrons will preferentially freeze out in to the deep state, which is strongly relaxed with the potential minimum centred at position Q'.

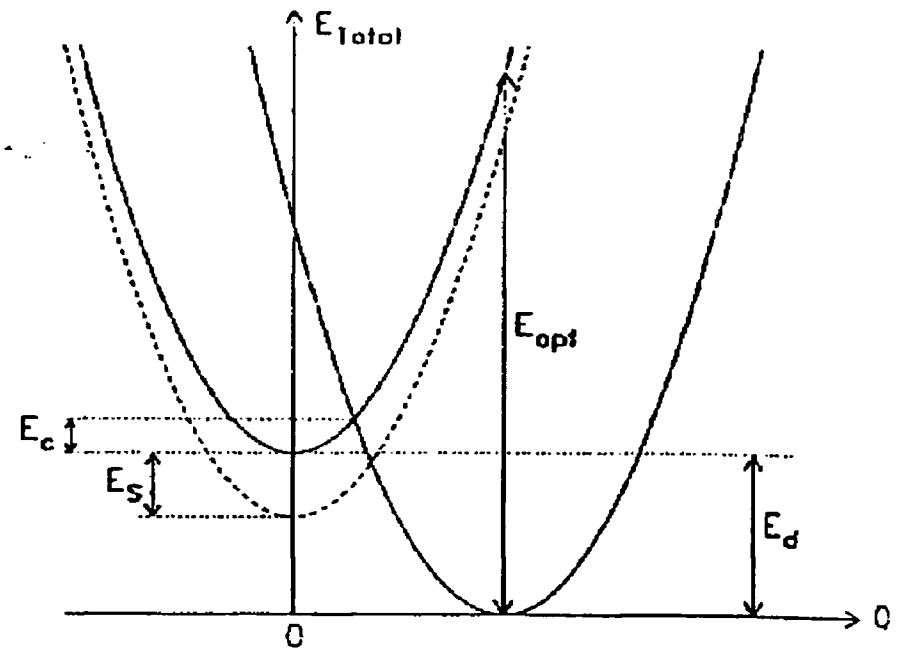

Figure 8.4 Configuration co-ordinate diagram for the DX centre

The electrons in the deep state are excited by photons of energy E_{OPT}, and then relax into the bottom of the left hand potential. Providing the temperature is sufficiently low, the electrons will have insufficient energy to cross the barrier of height E_C and return to the deep state. Hence the sample now has a metastable increase in the free carrier concentration. This will remain the case until the temperature is raised to the point that $k_B T > E_C$, and at this point the temperature is defined as the quenching temperature, T_Q. At $T < T_Q$ the electrons are now in the hydrogenic-like donor state and so can be excited to the conduction band to contribute to the conductivity.

8.3 The formation of bound magnetic polarons (BMP)

Two types of polaron are theoretically possible in a system such as CdMnTe:In. The free magnetic polaron occurs when a carrier is trapped, via the exchange interaction, in a magnetic potential well created by locally aligning the spins of the magnetic ions. [6] For a stable polaron to form the potential energy reduction, must exceed the gain in kinetic energy due to the localisation of the carrier. Possible experimental evidence for free polarons, which have been predicted theoretically, comes from the interpretation of a line in the photoluminescence spectra of CdMnTe by Golnik *et al.* [7] However, because of the general lack of convincing evidence for these polarons, they will not be discussed further.

The bound magnetic polaron, which has been observed experimentally,[8] is described below.

Consider an electron in the shallow donor band in a material, such as one that has been excited during photoconductivity. The Hamiltonian of this electron can be expressed as

$$H = H_B + H_C + H_M \qquad (8.1)$$

where H_B is the energy from the band, H_C the Coulomb energy which is equal to $\frac{e^2}{\varepsilon r}$, and H_M the magnetic Hamiltonian.

The magnetic Hamiltonian has two components, the first originates from the s-d interaction of the carrier and the localised spins, and the second part which is Zeeman-like. This can be expressed as [9,10]

$$H_M = -J_{12}\sum_i S_i \cdot s_i + g\mu_B H \cdot \sum_i s_i \quad (8.2)$$

where J_{12} is the s-d exchange interaction, S_i the spin of the magnetic ion, s_i the spin of the electron, g the Lande g factor, μ_B the Bohr magneton, and H the magnetic field.

Due to the s-d interaction the carrier creates a potential well which aligns the surrounding spins. This localisation is favoured because of the electrostatic attraction of the electron to the donor. The energy of the electron is further reduced by the alignment of its spin with that of the local magnetic moments. This alignment creates a region with a susceptibility that is far higher than the paramagnetic background of the sample.

The susceptibility of the polarons can be calculated from equation 8.3, [10]

$$\chi_P = \frac{N_D \mu_B 2}{4k_B T} \cdot g_{eff}^{\ 2} \cdot \left[\frac{1 + \frac{\varepsilon_p}{3k_B T}}{1 + \frac{\varepsilon_p}{k_B T}} \right] \quad (8.3)$$

where N_D is the donor concentration, μ_B the Bohr magneton, k_B Boltzmann's constant, T the temperature, g_{eff} the effective Lande g factor which can be calculated from $g_{eff} = g^* + \frac{\alpha\chi}{g\mu_B^{\ 2}}$.

where α is the antiferromagnetic exchange constant, and χ the susceptibility of the sample.

The polaron binding energy, ε_p, can be calculated from equation 8.4 [10]

$$\varepsilon_p = \frac{\alpha^2 \chi}{(g\mu_B)^2 32\pi a_B^{\ 3}} \quad (8.4)$$

8.4 Experimental observation of BMP

Experimentally polarons can be observed optically [8], and by their effect on the magnetotransport of samples [11], and by the small change in magnetisation at low field [12]. The magnetoresistance arising from the presence of polarons is very large and can be in excess of 7 orders of magnitude at 2T, as seen in $Gd_{3-x}V_xS_4$ by von Molnar *et al* [13] and is shown in figure 8.5 below.

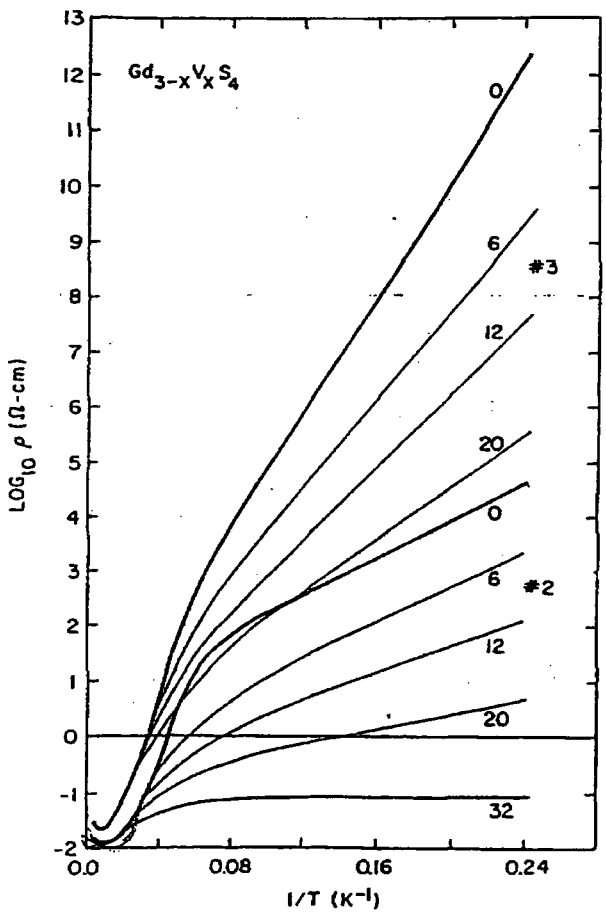

Figure 8.5 The magnetotransport of $Gd_{3-x}V_xS_4$ showing the effects of polaron dominated transport

In the figure, the values on the lines refer to the field in KOe, and V in the formula unit refers to the vacancy concentration in the sample.

8.5 Previous work on photomagnetisation

Photomagnetisation has been observed by a number of groups, the first of which was Krenn *et al* [14] who observed an increase in the magnetisation of HgMnTe under illumination from a CO laser with the use of an RF SQUID. Further work by this group has shown photomagnetisation from the increase in the conduction electron density in HgCdTe [15] using the same technique. Photomagnetisation in CdMnTe has been studied by Awschalom *et al* [16] who have also used a SQUID, and have achieved picosecond timescale measurements [17].

The only previously published work on persistent photomagnetisation of CdMnSeTe:In samples has been recorded by Wojtowicz *et al* [18]. They observe an increase in the susceptibility of their sample under illumination from infra red light, using a SQUID magnetometer. Indium contacts on the sample allowed simultaneous resistivity measurements to be performed, hence investigating the relation between ΔM the increase in magnetisation and ΔN_D the increase in the concentration of the donors.

The measured value of $\Delta N_D{}^{ELEC}$ from the electrical measurements and $\Delta N_D{}^{MAG}$ calculated from the change in magnetisation of the sample did not agree with $\Delta N_D{}^{ELEC}$, that being 50% higher than $\Delta N_D{}^{MAG}$. Wojtowicz *et al* [18] explained this discrepancy as being the result of electrons on the donors coupling antiferromagnetically when close to the metal insulator transition, and so a number of them are frozen into spin up / spin down pairs. Polarons can only form on 'free' spins, and so the discrepancy can be interpreted as the fraction of the spins that are frozen out. The carrier concentration observed by Wojtowicz *et al* [18] in their sample is ~1.5×10^{16} cm^{-3}, which is far below the value

expected for the metal insulator transition in CdMnTeSe:In, of approximately $6x10^{17}$ cm^{-3} [19]. Hence, it is unlikely that such an explanation is valid.

The work presented here, is in an attempt to check the validity of this explanation, by measuring the persistant photomagnetisation of a previously characterised sample, in a modified commercial Faraday balance system. This is only the second time that these measurements have been performed, and the first occasion by this method.

8.6 Experimental results

The magnetic data in this section was taken in the Faraday balance system that was outlined in section 5.3. The susceptibility of a sample of $Cd_{0.9}Mn_{0.1}Te$:In is shown in figure 8.6.

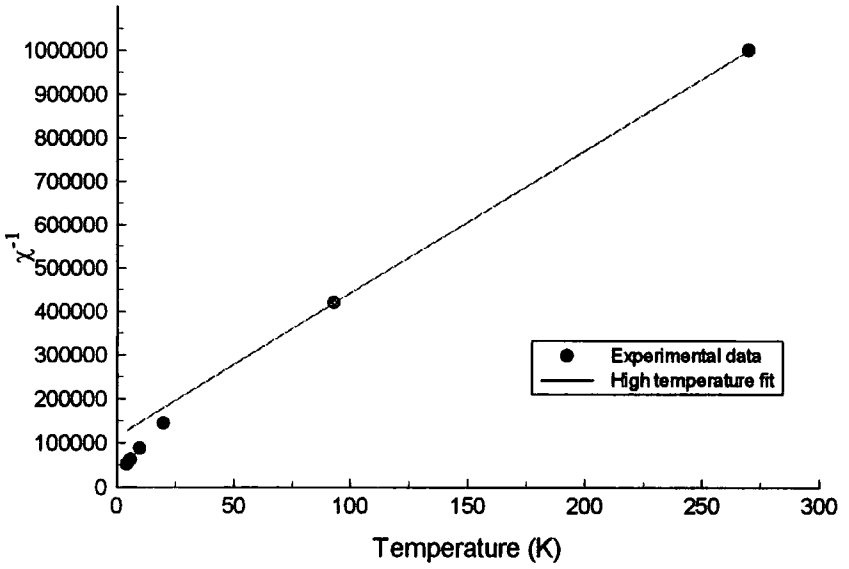

Figure 8.6 Susceptibility of $Cd_{0.9}Mn_{0.1}Te$:In

An extrapolation of the high temperature susceptibility, by use of a Curie Weiss fit, shows a value of $\theta = -34.96K$. This is very close to the expected value of $\theta = -35K$ that would be expected for this sample [19].

The photomagnetisation measurement was performed in a magnetic field of 0.1T, as this was the lowest field which would give the required signal to noise ratio. The temperature of the measurement was 4K. The resulting data is shown in figure 8.7.

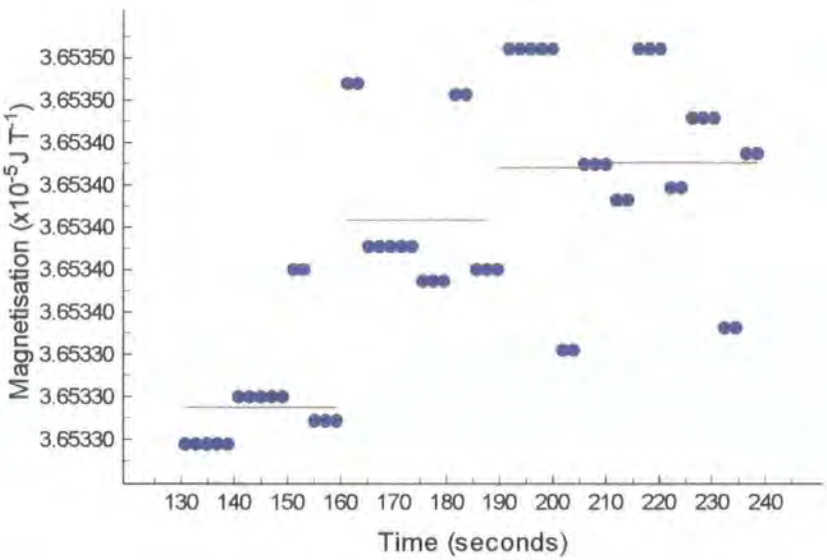

Figure 8.7 Observation of photomagnetisation in $Cd_{0.9}Mn_{0.1}Te$:In

In the above figure, the light is flashed on and off rapidly at 160, 190, and 210 seconds. The horizontal red lines represent the standard deviation of the magnetisation in that section of time. Further illumination beyond 240 seconds showed no further change, even under continuous illumination, and from this we conclude that the change in magnetisation has saturated.

The value of ΔM, the saturation photomagnetisation is $2.2 \times 10^{-9} JT^{-1}$, which corresponds to a change of 0.01%, which is over an order of magnitude smaller than the value of 0.4% observed by Wojtowicz *et al* [18].

The intensity of the incident illumination was measured *in situ* in the Faraday balance by means of a photodiode. The sample was contacted, and placed in an optical cryostat, and illuminated with light from the same source at the same incident intensity. The photoconductivity of the sample was measured at 4.0K, the temperature of the magnetic measurement, and then the resistance at 25.3K was measured. The sample was then transferred to the electrical transport rig that is outlined in section 4.3, where a characterisation of carrier concentration and resistivity at 25.3K. Because no Hall measurements are possible in this sample at 4.0K, the Hall data was taken at 25.3K, and so the resistivity at this temperature allows us to calculate the increase in carrier concentration at 4.0K.

Analysis of the spectra of the illumination source showed that it was very weak in the infra red part of the spectrum, the region generally used for the illumination of CdMnTe samples, given that the value of E_{OPT} is in the infra red part of the spectrum [2]. The spectra is shown below in figure 8.8, along with that of a normal tungsten bulb for comparison.

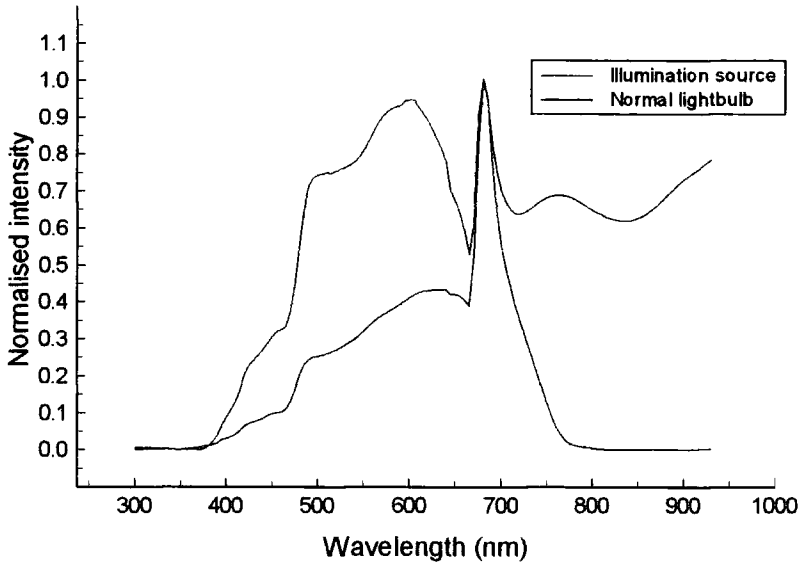

Figure 8.8 The spectra of the illumination source (not compensated for the spectral dependence of the detector)

The values of the resistance obtained are summarised in table 8.1 below.

Flash Number	R(4.0K)	R(25.3K)
0	>>300MΩ	79.42MΩ
1	13.8MΩ	0.932MΩ
2	7.74MΩ	0.526MΩ
3	3.85MΩ	0.338MΩ
4	2.65MΩ	0.238MΩ

Table 8.1 The resistance of the $Cd_{0.9}Mn_{0.1}Te$:In sample under illumination

Immediately after the removal of the illumination, the value of the resistivity is seen to relax towards a higher value, becoming stable after 2 minutes. This suggests that although the illumination source is creating persistent photoconductivity in the sample, it is

also creating conventional short lived photoconductivity. It is also possible that the photoionisation cross section of the DX centre is wavelength dependent, and the use of higher frequency light is not as efficient as the infra red normally used. At present no work has been performed to test this hypothesis.

The carrier concentration of the sample at the known resistances was then measured using an infra red LED for the illumination. This gave the graph that is shown in figure 8.2. A good fit to the data can be achieved using equation 8.5.

$$N_D^{ELEC} = 1.06\text{x}10^{22}\text{x(resistance)}^{-1.25} \quad (8.5)$$

and from this we can calculate that the illumination of the sample in the photomagnetisation experiment will have created $N_D^{ELEC} = 1.92\text{x}10^{15} cm^{-3}$.

Following the work of Dietl and Spalek [8,9] we can use the change in magnetisation to calculate the number of donors created on illumination. Using equation 8.3 we can calculate N_D^{MAG}.

$$\chi_P = \frac{N_D \mu_B^{\,2}}{4k_B T} \cdot g_{eff}^{\,2} \cdot \left[\frac{1 + \frac{\varepsilon_p}{3k_B T}}{1 + \frac{\varepsilon_p}{k_B T}} \right] \qquad (8.6)$$

Taking the polaron binding energy ε_p to have a value of 0.140meV [20], and g_{eff} to have a value of 40.2 [21], we can calculate that in order to achieve the observed polaron susceptibility of $0.757\text{JT}^{-2}\text{m}^{-3}$, we would require a donor concentration of $N_D^{MAG} = 1.28\text{x}10^{15}\text{cm}^{-3}$. This compares favourably with the observation made in the Hall measurements of $N_D^{ELEC} = 1.921\text{x}10^{15}\text{cm}^{-3}$.

Other work on the photomagnetisation of CdMnTe:In by Terry *et al* [22], has shown the observation of a polaron susceptibility of $7.32JT^{-2}m^{-3}$, with a change in donor concentration of $1.5x10^{17}cm^{-3}$. Combining the results of Wojtowicz *et al*, Terry *et al* and the present work leads to the observation that there must be a mechanism so that the measured carrier concentration does not equal the number of polarons formed.

8.7 Model for polaron formation in the band tail

Although the formation of magnetic polarons is expected to strongly influence the magnetotransport of a sample, Stankiewicz [23] has measured persistent photomagnetisation in samples of $Cd_{1-x}Mn_xTe$ with $x<0.01$ which do not show the expected negative magnetoresistance (see section 8.4). We propose an alternative model to that of Wojtowicz *et al* to qualitatively explain this phenomena.

Before illumination, the sample consists of DX centres lying in the deep state, and a shallow donor band just below the conduction band edge. This is shown in figure 8.9.

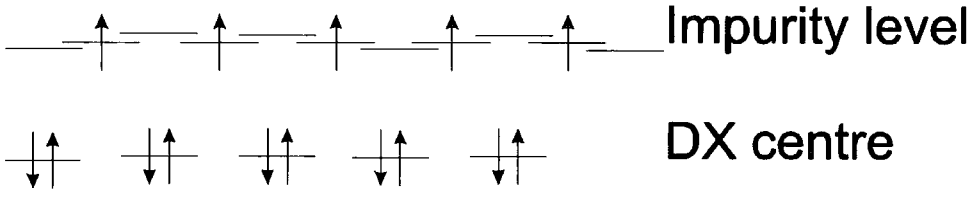

Figure 8.9 CdMnTe before illumination

Upon illumination, one of the electrons from the deep state is excited to the donor band, and the remaining electron also moves into this band as the indium ion returns to the substitutional site. Polarons will be formed at these centres, and the transport of the system will be affected. The newly formed donor state may only be in the tail of the donor band, rather than close to the Fermi energy. The transport of the sample is determined by

the carriers excited from the Fermi energy to the conduction band edge. Now as the newly created donors in the band tail will not affect the transport. This is shown in figure 8.10.

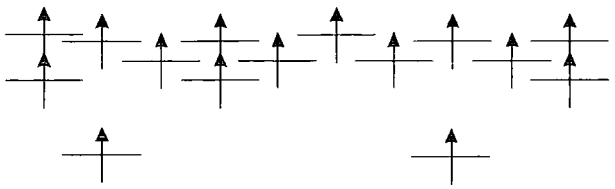

Figure 8.10 Polaron formation after illumination

The 'Deeper' shallow donors in the band tail, shown in the above figure, will be more likely to produce magnetic polarons, because of the high electrostatic binding of the electron, as discussed in section 8.3 Thus these only account for a fraction of the number of created donors, and so the number of polarons formed will be smaller than the donor concentration measured by the Hall effect, which samples only those electrons excited to the conduction band edge.

8.8 Conclusions

The persistent change in the magnetisation of a sample of $Cd_{0.9}Mn_{0.1}Te$:In has been measured using a modified commercial Faraday balance magnetometer. The change in magnetisation has been compared to the Dietl and Spalek model of polaron formation, and the donor concentration in the sample calculated from this, $\Delta N_D^{MAG} = 1.28\text{x}10^{15}\text{cm}^{-3}$. The donor concentration has been calculated from Hall data, $\Delta N_D^{ELEC} = 1.921\text{x}10^{15}\text{cm}^{-3}$, and a model has been proposed based on donors in the band tail, to explain the discrepancy between the two values obtained in the present work and that reported by Wojtowicz *et al* [18].

Reference List Chapter 8

[1] Khatchatunyan, K., Kaminska, M., Weber, E.R, Becla, P., Street, R.A., Phys Rev, **B40**, (1989), 6304

[2] Theis, T.N., Mooney, P.M., Parker, B.D., J Electron Matter, **20**, (1991), 35

[3] von Molnar, S., Terry, I., Becla, P., Penney, T., McElfresh, M.W., Proc Conf Localistaion 1990, **Inst Phys Conf ser 109**, (1990), 29

[4] Terry, I., Penney, T., von Molnar, S., Rigotty, J.M., Becla, P., Solid State Comm, **84**, (1992), 235

[5] Sheinman, M.K., Shik, A.Y., Sov Phys Semicon, **10**, (1976), 128

[6] Kasuya, Solid State Com, **8**, (1970), 1543

[7] Golnik, A., Ginter, J., Gaj, J., J Phys, **C16**, (1983), 6073

[8] Planel, R., Gaj, J.,Guillaume, B., Proc 1st Intl Meeting on Magnetic Semiconductors, Montpellier, J Phys Coll, **41**, (1980), C5

[9] Dietl, T., Spalek, J., Phys Rev Lett, **48**, (1982), 355

[10] Dietl, T., Spalek, J., Phys Rev, **B28**, (1983), 1548

[11] Heikes, R., Chen, C., Physics, **1**, (1964), 159

[12] Holtzberg, F., McGuire, T., Methfessel, S., Suits, J., Phys Rev Lett, 13, (1964), p18

[13] von Molnar, S., Methfessel, S., J Appl Phys, **38**, (1967), 959

[14] Krenn, H., Zawadzki, W., Bauer, G., Phys Rev Lett, **55**, (1985), 1510

Krenn, H., Kaltenegger, K., Dietl, T., Spalek, J., Bauer, G., Phys Rev, **B39**, (1989), 10918

[15] Enichlmair, H., Kaltenegger, K., Krenn, H., Bauer, G., Dietl, T., Humenberger, J., J Cryst Grow, **117**, (1992), 844

[16] Awschalom, D.D., Warnock, J., Rozen, J.R., Ketchen, M.B., J App Phys, **61**, (1987), 3532

[17] Awschalom, D.D., Smyth, J.F., Samarth, N., Luo, H., Furdyna, J.K., J Luminescence, **52**, (1992), 165

[18] Wojtowicz, T., Kolesnik, S., Miotowski, I., Furdyna, J.K.,, Phys Rev Lett, **70**, (1993), 2317

[19] Oseroff, S.B., Phys Rev, **B25**, (1982), 6584

[20] Calculated from data in Petersen, D.L., *et al*, Phys Rev, **B32**, (1985), 323

[21] Calculated from data in Krenn, H., Kaltenegger, K., Dielt, T., Spalek, J., Bauer, G., Phys Rev, **B39**, (1989), 10918

[22] Terry, I., *et al*, unpublished

[23] Stankiewicz, J., Private communication

Chapter Nine Conclusions

9.1 Summary of the work on HgMnTe

The major observation of this work is that the transport and magnetisation of layers of $Hg_{1-x}Mn_xTe$ grown by MOVPE is dominated by the existence of MnTe clumps in the samples. This is supported by the work of Munekata *et al* [1] who, in their studies of MBE grown $In_{1-x}Mn_xAs$, found that for certain values of x, their measurements were dominated by the existence of MnAs, a ferromagnetic material. The idea of the clumps in the HgMnTe samples is based on the observation of the anomaly in the resistivity (see section 6.9.2), the saturating room temperature magnetisation (section 7.1) and the magnetoresistance under illumination.

The formation of clumps in HgCdTe is a well documented fact, and it has been shown by Edwall *et al*, [2] that HgTe forms precipitates during growth by MOVPE. Other work by Jones *et al* [3] has shown that the formation of these precipitates is higher close to dislocations, such as those close to the CdTe/HgMnTe boundary in these samples [4].

The growth of these clumps in the samples leads to speculation of their crystal structure. The HgMnTe samples themselves are in the expected zinc blende structure, and from a crystallographic viewpoint it would be more logical for the MnTe to form clumps in the same structure. This would seem to explain the magnetoresistance of sample MMT34, and the resistance anomalies, where the effect is noticeable close to the 60K Neel temperature of zinc blende MnTe. [5] In contrast to this, the observation of weak ferromagnetism at room temperature, which is possibly due to vacancy ordering, suggests

the existence of NiAs MnTe, as it has a Neel temperature of 310K [6]. However, the Interdiffused Multilayer Process (IMP) used in the fabrication of these samples grows very thin layers of alternating MnTe and HgTe before diffusing them to form HgMnTe. Because the layers of MnTe are so thin it is expected that the MnTe will grow in the zinc blende structure.

The clumps in the material have been observed directly, via the use of high resolution X-ray diffraction by Moore [7], and also via the use of EDAX. The figure below shows the manganese concentration across the surface of sample MMT38A. The average is taken from the statistical deviation of the points, and agrees well with the value used in the previous chapters.

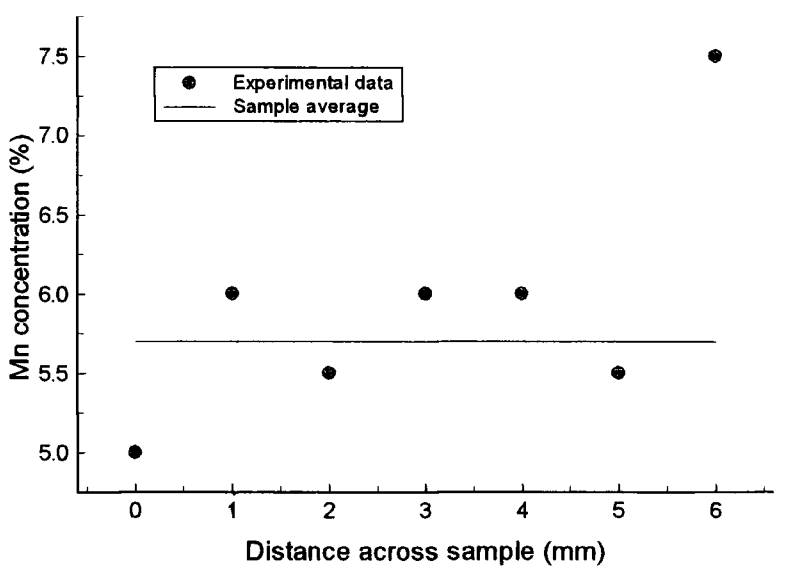

Figure 9.1 EDAX trace of sample MMT38A

The point to the right hand end of the graph is taken from one of the numerous dark looking areas on the sample surface. Note that the value obtained from EDAX will

not correspond to true MnTe, as the depth of penetration of the electron beam will be far greater than the spatial extent of the clump, and consequently will include contributions from the surrounding HgMnTe.

One question that should be asked is, does the existence of the clumps originate from a problem in the growth system used? Evidence against this conclusion comes from the fact that Hallam [8] investigated the electrical properties of a few samples produced by IMP, and did not observe any of the anomalous behaviour reported in this work. However the magnetic properties of the samples were not investigated, and it is possible that such truly bulk measurements might have revealed more of the true nature of the materials.

It is likely that the behaviour of the sample is very sensitive to the growth conditions, and it has been shown [9] that the dynamics of the growth process are generally not reproducible, and turbulent flow can occur, giving rise to unexpected sample properties. In general the samples used in this study have shown the existence of some wonderfully interesting behaviour, and have given rise to the observation of some interesting physics. However at the present time, the reproducibility of the samples is not sufficiently high to be of commercial use for device fabrication.

9.2 Further work

A number of other HgMnTe samples have been grown by IMP which have, as yet remained uninvestigated. It would be interesting to study these specimens to ascertain whether they show similar properties to those already investigated. Further investigation is also required in to the temperature dependence of the magnetic susceptibility of the

samples that show the anomalous transport, and the persistent photoconductivity, in an effort to gain a better understanding of the mechanisms involved.

The work on the AlGaAs Hall device, outlined in section 5.2, should be continued using a paramagnet whose magnetic properties are known in the temperature range of interest. Once such a calibration has been undertaken, the device will be a very useful and convenient probe of the magnetisation of the DMS samples.

Finally, the temperature dependence of the photomagnetisation of CdMnTe:In needs to be investigated to enable a more complete comparison to theory of bound magnetic polarons to be made. Also, it would be interesting to study the variation of the photomagnetisation as a function of the localisation radius of the bound electron, in the region of the metal-insulator phase transition.

Reference List Chapter 9

[1] Soo, Y.L., Huang, S.W., Ming, Z.H., Kao, Y.H., Munekata, H., Chang, L.L., Phys Rev, **B53**, (1990), 4905

[2] Edwall, D.D., Gertner, E.R., Bublac, L.O., J Cryst Growth, **86**, (1988), 240

[3] Jones, I.P., Cheng, T.T., Aindow, M., Gough, J., Graham, A., Giess, J., J Cryst Grow, **159**, (1996), 1096

[4] Tatsuoka, H., Durose, K., Funaki, M., IOP Conf Ser, **134**, (1993), 421

[5] Ando, K., Takahashi, K., Okuda, T., J Mag and Mag Mat, **104-107**, (1992), 993

[6] Komatsubara, T., Murakami, M., Hirahara, E., J Phys Soc Japan, **18**, (1963), 356

[7] Moore, C.D., 'X-Ray scattering studies of compund semiconductors', PhD thesis, University of Durham, 1997

[8] Hallam, T.D., 'The characteristaion of epitaxial layers of the dilute magnetic semiconductor $Hg_{1-x}Mn_xTe$', PhD thesis, University of Durham, 1995

[9] Funaki, M., Brinkman, A.W., J Cryst Growth, **139**, (1994), 211